Title
On the Sun's faintest coronal hard X-rays

Permalink
https://escholarship.org/uc/item/11n850dr

Author
Buitrago Casas, Juan Camilo

Publication Date
2022

Peer reviewed|Thesis/dissertation

On the Sun's faintest coronal hard X-rays

By

Juan Camilo Buitrago Casas

A dissertation submitted in partial satisfaction of the

requirements for the degree of

Doctor of Philosophy

in

Physics

in the

Graduate Division

of the

University of California, Berkeley

Committee in charge:

Professor Stuart Bale, Chair
Professor David Attwood
Professor Lindsay Glesener
Professor Forrest Mozer

Spring 2022

On the Sun's faintest coronal hard X-rays

Abstract

On the Sun's faintest coronal hard X-rays

by

Juan Camilo Buitrago Casas

Doctor of Philosophy in Physics

University of California, Berkeley

Professor Stuart Bale, Chair

Solar flares are the most vigorous explosive phenomena in our solar system. They release up to $\sim 10^{33}$ erg of magnetic energy in the Sun's corona in times that range from minutes to hours. Some 10 to 50% of the flare energy goes into electron acceleration. Among other processes, when these electrons interact with the ambient plasma, they produce bremsstrahlung radiation in hard X-rays (HXRs). Analyses of flare HXRs are critical for understanding energy release dynamics, acceleration mechanisms, and their connection with other phenomena in the corona. One of these phenomena is coronal heating, an open problem in heliophysics. This problem seeks to clarify why the Sun's coronal temperature is up to three orders of magnitude higher than that at the Sun's surface.

Coronal temperatures demand a mean energy input between $\sim 10^5$ and 2×10^7 erg cm^{-2} s^{-1}. Multiple observations have proven that medium and large-size flares together do not contribute enough energy to account for these input power requirements. Instead, a popular idea proposes that the solar atmosphere is filled with small impulsive heating events releasing magnetic energy in the corona, called nanoflares. If nanoflares follow the same physics as their larger counterparts, they should emit hard X-rays (HXRs) but with substantially fainter intensity. A copious and continuous presence of nanoflares would result in sustained HXR emission. These nanoflares could deliver sufficient energy into the Sun's corona, to account for its high temperatures. To date, there has not been any direct detection of such persistent HXRs emitted from the quiescent Sun. However, ~ 12 days of solar off-pointing observations of the Reuven Ramaty High Energy Solar Spectroscopic Imager (RHESSI) during periods of quiescent activity led to HXR upper limits. In the 6-12 keV energy range, e.g., this upper limit is 9.5×10^{-4} photons s^{-1} cm^{-2} keV^{-1}.

Observing faint HXR emission is challenging because it demands instruments with high sensitivity and dynamic range. RHESSI has insufficient sensitivity to detect such faint sources, especially in the form of a broad, diffuse signal rather than the bright, compact signals for which RHESSI was designed. The Focusing Optics X-ray Solar Imager (FOXSI)

sounding rocket experiment excels in these two attributes. FOXSI has a sensitivity of $\sim$ 0.0032 photons cm^{-2} s^{-1} keV^{-1} ($\sim$50 times that of RHESSI) at 8 keV and a dynamic range of $\sim$100 for sources $>$ 30 arcsec apart. FOXSI achieves such a superior performance by pairing nested grazing-incidence Wolter-I mirrors with low-noise semiconductor detectors optimized for high energies. FOXSI's direct focusing capabilities allow quiet regions of the corona to be isolated to look for the presence of HXR sources.

This thesis constrains the quiet Sun emission in the 5-10 keV energy range using FOXSI observations from the second and third rocket flights (FOXSI-2 and -3). To fully characterize FOXSI's sensitivity, this thesis presents a thorough optics calibration and a ray-tracing simulation to assess ghost ray backgrounds generated by sources outside of the telescope field of view. This work demonstrates a Bayesian approach to provide upper thresholds of quiet Sun HXR emissions and probability distributions for the expected flux of a quiet-Sun HXR source when it is assumed to exist. For FOXSI-2 and -3, such upper limits are 4.5×10^{-2} photons s^{-1} cm^{-2} keV^{-1} and 6.0×10^{-4} photons s^{-1} cm^{-2} keV^{-1}, respectively (both in the 5-10 keV energy range). These two limits are similar to that of RHESSI in the 6-12 keV energy band (9.5×10^{-4} photons s^{-1} cm^{-2} keV^{-1}) but with an important difference: it took $\sim$1/2600 less integration time for FOXSI to get enough statistics to yield these equivalent limits. The FOXSI-2 limit presented in this doctoral work is the first-ever quiet Sun upper threshold in HXR estimated from observations performed during a period of high solar activity. This dissertation's quiet Sun HXR analyses during a solar cycle minimum are the first scientific results that use the $\sim$ 6.5 minutes of the FOXSI-3 rocket observations. A possible future spacecraft using FOXSI's concept would allow enough observation time to constrain the current HXR quiet Sun limits further or perhaps even make direct detections. This last objective would demand observations of a few hours at the very least and (ideally simultaneous) onboard measurements of the backgrounds. Any upper quiet Sun HXR limit constrains the parameter space (e.g., the index and cutoff energy for thick target power-law models) that nanoflare electron energy distribution can have. The limits found in this doctoral work suggest very steep spectra, i.e., $>$ 5 power-law indexes when we assume nanoflare accelerated electrons follow a thick target model (in agreement with earlier RHESSI-based results).

Dedicado a mi madre Miriam Casas Casas. Su trabajo constante y amor de madre son la razón de fondo de este éxito y el de mis tres hermanos.

Contents

List of Figures

List of Tables

Acknowledgments

First and foremost, I would like to thank my supervisor, Professors Stuart Bale, and mentor, Professor Lindsay Glesener (Linz). Their consistent assistance and dedicated involvement in every step throughout my Ph.D. process are among the main reasons I am successfully coming to the end of this journey today. I thank both of you very much for your constant support and understanding over these past years. Special thanks to Linz, who has been an extraordinary role model and perceptive and cheerful mentor in my professional life. Linz will always have my gratitude for have positively challenged me every time I needed it.

I would also like to show gratitude to the other members of my dissertation committee, Professor Forrest Mozer and Professor David Attwood. Forrest raised several precious questions during my qualifying exam. I hope I managed to address several of them adequately. In 2016 I took David's class on X-ray interaction with matter. His enthusiasm for the topic made a strong impression on me. I have always carried positive memories of his classes and tried to apply what I learned there to my field.

I want to express my appreciation to Dr. Säm Krucker, who has supervised and supported my work for FOXSI. Thanks to Dr. Steve Christe for many valuable discussions and Dr. Juan Carlos Martínez Oliveros for his limitless mine of snarky comments. I'd especially like to thank Juan Carlos for frequently allowing me to speak my mind more freely than would probably be reasonably advised.

In the Fall of 2017 and the Spring of 2018, I went to the Redstone Arsenal at the NASA Marshall Space Flight Center (MSFC) in Huntsville for several weeks to do measurements to characterize the FOXSI optics. My time at the Stray Light Facility (SLF) was highly productive. Working with the heliophysics and X-ray optics groups was an extraordinary experience. Much of the analysis presented in Chapter 4 was possible thanks to the hard work of many people during my visit to Marshall. I want to explicitly thank Dr. Brian Ramsey, Dr. Amy Winebarger, Dr. Sabrina Savage, Dr. Wayne Baumgartner, Dr. Patrick Champey, Dr. Stephen Bongiorno, and the rest of the MSFC team for kindly assisting my work at the SLF. I must also thank Sasha Courtade, and Dr. Athiray Subramania for their tremendous collaboration during the optics calibration process.

I will carry unforgettable memories from my time at the Space Sciences Laboratory. Many fabulous fellows and researchers have influenced positively on me. I cannot name them all but want to thank Dr. Hazel Bain, Dr. Claire Raftery, Dr. Pascal Saint-Hilaire, Dr. Hugh Hudson, Dr. Jim McTiernan, Dr. John Bonnel, Dr. Nicole Duncan, Sam Badman, Roger Roglans, Chris Moeckel, Gwen Hanley, and Claire Gasque. I would also like to show gratitude to all members of the FOXSI team for the fascinating moments around getting ready to launch rockets. Special thanks to Dr. Juliana Vievering, Dr. Sophie Musset, Dr. Noriyuki Narukage, Dr. Shin-nosuke Ishikawa, Paul Turin, Gregory Dalton, and the many

other members of the FOXSI team.

My fellow Jessie Duncan traveled all the way from the East coast to Berkeley in the Spring of 2022 to join this dissertation writing adventure. We both kept accountable to each other during long hours of writing and more writing. Thanks Jessie!

I will never forget our first years of PhD teaching the 111 lab and doing HWs with Joe Broz, Sam Ciocys, Dylan Rees, Shawn Beckman, and Jessica Avva. I look forward to witnessing the successes my talented Fellows will accomplish in their lives.

To get to this point in my professional life, critical people in the past played a significant role in my formation. Among many great scientist and professors, I want to give special thanks to Professor Benjamín Calvo-Mozo and Santiago Vargas Dominguez. They taught me their you passion for Science and for understanding our star. Thanks to both of you!

Getting through my dissertation not only required academic support. There are many people I have to thank for their constant tolerance, patience, and love during the past years. I must thank Van and Aunyce for being my roommates during my entire PhD. Thanks for creating the most delicious chili beans with cheese and for unforgettable nights becoming Lego Masters while watching Lego Masters (but the good version, the Australian!).

Last but not least, many heartfelt thanks to my family. I decided to write the following lines to them in my native language, the same language I have always used with them to truly express our feelings.

Hoy particularmente me siento muy honrado de mis orígenes. Me siento infinitamente agradecido con mi madre, esa campesina Raquireña, que con su profundo amor y dedicación de toda una vida ha sido el cimiento de una familia muy fuerte. Ni mi madre ni yo fuimos conscientes del poder transformador que tuvieron todas las horas que ella dedico en mi niñez a sentarse a aprender conmigo tareas tan complejas en su momento como lo fue dividir por dos cifras. Gracias mamá. Tu esfuerzo es la razón de que mis hermanos y yo estemos recogiendo grandes frutos. Te amamos. Mi padre nos enseño el trabajo duro y determinación extrema por alcanzar nuestros objetivos. Sin duda esos valores también tuvieron un gran efecto en mis hermanos y en mi.

Quiero agradecer a la flaca, a la gorda, a lala y a gabys por su incesante apoyo a pesar de la gran distancia que hay entre Bogotá y Berkeley. Ellos probablemente no dimensionan lo mucho que los amo, los extraño, y lo que significan en mi vida.

Ciertamente, este paso profesional en mi vida no hubiera sido posible de no ser por el amor contante y apoyo de mi prometida y próxima esposa Andrea López. Desde el día en que decidimos construir un hogar a dos manos, hemos sido los mejores cómplices uno del otro. Juntos, somos un equipo imparable. Disfruto ver sus logros y la forma en que trabajamos por hacernos mejores humanos mientras caminamos de la mano por la vida. Uno al lado del

otro siempre. Me emociona mucho pensar en las muchas aventuras y buenos momentos que han de venir para nuestro hogar en todas las décadas que nos quedan por delante.

Chapter 1

Introduction

The Sun is the most investigated star and the primary object to validate stellar models (Tayler, 1997). Despite being the most understood star, there are still many open questions on its physics that the heliophysics community continuously explores. Among these puzzles lies the coronal heating problem, i.e., why the Sun's upper atmosphere's temperature is millions of kelvin higher than its surface (e.g., Aschwanden et al., 2007). Numerous hypotheses try to answer this question, some of them relying on detecting the faintest solar hard X-rays (HXRs), which is the gist of this thesis.

1.1   The Sun as a physical system

Table 1.1 summarizes the main parameters when the Sun is considered as a physical system. Under the Harvard spectral classification system, developed by Annie Jump Cannon and Cecilia Payne, the Sun is a G2V star (Phillips, 1995). The letter G classifies the Sun by color as a yellowish-white star with weak hydrogen lines. The number 2 indicates that the Sun is a hot star in the G-class. The roman number five (V) represents that the Sun remains in hydrostatic equilibrium as described by the main sequence stars' physics defined on the Hertzsprung–Russell diagram (Chandrasekhar, 1957).

According to the standard solar model, the Sun generates 99% of its power within $\sim 0.25 R_\odot$ from its center by nuclear fusion reactions, mainly via the proton-proton chain (Bahcall et al., 1990). Every second, 4×10^{38} protons convert into helium nuclei, releasing 4×10^{26} Watts. Due to the high opacity of the solar interior, statistically, it takes from 10^4 to 2×10^5 years for this energy to reach the solar surface (Mitalas et al., 1992). An interested reader can find a classic review of the nuclear energy release and posterior transport to the surface in Cox et al. (1991).

Some of the most remarkable physical processes occurring at the Sun involve its inherent magnetic field. The scientific consensus hypothesizes that the global solar magnetic field is

Star	G2V (yellow dwarf)
Mass composition	73% H, 25% He, + heavier elements
Energy	Nuclear fusion
Trans. Energy	Radiation y convection
Temperature	Core:15×10^6K Photosphere: 6×10^3K Corona: 5×10^6K
Mean density	1.4×10^3 kg m^{-3}
Radius ($R_\odot$)	$\sim$700.000 km
Mass-loss rate	10^9 kg s^{-1}

Table 1.1: Primary parameters describing the Sun as a star.

generated via a dynamo at $\sim 0.7R_\odot$ in a region named the tachocline (Hughes et al., 2007). Together with the solar differential rotation, the global solar magnetic dipole produces a relatively rapidly changing magnetic configuration observed in zones over the solar surface. Abrupt reconfiguration of the magnetic field causes all sorts of eruptive events, e.g., solar flares (e.g., Grimes et al., 2020).

1.1.1 The Sun in zones

The Sun's physics follows specific regimes in three distinct solar interior regions, known as the **core**, **radiative**, and **convection zones**. The outermost parts of the Sun distribute into the photosphere, chromosphere, transition region, and the corona, where the solar magnetic field actively influences the dynamics there. Figure 1.1 summarizes the whole solar structure in zones. The solar center is an enormous nuclear reactor continuously converting nuclear energy into other forms of energy that flow across the radiative zone via radiative diffusion (Eff-Darwich et al., 2012). Radiative diffusion is the most efficient energy transport process until $\sim 0.7R_\odot$, where a thin discontinuity layer, namely the tachocline, is located (Hughes et al., 2007). From that layer, the energy is more efficiently transported outward via convection. The scientific community widely holds that a dynamo at the tachocline is responsible for the Sun's large-scale magnetic field (see for instance Archontis et al., 2004; Miesch, 2005 and Fan, 2009).

The Sun can be modeled as being in thermal equilibrium, which means that the energy generation by nuclear fusion inside the star balances out energy leakage out of the star (e.g., Christensen-Dalsgaard, 2021). Because of the Sun's spherical symmetry, for any spherical shell within the solar interior of radius r, the thermal balance is expressed via

$$\mathcal{L}_{r+dr} - \mathcal{L}_r = 4\pi r^2 \rho \epsilon \, dr, \tag{1.1}$$
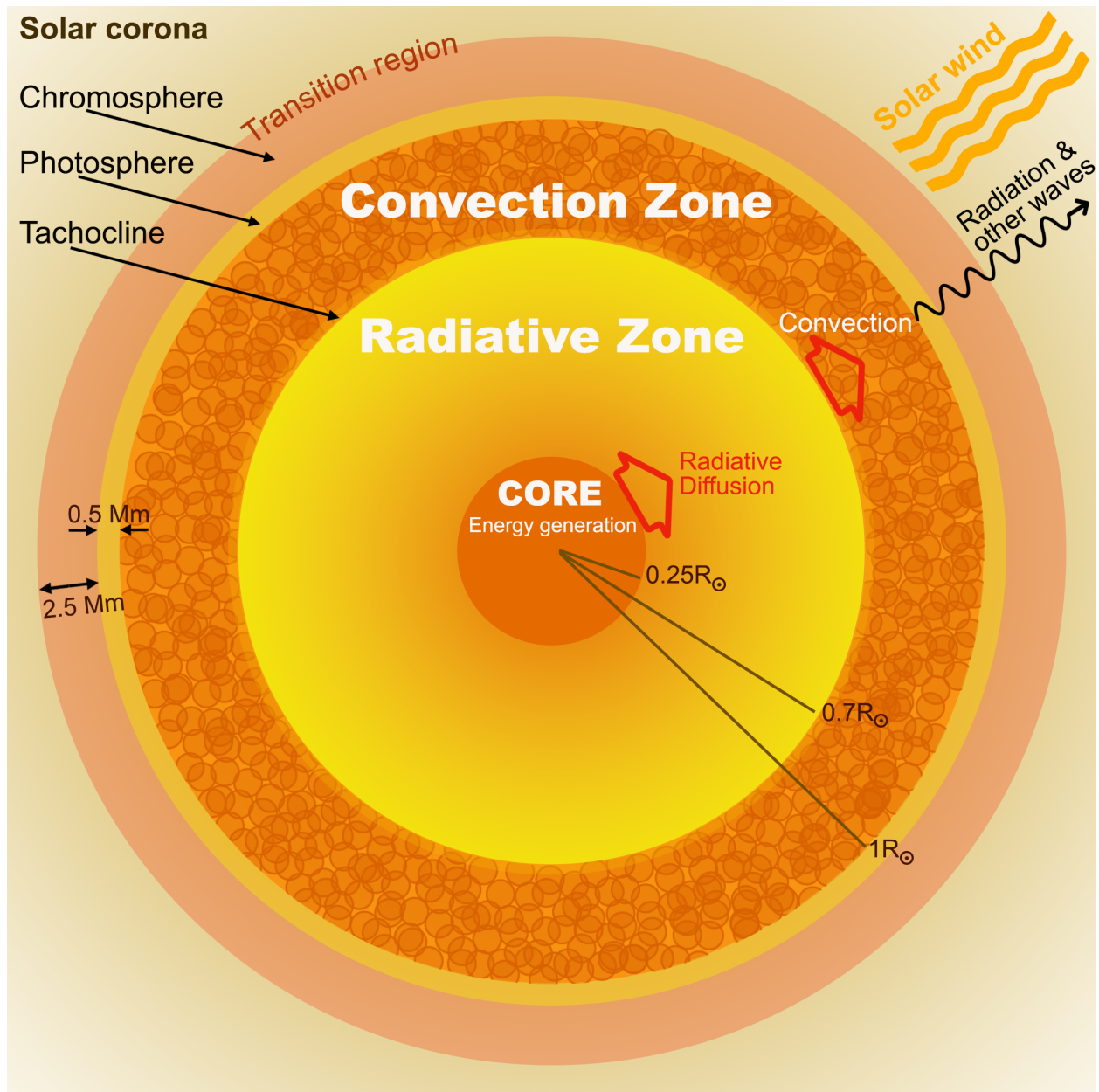
Figure 1.1: Illustration (not drawn to scale) of the various concentric layers making the structure of the Sun. The convection zone surrounds the radiative region, which covers the core. In the upper atmospheric layers, the boundary between the chromosphere and corona (the transition region) is highly variable, but I have represented a standard quiet Sun situation. For every layer, I have highlighted the primary energy transport mechanisms.

where $\mathcal{L}_r$ is the total power, or luminosity, entering (or leaving) the shell's inner face; $\mathcal{L}_{r+dr}$, ρ is the local mass density, and ϵ is the energy generation rate per unit mass. Equation 1.1 in its Lagrangian form is

$$\frac{d\mathcal{L}_r}{dM} = \epsilon,$$

with $dM = 4\pi r^2 \rho \, dr$ (Priest, 2014). A wide range of physical factors come into the thermal balance expression. The energy generation rate (ϵ) depends on the type of star. For the Sun, the main two ways of fusing hydrogen (^{1}H) into helium (^{4}He) are the proton-proton (pp) chains and the carbon-nitrogen-oxygen (CNO) cycles (Bahcall et al., 1996; Adelberger et al., 2011; Collaboration et al., 2020; Wilson, 2021). The luminosity, which balances out the energy generation, heavily depends on the major energy transport mode among the usual three: radiation, convection, and conduction. Fick's law can represent the energy transport dynamic within the solar radiative zone.

$$\mathcal{L} = -4\pi r^2 \, \mathcal{D} \, \frac{d(aT^4)}{dr}, \tag{1.2}$$

where aT^4 is the classic radiation density and $\mathcal{D}$ a diffusion coefficient which depends on the opacity of the medium (κ), $\mathcal{D} = c/3\kappa\rho$ (c is the speed of light) (Hansen et al., 2012).

Above $\sim 0.7 R_\odot$ the temperature gets low enough for some electrons to combine with ions producing a high opacity. The highly opaque plasma prevents radiation from being an effective transport process. The energy is accumulated there, which dramatically increases the temperature gradient, which according to equation 1.2 is

$$\frac{dT}{dr} = -\frac{3\kappa\rho}{aT^3} \frac{\mathcal{L}}{4\pi r^2}. \tag{1.3}$$

The high-temperature gradient produces convective instabilities. Plasma blobs that are hotter than their surroundings rise outwards in turbulent cells until the physical parameters are such that the opacity no longer prevents energy from being radiated (e.g., Basu, 2019). The cold plasma loses its buoyancy and sinks. The upper spherical layer where the convective cells release their heat excess in the **photosphere** (historically known as the solar surface). There, convective cells dominate in two types, *granulation* (sizes on the order of 1 Mm) and *supergranulation* (cell conglomerates of 20–70 Mm in size). Granulation is not the only phenomenon observed in the photosphere. Sunspots, faculae, prominence, pores, *plages* (French for beaches), bright points, and others are photospheric phenomena produced by

the solar magnetic field's structure and dynamics (e.g., Chitta et al., 2020).

The **chromosphere** is a spherical shell (2.5-5 Mm thick) of the solar atmosphere just above the photosphere and below the transition region. The chromosphere particle density decreases outwards in a complex way (see Figure 1.2) from $n \approx 10^{18}$ cm^{-3}, in the photosphere proximity, down to $n \sim 10^9$ cm^{-3} at the frontier with the transition region (Carlsson et al., 2019). In addition to the low densities, the relatively low temperatures (from ~ 3800 K up to tens of thousands of Kelvins) make the chromosphere a region dominated by emission lines rather than absorption spectra. In particular, the chromosphere has a strong emission at 6563 Å, corresponding to the first line of the Balmer series (Hα) (Leenaarts et al., 2012). The chromosphere's plasma trace magnetic field lines into a wide range of phenomena, including filaments (loops on disk), prominences (loops prolonging off the solar limb), spicules, brighter network cells, periodic (and quasi-periodic) oscillations, etc (Athay, 2012).

The **transition region** exists on top of the chromosphere, where several transitions in the solar atmosphere's physics occur as a response to the coronal heating-up. The transition region is **not** a thin static spherical shell at a particular solar radius. Instead, it is present as a narrow layer the quiet Sun, while it might take the form of spicular jets near coronal loops and erupting events (Bewsher et al., 2002). These phenomena produce ultraviolet (UV) and extreme ultraviolet (EUV) emission lines (dominated by ions such as CIV, OIV, and SiIV) and radio emission in the 10 cm to 1 m wavelength range, which together are observably used to diagnose physical conditions in the transition region(Mariska, 1992; Peter, 2001). One of the most outstanding features characterizing the transition region is its severe temperature gradient, from $\sim 2 \times 10^4$ K at its base up to $\sim 10^6$ K at the corona's verge (see figure 1.2). Physical processes pass from a collisional and partially ionized regime in the chromosphere to a collisionless and fully ionized plasma in the corona (Fontenla et al., 1993). This region plays an essential function in the energy and mass transfer in both solar eruptions and the quiescent Sun, a cornerstone to understanding coronal heating and solar wind origin. According to Tian (2017), high-resolution imaging and spectroscopic observations of the upper transition region and the corona will allow us to trace mass and energy from the lower atmosphere to the corona and understand the dynamics of eruptive phenomena in the corona.

The **corona** is the outermost part of the Sun's atmosphere. Its lower boundary is the Alfven surface, at $\sim 10^7$ km (Kasper et al., 2021) from the photosphere. The corona permeates the entire solar system beyond the transneptunian objects out to the heliopause, at $\sim 1.8 \times 10^{10}$ km from the Sun (Gurnett et al., 2019). The corona temperature is 150 to 450 times higher than the photosphere, but its electron density exponentially falls off with the solar surface's distance: $\sim 10^6$ cm^{-3} at 2 $R_\odot$ from the solar center, and $\sim 10^4$ cm^{-3} at 10 $R_\odot$ (Aschwanden, 2006; Priest, 2014). These low densities make the corona much
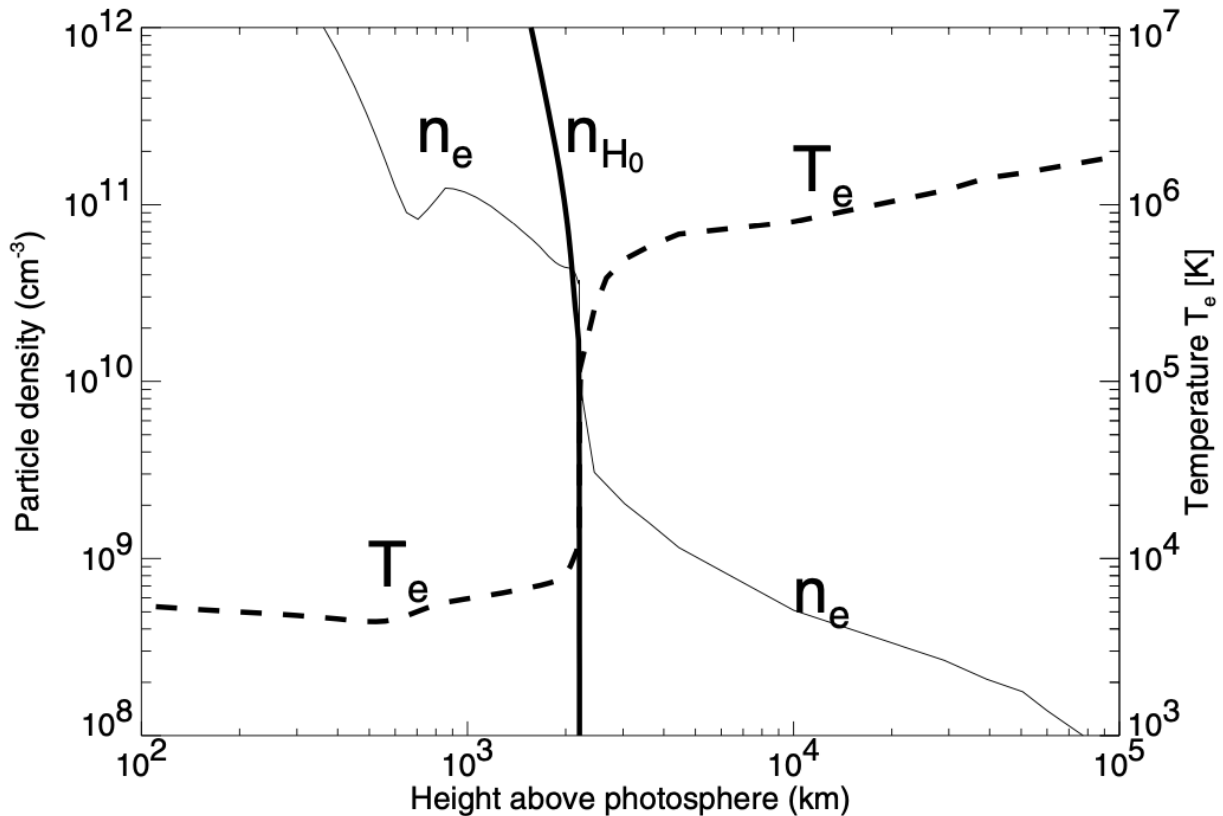
Figure 1.2: Fontenla et al. (1990) model of the quiet chromosphere's temperature and density joined with a model by Gabriel (1976) of the lower corona. Note the sudden sharp temperature rise at the transition region (~ 2.5 Mm) in around three orders of magnitude. Figure from Aschwanden (2006).

dimmer in white light than the photosphere and observable from Earth only during total solar eclipses or from space using coronographs (like those in the mission Solar Terrestrial Relations Observatory (STEREO), Thompson et al. (2003)). In X-rays and EUV, the lower solar atmosphere emission is negligible compared to the corona. Our atmosphere absorbs these high-frequency radiations, so to observe solar X-rays (and EUV), we need space instruments such as Yohkoh (Acton et al., 1992), Hinode (Kosugi et al., 2007), the Ramaty High-Energy Solar Spectroscopic Imager (RHESSI, Lin et al., 2003), the Spectrometer Telescope for Imaging X-rays (STIX, Krucker et al., 2020), the Nuclear Spectroscopic Telescope Array (NuSTAR, Grefenstette et al. (2016)), and the Focusing Optics X-ray Solar Imager (FOXSI, Glesener et al., 2016). FOXSI is the main instrument of this thesis, and it is explained in detail in chapter 3. RHESSI was a NASA solar dedicated observatory that used collimator-based Fourier-transform imaging to observe solar X-rays and gamma-rays

over a 3 keV to 17 MeV energy range. RHESSI provided meaningful results for our better understanding of the Sun in X-rays. Later in this dissertation (Chapter 6) I use previously published results by other authors based on RHESSI data to compare the novel analyses I present for the faintest solar X-rays observed with FOXSI.

1.2   Solar corona phenomena

Three prime structural regimes encompass coronal phenomena: coronal holes, magnetic loops, and X-ray (and EUV) bright points (Priest, 2014).

Coronal holes are extensive zones where the plasma is less hot and less dense than in their vicinities (Wilhelm, 2006; Cranmer, 2009). The magnetic field lines in these regions are so elongated, stretching far into the solar system, that they are usually considered as open lines for practical purposes (Bilenko et al., 2016). When coronal holes occur in the solar poles, they exhibit mainly two kinds of structures: polar plumes (or coronal rays) that last for days outlining the local magnetic field lines (DeForest et al., 2001); and polar jets, which are dense impulsive bursts that sometimes emit hot X-rays (e.g., Paraschiv et al., 2015).

Magnetic (or coronal) loops are a direct consequence of the twisted solar magnetic field lines within the Sun (e.g., Ebrahimi et al., 2017). They primarily emit in EUV and soft X-rays, displaying a wide range of geometric configurations (e.g., Priest, 2014; Reale, 2014). Their loop feet usually root in active regions and/or newly emerging magnetic fluxes (e.g., Priest, 1978). The most extensive loops have lengths of about ~ 500 Mm, and their temperatures and densities in the quiet corona range from 2 to 3 MK and from 10^{14} to 10^{15} m^{-3}, respectively (e.g., Craig et al., 1978; Klimchuk et al., 2008). They form and dissipate over periods of seconds to days. Very recently, observations from the sounding rocket Hi-C demonstrated that coronal loops consist of many thin strands as small as ~ 200 km, though the more typical widths are closer to half a Mm (e.g., Williams et al., 2020b; Williams et al., 2020a). Coronal loops are essential in studying plasma flow from the lower solar atmosphere to the corona. Because the loops are highly localized, they are fundamental to understanding plasma filling, dynamic flows, and possible consequences on coronal heating (e.g., Nakariakov et al., 1999; Reale, 2014).

Coronal bright points are crucial for understanding solar activity. They uniformly populate the solar atmosphere, including the quiet Sun, coronal holes, and the vicinity of active regions (e.g., Madjarska, 2019). When observed in X-rays, they exhibit a point-like structure with typical sizes of 20 - 30 arcsecs and an enhanced emission 5 - 10 times that of their surroundings (e.g., Golub et al., 1974; Strong et al., 1992; Madjarska, 2019). They have an average lifetime of eight hours (e.g., Alexander et al., 2011). In EUV, coronal bright

points show small-scale loops with cooler loops underneath hotter ones connecting opposite magnetic polarity kernel feet (e.g., Zhang et al., 2001; McIntosh et al., 2005). These bright points are not isolated; instead, they usually concentrate in networks at supergranulation cells' junctions evolving in time scales of ~ 5 minutes (e.g., Madjarska, 2019). Estimating the daily occurrence rate of coronal bright points depends on instrument factors like spatial resolution, photon statistics, acquisition time, etc. For instance, in EUV at 193 Å such an averaged daily value is ~ 570, but at 284 Å the amount observed bright points are ~ 150 times fewer than the ones observed in 193 Å (e.g., Madjarska, 2019). Coronal bright points follow very similar dynamics as coronal loops but smaller in size, with reduced temperatures ($\log T(K) \sim 4 - \log T(K) \sim 6.6$) and densities ($10^8 - 10^{10}$ cm^{-3}) (e.g., Simon et al., 1972; Del Zanna et al., 2003; Ugarte-Urra et al., 2004). Continuous coronal bright point radiation predominantly occurs at middle-low energies shaping into a Maxwellian spectrum, emitting mainly in EUV and soft X-rays (e.g., McIntosh et al., 2005; Saar et al., 2009). Coronal bright points' spectra might also contain a non-thermal component following a power-law energy distribution with a negative index. Even if such a non-thermal counterpart exists, its emission at higher energies (i.e. hard X-rays) would be rather faint and challenging to observe (e.g., Bakke et al., 2018). New technologies are required to search for this kind of faint emission.

Coronal bright points are a consequence of small-scale magnetic reconnection. Large-scale reconnection leads to larger eruptive events in the corona, like prominence eruptions, solar flares, and coronal mass ejections. Solar flares are the central phenomenon studied in this work. Their physics is extensive, so chapter 2 is fully dedicated to present their structure and dynamics.

1.3 Scope of work

This doctoral work presents one of the most striking solar physics puzzles: coronal heating, and describes how faint hard X-ray observations can contribute to its solution. Here, I analyze the faintest sources of solar hard X-rays by using observations from the Focusing Optics X-ray Solar Imager (FOXSI) sounding rocket, which includes quiet Sun areas. I was closely involved in building and flying the instrument for its second and third flights. I use calibration data of the FOXSI optics and a ray-tracing simulation to characterize and reduce observational background. This characterization maximizes the overall sensitivity of the observations for the quiet Sun emission in HXRs. Chapter 2 presents our state-of-the-art understanding of the physics of solar flares, particle acceleration, and their connection with faint hard X-rays and coronal heating. Chapter 3 introduces the FOXSI sounding rocket payload as a next generation solar dedicated instrument with focusing optics and cutting-edge X-ray semiconductor detectors. In Chapter 4, I provide details of the FOXSI optics and calibration results of their performance. Chapter 5 describes the use of a ray-

tracing simulation to characterize the ghost-ray background in the FOXSI rocket experiment. Chapter 6 covers analyses of quiet Sun hard X-rays observed with past flights of FOXSI, having as the primary goal to set new upper HXR limits for the quiescent corona. At the end of the chapter, I assess whether nanoflares' collective occurrence are energetic enough to heat the corona. Finally, Chapter 7 outlines a summary of my dissertation and presents my conclusions.

Through the development of my doctoral work, I had the opportunity to work alongside a dozen senior and early career scientists and engineers to bring the FOXSI concept into design, building, testing, and flight. To help evaluate my work, I describe here the contributions I made to the material included in this dissertation. Chapter 2 is my own summary of other's people work in the solar physics community. Chapter 3 covers the FOXSI instrument and launch campaigns (these were a team effort in which I was one of the core personnel). Chapters 4 and 5 present calibrations and simulation analysis I led. Chapters 6 is the analysis of hard X-ray emission from quiet Sun regions for which I am the primary author.

Chapter 2

Solar flares and their connection with coronal heating

Among the solar system's eruptive phenomena, solar flares are the most energetic and violent events produced. An enormous amount of magnetic energy gets released into plasma heating and non-thermal processes (Somov, 2012a). Flares happen in the corona with a variety of shapes and sizes, ranging from the least energetic (nanoflares releasing $\sim 10^{24}$ erg) to the most vigorous with energies released on the order of $\sim 10^{33}$ erg (e.g. Hudson, 1991; Aschwanden et al., 2014). In these processes, there are increases in solar brightness in all wavelengths at the flare location in the corona, chromosphere, and photosphere (e.g. Svestka, 2012). During a flare, the surrounding plasma heats to temperatures beyond tens of million Kelvin (for a medium-sized or large flare), significantly increasing (by two orders of magnitude or more) thermal emission in EUV and X-rays (Tandberg-Hanssen et al., 1988; Longcope, 2020). Traditionally, the maximum flux in the 1 to 8 Å band-pass sets the flare magnitude (size[1]) (e.g., Aschwanden, 1994; Ryan et al., 2012). Flare frequency relates inversely with size, meaning that smaller bursts are produced more regularly than their counterparts (e.g., Hudson, 1991; Christe et al., 2008). To identify solar flares' physics, the scientific community has established a model framework to understand these eruptive events' typical scenario, named the CSHKP (Carmichael, Sturrock, Hirayama, Kopp, and Pneuman) model for a solar flare (Shibata et al., 1995; Aulanier et al., 2013). According to this model, a current sheet forms first in the corona, where antiparallel magnetic field lines reconnect at an X-point (Priest et al., 2002). Such reconnection drives the conversion of previously-stored magnetic energy into other forms of energy like heat, radiation, and particles' energization into non-thermal distributions (Longcope, 2020). Below, section 2.1 explains the CSHKP model in more detail. For now, from this model it follows that some energy gets injected downward to deeper layers of the solar atmosphere, and some gets ejected upwards into the higher corona. Because flares energetically feed the corona, they are suitable candidates to explore scenarios to explain the coronal heating problem, i.e., why the solar corona is remarkably hotter than

---

[1]See https://www.swpc.noaa.gov/products/goes-x-ray-flux

underneath layers (e.g., Hudson, 1991; Yang et al., 2018; Vlahos et al., 2021).

2.1 The Standard Flare Scenario

Shibata et al. (1995) coined the term CSHKP model of a flare, referring to a standard 2D framework based on the concepts presented by Carmichael (1964), Sturrock (1966), Hirayama (1974), and R. Kopp et al. (1976) to understand the physical processes that occur during a solar flare. Almost two decades after, Aulanier et al. (2013) and T. Li et al. (2021), for example, proposed expanding to a conceptual model in 3D to suit the observations better. More recently, Chen et al. (2015) presented observational evidence of parts evoked in the standard flare model that were still controversial to date (a termination shock driving particle acceleration).

Figure 2.1 represents the primary schematic of the standard flare model. The restructuring of the magnetic field lines into a solar loop triggers (and drives) a solar flare. The reconnection at the X-point (Figure 2.1A) releases energy initially stored in the magnetic field, accelerating particles (electrons and ions) both upward and downward (Figure 2.1B). The downward traveling particle beams collide with the ambient chromosphere depositing their energy there. The particle decelerations in these collisions produce Bremsstrahlung radiation (free-free emission), observable as hard X-ray footpoints (Figure 2.1C). This impulsive dynamic results in a heated chromospheric plasma (Neupert, 1968) that expands and ablates into the corona, filling the newly reconnected magnetic loops and making them visible in EUV and soft X-rays. Frame D in Figure 2.1 illustrates this final stage, known as chromospheric evaporation. Although what I outlined above is the recognized standard model for a solar flare, numerous other authors have published a diverse set of scenarios to understand solar flares' structure and dynamics. Hugh Hudson (a.k.a the Archivist in this context) has grouped cartoons portraying such interpretations for decades. Hugh keeps the Grand Archive of Flare and CMEs Cartoons at http://www.astro.gla.ac.uk/cartoons/. Hopefully, my cartoon gains its place in such an exclusive collection!

2.1.1 Magnetic reconnection

In general, highly conductive magnetized plasmas can exhibit violent rearranging of their magnetic topology, converting magnetic energy into other forms of energy like kinetic, heat, and non-thermal particle energization (e.g., Biskamp, 1996; Yamada et al., 2010; Arnold et al., 2021). Magnetic reconnection drives such a process (e.g. Gonzalez et al., 2016). Aschwanden (2006), e.g., discusses that the most recent theoretical approaches to understanding magnetic reconnection use ideal magnetohydrodynamics (MHD) but predicts timescales that mismatch observed reconnection times, both in laboratory experiments and in astrophysical objects (more detail is given later in this section). In particular, solar flares' impulsive phases happen within hundreds to thousands of seconds, several orders of magnitude shorter than
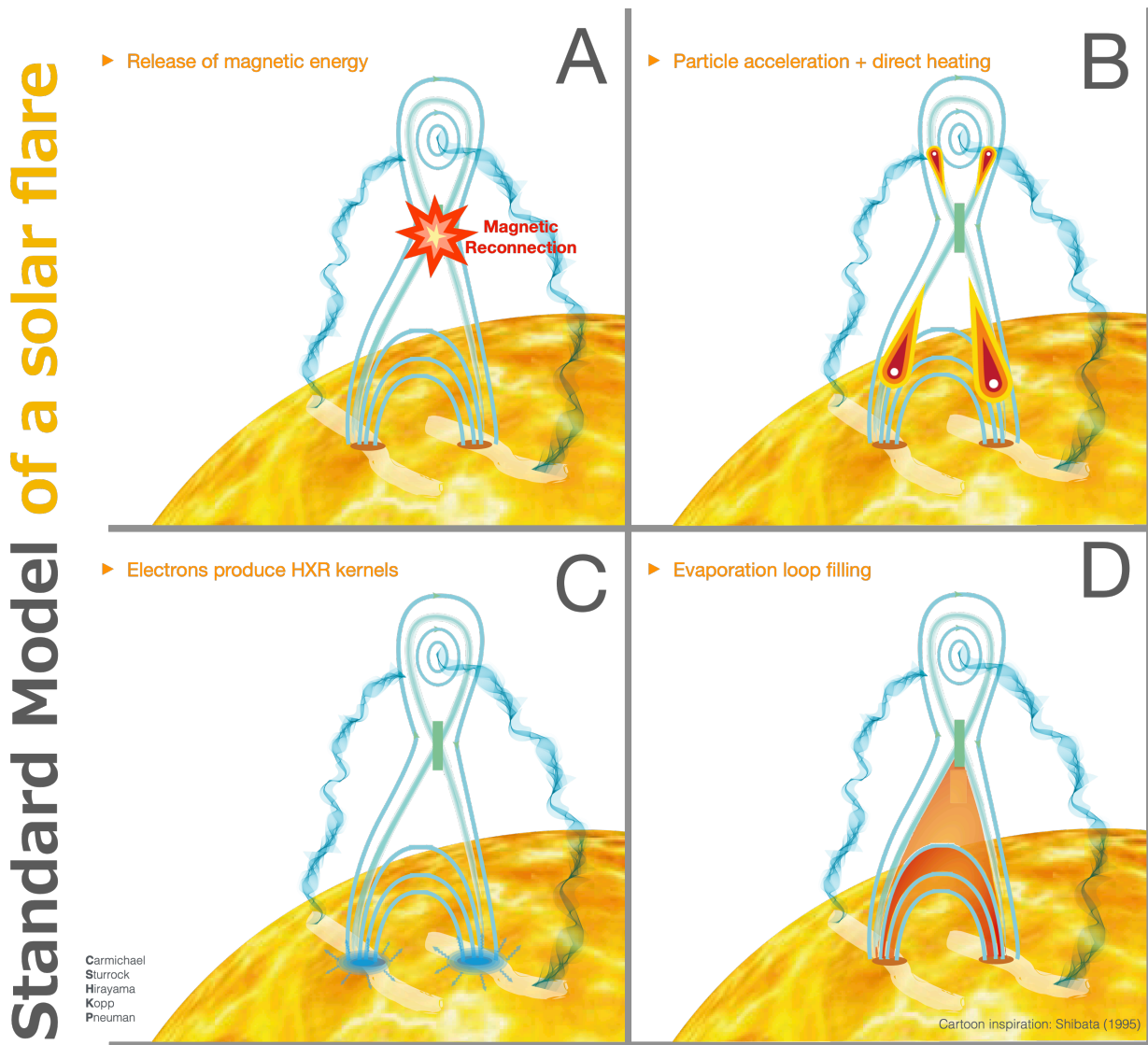
Figure 2.1: The standard CSHKP model for solar flares. **A**. Anti-parallel magnetic field lines reconnect at the X-point (red star) and form a current sheet. Charged particles energize into X-point surroundings via one or more physical mechanisms not fully understood to date. **B**. The particles are ejected from the reconnection region, forming jets that either escape into the higher corona or precipitate downwards along the loop structure into more dense chromospheric plasma. **C**. Collisions between the jets and the background plasma cause the beam particles to slow down and ultimately stop, emitting non-thermal bremsstrahlung radiation in the form of hard X-ray kernels (footpoints). **D**. The ambient plasma gets heated and rises, filling the newly reconnected flare loop observed in EUV and soft X-rays.
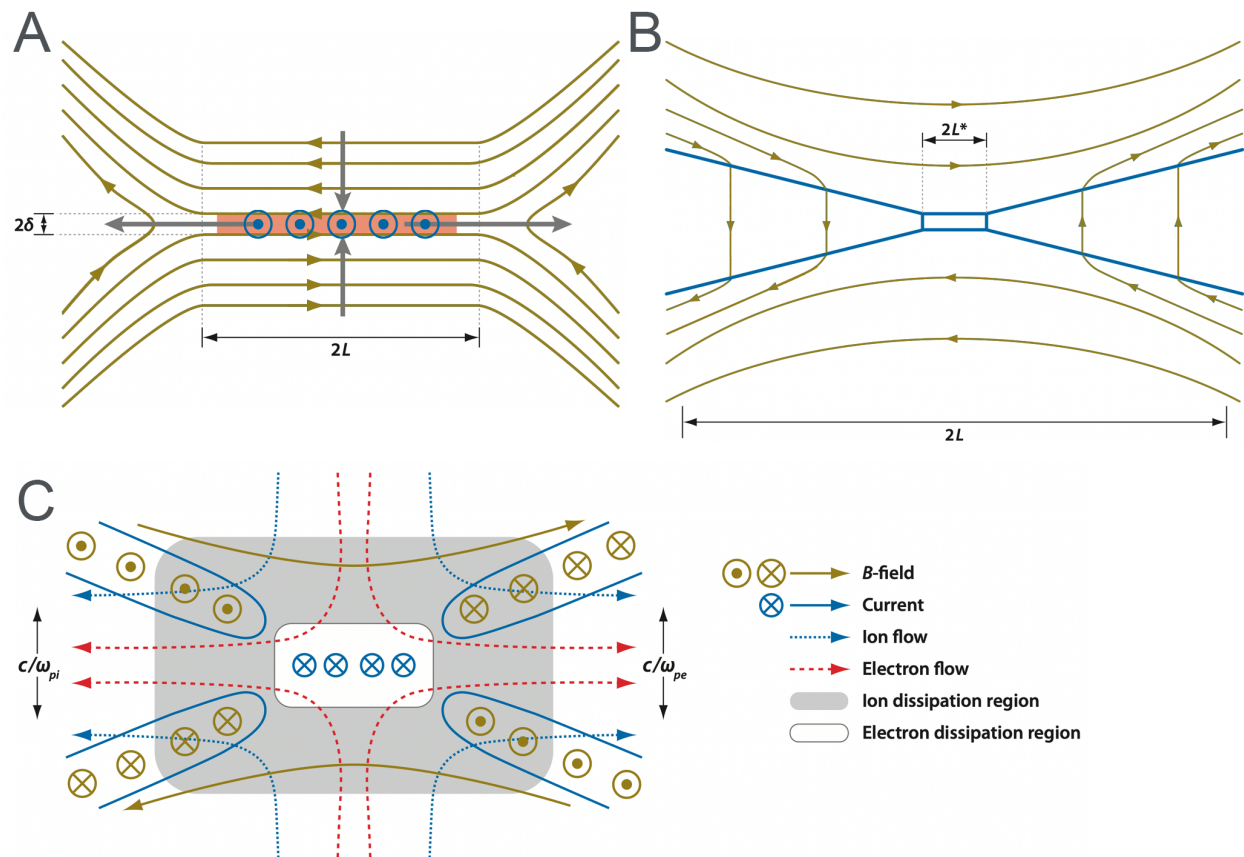
Figure 2.2: Illustrations of Sweet-Parker (A), Petschek (B), and Hall (C) reconnection geometry. Images modified from Zweibel et al. (2009).

classic MHD estimates even when adding turbulence and kinetic phenomena (e.g. Yokoyama et al., 1994; Kulsrud, 2001). Numerous models try to make approaches to suit observed reconnection times, but none has fully succeeded (e.g. Tsuneta, 1996; Janvier, 2017). One of the most likely scenarios hypothesizes that turbulence in the immediate vicinity of reconnection strongly scatters electrons, further increasing resistivity, which boosts the magnetic field's reconnection (e.g. Somov, 2012c).

Parker (1957) and Sweet (1958) independently established one of the earliest frameworks to study the dynamics of magnetic reconnection. The Sweet-Parker model describes a relatively slow 2D reconnection driven by an extended and narrow electric current sheet (e.g. Zweibel et al., 2009). Figure 2.2.A shows a simple cartoon illustrating the primary magnetic reconnection dynamics as proposed in the Sweet-Parker model. Two horizontal anti-parallel current-carrying magnetic fields come together towards the figure's center, forming a current sheet at their junction. In this model, plasma vertically inflows (from top and bottom) into

the current sheet, diffusively expands, and outflows horizontally. The outflow speed (v_{out}) depends on the magnetic field (B_{in}) coupled to the in-flowing plasma via energy conservation:

$$\frac{|B_i|^2}{8\pi n} = \frac{1}{2}m_e v_{out}^2 \tag{2.1}$$

where n is the number density at the outflow region and m_e is the mass of an electron (9.1×10^{-28} g). Using typical coronal values for B_i ($\sim$10 - 300 Gauss), n ($\sim 10^9$ cm^{-3}) in equation 2.1, the expected outflow kinetic energy per particle for accelerated electrons range from ~ 2.5 keV to $\sim$2.2 MeV. These estimated energies agree with the typical non-thermal energies observed in flares (some keV, up to MeV).

The Sweet-Parker model predicts much larger time scales than those observed in flares, mostly because the plasma must flow through a long and thin, very resistive reconnection region. Though the Sweet-Parker model does not resemble flare reconnection times and their observed non-thermal energies, it is still widely used because of its 2D simplicity and compliance when numerically modeling solar flares reconnections (e.g. Aschwanden, 2006). Petschek (1964) addressed this issue by proposing a faster reconnection model where the reconnection region's length is comparable to its width (see figure 2.2.B). In Petschek's model, stationary slow mode shocks separate the inflow and outflow regions, and the reconnection rate (R) is given by (e.g., Ji et al., 1999)

$$R = \frac{\pi}{8\ln(Lv_A/\eta)}, \tag{2.2}$$

where L is the reconnection segment length (typically of order 10^9 cm in the solar corona), v_A is the Alfvén speed ($\sim 10^8$ cm s^{-1}), and η the magnetic diffusivity ($\lesssim 10^5$ cm^2 s^{-1}). For the corona, $Lv_A/\eta \sim 10^{12} - 10^{14}$ (e.g. Uzdensky, 2003), which leads to a solar flare duration of a few months. This time is very large compared to usual reconnection times in solar flares (10^2-10^3 s). Petschek model is hard to numerically simulate using MHD due to the strongly-enhanced resistivity required in the diffusion region (e.g. Baty et al., 2014).

The two models presented above, Sweet-Parker's and Petschek's, offer a steady-state framework for the reconnection requiring high collisional processes at the central diffusion region. Yet, neither of the two models addresses the riddle of how the overall reconnection dynamics begins (gets triggered). Cassak et al. (2006) proposed a collisionless model that uses the Hall effect to explain high reconnection rates and the physical origin of the process. Very recently, Liu et al. (2022) published a first-principles theory where they propose the Hall electromagnetic fields in antiparallel reconnection configurations as the cause of fast reconnection rates.

For the Hall effect to come into action, a pre-flare steady-state Sweet-Parker type environment is needed. Once the Sweet-Parker reconnection region reaches a minimum length, the whole reconnection region transits to a new collisionless Hall effect domain (e.g. Zweibel et al., 2016). This moment sets the start of the impulsive phase of a flare. Mathematically, the Hall reconnection requires adding a $\vec{J} \times \vec{B}$ term into the generalized Ohm's law (e.g. Zweibel et al., 2009),

$$\vec{E} + \vec{v} \times \vec{B} = \eta\vec{J} + \frac{1}{en_e}\left(\vec{J} \times \vec{B}\right) \tag{2.3}$$

where $\vec{E}$ and $\vec{B}$ are the electric field and magnetic fields respectively, $\vec{v}$ is the convective velocity of the plasma, $\vec{J}$ is the current density, e is the charge of an electron, n_e is the electron's number density, and η is the resistivity.

The terms on the right-hand side of equation 2.3 dominate the dynamics at scales smaller than the ion gyroradius. At those scales, electrons decouple from ions and whistler rather than Alfvén waves dominate the process. Whistler waves lead to much faster reconnection rates (up to six orders of magnitude rapidly than rates predicted by the Sweet-Parker model in the solar corona, e.g. Drake et al. (2008), Birn et al. (2001), and Huba et al. (2004)). Figure 2.2.C illustrates the Hall reconnection schematics where separated streams of electrons and ions are sources of currents within the plane and their quadrupole out-of-plane magnetic field counterparts (e.g. Malyshkin, 2008; Zweibel et al., 2009).

Yamada et al. (2010) made a thorough review of the magnetic reconnection physics for laboratory and space plasmas, including theory, astrophysical observations, and laboratory results. They attempt to give an overall interpretation of the modern understandings and findings of magnetic reconnection. They highlight the significance of considering two-fluid physics to account for faster reconnection times. They concluded that a comprehensive understanding of the reconnection environment should encompass an in-depth study of the neutral sheet[2], Hall currents, guide field effects, collisions, and turbulence around the dissipative region. Magnetic reconnection is recurrent topic of discussion within the academic community because of its profound implications not only in the physics of space plasmas but also in novel technological applications (e.g., Yamada, 1999). In particular, magnetic reconnection at solar flares is an imperative topic. The interested reader can find detailed explanations of this physics in books like Aschwanden (2006), Somov (2012a), Somov (2012c), and Gonzalez et al. (2016), and the very recently published book by Yamada (2022).

---

[2]The *neutral sheet* is name given to the center of a current sheet formed when magnetic field lines nearly antiparallel meet.

2.1.2 Particle acceleration mechanisms

Two different types of detections, near-Earth *in situ* solar energetic particles (SEPs), and remote solar flare radiation, are proof of particle acceleration in solar flares (e.g., Krucker et al., 2007; Petrosian, 2016). Specifically, the spectral index of SEPs and hard X-ray radiating electrons correlate with one another in cases with a close temporal correlation during the earlier (prompt) stages of their detections (e.g., Lin, 2005; Petrosian, 2016). In a flare, whatever is the magnetic reconnection topology (see section before), it is by now well established that a considerable portion of the magnetic energy released ($\sim 10^{33}$ erg) goes into accelerating charged particles (e.g., Tsuneta, 1995; Gordovskyy et al., 2010; X. Li et al., 2017). Understanding this energy conversion (from magnetic to kinetic) is a current central research topic in solar physics and heliophysics. It also has direct consequences on the comprehension of other astrophysical bodies where charged particles accelerate. Electron (and sometimes ion) dynamics are diagnosed using solar observations at multiple wavelengths (e.g., Aschwanden, 2002). Primarily, hard X-rays are essential to study flare non-thermal particle acceleration (e.g., Gordon D Holman et al., 2011; Krucker et al., 2013a; Simões et al., 2013). In this section, I briefly review the principal elements of the contemporary particle acceleration theories to then move to observational evidence of this phenomenon.

In solar flares, particle acceleration occurs in two phases (e.g., Benz, 2017)). A first prompt energization happens in a fraction of a second over a group of already thermalized electrons. They gain more than two orders of magnitude of their initial energy (0.1 keV) during this initial phase (e.g., Kiplinger et al., 1984). During a second delayed phase, another class of acceleration processes, possibly via shock waves, eject electrons into the interplanetary space that are subsequently observed as near-Earth solar energetic particles (SEPs, e.g., Benz (2017)). The prompt phase is directly linked with hard X-ray emissions, which spectroscopically remain close to a Maxwellian distribution and most of the time exhibit a non-thermal tail (e.g. Saint-Hilaire et al., 2005). The SEPs tend to be harder than the hard X-ray radiating electrons for the delayed phase, thought to be associated with fast coronal mass ejections (e.g., Petrosian, 2016).

At the most elementary level, the fundamental physics of charged particles moving into electric and magnetic fields is covered in several electrodynamics textbooks (e.g., Jackson, 1999). For specific applications to the solar corona, Somov (2012b), for instance, describes the dynamic in detail from a rather theoretical point of view. In the most general form, the equation of motion that describes the movement of a charged particle accelerated by electric $\vec{E}(\vec{r}, t)$ and magnetic $\vec{B}(\vec{r}, t)$ fields is given by the Lorentz force.

$$\frac{d\vec{p}}{dt} = q \left(\vec{E}(\vec{r}, t) + \frac{1}{c} \, \vec{v} \times \vec{B}(\vec{r}, t) \right) \tag{2.4}$$

where c, is the speed of light, $\vec{p}$, $\vec{r}$, and q are the momentum, position and charge of the

particle, respectively. In the most simple reconnection models, Sweet-Parker and Petschek, an electric field $\vec{E}$ along a current sheet is the one responsible for particle acceleration. For solar flares, this type of DC acceleration is categorized by whether the magnitude of $\vec{E}$ is smaller or larger than the critical Dreicer field $\mathcal{E}_D$ (Dreicer, 1959; Aschwanden, 2006),

$$\mathcal{E}_D = \frac{q \ln \Lambda}{4\pi \epsilon_0 \lambda_D^2} \tag{2.5}$$

where q is the particle charge, $\ln \Lambda$ the Coulomb logarithm, ϵ_0 the electric permittivity, and λ_D is the Debye length. For sub-Dreicer electric field acceleration, electrons with enough energy to overcome the ion drag force accelerate in a "runaway" process (e.g., Holman, 1985; Holman, 1995; Aschwanden, 2002), with a speed given by

$$v = v_{Thermal}\sqrt{\mathcal{E}_D/E_{||}}, \tag{2.6}$$

with $v_{Thermal}$ the thermal speed of the electrons, and $E_{||}$ the component of $\vec{E}$ parallel to $\vec{B}$. In the case of super-Dreicer DC electric acceleration, the energy U that the particle obtains in the acceleration process is

$$U = q\,\frac{B_{||}}{B_\perp} E_{||}\,\delta, \tag{2.7}$$

where δ is the width of the current sheet. Other two important parameters that characterize DC electric field acceleration are the time variability (quasi-static versus fast) and the magnetic field topology (See chapter 11 in Aschwanden, 2006, for more details). One of the most significant challenges of this DC electric field acceleration model is the difficulty in maintaining a large-scale unfragmented $\vec{E}$ field. For charged particles to accelerate via a fragmented field would imply the existence of return currents canceling the original accelerating DC field (e.g., Alaoui et al., 2021).

Acceleration via DC electric fields is not the only mechanism capable of transferring magnetic energy into accelerated particles. Other processes could perform such an effect. The most broadly considered are usually tailored into three classes (e.g., Melrose, 1990; Benz, 2002; Benz, 2017; Zharkova et al., 2011). i) DC electric field acceleration (just discussed), ii) first and second-order Fermi acceleration (shocks), and iii) stochastic acceleration (e.g., Fokker-Planck acceleration). More recently, Fletcher et al. (2008) proposed the Lorentz force as the primary driver of particle acceleration, sometimes with direct implications on the solar atmosphere's acoustic responses (e.g., Alvarado-Gómez et al., 2012). Last year, Che et al. (2020), reported an investigation about a novel type of reconnection acceleration driven by electron Kelvin–Helmholtz instabilities (expanding magnetic vortices) along strong

guide field lines. Among all these possible theoretical explanations for particle acceleration, more likely, more than one of them occurs during a particular flare. The magnetic field's geometry and other secondary parameters would possibly set which process would drive particle acceleration among all these potential scenarios (and maybe others).

Flare particle acceleration details are still obscure from the theoretical point of view. However, for example, Benz (2017) claims that for him and others (e.g., Miller et al., 1997; Schlickeiser et al., 1998; Schlickeiser et al., 1998), the preferred, although not broadly accepted, acceleration scenario for solar flares is stochastic acceleration by the magnetic field component of low-frequency waves. Observations have not excluded this stochastic acceleration approach, as is the case for other theoretical models (i.e., acceleration by high-frequency Langmuir waves, current sheets, large-scale stationary electric fields, and shock acceleration). The partial success of stochastic acceleration by low-frequency waves may lie in the versatility that the equation of motion, the Fokker–Planck equation, has to aggregate diffusion and convective terms of different nature.

$$\frac{\partial f(\vec{p})}{\partial t} = \left(\frac{1}{2} \sum_{i,j} \frac{\partial^2}{\partial p_i \partial p_j} D_{ij} - \sum_i \frac{\partial}{\partial p_i} F_i \right) f(\vec{p}) \tag{2.8}$$

$f(\vec{p})$ is the particle distribution in a generalized phase space (canonical coordinates and momenta). The diffusion and convective coefficients (D_{ij} and F_i, respectively) can be added according to the different physical processes regarded in the particles' kinematics (e.g., wave acceleration, Coulomb collisions, etc.).

Aschwanden (2006) summarizes in a table (Table 2.1.2 in this dissertation) some of the more successful particle acceleration models. For more details, the interested reader can go directly to chapter 11 in (Aschwanden, 2006) and the references therein.

2.1.3   Time evolution at different wavelengths

A flare emits in virtually every wavelength (e.g., Longcope, 2020). Contrary to the Sun, whose photosphere as a whole emits as a black-body with peak at $\sim$ 500 nm (e.g., Carroll et al., 2010), solar flare spectra do not follow a single Planckian behavior. Instead, flare brightness at a specific wavelength strongly depends on the wide range of physical processes occurring during the eruption, e.g., Bremsstrahlung emission, synchrotron radiation, ionization, among others. The flare's radiation bulk is located in the visible continuum (e.g., Hudson, 2010). However, even a large flare adds to the bolometric solar continuum only by about $\sim 0.01\%$ (Woods et al., 2004; G. Kopp et al., 2005; Kretzschmar et al., 2010). Very recently, for instance, Milligan (2021) reported an average increment of $\sim 4\%$ for large flares when observed at the Lyman-Alpha line (just beyond the visible) with the EUV Sensor on the Geostationary Operational Environmental Satellite 15 (GOES-15). In general, it is chal-

Acceleration Mechanisms	Electromagnetic fields
DC electric field acceleration:	
- Sub-Dreicer fields, runaway acceleration	$|\vec{E}| < E_D$
- Super-Dreicer fields	$\vec{E}| > E_D$
- Current sheet (X-point) collapse	$\vec{E} = -\vec{u}_{inflow} \times \vec{B}$
- Magnetic island (O-point) coalescence 4	$\vec{E}_{conv} = -\vec{u}_{coal} \times \vec{B}$
- (Filamentary current sheet: X- and O-points)	
- Double layers	$\vec{E} = -\nabla V$
- Betatron acceleration (magnetic pumping)	$\nabla \times \vec{E} = -(1/c)(dB/dt)$
Stochastic (or second-order Fermi) acceleration:	
Gyroresonant wave-particle (weak turbulence) with:	
- whistler (R-) and L-waves	$\vec{k}||\vec{B}$
- O- and X-waves	$\vec{k} \perp \vec{B}$
- Alfvén waves (transit time damping)	$\vec{k}||\vec{B}$
- Magneto-acoustic waves	$\vec{k} \perp \vec{B}$
- Langmuir waves	$\vec{k}||\vec{B}$
- Lower hybrid waves	$\vec{k} \perp \vec{B}$
Shock acceleration:	
Shock-drift (or first-order Fermi) acceleration	
- Fast shocks in reconnection outflow	
- Mirror-trap in reconnection outflow	
Diffusive-shock acceleration	
More recent models:	
- Lorentz Force	$\vec{F}_L = \vec{E} + \frac{1}{c}\vec{v} \times \vec{B}$
- Kelvin–Helmholtz vortices along strong guide fields	

Table 2.1: Overview of particle acceleration mechanisms in solar flares. Taken and slightly modified from chapter 11 in Aschwanden (2006).

lenging to detect flares as increments in the bolometric solar luminosity. Instead, studying flares focuses on specific wavelengths, for which flare time evolutions encompass four phases; a pre-flare phase, an impulsive phase, a flash phase, and a gradual (decay) phase (e.g., Benz, 2017). Figure 2.3 illustrates a characteristic time evolution behavior of a flare for various wavelengths.

Traditionally, at a specific wavelength, a flare's time evolution follows one of two characteristic behaviors, impulsive or gradual. Gamma-rays and HXRs come primarily from loop footpoints (see top two panels in Figure 2.3). Microwaves come from the corona. Gamma-rays, HXRs, and microwaves exhibit a very short but impulsive light curve (1-10 minutes).
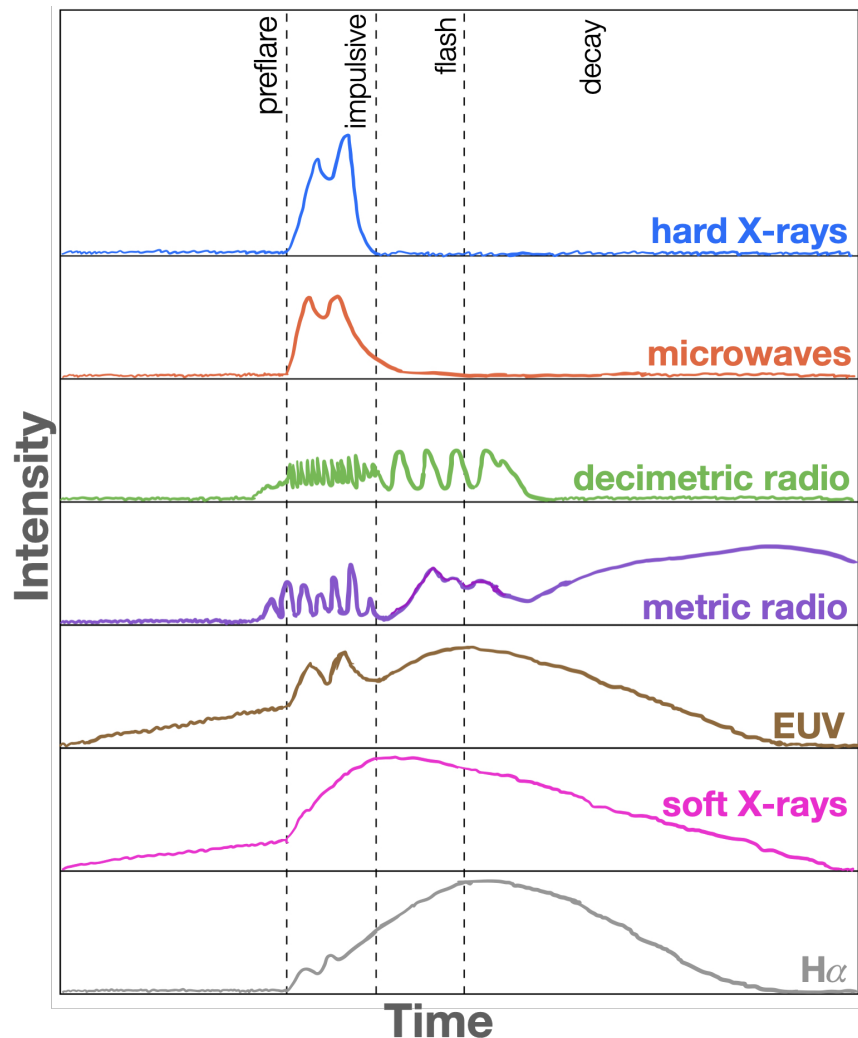
Figure 2.3: Illustration of a typical flare time evolution at a traditional set of wavelengths. Inspired by (Benz, 2002). Just before the flare triggers, coronal plasma near the magnetic reconnection region gets visible in soft X-rays and EUV because it slowly heats up. Most of the stored magnetic energy is released during the impulsive phase of a flare, and a large number of charged particles get energized. Some of these particles are trapped and cast in the three radio bands schematized here. In most cases, when the impulsive phase ends, the thermal soft X-ray emission reaches its maximum. During the flash phase, the heat is distributed further. In the last phase (decay), the low coronal plasma slowly returns to near its original conditions.

Emissions in soft X-rays, Hα and EUV, evolve gradually because of their coronal thermalized plasma nature (see last three rows in figure 2.3). The peak of EUV emission defines

the flash phase. At this time, the energy in electrons accelerated dominates the total flare energy (see, e.g., Kane, 1974; RP Lin, 1974; RP Lin et al., 1976). After rising during the impulsive and flash phases, their decay phase is more gradual and lasts longer (from the order of ~10 minutes to tens of hours). Other radiation in decimetric and metric radio emission display semi-periodic pulse-like evolution (panels three and four from top to bottom in figure 2.3). HXRs and microwaves observed during the impulsive phase of a flare seem to originate from the interaction of a beam of electrons and denser plasma in the lower corona and chromosphere (loop footpoints). Previous HXR spectral studies, e.g., Krucker et al. (2008), showed a non-Maxwellian distribution (non-thermal) and noted that over specific cutoff energy (not to be confused with the X-ray rollover energy), the spectra fit a power-law-like form. Such HXR spectral behavior manifests at least during the impulsive phase of flares, produced by non-thermal electron beams injected towards lower layers of the solar atmosphere. Studying non-thermal HXR time evolution is important because they offer a direct proxy to understand the dynamics of non-thermal electrons accelerated during solar flares.

2.1.4 Flare scaling: Microflares & nanoflares

During large and medium-sized flares, energies of typically $\sim 10^{28} - 10^{32}$ erg are released (e.g., Ning, 2008). How frequently a flare happens against the energy it releases is a question that the solar physics community has addressed during the last decades. Hudson (1991) was one of the first to propose that flare occurrence (N) follows a power-law distribution as a function of the total flare energy (E), $dN/dE \propto E^{-\alpha}$. Hudson (1991) was also one of the firsts authors to construct a solar frequency diagram using results of various solar X-ray observations from 1971 to 1989 (see figure 2.4.A). Iain G Hannah et al. (2008) updated such diagram, including data from RHESSI and data from EIT, TRACE, and SXT analyzed previously by other authors (see figure 2.4.B). They found α values close to 2 but with deviations for each instrument subset. Whether α is greater or less than two has a profound significance that can be understood when evaluating the total energy (E_{total}) released by the flare,

$$E_{\text{total}} \propto \int_{E_{min}}^{E_{max}} E \, \frac{dN}{dE} \, dE = \frac{1}{2-\alpha} \, E^{2-\alpha} \Big|_{E_{min}}^{E_{max}} \tag{2.9}$$

From equation 2.9, two different regimes differentiate depending on whether α is greater or less than 2. If $\alpha < 2$, larger flares drive the total energy. Otherwise, the lower-energy side of the plot in figure 2.4 drives E_{total}. Hudson (1991) found that the integrated energy release by large flares is insufficient (by at least two orders of magnitude) to account for the coronal heating energy requirements. For flares to be a viable mechanism for coronal heating, smaller flares should dominate the integrated energy release into the corona. Very recently, Aschwanden et al. (2021) and Aschwanden (2022) have tested Hudson's power-law hypothesis
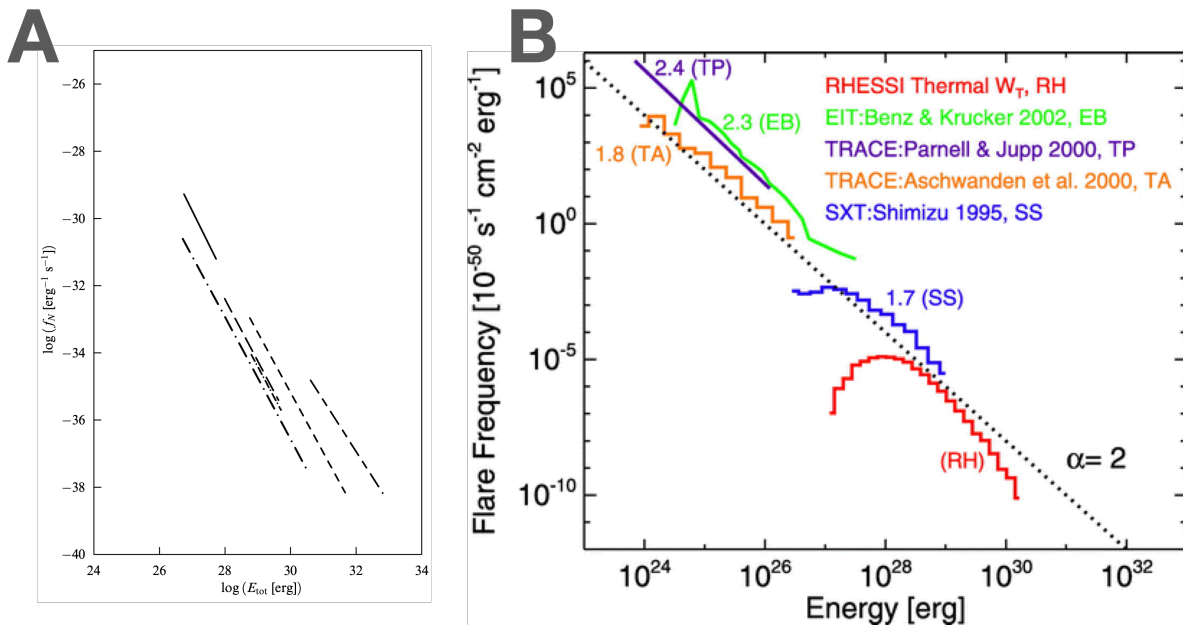
Figure 2.4: Frequency distribution of solar flares as a function of their energy. **A**. Diagram constructed by Hudson (1991) using data from various solar X-ray observations in the 1971-1989 period. **B**. Updated diagram by I. Hannah et al. (2011) including 9161 bursting events observed with RHESSI. I. Hannah et al. (2011) plotted their RHESSI data on top of previous analyzed observations by Shimizu (1995), Krucker et al. (1997b), Aschwanden et al. (2000), Parnell et al. (2000), and Benz et al. (2002). Although both diagrams are in log scale, flare frequency units between diagram A and B are different because Iain G Hannah et al. (2008) divide by the solar surface area in cm^2, while Hudson (1991) does not.

for the Sun and other solar-like stars. Aschwanden et al. (2021) report that for background-subtracted solar flares, the power-law index is $\alpha = 1.57 \pm 0.19$, quite different from values obtained with data without (or with insufficient) background subtraction ($\alpha = 2.20 \pm 0.22$). Below, subsection 2.2.3 discusses how significant these spectral index values are to assess non-thermal radiation at solar flares. Independently of the actual value of α, the power-law cannot extend limitlessly on either of its sides, smaller on the left and larger on the right of Figure 2.4. Constraining both ends of the power-law is a subject of investigation. Schrijver et al. (2012) and Aschwanden (2019b), e.g., have explored the problem of constraining the largest possible flare that can occur at the Sun. Particularly Schrijver et al. (2012) present indirect statistical arguments to claim that flares have likely not substantially exceeded the GOES X30 type in the past four centuries. Parker (1988) hypothesized the existence of tiny bursting solar events, compared to standard-sized flares, releasing six to nine orders of magnitude less energy than ordinary flares. Parker (1988) coined the term nanoflares to

refer to such smallest events. In 1994, Cargill estimated that a collection (many hundreds) of widespread nanoflares can produce temperatures of ≥ 5 MK. Aside from the term nanoflares, modernly, some authors use expressions like "network flares", "networking heating events", "EUV brightenings", "solar campfires", etc. This thesis uses the term nanoflares to refer to non-resolvable (in hard X-rays) impulsive energy release events that occur in the solar corona. These nanoflares could eventually be responsible for heating the corona (see section 2.3).

Several efforts have tried to resolve small bursting events observationally at lower energies (soft X-rays and EUV. See, e.g., Benz et al., 1997; Cirtain et al., 2013b; De Pontieu et al., 2014; Reva et al., 2018; Subramanian et al., 2018; Testa et al., 2020; Antolin et al., 2021). They occur individually in small-scale loops in the quiet Sun and as aggregates in non-flaring active regions[3] (see more details below in section 2.3). Their time profile contains an impulsive rise and a decay, which correlates with a time delay between high- and low-temperature bands ($T \approx 1 - 2$ MK. See, e.g., Krucker et al., 2000; Benz, 2017). Because these individual EUV and soft X-ray brightenings exist at relatively low temperatures, they emit extremely faint hard X-rays (see, e.g., Glesener et al., 2017; Iain G Hannah et al., 2019; Cooper et al., 2020; Cooper et al., 2021; Vievering et al., 2021). Some efforts have used RHESSI data to set upper limits on hard X-ray quiet Sun emission (Iain G Hannah et al., 2007; Iain G Hannah et al., 2010), but no direct detections have been reported to date. Most recently, Marsh et al. (2018) searched for hard X-ray quiet Sun transient events with the NuSTAR telescope. But, their estimated temperature and emission measure upper limits were not low enough to correspond to quiet Sun brightenings, as seen in previous soft X-ray observations.

Recently, Bogachev et al. (2020) completed a review of this topic and concluded that the exact nanoflares' structure and mechanism had not been fully determined. Bogachev et al. (2020) questioned whether it was correct to classify nanoflares as flares at all. Hudson (1991) suggested that Parker's nanoflares must have a different distribution function and may also have different physics. In that context, Hudson (1991) defined a *solar microflare* as an eruptive event member of the regular X-ray burst population, with the same physical parameters as their larger counterparts, where the released energy is small. Microflares are of particular interest as they can clarify whether thermal or non-thermal energy predominates in their X-ray emissions and how often that energy gets released (see, e.g., Robert Lin et al., 1984; Krucker et al., 2003; Christe et al., 2008; I. Hannah et al., 2011; Iain G Hannah et al., 2019; Glesener et al., 2020; Athiray et al., 2020; Duncan et al., 2021a; Vievering et al., 2021). Christe et al. (2008), I. Hannah et al. (2011) and Glesener et al. (2020), e.g., have shown that the physics of microflares is somewhat similar to that of medium and larger magnitude solar flares. They occur in active regions at coronal loop-like structures and exhibit a thermal (and

---

[3]A non-flaring active region is a region that at the moment of the observation does not exhibit a medium to a large solar flare. Yet, they can host EUV and soft X-ray brightenings (tiny flare-like events) and microflares.

occasionally non-thermal) spectral component. Their time evolution shows two stages, an impulsive and a decay phase. Knowing the characteristics of these microflare energy releases is important to assess how strong are their contributions at heating the corona.

2.2   Solar flares in X-rays

X-rays are one of the primary signatures of solar flares. A solar flare energizes electrons that travel through the corona, producing bremsstrahlung X-rays via inelastic Coulomb collisions. Analyzing X-rays emitted during solar flares is crucial to understanding the structure and dynamics of the associated energetic electron populations. Due to our atmosphere's high efficiency in absorbing short wavelength electromagnetic radiation, observing solar X-rays requires using specialized telescopes above the bulk of the Earth's atmosphere (e.g., satellites, sounding rockets, and high-altitude balloons payloads). A typical flare spectrum in X-rays has two distinct components, thermal at low energies and non-thermal at higher energies. For astrophysical purposes, X-rays are classified as soft or hard depending on whether the X-rays are low or high energy radiation, respectively. There is a bit of variation in these terms, particularly for solar flare studies, but the general agreement is to use the *soft* prefix to refer to radiation on the order of $\sim$ one keV (emitted by heated plasma with T $\sim$ 1.5 - 100 MK), and *hard* for higher energies. Thermal bremsstrahlung processes dominate the emission of solar flare hard X-rays at their low energy end. Flare hard X-ray spectra are power-law distributed and dominated by non-thermal processes at higher energies.

The treatment in this section is adapted from the review that Aschwanden (2006) does in chapters two and thirteen about solar X-ray bremsstrahlung radiation. The primary physical phenomena producing solar X-rays is bremsstrahlung (braking-free-free) radiation by electrons scattering off ions within the ambient solar atmosphere. In general, the Coulomb scattering of a charged particle encountering heavy charged target particles is classically described using the Rutherford formula (Rutherford, 1911) for the cross section (σ) as a function of the solid angle ($d\Omega$),

$$\frac{d\sigma}{d\Omega} = \left(\frac{e^2}{2pv}\right)^2 \csc^4\left(\frac{\theta}{2}\right) \tag{2.10}$$

where e and θ are the electric charge and angle of the incoming particle, respectively; $v = \beta c$ and $p = \gamma\beta mc$ are the velocity and momentum of the particle (with β and γ the usual relativistic factors, and m the electron mass).

For elastic scattering, the 4-momentum transfer squared (Q) is

$$Q^2 = 4p^2 \sin^2(\theta/2) = 2p^2(1 - \cos\theta). \tag{2.11}$$

Using $d\Omega = 2\pi \sin\theta d\theta$, after some math (see Chapter 15 in Jackson, 1999, for details), equations 2.10 and 2.11 yield to

$$\frac{d\sigma}{dQ} = 8\pi \left(\frac{Ze^2}{\beta c}\right) \frac{1}{Q^3},$$ (2.12)

where Ze is the charge of the ion. The *differential radiation cross section* (Q_r) is defined as

$$\frac{dQ_r}{dQ} = \frac{dI}{d\omega}\frac{d\sigma}{dQ}(Q),$$ (2.13)

where $dI/d\omega$ is the energy radiated (I) per unit frequency (ω). For low frequencies $(\omega \to 0)$, $dI/d\omega$ is

$$\lim_{\omega \to 0}\frac{dI}{d\omega} = \frac{2}{3\pi}\frac{e^2}{m^2c^3}Q^2$$ (2.14)

replacing equation 2.14 and 2.12 in expression 2.13, we get

$$\frac{dQ_r}{dQ} = \frac{16}{3}\frac{Z^2e^2}{c}\left(\frac{e^2}{mc^2}\right)^2\frac{1}{\beta}\frac{1}{Q}.$$ (2.15)

Integrating 2.15 over the 4-momentum Q,

$$\frac{dQ_r}{dQ} = \frac{16}{3}\frac{Z^2e^2}{c}\left(\frac{e^2}{mc^2}\right)^2\frac{1}{\beta^2}\int_{Q_{min}}^{Q_{max}}\frac{dQ}{Q}.$$ (2.16)

Considering conservation of energy and momentum for non-relativistic interactions,

$$Q_r = \frac{16}{3}\frac{e^6}{mv^2c^3}\ln\left[\frac{(\sqrt{\varepsilon} + \sqrt{\varepsilon - h\nu})^2}{h\nu}\right],$$ (2.17)

where $\varepsilon = p^2/2m$ is the kinetic energy of the electron, and $h\nu$ is the energy of the outgoing photon. Q_r has units of [Area]·[Energy]·[time]. Equation 2.17 leads to the known *Bethe-Heitler* cross section (e.g., Hudson, 1978),

$$\sigma(\varepsilon, h\nu) \approx \frac{8}{3}\alpha r_e^2 mc^2\frac{1}{h\nu\varepsilon}\left[\sqrt{\frac{\varepsilon}{h\nu}} + \sqrt{\frac{\varepsilon}{h\nu} - 1}\right],$$ (2.18)

being α is the fine structure constant and r_e the classical radius of the electron. The radiation cross section $Q_r(v, \nu)$ in equation 2.17 is related with the photon cross section $\sigma(\varepsilon, h\nu)$ in equation 2.18 via (see, e.g., Lang, 1980)

$$\sigma(\varepsilon, h\nu) = \frac{2\pi \, Q_r(v, \nu)}{h^2\nu}.$$
(2.19)

Note that $\sigma(\varepsilon, h\nu)$ has units of [Area]/[Energy]. The radiated intensity, $dN/dt \, d(h\nu)$, from a volume V of plasma, depends on the incoming electron velocity v, and the number of collisions between electrons and ions, which is $\int_V n_i n_e dV$, where n_i and n_e are the number density of ions and electrons, respectively. Thus,

$$\frac{dN_{photons}}{dt \, d(h\nu)} = \int_{h\nu}^{\infty} \sigma(\varepsilon, h\nu) v(\varepsilon) \left(\int_V n_i n_e(\varepsilon) dV \right) d\varepsilon.$$
(2.20)

Equation 2.20 relates the photons' energy distribution with that of any electron distribution. However, an appreciable flux in X-rays would be observable only if the electron distribution contains a relatively high number of energetic (flare-heated or accelerated) electrons. This is why observing flare X-rays is a direct method to infer flare energized electron distributions through their interaction with the low coronal and chromospheric plasma.

2.2.1 Spectral lines and differential emission measure

X-ray emission from the Sun, and in particular from solar flares, can can contain spectral line in case of a bound-bound transition or be a continuum if the transitions are free-free or free-bound (a.k.a. recombination). Assessing X-ray line fluxes based on models allows diagnosing the flare plasma ambients' physical parameters like electron density and temperature profiles. Much of this section is an adaptation from Aschwanden (2019a) and relies on X-ray Spectroscopy of the Solar Atmosphere studies documented in K. J. Phillips et al. (2008), Feldman et al. (2003), and Doschek et al. (2010), and Kohl et al. (2006). Aschwanden (2019a) lists in table 2.2 of his book several space-borne solar-dedicated instruments capable of performing spectroscopy in EUV and soft X-rays. Instrument characteristics like energy and spatial resolutions, dynamic range, wavelength coverage, and sensitivity are essential to studying solar flares spectroscopically. The same features extrapolate to spectral studies at higher energies, i.e., hard X-rays. In particular, combining spectroscopic and imaging capabilities (imaging spectroscopy) is desired for these kinds of analyses. Hard X-ray imaging spectroscopy makes it possible to assess the space, time, and energy distribution shapes for any sub-region observed on the solar disk.The success of this sort of analysis lies in the ability to diagnose temperature and density profiles of coronal structures. For example, doing imaging spectroscopy of flares requires small fields-of-view but high time cadences. Several authors (see for example Ren et al., 2004; Landi et al., 2006; Del Zanna et al., 2015) have led

thorough calculations of synthetic spectra with the CHIANTI database to determine spectral lines and continuum emission contributions by sampling differential emission measures for the different coronal regions. Aschwanden (2019a), e.g., defines the *differential emission measure* (DEM) distribution function as "an instrument-independent function that characterizes the electron and temperature of an optically-thin structure that emits EUV and soft X-rays". The DEM can also be expressed in terms of the number density of electrons (n_e) squared integrated along the line-of-sight z,

$$DEM(T) = n_e^2 \frac{dV}{dT} \quad [\mathrm{cm}^{-3}\mathrm{K}^{-1}]. \tag{2.21}$$

The DEM is convolved with the instrumental response functions $R_\lambda(T)$, and integrated over a range of thermal plasma temperatures, to get an estimate of the flux in EUV and/or X-rays (f_λ),

$$f_\lambda = \int_T DEM(T) R_\lambda(T) \, dT. \tag{2.22}$$

Getting a particular DEM function requires either a forward-fitting of a parameterized solar plasma model or inverting the integral equation 2.22. Table 2.2.1 summarizes the most used methods to estimate DEM functions.

2.2.2 Thermal radiation

According to the standard solar model, particle beams precipitating along magnetic loops towards lower solar atmosphere layers heat the ambient plasma at the loop footpoints via collisions during the impulsive phase of a flare. Then, the heated plasma expands into the loop until thermalizing the surrounding ambient. At that point, all particle distributions, $f(v)$, are Maxwellians. Particularly for electrons,

$$f(v)dv = \left(\frac{2}{\pi}\right)^{1/2} \left(\frac{m}{k_B T}\right)^{3/2} n_e v^2 \exp\left(-\frac{mv^2}{2k_B T}\right) \, dv \quad [\mathrm{cm}^{-3}], \tag{2.23}$$

where m, T, v, n_e are the mass, temperature, velocity, and number density of electrons, respectively. k_B is the Boltzmann constant. This electron's temperature is high enough for solar loops that the emitted bremsstrahlung radiation spawn over X-ray wavelengths. This electron's temperature is high enough for solar loops that the emitted bremsstrahlung radiation spawn over X-ray wavelengths. In X-rays, bremsstrahlung is the primary emission mechanism. Other processes, like synchrotron, recombination, and inverse Compton scattering, are too weak to be detectable at these wavelengths (e.g., Kontar et al., 2011). According to, e.g., Aschwanden (2006), the thermal emission spectrum $I(\varepsilon)$, in this case, is

DEM inversion methods	
Method	**Methodical descriptions**
Monte Carlo forward-fitting	Golub et al. (2004)
Monte Carlo Markov Chain (MCMC)	Kashyap et al. (1998)
Bayesian iterative method	Goryaev et al. (2010)
Bayesian inversion	Guennou et al. (2012)
Regularized inversion	Iain G Hannah et al. (2012)
Filter ratio methods	
Method	**Methodical descriptions**
Two-filter ratio	Weber et al. (2005)
Three-filter ratio	Aschwanden et al. (2005)
Color-color	Noglik et al. (2007)
DEM forward-fitting methods	
Method	**Methodical descriptions**
Single or multi-Gaussian DEM	Aschwanden et al. (2011)
Spatial synthesis (Gaussian DEM)	Aschwanden et al. (2013)
Spatial synthesis (sparse solution)	Cheung et al. (2015)
Emission measure loci methods (EMI)	
Method	**Methodical descriptions**
Inverse response functions	Landi et al. (2002)

Table 2.2: List of most used *differential emission measure* (DEM) reconstruction methods. Adapted from table 2.3 in Aschwanden (2019a). The Monte Carlo forward-fitting method has been used in previous works to perform DEM analysis using FOXSI observations together with Hinode/XRT and SDO/AIA (Ishikawa et al., 2014; Ishikawa et al., 2017; Athiray et al., 2020)

$$I(\varepsilon) \propto \int_V \frac{\exp(-\varepsilon/k_B T)}{T^{1/2}}\, n_e^2\, dV \quad [\mathrm{keV\ s^{-1}\ cm^{-2}\ keV^{-1}}] \tag{2.24}$$

where the proportionality constant is $\sim 8.1 \times 10^{-39}$ for solar flare typical parameter values according to, e.g., Brown (1974). In most cases, a single thermal distribution (isothermal) is enough to characterize spectrum flares (e.g., Vievering et al., 2021; Sahu et al., 2020). However, for some instances, multiple temperatures Maxwellian and/or a non-thermal component need to be added to fully account for the X-ray radiation of one of the eruptive solar events (e.g., Battaglia et al., 2015; Fleishman et al., 2021).

2.2.3 Non-thermal radiation

Solar flares accelerate charged particles as one of the consequences of releasing magnetic energy after a magnetic reconnection. Such energized particles travel through nearby coronal plasmas colliding with surrounding particles via Coulomb processes. The collision frequency, ν_C, scales with particle energies, E, as $\nu_C \sim E^{-3/2}$ (see, e.g., Somov, 2012b). For typical coronal densities ($n_e \sim 10^9$ cm^3), electrons with energies of about 100 keV and over traveling Sun-inwards along loop legs rarely collide until reaching the denser chromosphere, where densities rise up to $n_e \sim 10^{11}$ cm^3 (see, e.g., Longcope, 2020). Once there, electrons deposit their energy at the loop feet producing hard X-rays footpoints via bremsstrahlung (a process known as thick-target emission, Tandberg-Hanssen et al. (1988)) and the subsequent chromospheric evaporation. The rare collisions of higher energy electrons ($\gtrsim 100$ keV) with the ambient plasma before reaching the loop footpoints is the reason why, at these high energies, the electron distribution function is weakly thermalized. This is not the case for low energy electrons (~ 1 keV) which distribution function rapidly gets into a Maxwellian due to their comparatively high-frequency collision rates. From the total initial kinetic energy (E) of an electron, a small fraction converts to photons via bremsstrahlung with energies $\varepsilon_{photon} \leq E$. Observing those photons in X-rays is the most direct diagnostic of the electron populations as a function of their energy. Observations of solar flare spectra empirically show that the distribution function is usually a mix between a thermal component (Maxwellian with $I(\varepsilon) \sim \sqrt{\varepsilon} \exp{(-\varepsilon/k_B T)}$) at low energies with a power-law shape, $I(\varepsilon) \sim \varepsilon^{-\gamma}$ restricted to $\varepsilon \geq \varepsilon_c$, at higher X-ray frequencies. ε_c is the cut-off energy set at a value such that the thermal component of the solar spectrum dominates the emission at lower energies, and the power-law does it for higher energies. The right frame in figure 2.5 shows the X-ray spectrum of a flare that happened on July 19th, 2012, at 5:58 UT with a typical profile. That spectrum shows a clear thermal component in green joined with two non-thermal power-law components (in blue and red) that Krucker et al. (2013a) argue come from two distinct regions of the flare (see left image in figure 2.5).

According to the thick target model (e.g., Brown, 1973; Tandberg-Hanssen et al., 1988), the accelerated electrons, initially with a power-law type distribution function ($F(E) \sim E^{-\delta}$), produce a power-law photons spectrum, $I(\varepsilon) \sim \varepsilon^{-\gamma}$, having the spectral indexes relating by $\gamma = \delta - 1$ at the chromospheric footpoints of a flare. Since observations show photon indexes $\gamma \geq 2$, that implies electron's indexes $\delta \geq 3$. When the same power-law distribution of electrons transit coronal plasma, where densities are lower, the bremsstrahlung emission will have a power-law index $\gamma = \delta + 1$ according to the thin target model (see, e.g., Tandberg-Hanssen et al., 1988; Longcope, 2020).

2.3 Coronal heating, an open puzzle

In solar and heliophysics, the corona heating problem relates to the puzzle of identifying and understanding the mechanism(s) causing corona's temperatures to be up to a thousand
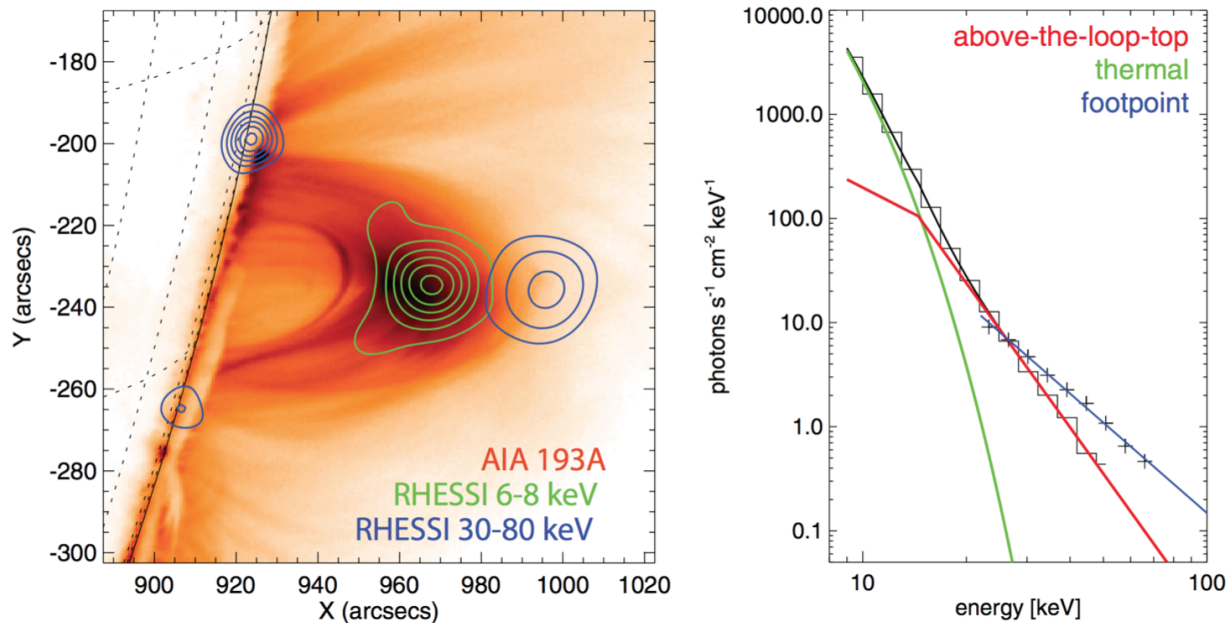
Figure 2.5: *Left*: SDO/AIA-193 image of the region where the SOL2012-07-19T05:58 (M7.7)
happened. The blue and green contours are X-rays observed with RHESSI at 6-8 keV and
30-80 keV, respectively. *Right*: Spectrum of the SOL2012-07-19T05:58 (M7.7) showing the
typical thermal emission at lower energies (green) and power-law components at higher
energies (blue and red). Image taken from Krucker et al. (2013a).

times hotter than the solar surface (e.g., Klimchuck, 2004; Klimchuk, 2006). These tem-
peratures demand a mean energy input of $\sim \times 10^5$ - 2×10^7 erg cm^{-2} s^{-1} (Withbroe et al.,
1977). Among the various plausible hypotheses proposed to explain this problem, the two
strongest candidates are i) MHD wave dissipation (e.g., Van Ballegooijen et al., 2011) and
ii) copious low energy magnetic reconnections (or "nanoflares" as coined by Parker (1988))
(see, e.g., Aschwanden, 2000; Bogachev et al., 2020). Klimchuk (2006) pointed out that,
when examined thoroughly, most plausible coronal heating explanations imply non-thermal
heating that happens impulsively on individual flux tubes (strands). If such small impulsive
events follow a scaled-down physics of larger flares, energized non-thermal electrons during
the small ubiquitous reconnections in the corona should be the base for heating the coronal
plasma. There are two primary lines of observational evidence supporting the presence of
such miniature impulsive energy releases in the corona. There are two primary lines of ob-
servational evidence supporting the presence of such miniature impulsive energy releases in
the corona. They have been observed i) as individual distinguishable events and ii) as an
aggregate in non-flaring active regions.

Cirtain et al. (2013a), e.g., reported observations of individual reconnecting magnetic
braids in a coronal active region using data from SDO/AIA and the Hi-C sounding rocket.
Cirtain et al. (2013a) claimed that the observed small impulsive events dissipate sufficient
energy to heat the surroundings to several million K. Testa et al. (2014) also found obser-
vational evidence of small individual impulsive ($\lesssim$30 seconds) heating events. Testa et al.
(2014) used data from the Interface Region Imaging Spectrograph (IRIS) to reveal rapid
intensity variabilities ($\sim$20 to 60 seconds) at the footpoints of coronal loops. They estimated
that their observed nanoflares deposited $\lesssim 10^{25}$ erg in the lower layers of the solar atmo-
sphere. More recently, Antolin et al. (2021), using coordinated multi-band high-resolution
observations (including SDO/AIA, IRIS, and the Hinode/Solar Optical Telescope), reported
evidence of very fast and bursty nanojets in a loop-like structure at the limb of the Sun. The
observed strands yielded an estimated total energy released of $\sim 10^{25}$ erg.

Aggregates of impulsive energy release events are the explanation given by Warren et
al. (2003) to justify their observations of warm dense coronal loops. They observed an
active region above the limb with SOHO/SUMER and found evidence of overdense plasma
($\sim 10^8$ cm^{-3}) at temperatures of $\sim$1 MK. Winebarger et al. (2011) built a steady heating
model to interpret observations they performed of an active region using Hinode/XRT and
Hinode/EIS. They found the DEM to be broad ($6.3 < \log T < 6.7$), peaking around 3 MK.
Their findings are also consistent with a myriad of frequent heating events in the coronal
active region they observed. In 2013, Del Zanna presented simultaneous SDO/AIA and
Hinode/EIS observations of multiple active regions. He found that in most cases, there
is evidence of a hotter ($\lesssim$ 2.5 MK) emission still unresolved even at the Hi-C resolution
(0.25 arcsec). One of the most convincing evidence of nanoflare heating is the active region
observations performed by the EUNIS-13 sounding rocket instrument. EUNIS-13 detected
the Fe XIX line clearly at 592.2 AA produced by the hot active region plasma (T$\sim$ 9 MK).
Brosius et al. (2014) claimed that this observation provides strong evidence for the nanoflare
heating model of the solar corona.

Faint hard X-rays produced by nanoflares are expected from the hottest plasma in the
quiet Sun's corona and non-flaring active regions. According to, e.g., Bradshaw et al. (2011),
two primary reasons cause their faintness. i) The relatively low-density coronal conditions
that induce an intense downward heat flux, resulting in a somewhat slow chromospheric
evaporation. This evaporation efficiently performs effective conductive plasma cooling for
every rapid nanoflare chunk of energy being released in the corona. This cooling prevents
the high-temperature plasma from getting dense enough to emit intensively in hard X-rays.
ii) A strong "inertia" of the ionization equilibrium prevents nanoflares from changing the
ionization state of the surrounding coronal plasma due to nanoflares' short heating time
scales. The low number of produced highly charged ions makes the emission in hard X-
rays much weaker than that from plasmas at the same high temperatures under ionization
equilibrium conditions.

Using Hinode/XRT and RHESSI observations, several efforts have aimed to observe
nanoflare hard X-rays. Though no definitive direct detection has been claimed, some con-
straints of the ~ 5 MK plasma emission have been reported (e.g., Reale et al., 2009; Schmelz
et al., 2009). In particular, McTiernan (2009) presented evidence of $\sim 5 - 10$ MK plasma
presence in non-flaring active regions. McTiernan (2009) achieved these results by perform-
ing analyses over RHESSI data captured during quiescent periods observed from 2002 to
2006. Using a similar approach but using CORONAS-PHOTON/SphinX data, Miceli et al.
(2012) reported a detection of scorching plasma in the quiescent corona at T$\sim$ 7MK with
an emission measure of $\sim 2.7 \times 10^{44}$ cm^{-3}. In 2014, Del Zanna et al. assessed elemental
abundances and temperatures of quiescent solar active region cores using older X-ray ob-
servations obtained by a sounding rocket and by the Solar Maximum Mission (SMM) Flat
Crystal Spectrometer (FCS). They found direct evidence that the emission measure at $\sim$3
MK has a very steep negative slope, with very little plasma at $T \gtrsim 5$ MK. Combining hard
X-rays observed with FOXSI-2, SDO/AIA, and Hinode/XRT data, Ishikawa et al. (2017)
revealed the presence of hot plasma over 7 million Kelvin for a non-flaring active region.
More recently, Marsh et al. (2018) analyzed data from the FOXSI sounding rocket and the
NuSTAR spacecraft to constrain properties of active region nanoflares using EBTEL simula-
tions [4]. They reported heating amplitudes between 0.02 and 13.0 erg cm^{-3} s^{-1} for the single
quiescent active region observed by FOXSI-2 on 2014 December 11. NuSTAR observations of
another active region yielded a narrower heating amplitude range of 0.23-0.32 erg cm^{-3} s^{-1}.
Marsh et al. (2018) attributed the discrepancy to differences in spectral coverage between
the two instruments and intrinsic differences among the observed active regions.

For nanoflares, with energies of $E \sim 10^{24}$ erg, hard X-rays are far fainter than those
from larger flares and therefore challenging to detect due to the limited sensitivity of the
current instruments. Consequently, up to date, the role that nanoflare non-thermal particle
processes have in heating the quiescent corona remains ambiguous at best.

According to the coronal heating nanoflare hypothesis, it is possible that all the observa-
tional efforts discussed above contained a myriad of individual, so far unresolvable, faint hard
X-ray small kernels. Observing them requires instruments with superior dynamic ranges and
sensitivities. Focusing optics for X-rays offer such capabilities. The Focusing Optics X-ray
Solar Imager sounding rocket payload uses that type of technology and is the center of the
topic of the rest of this dissertation.

---

[4]See Klimchuk et al. (2008), Cargill et al. (2012a), and Cargill et al. (2012b), e.g., for generalities of
EBTEL simulations.

Chapter 3

The Focusing Optics X-ray Solar Imager (FOXSI)

The Focusing Optics X-ray Solar Imager (FOXSI) is the first solar-dedicated NASA sounding rocket experiment that performs imaging spectroscopy in hard X-rays (HXRs) using direct focusing techniques (see Figure 3.1). FOXSI has improved the sensitivity and imaging dynamic range by orders of magnitude compared to its predecessors (e.g., RHESSI), demonstrated in three successful flights (2012, 2014, and 2018). Here after FOXSI-1, -2, and -3, respectively. FOXSI is currently funded to flight a fourth time in NASA's first solar flare campaign. The FOXSI rocket payload is a pathfinder to indicate the sort of scientific accomplishments that a solar-dedicated spacecraft based on this technology could achieve in the future. All details of the original concept for the design of the FOXSI payload (and first launch) can be found in Glesener (2012).
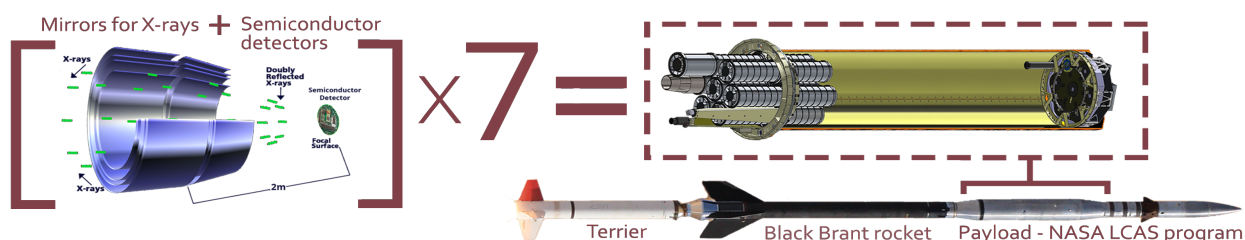
Figure 3.1: FOXSI integrates seven sets of X-ray mirrors paired with semiconductor detectors optimized to perform imaging spectroscopy of the Sun in the 4-20 keV energy range. FOXSI is the payload of a sounding rocket payload successfully flown three times as part of NASA's Low-Cost Access to Space (LCAS) program.

A number of papers in the literature provide sufficient details on key aspects of the FOXSI experiment. Krucker et al. (2013b) and Krucker et al. (2014) describe the original payload

and first scientific results of the mission. Glesener et al. (2016) provides an overview of the first two flights of the experiment. Christe et al. (2016b) describes major updates made for the second flight as well as details on the mirror shell prescription. Musset et al. (2019), Athiray et al. (2017) and Furukawa et al. (2019) describe the hardware upgrades for the 3rd flight of the sounding rockets.

Details of payload and key science results can be found in Krucker et al., 2013b; Krucker et al., 2014; Glesener et al., 2016; Christe et al., 2016b; Ishikawa et al., 2017; Buitrago-Casas et al., 2017a; Musset et al., 2019; Athiray et al., 2017; Furukawa et al., 2019; Athiray et al., 2020; Buitrago-Casas et al., 2020; Vievering et al., 2021; Buitrago-Casas et al., 2021.

This chapter begins by discussing different novel optics elements used to work with X-rays. I emphasize the implementation of these different techniques to observe solar X-rays, indicating when they have been part of a space instrument or what kind of solar applications can come in the future. Then, I explain the fabrication process implemented to produce the FOXSI optics at the NASA Marshall Space Flight Center. Next, I present some important factors of the detectors used on each rocket flight. Then, I highlight significant science aspects learned at each of the three rocket campaigns. I finalize the chapter presenting some of the technical and scientific goals we expect to achieve with the fourth flight of the FOXSI rocket, which intends to observe a medium to large size solar flare. My contributions to this work are described in Buitrago-Casas et al. (2021).

3.1   The challenge of focusing X-rays

This section mainly outlines relevant items found with thorough details in Chapter 10 of Attwood (2016).

For many applications, it is important to manipulate photons in the X-ray energy band with high precision. This manipulation is possible by using several optics designs that use the usual physical principles of light and matter interaction, but optimized for high energies. Such designs use standard physics of reflectiveness, refractiveness, and diffraction applied to flat, curved, and multilayer mirrors; gratings (transmission and reflection), zone plates, crystals, and lenses.

In general, the scattering and refractive index $n(\omega)$ (as a function of the frequency ω) of certain material can be written in terms of the complex expression

$$n(\omega) = 1 - \frac{2\pi n_a r_e c^2}{\omega^2} \left[f_1^0(\omega) - i f_2^0(\omega) \right], \tag{3.1}$$

where n_a is the atomic density, $r_e = e^2/4\pi\epsilon_0 m c^2$ is the classic electron radius, c is the light speed, and $[f_1^0(\omega) - i f_2^0(\omega)]$ is known as the *complex atomic scatter factor* after reducing

it for short frequencies and small incidence angles of the photons (superscript zero). Values of f_1^0 and f_2^0 have been tabulated for all elements from H to U by Henke et al. (1993), (Soufli et al., 1997), and Gullikson (2021) using the Kramers-Kronig relations and measurements of radiation absorption in materials of interest (C, O, Ir, Ni, Si, Au, etc).

For X-rays, the refractive index n in equation 3.1 differs from unity only a small amount (which is not the case for visible light). This is why for high energies, n it is commonly simplified as

$$n(\omega) = 1 - \delta + i\beta. \tag{3.2}$$

A very small δ (real part of n) enables total external reflections for X-rays. β decreases for hard X-rays inhibiting absorption, and most materials become transparent for higher energies. At these energies, the reflectivity of a specific material ($R_\perp \simeq (\delta^2 + \beta^2)/4$) is typically very small and restrained to glancing angles of incidence smaller than the critical angle for total external reflection,

$$\theta_c = \sqrt{2\delta}. \tag{3.3}$$

X-ray mirrors follow the usual specular reflection despite the small incident angles, i.e., the angles of reflection and incidence are equal for all wavelengths (achromatic nature). However, for a mirror to reflect X-rays, it needs to hold two main characteristics: i., it needs to be composed of a high-Z (Z is the atomic number) material, and ii, it must have a highly polished surface. Shaping the mirror into a particular geometry will make it perform desirably. For X-ray mirrors, their geometrical shape is known as the figure and their roughness as the finish (usually in the order of the Å). Thus, the performance of a particular mirror will be determined by the quality of its *figure* and its *finish*. Shaping the mirrors into a specific geometry is achievable with techniques like direct bending, grinding, polishing, and electroforming techniques that use controlled delivery of ultrafine reactive particles.

Due to the small angle, X-ray mirrors shaped to focus large amounts of photons usually have large focal distances (commonly in the order of meters). Shortening these focal distances is possible by coating the mirrors with materials such as gold (which additionally can serve as a low pass filter). The coating material becomes the dominant factor for the reflective performance of an X-ray mirror. Figure 3.2 shows the X-ray reflectivity of a mirror coated with an 8 Å finish Iridium layer for a set of incidence angles (0.1°-12.8°). From this figure it is clear that the smaller the grazing angle, the better reflectivity performance at higher energies. It also explains why mirrors for higher energies require much larger focal distances.

---

[1]http://www.rxollc.com/idl/
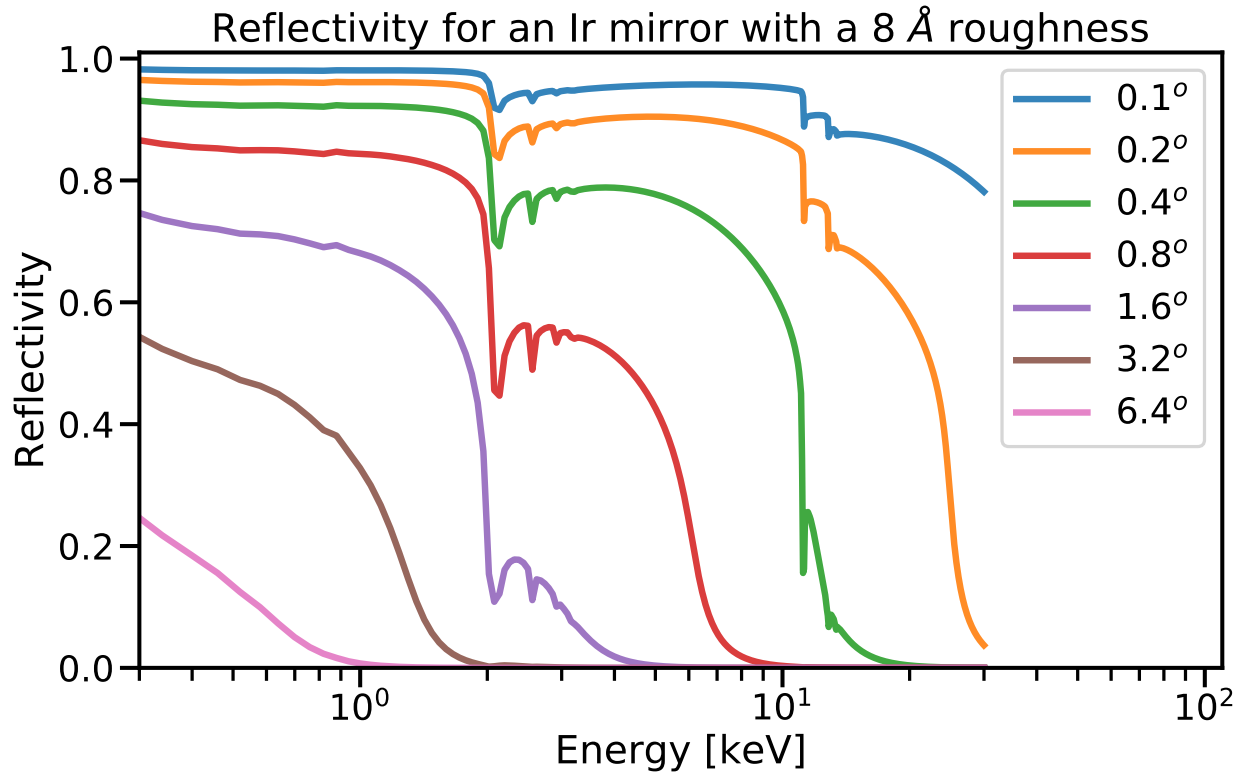
Figure 3.2: Reflectivity for 0.1-30 keV X-rays as a function of glancing incidence angles (0.1º-12.8º) for a mirror coated with Iridium with a finish of 8 Å. I obtained these curves using the IMD package for IDL (Windt 1998)[1]. FOXSI's optics uses a geometry optimized for incident angles between 0.23° and 0.4°.

Figure 3.3 displays the reflectivity as a function of photon energy for mirrors of Iridium with finishes ranging from 1 Å to 1024 Å. All curves in Figure 3.3 were computed for a single incidence angle of 0.23°. From this figure it is evident that more polish of a mirror, the better reflectivity performance. Note that despite the smoothness of the mirror surface, there is a hard cutoff below 20 keV.

3.1.1 Wolter mirrors

X-ray mirrors need to be shaped into a particular geometry to direct all incoming rays over a common focal point. Following classical geometrical optics, such a feature is achievable using conic section geometries (ellipses, parabolas, and hyperbolas). X-ray mirrors are shaped into conic section geometries with parameters that allow very shallow incidence angles. In 1948, Kirkpatrick et al. proposed more elaborated compositions of X-ray mirrors in pairs. A few years later (1952), Wolter published a generalization of Schwarzschild mirrors adapted
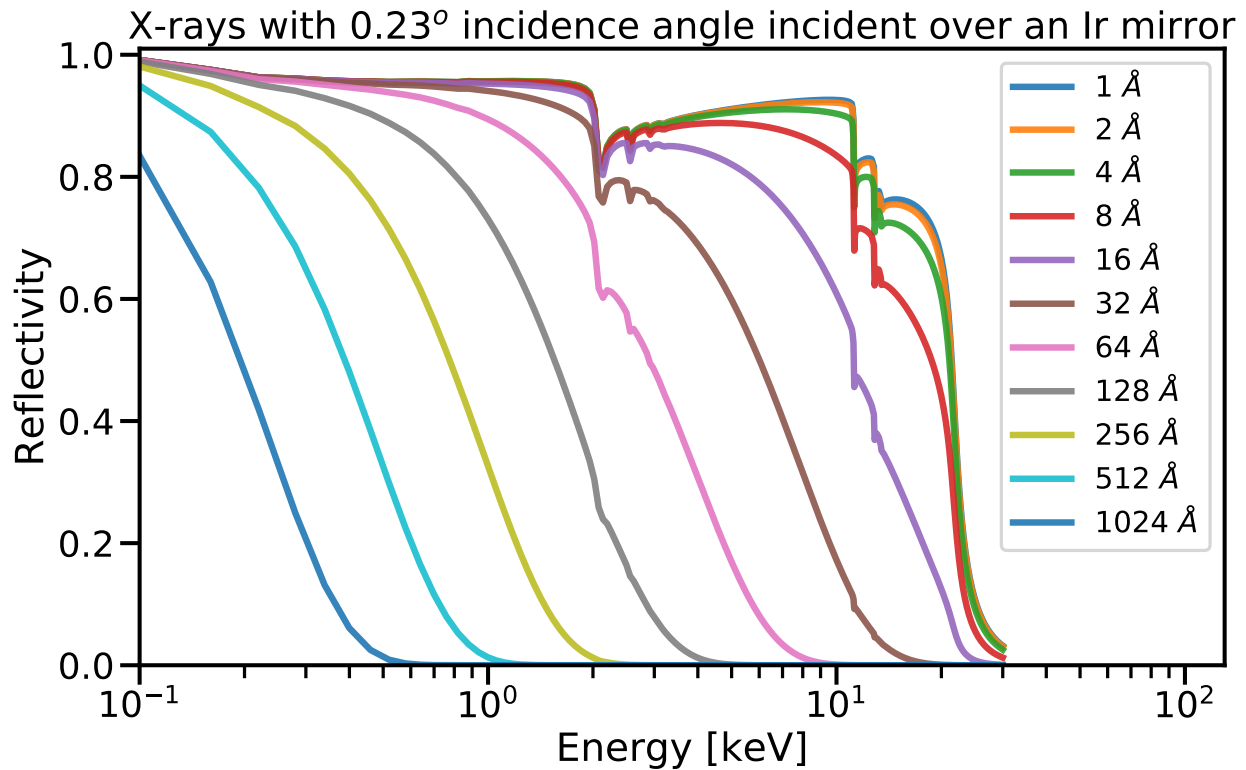
Figure 3.3: Reflectivity for 0.1-30 keV X-rays as a function of coating roughness (1 Å-1024Å) of an Iridium mirror. These data were computed for X-rays with a grazing incidence angle of 0.23^o. I used the IMD package for IDL (Windt 1998).
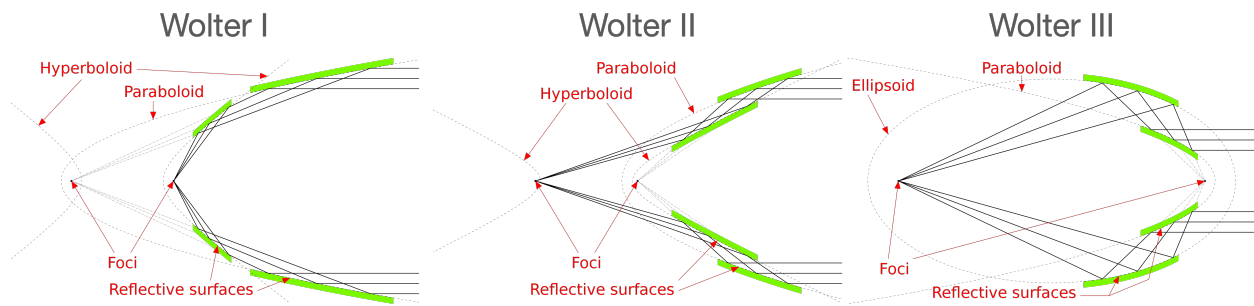
Figure 3.4: Wolter I, II, and III design for X-ray mirrors. These mirrors, designed originally by Wolter (1952), use two reflective shells shaped into conic sections to focus X-rays. The Wolter-I geometry has the advantage that it can be made in a monolithic piece. *Link to the original Figure*:
https://en.wikipedia.org/wiki/Wolter_telescope/media/File:Wolter-I.svg, CC BY-SA 4.0.

to glancing incidence for X-ray imaging. Wolter's paper outlines three ways of building X-ray telescopes coupling two mirrors shaped into different kinds of conic section geometries. Modernly, the three designs are known as Wolter I, II, and III (see Figure 3.4). The most significant advantages of these optics designs over others are their wider field of view and reduced comma effect. Wolter I schemes have the additional benefit that mirrors incorporating this geometry can be made in a single piece (monolithic). This is advantageous in terms of co-aligning the mirrors to the same optical axis (e.g., VanSpeybroeck et al., 1972). Fabrication techniques involving growing material over a desired shape (like the case of electroformation) also benefit directly from the Wolter-I design.

When fabricating X-rays mirrors, the figure and finish precision are crucial parameters. Several groups have developed various techniques to achieve these requirements in the last few decades. These techniques include grinding (e.g., Ohmori et al., 2020) and polishing (e.g., Spiller, 1990), bending a polishing flat (e.g., Howells et al., 2000), elastic emission machining (e.g., Yamauchi et al., 2003), and use of mandrels (e.g., Ramsey et al., 2004; Mimura et al., 2020). The last one is the one used for producing the FOXSI optics (e.g., Krucker et al., 2011).

3.1.2 Other novel ways of focusing X-rays

Reflecting X-rays using mirrors shaped into Wolter geometries is not the only way of focusing high-energy photons. Other methods take advantage of standard radiation-matter interaction (e.g., reflection, diffraction, and refraction) to make photons converge over a common focal plane. Figure 3.6 (taken from Attwood, 2016, Chapter 10) summarizes some of the most used techniques for focusing EUV and X-rays using typical forms of reflective, diffractive, and refractive optics. In this section, I briefly highlight some of the most notable features of most of the techniques in Figure 3.6. I emphasise the application of these optics to solar observations when possible. I begin with Kirkpatrick-Baez telescopes and multilayers since I already discussed mirrors' generalities to reflect short-wavelength photons above.

3.1.2.1 Kirkpatrick-Baez mirrors

Wolter-I mirrors are expensive to fabricate. A cheaper option is Kirkpatrick-Baez optics, which are crossed arrays of parabolic mirrors arranged for grazing incidence double reflections (see Figure 3.5). Recent works (e.g., Hudec et al., 2018; Longcope et al., 2019), have looked into the feasibility of producing actual Kirkpatrick-Baez optics for astrophysical observations. In particular, Longcope et al. (2019) has shown that by restraining flat "slats" of commercially available glass in high-precision grooves, it is possible to construct a Kirkpatrick-Baez telescope system. This new approach offers a sufficiently high effective area with a reasonable resolution for astrophysical (and solar) applications.
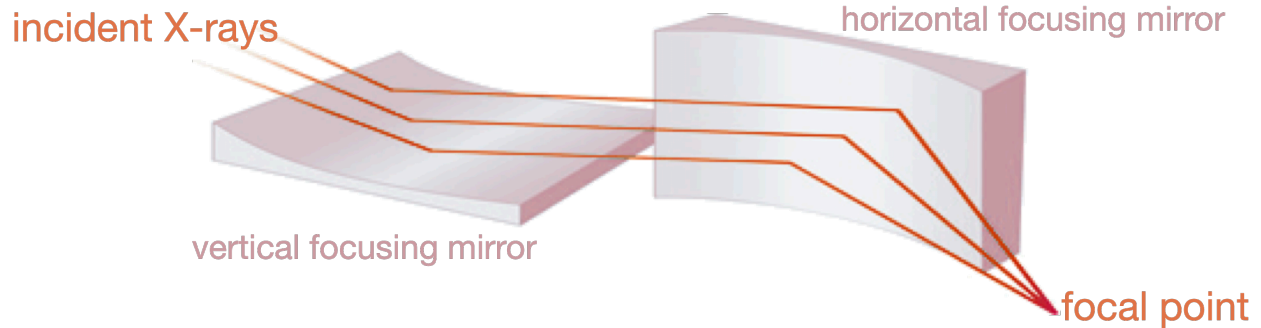
Figure 3.5:   Kirkpatrick-Baez mirrors.

3.1.2.2   Multilayer mirrors

For a broad (achromatic) spectral coverage both Kirkpatrick et al., and Wolter designs are used with uncoated mirrors. When the goal is to narrow the spectral bandwidth, the mirrors are coated with graded multilayer coatings meeting the Bragg condition everywhere on the surface. Bragg's law assert that

$$m\lambda = 2d\sin\theta, \tag{3.4}$$

with d being the thickness of one bilayer pair, λ the wavelength of an incoming X-ray, θ the incidence angle, and m an integer number. The setting of high Z material thickness to bilayer period ratio (Γ) is important when fabricating multilayer mirrors. Γ is defined as

$$\Gamma = \frac{\Delta t_H}{\Delta t_H + \Delta t_L} = \frac{\Delta t_H}{d}, \tag{3.5}$$

where Δt_H and Δt_L are the thicknesses of high Z and low Z (spacer) materials, respectively. Additionally, in a multilayer mirror, each material has its corresponding refractive index following equation 3.1 and 3.2. Thus, the net performance of a multilayer mirror is obtained as the sum of all reflected rays at each interface.

The Nuclear Spectroscopic Telescope Array (NuSTAR) is a space telescope implementing 133 concentric mirror shells coated with Pt/SiC and W/Si multilayers shaped into a conical approximation of a Wolter-I figure (e.g., Harrison et al., 2013). NuSTAR was designed primarily to detect hard X-rays from faint astrophysical sources outside our solar system. However, by the end of 2021, NuSTAR has pointed to the Sun 28 times to observe solar X-rays. See details of all these observations campaigns here: https://ianan.github.io/nsigh_all/. Other space instrument using multilayers to observe the Sun is the Atmospheric Imaging
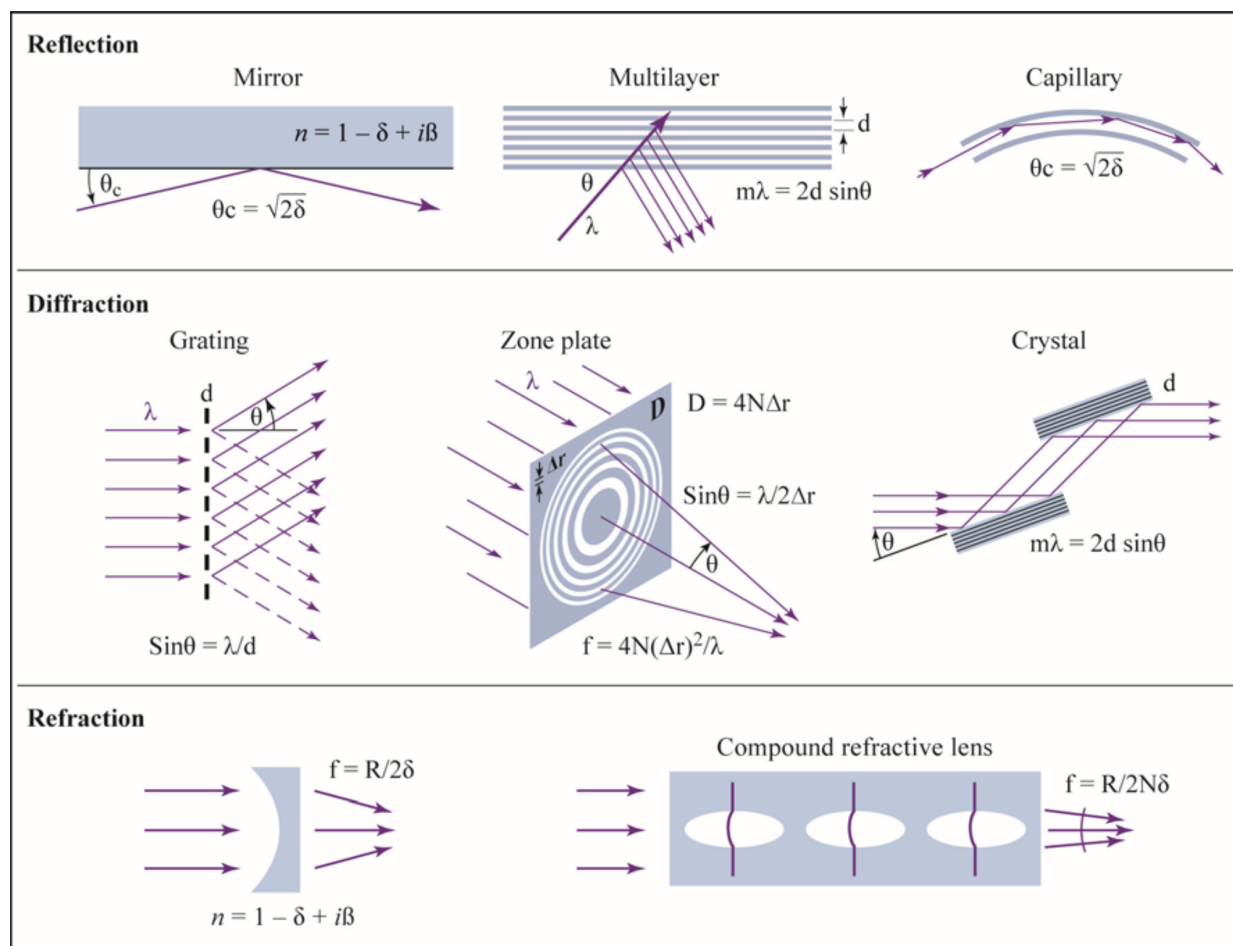
Figure 3.6: Common optical techniques used for focusing photons. These techniques require small incidence angles and grid distances for shorth wavelength rays. Materials used for these kinds of optics should have properties accounting for specific short photon wavelengths. These properties include (but are not limited to) capturing the complex atomic scattering factors and refractive and reflective indices. Figure from Attwood (2016), Chapter 10.

Assembly (AIA) onboard the Solar Dynamic Observatory (SDO). However, AIA/SDO is optimized for observations in a narrow band of EUV radiation and normal photon incidence angles (e.g., Soufli et al., 2005).

Recently, several groups (e.g., Dhez, 1987; Aquila, 2009) are using multilayer mirrors for controlling and measuring light polarization. However, existing technology only allows photons reflecting with angles near 45° to benefit from these polarization applications. Future solar space instruments could benefit from the polarization measuring power that multilayer mirrors offer. The use of multilayer optics is been extended to higher energies, now going even above 100 keV (e.g., Brejnholt et al., 2014).

3.1.2.3 X-ray capillary optics

X-ray capillary optics work under the same physical principles as standard optical fibers (e.g., Okoshi, 2012). Rays coming into a capillary (or fiber) overcomes total external reflections upon the internal surface. Particularly, capillaries need to use high Z materials with very smooth (low roughness) internal surfaces for short-wavelength photons (e.g., Bilderback, 2003). The upper right panel in Figure 3.6 shows a photon going through a single capillary via multiple total external reflections from the internal capillary surface. Manufacturers produce bundles of capillaries shaped in particular forms via heating and pulling (e.g., Gibson et al., 2002). Most single-bounce capillaries work at energies ranging from a few keV to tens of keV (e.g., Trivedi et al., 2020). Their high dependence on the internal surface's critical angle is sometimes used to set capillaries as band-pass filters (e.g., Engström et al., 1991). Capillaries have proved to work in space for high-energy observations (primarily electrons) as part of multi-channel plate detectors (e.g., Schmitz, 2011). During FOXSI's third campaign, we evaluated multi-capillary as a possible solution to reduce instrumental background. Among the variety of companies that provide optical fibers for X-rays, we chose to work with X-ray Optical Systems (XOS). XOS and we developed a multi-capillary device concept to mitigate a specific background known as ghost-rays. Chapter 5 gives details of how ghost-rays are produced and shows strategies we assessed to diminish them. The device we developed with XOS consisted of several straight cylindrical multi-capillaries optics bundled together. The common goal of the multi-capillaries XOS (and other companies) produce is to get X-rays within the fibers and focus them into a single spot by curving the bundles in specific shapes. For FOXSI, our goal was different. We wanted to use the fibers as collimators to absorb X-rays coming in off-axis angles larger than the arctan of the inverse of the fibers aspect ratio. XOS fabricated a customized multi-capillary bundle for us with very rough internal surfaces to minimize the internal X-ray reflection of the fibers. Figure 3.7 shows the outcome of an experiment XOS ran to test the internal reflectivity of these customized multi-capillaries.

X-ray capillary optics have plenty of possible applications in space sciences. We have identified the potential use of this technology as collimators for reducing ghost-rays in pay-
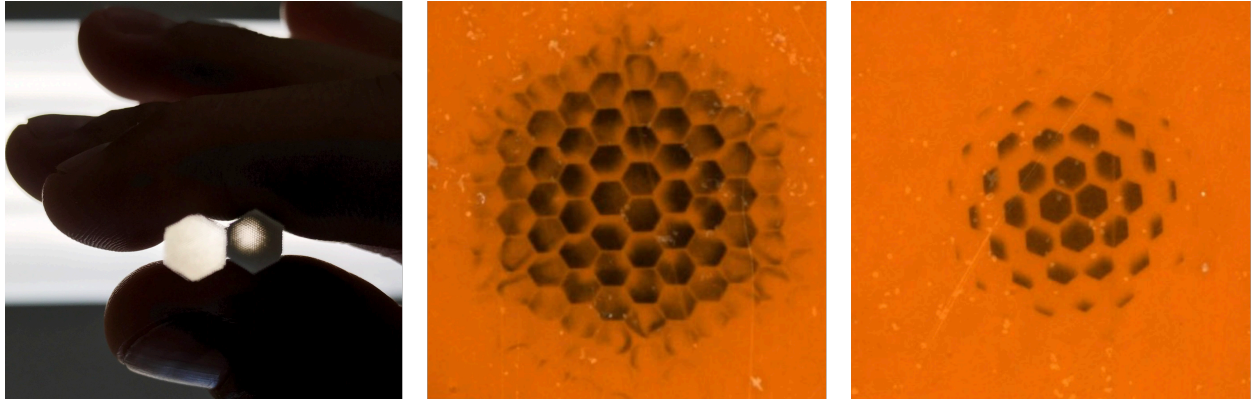
Figure 3.7: Multi-capillary bundles produced by the X-ray Optical Systems (XOS) company in Albany, New York. In this figure, we show two bundles with different internal reflectivities. One bundle has the standard internal reflectivity fabricated by XOS, while the second was modified to increase its internal roughness (decrease of reflectivity). *Left*: A photograph of the two bundles while aligning them to an ordinary office lamp to visually inspect their reflectivities. The left bundle uses standard fabrication parameters, while the one on the right was modified to decrease its reflectivity. The same two bundles were set on an optical bench and illuminated with X-rays at five keV to test their reflectivity properties for higher energies. The results of those tests are shown in the *center* for the standard bundle and on the *right* for the customized bundle. *Pictures courtesy of Jared Sachs (jsachs@xos.com), X-ray Optical Systems Company Albany, New York.*

loads using Wolter-I mirrors for solar X-ray instruments (all the details can be found in Buitrago-Casas et al., 2017). I see other potential application of X-ray capillaries in Cube-Sats to maximize the observed X-ray flux focus onto the semiconductor detector of a solar spectrograph.

3.1.2.4 Transmission gratings

Diffraction is another convenient way of focusing X-rays. The second row in Figure 3.6 shows three usual methods used in a wide variety of applications. In particular, transmission gratings are examples of optical devices using constructive interference of diffracted radiation to focus light of specific wavelengths on determined spots. A grating is characterized by a scale of d (distance between two consecutive holes). When an angle θ (known as the Bragg angle) is such that the path length is an integer number (m) of the incoming wavelength radiation,

$$\sin \theta = m \frac{\lambda}{d} \tag{3.6}$$

(which is just a factor of two different from equation 3.4), a constructive interference is produced at the focal plane. In general, in astrophysics, and particularly in solar physics, X-ray transmission gratings are used near the focus of X-ray telescopes as spectroscopic tools. The goal is usually to isolate spectral features associated with certain emission/absorption lines. In general, in astrophysics, and particularly in solar physics, X-ray transmission gratings are used near the focus of X-ray telescopes as spectroscopic tools. The goal is usually to isolate spectral features associated with certain emission/absorption lines. The Marshall Grazing Incidence X-ray Spectrometer (MaGIXS) sounding rocket experiment is a recent example of such an instrument. MaGIXS is optimized to spatially resolved soft X-ray spectra of the solar atmosphere in the 0.5-2.0 keV range. It consists of a single Wolter-I mirror, a slit, and a spectrometer that comprises simple X-ray parabolic mirrors paired with **diffraction gratings**. All the details of MaGIXS can be found in, e.g., Kobayashi et al. (2018) and Champey et al. (2019), and Vigil et al. (2021).

3.1.2.5 Fresnel zone plates

The Fresnel zone plate lens is a more advanced optical device using interfering radiation via diffraction. These lenses are circular diffraction gratings with apertures of equal area (equal diffraction power), i.e., increased radial gaps towards the center of the lens (see the middle illustration of the second row in Figure 3.6). The Fresnel zone plates focus positive order interference (e.g., $m = 1$) to a single spot while preserving the imaging properties of standard lenses. Because Fresnel zone plates are gratings, they can operate at higher interference orders (example $m = 3$). At higher orders, a Fresnel zone plate could theoretically offer a better spatial resolution at the cost of lowering its efficiency. The spacing among consecutive gratings in a Fresnel zone plate lens must follow the relation given in equation 3.6. The lenses produce constructive interference (first order) at a focal distance (f) constrained by the following Pythagorean expression,

$$f^2 + r_i^2 = \left(f + \frac{i\lambda}{2} \right)^2, \tag{3.7}$$

where r_i is the radius of the i-th zone aperture in the plate. Solving for r_i, we get

$$r_i^2 = i\lambda f + \frac{i^2\lambda^2}{4}. \tag{3.8}$$

For very short wavelengths (i.e., X-rays) and $f \gg i\lambda$,

$$r_i \approx \sqrt{i\lambda f}. \tag{3.9}$$

Since the sixties, Fresnel zone plate lenses have been extensively used for solar X-ray imaging applications (e.g., Elwert, 1968; Dijkstra et al., 1971; Kramer et al., 1977). More recently, teams at the NASA Goddard Space Flight Center (GSFC) have led an adaptation of the Fresnel zone plate lens concept known as **photon sieves** (e.g., Davila, 2011; Vievering, 2012). These devices resemble the pattern of Fresnel zone plates, but instead of full continuous gaps, they have pinholes of various sizes. One of the most attractive features of both Fresnel zone plates and photon sieves is their capacity to focus X-rays of different energies (wavelengths) at different focal lengths. Some authors have probed the success of using photon sieves to generate images of the Sun in EUV and H-alpha (e.g., Artzner et al., 2003; Vievering, 2012). The general problem with photon sieves for solar X-ray observations is their limited aperture area. This limitation becomes a disadvantage for low emission photon sources, as is the case for solar X-rays and gamma rays (e.g., Kipp et al., 2001). According to Dennis et al. (2012), imaging the Sun at the known 6.7 keV iron line complex using current photon sieves would require a ~ 100 m focal length. Following equation 3.9, shortening such focal length would demand decreasing the radii r_i of the photon sieves (or the Fresnel zone plate, for that matter). Another future possibility would be to accommodate the Fresnel zone plate lenses and the detectors in two separate small satellites (CubeSats). This solution would require very high precision in controlling the position of the two spacecraft at all times (e.g., Skinner et al., 2013).

3.1.2.6 Crystal structures

Crystal structures are a powerful tool to manipulate light (and X-rays, for that matter). By orienting crystals into particular angles, crystals can control energy resolution, angular divergence, intensity, and polarization of X-rays depending on the energy of the photons and incoming angle. A specific example of a crystal with a wide variety of applications is *Laue* lenses.Unlike multilayer mirrors, Laue lenses use the crystal thickness to make the X-rays interfere coherently to increase the diffraction efficiency. A Laue lens is a zone plate shaped in a linear configuration. It is able to focus X-rays with energies above 100 keV depending on the material of the crystal. Crystals are commonly used as one of the optical components for solar X-ray instruments. One example of that kind of instruments is **flat crystal spectrometer** flown as part of the Solar Maximum Mission (e.g., K. Phillips et al., 1982) and the *REntgenovsky Spektrometr s Izognutymi Kristalami* (RESIK) which was part of the payload of the Russian CORONAS-F solar mission (e.g., Sylwester et al., 2005). Laue lenses have been tested for astrophysical purposes (e.g., Camattari et al., 2018) as part of missions like ACT (e.g., Boggs, 2006), GRI (e.g., Knödlseder et al., 2009), CLAIRE (e.g., Ballmoos et al., 2005), MAX (e.g., Barrière et al., 2006), and HAXTEL (e.g., Frontera et al., 2005).

According to Virgilli (2021), observing hard X-rays and soft gamma rays have reached a point when it is mandatory to change the operational principles of the telescopes used for these purposes. The current instruments do not have enough sensitivities. That under-

performance can be solved by using, for instance, Laue lenses to focus the radiation from a few tens of keV up to ∼1 MeV. We expect to see rapidly increased use of improved ways of focusing on high-energy photons for astrophysical (and solar) applications in the near future.

3.1.3 X-ray imaging using indirect techniques

Focusing optics is not the only way of imaging X-rays. Some other methods, broadly known as indirect imaging techniques, can generate X-ray images of sources at a distance (in particular, images in X-rays and even gamma rays of the Sun and other astrophysical objects, e.g., Hurford, 2013). Very recently, Piana et al. (2022) published a review of these X-ray imaging techniques when optimized for solar flare observations. In this short section, I briefly outlook key aspects of what is presented in Piana et al. (2022) about these techniques, but I encourage an interested reader to go to the source (and references therein) for details.

In 1980 NASA launched the Hard X-ray Imaging Spectrometer (HXIS) on the Solar Maximum Mission (SMM), staying in orbit for nine years. This instrument used collimators to image the Sun in the 3.5-30 keV energy band. The HXIS primary optical element was a collimator with multiple narrow long pinholes aligned toward different areas on the Sun. X-rays from each of these areas reached an energy-sensitive detector (mini-proportional counters), so the instrument performed imaging spectroscopy of the Sun on a 6.4 arcmin field of view (Van Beek et al., 1980).

A simple pinhole (∼ 100 microns in diameter for a ∼ 10 cm focal plane) can produce an image of the Sun in X-rays (see, e.g., the experiment carried out by Blake et al. in the early sixties). If several compact sources are pointed at once with simple pinholes, they can not be distinguished from each other. This issue can be solved by using coded aperture masks, which cast as many shadow patterns to a focal plane as compact sources within the field of view (Cieślak et al., 2016). The Neil Gehrels Swift mission, launched in 2004, is an example of a space mission that uses this type of optics (e.g., Gehrels et al., 2004).

3.1.3.1 Rotation Modulation Collimator

In 1965, Minoru Oda proposed to use two parallel sets of identical grids as a way of getting higher spatial resolution imaging of astronomical objects with a rather broader field of view. Figure 3.8 shows a sketch of Minoru Oda's collimator (Oda, 1982). Depending on the incidence angle of the incoming X-rays, the detector will register a distinct flux. For compact sources with angular sizes less than p/L (pitch and length in Figure 3.8, respectively), the intensity fractions that go through each pair of slits in the grid will vary between the two extremes of the grids. If we synchronously change the orientation of the two grids in a controlled way, then the location of that hypothetical source could be determined. This procedure is the basic principle used for astrophysical applications by spacecraft like the Solar X-ray Telescope (Hinotori SXT, Tsuneta et al. (1991)) and the Reuven Ramaty High Energy Solar Spectroscopic Imager (RHESSI, Lin et al. (2003)). Another more recent payload
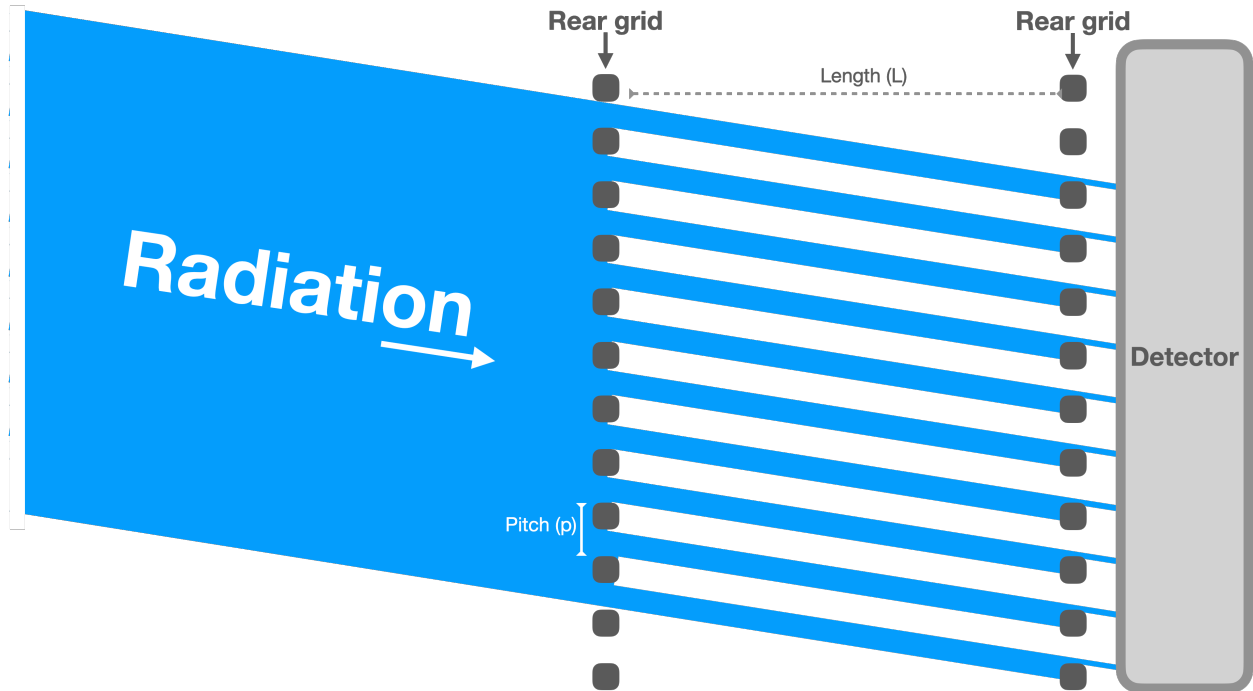
Figure 3.8:   Sketch of the fundamental optical principle that modulation collimators use. Only X-rays that pass through the slits of the two identical grids can reach the detector. Depending on the direction the radiation comes from, the detector captures a distinct intensity.

that uses modulation collimator techniques to image the Sun in X-rays is the Spectrometer/Telescope for Imaging X-rays (STIX, Krucker et al. (2020)), one of the instruments in Solar Orbiter (Müller et al., 2020). STIX uses 32 pairs of identical slits but aligned toward slightly different angles to one another to produce a coarse Moiré pattern over the detectors.

3.1.4   The necessity of a high dynamic range and sensitivity in hard X-rays instrument for solar observations

Although observing solar X-rays via indirect imaging techniques can give outstanding spatial resolution, direct focusing is the way to get high sensitivity and adequate dynamic range. FOXSI is the first sounding rocket payload to observe solar hard X-rays using direct focusing. FOXSI has a sensitivity of ~ 0.0032 photons cm^{-2} s^{-1} keV^{-1} ($\sim$50 times that of RHESSI) at 8 keV and a dynamic range of $\sim$100 for sources > 30 arcsec apart (Krucker et al., 2011; Glesener, 2012).

FOXSI is thought of as a pathfinder to guide the technology required for a next-generation

hard X-ray solar dedicated telescope. Among the many focusing schemes described above, Wolter mirrors have been proven to provide an optimal platform leading to the successful exploration of X-rays for astrophysical purposes. Among the Wolter configurations (I, II, or III), the type I Wolter mirrors offer the additional benefit that the two required segments (paraboloid and hyperboloid) can be part of a single monolithic mirror. This extra advantage is part of the primary reasons Wolter-I optics have been extensively used in X-ray astrophysical space telescopes (e.g., the Nuclear Spectroscopic Telescope Array, Chandra, and the Imaging X-ray Polarimetry Explorer more recently). The FOXSI rocket implements Wolter-I mirrors fabricated by the NASA Marshall Space Flight Center (below, subsection 3.2.1 describes in detail the manufacturing process). The mirrors produced at Marshall have been proven to offer a high precision finish and outstanding performance at a relatively low cost in the High-Energy Replicated Optics (HERO) program (Ramsey et al., 2002).

3.2 The FOXSI optics: Overview

The FOXSI sounding rocket program is a multi-institutional mission which primary goal is to develop and test grazing-incidence optics and semiconductor detectors optimized for hard X-ray solar observations. For the optics, FOXSI uses a set of 7 Wolter-I figured grazing-incidence X-ray telescope modules to perform imaging spectroscopy of solar hard X-rays from ~ 4 keV to ~ 20 keV (e.g., Krucker et al., 2009; Krucker et al., 2013b). The parameters of the optics, such as diameters and focal length, were set to suit the payload of a NASA Terrier-Black-Brant sounding rocket. These optics were produced at NASA Marshall applying a low-cost electroformed nickel alloy replication process, whereby nickel mirrors are electro-deposited onto super-polished mandrels. For increased effective area, shells of various radii are coaxially nested together into modules of 7 or 10 mirrors. The averaged resolution of the integrated modules was measured in the laboratory to be 4.3±0.6 arcsec (FWHM) and 27±1.7 arcsec (half-power diameter; HPD) for an on-axis source (Christe et al., 2016b; Krucker et al., 2013b). The payload uses seven 60 cm long telescope modules, each one containing 7 or 10 concentrically nested Wolter-I mirror shells, all with a focal length of 2 m. The mirrors are optimal for graze angles ranging from 0.23 to 0.37 degrees. Constrained to the FOXSI Si detector square area, the nominal field of view (FOV) is 16×16 arcmin^2. Each optical module includes circular blockers at the front and rear apertures added as a baseline to mitigate stray light (see Chapter 5 for details). The circular blockers are 1.55 mm thick aluminum disks with 37.5 mm (front) and 31.4 mm (rear) radii for a 7-mirror module and with 31.0 mm (front) and 26.2 mm (rear) radii for a 10-mirror module. Table 3.1 summarizes the main physical parameters used for the FOXSI optics.

A primary advantage of the production method used at NASA Marshall is that multiple mirrors can be fabricated via replication by using a single mandrel, which substantially lowers the cost of producing identical optics.

Number of telescopes in the FOXSI rocket payload	Seven		
Mirror geometry	Monolithic Wolter-I figures		
Fabrication technique	Electroformed-nickel replication		
Focal length	2 m		
Paraboloid segment length	30 cm		
Hyperboloid segment length	30 cm		
Field of view	16.6×16.6 arcmin^2		
	Shell #	**Front**	**Inner**	**Rear**
	Shell 1	5.345	5.15	4.56
	Shell 2	5.085	4.9	4.335
	Shell 3	4.835	4.66	4.125
	Shell 4	4.595	4.43	3.92
Mirror Radii [cm]	Shell 5	4.365	4.21	3.725
	Shell 6	4.15	4.0	3.54
	Shell 7	3.94	3.8	3.36
	Shell 8	3.725	3.59	3.18
	Shell 9	3.51	3.38	2.995
	Shell 10	3.29	3.17	2.805

Table 3.1: Summary of the more important physical parameters used on the FOXSI rocket optics. The bottom part of the table displays the optics prescription for each of the 10 Wolter-I mirrors designed for the rocket's payload.

3.2.1   Wolter-I mirror production process

A detailed description of how the FOXSI optics are fabricated can be found in Ramsey et al., 2002 and Ramsey, 2005. This section gives a short overview of such a production process.

Dr. Brian Ramsey has led a team of scientists and engineers at the NASA Marshall Space Flight Center to fabricate the FOXSI optics. They implemented an optimized electroformed nickel replication technique to shape the mirrors into Wolter-I geometries. These shapes are achieved by first machining aluminum mandrels, with electroless nickel plating, to the correct figure. The mandrels were then polished to the desired finish (roughness), which for FOXSI was < 10 Å RMS (see Figure 3.3). The procedure continues with a plating bath submersion of the mandrels into a plating bath to form a thin layer (~ 0.25 mm thick) of a nickel-cobalt alloy that gets adhered to the mandrel via electrodeposition. The mandrel and the thin electrodeposited layer are then very slowly cooled to room temperature until the layer gently separates from the mandrel due to different thermal expansion coefficients of the materials. Via a sputtering process, the interiors of the nickel layers (now the mirrors) are coated with 0.05 μm of iridium to increase their reflectivities at higher energies (see Figure 3.2). The dimensions of the ten mirror geometries used for FOXSI are summarized in Table
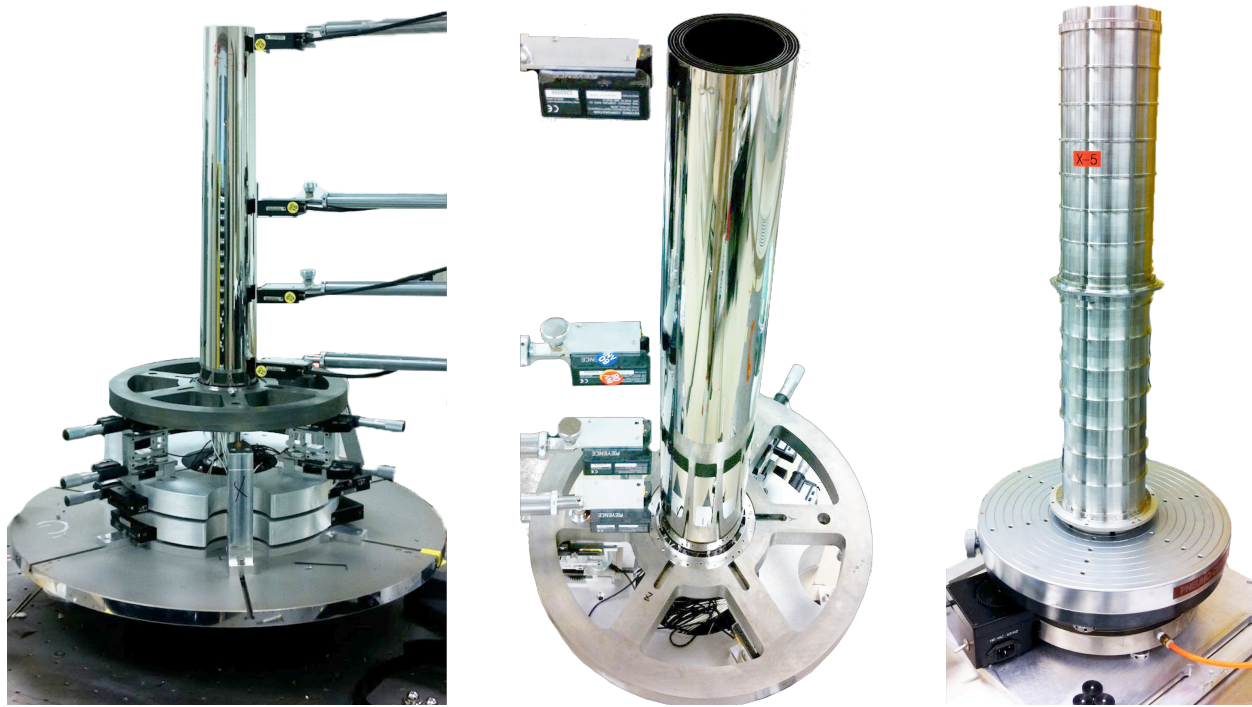
Figure 3.9:   Wolter-I mirrors used for FOXSI. The *left* and *central* photos show the procedure to next and co-align the mirrors in sets of seven or ten shells. The mirrors are structural bonded to the front using clips and UV cured epoxy. The picture on the *right* show one of the stainless steel housing used to encase the mirrors.

3.1.

To maximize the effective area of the FOXSI instrument, single mirrors of different dimensions (from Table 3.1) were axially nested together and aligned to a common focus (Gubarev et al., 2005; Gubarev et al., 2006). For the first FOXSI campaign, all mirrors were grouped into optics modules of seven shells. For the second campaign, two modules were upgraded to have ten mirror shells. Two other FOXSI modules were upgraded to ten mirrors for the third rocket campaign. FOXSI-3 had four 10-shell optics and three 7-shell original modules.

A spider support fixture holds the mirror shells at the optics aperture. A set of clips are bonded to the mirror's front with two-part epoxy. The clips are bonded to the spider fixture using UV cured epoxy. See left and central pictures in Figure 3.9. With the mirror co-aligned and bonded to the front fixture, a second spider structure is set on the rear end of the mirrors, and its grooves are filled with RTV to allow vibration damping.

Once co-aligned, the complete sets of mirrors are encased in stainless steel housings, as observed in the right picture of Figure 3.9. Figure 3.10 shows a simplified infographic of the
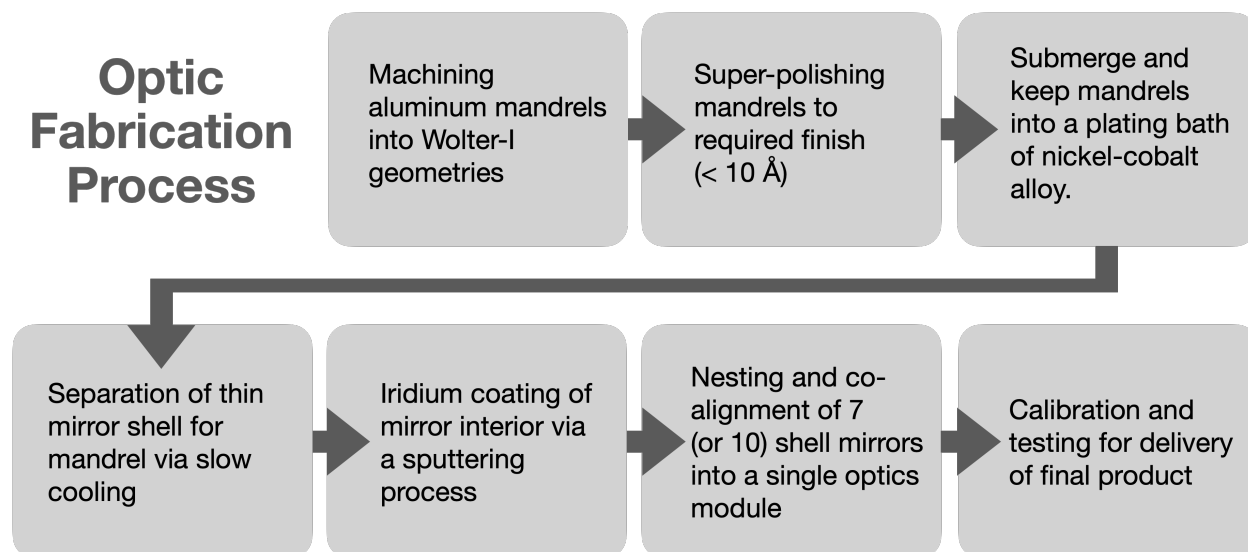
Figure 3.10: Infographics of the optics fabrication process implemented at the NASA Marshall Space Flight Center to produce the FOXSI Wolter-I mirrors.

Shell #	1	2	3	4	5	6	7	8	9	10
Incident Angle [arcmin]	24.08	22.85	21.62	20.40	19.18	18.54	17.32	16.68	16.04	14.82
Geometric Area [cm^2]	6.43	5.80	5.22	4.68	4.18	3.84	3.40	3.10	2.81	2.44
Corrected Area [cm^2]	5.02	4.53	4.07	3.65	3.25	3.00	2.65	2.42	2.20	1.90

Table 3.2: The incident angles are calculated using a conic approximation for the parabolic segment of each mirror and considering a source located 104 m away from the optics entrance. The geometric areas correspond to the annuli cross-sections defined by the *front* and *inner* radii of each shell in Table 3.1. I added a third row containing a 15% reduced area to account for the spiders' shades.

procedure applied to fabricate the FOXSI optics. The calibration and performance testing of the modules are discussed later in Chapter 4.

3.2.2   FOXSI optics theoretical effective area

Figure 3.11 shows the theoretical effective area vs. energy for the mirrors of the FOXSI optics. To generate this figure, I used the reflectivity vs. energy for X-rays with a specific incident angle hitting a mirror of a given material and finish. I multiply that reflectivity by the geometrical cross-section of the individual mirrors in an optics module (see Table 3.2) to get the final theoretical effective area. The material I consider for the mirrors is Iridium and a 10 Å finish.
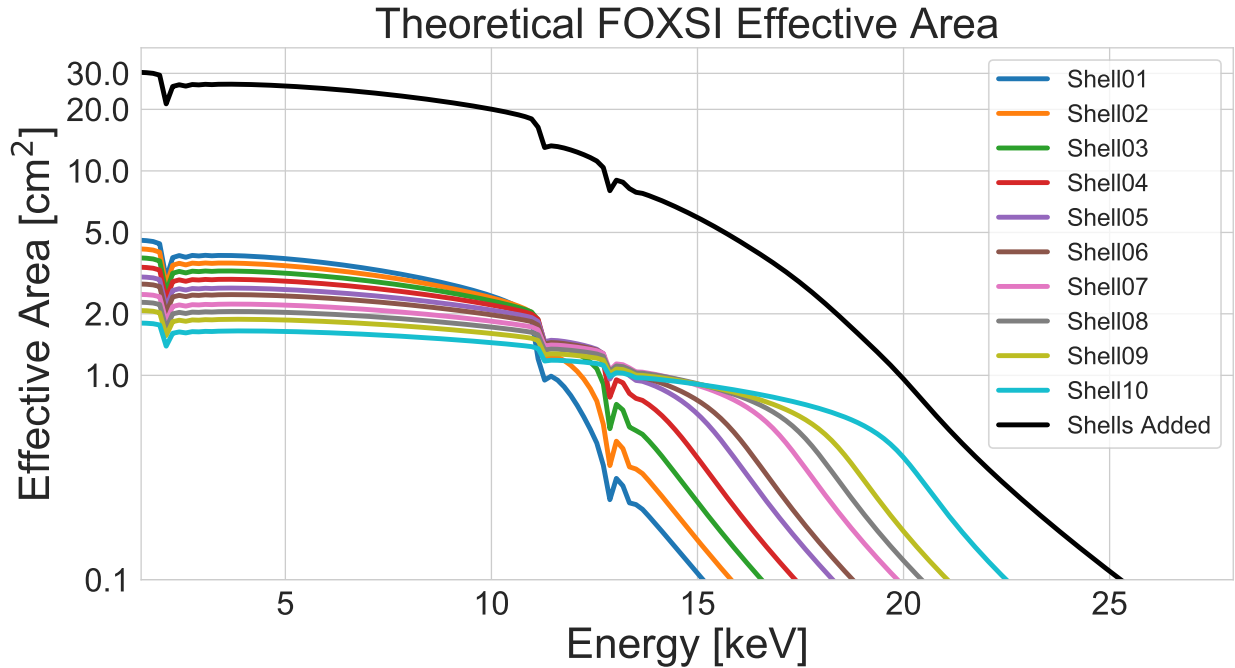
Figure 3.11:   Theoretical effective area of the 10 individual mirrors of the FOXSI optics (in colors). The effective area for all shells combined is shown in black. These curves were obtained using Windt data in the XOP v2.4 widget for 10 Å roughness mirrors and the parameters from Table 3.2.

The reflectivity is obtained using the X-ray Oriented Programs (XOP) v2.4 IDL widget-based driver program. The XOP widget was developed by a collaboration between the ESRF French society and the Advanced Photon Source Facility (Río et al., 2011).

The reflectivities were calculated in XOP using the following procedure. Select `Optics` from the main menu, then `Mirrors and Filters`, then `DABAX: xf1f2`. A new window pops up where the mirror's parameters can be set. For the `Dataset`, I used `f1f2_Windt.dat` (Windt, 1998). For the `Material formula`, I chose Iridium (Ir). Then one can select to calculate `reflectivity-unpol` (unpolarized). The user must input the mirror `roughness` in Å and the `grazing angle` in mrad. The widget's output is a plot of the reflectivity vs. energy that can be saved as a plain text file. The reflectivity vs. energy curves for every mirror (and all added together) are shown in Figure 3.11.

More key features of the FOXSI optics are discussed in detail in Chapter 4. Mainly, all the work I led for the optics calibration, including the measurements of the effective area and the point spread function. I will invest the remaining sections in this chapter to describe other components of the FOXSI payload, the detectors, and the Solar Aspect and Alignment

System (SAAS).

3.3   The FOXSI detectors: Overview

The FOXSI optics modules focus X-rays 2m behind the center of the mirrors. There, detectors are placed to measure every photon's timing, position, and energy. Such information has been registered using semiconductor detectors of three kinds: double-sided strip silicon (or cadmium telluride) detectors, and a CMOS pixeled sensor. This last one only flew on FOXSI-3.

A wide variety of textbooks cover the topic of semiconductor detectors thoroughly (see, e.g., Leo, 2012) as an excellent source to go for the interested reader. This section will briefly highlight some semiconductor detector features that I believe are essential to understanding FOXSI's global performance. A more detailed description of the FOXSI detectors, and their physics, can be found in Glesener (2012) and Vievering (2019).

3.3.1   Semiconductor detectors: generalities

Semiconductor materials are crystalline structures whose outermost shell electrons move according to an energy band arrangement (a valence band, a forbidden energy gap, and a conduction band). The energy gap in semiconductors is typically a few eV. At low enough temperatures (the specific temperature value depends on the particular material), most of the electrons in the crystal remain in the valence band. When a sufficient high-energy photon (or charged particle) is incident on the crystal, it can transfer its energy to a (or a group of) electron(s) in the valence band, creating an electron-hole pair. Electrons in the outermost atomic energy shells can jump from the valence to the conduction band if sufficiently energized. The exact values of such energies mainly depend on the crystal's bandgap. Such bandgap is 1.12 eV and 1.52 eV at room temperature for Si and CdTe, respectively (e.g., Knoll, 2010). If an external voltage difference (V) is applied over the crystal, the electron (hole) created will move following the direction of (contrary to) $\vec{\nabla}V$, creating a current $\vec{I}$. The magnitude of $\vec{I}$ will primarily depend on the voltage strength and the mobility of the charge carriers in the crystal. Properly measuring $\vec{I}$ is a way to determine the energy of the incoming photon (or charged particle) responsible for creating the electron-hole pairs.

The functioning of a semiconductor as a detector depends on the implementation of semiconductor junctions. A simple example is an np junction formed by juxtaposing an n-type and a p-type semiconductor. An n-type (p-type) material is made by adding a few parts per million of a *donor* (*acceptor*) impurity to the crystal. These impurities are atoms with one more (less) valence electron in their outermost shell.

p-n junctions form a particular zone, the *depletion zone*, at the interface of the two

semiconductor types. The depletion zone gets enlarged by applying a reverse-bias voltage to the p-n crystal (negative voltage on the p-side). The depletion zone is the volume in the crystal sensitive to radiation. This zone has a lower conductivity compared with that of the intrinsic material, so a created electron-hole pair is easily swept out by the voltage gradient, producing a measurable signal. Enlarging the depletion zone improves the performance of the crystal as a detector. For photons with energies under ∼20 keV interacting with a Silicon crystal, the primary energy transfer mechanism is photoelectric (this is the primary case for FOXSI).

FOXSI has included double-sided Si strip detectors in its three successful flights to record X-rays with energies from ∼4.5 keV up to ∼20 keV. For FOXSI-2 and -3, two detectors were replaced with similar devices having CdTe strips instead. CdTe has a better quantum efficiency at higher energies than Si. For FOXSI-3, one extra Si detector was replaced with a back-illuminated Si CMOS sensor optimized for soft X-ray observations (0.5-5.0 keV). Currently, FOXSI is funded to fly a fourth time, when one of the detectors will be a Timepix. This detector uses a pixelated sensor controlled by a field programmable gate array (FPGA). The following sections give more details about each of the detectors used in the FOXSI rocket payload.

Below, I briefly summarize the three types of detectors that have debuted (or will debut) as part of the FOXSI payload; double-sided strip detectors, back-illuminated CMOS sensors, and CdTe pixelated detectors (Timepix).

3.3.2 Double-sided Si and CdTe strip detectors for HXRs

FOXSI has implemented Si and CdTe double-sided strip detectors with a fine position resolution, and high count rate capabilities for its three already successful flights. Only the CdTe version will fly in FOXSI-4, given its better efficiency at higher energies.

These detectors use strip pitches of 75 μm and 60 μm for Si and CdTe, respectively. Given the optimized electrode structure that these detectors have, charge sharing analysis can enable sub-strip resolution (e.g., Duncan et al., 2021b). These devices utilize an application-specific integrated circuit (ASIC) and an FPGA optimized for high-speed readouts to support the higher count rate of solar sources (Furukawa et al., 2019). FOXSI's double-sided CdTe strip detectors are provided by Kavli IPMU and JAXA/ISAS. These detectors, sensitive to hard X-rays above ∼3 keV, will be upgraded for a net 10x improved count rate for FOXSI-4 compared to the detector previously flown in the FOXSI payloads.

3.3.3 Back-illuminated CMOS sensor

The FOXSI-3 experiment also included a soft X-ray Complementary Metal-Oxide Semiconductor (CMOS) sensor that produced the first photon-counting soft X-ray image of the Sun (Narukage et al., 2020). The CMOS is a 2048 × 2048 pixelized sensor, with an 11 μm pixel
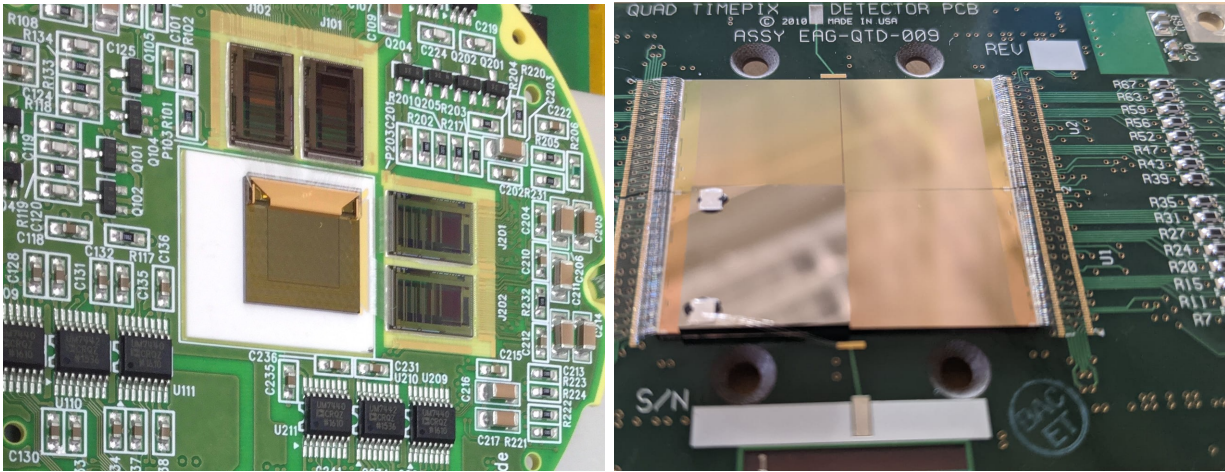
Figure 3.12: *Left*: Photo of a double sided CdTe strip detector flown in FOXSI-3. The strip pitch is 60μm. For more information see Furukawa et al. (2020). *Right*: Photo of a pixelated Timepix3 detector expected to fly in FOXSI-4.

size, sensitive to X-rays with energies in the 0.5-5.0 keV range. Over a central subarea of 100×2048 pixels, the sensor operates at high speed of one thousand frames per second, suitable for observations of large solar flares in a payload like FOXSI. The CMOS sensor is provided by the National Astronomical Observatory of Japan in collaboration with Gpixel[2]. Together with a FOXSI optics module, this detector forms the Photon Energy Imager in soft X-rays (PhoEnIX), which field of view can be seen in Figure 3.13 (flown only in FOXSI-3).

3.3.4   CdTe pixelated detectors (Timepix3)

FOXSI-4 will debut for the first time the use of a novel CdTe pixelated detector with a Timepix3 readout for solar observations. The Timepix3 is a 256×256 hybrid pixelated readout ASIC bump bonded to a 1 mm thick CdTe sensor with a 55 μm pixel size(Turecek et al., 2018, e.g.,) (Figure 3.12, right). The international Medipix collaboration hosted by CERN[3], of which the University of California Berkeley's Space Sciences Lab (UCB/SSL) is a member, has been responsible for developing the Timepix3 based detector. The ASIC has two readout modes: data-driven and frame-based. In the data-driven mode, the readout system produces a data packet with energy measurements (time over threshold), time of arrival, and pixel I.D., directly after a photon hits a pixel. Crucially, during this process, the rest

---

[2]https://www.gpixel.com

[3]CERN is a French acronym that stands for *Conseil Européen pour la Recherche Nucléaire* (European Council for Nuclear Research), which is one of the world's largest and respected centres for research in high energy physics.
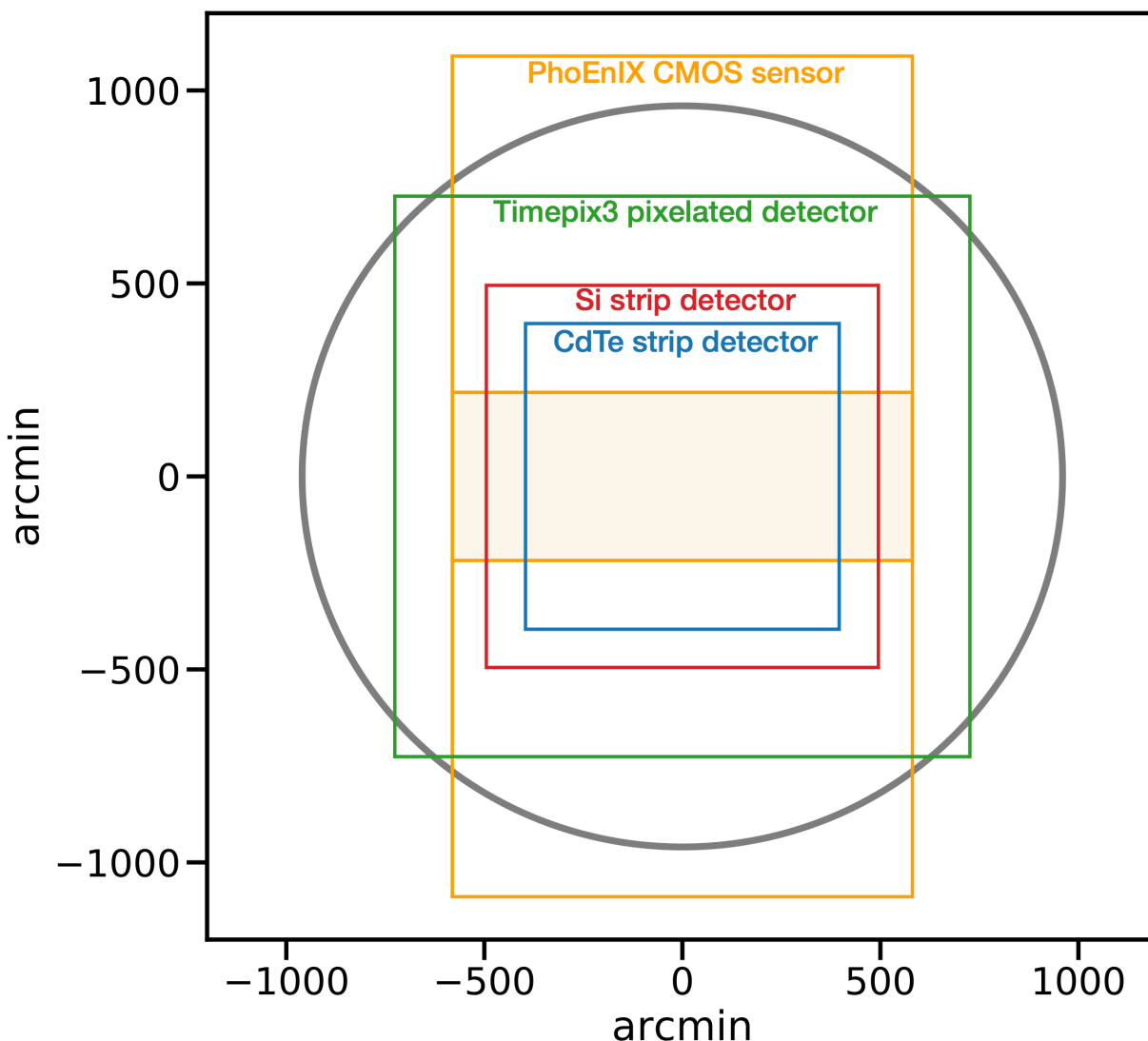
Figure 3.13: Field of view of the different types of detectors part of the FOXSI program. For reference, the grey circle represents the nominal solar disk. The central shaded region in orange shows a part of the PhoEnIX CMOS sensor that performs a higher rate of 1000 frames per second.

of the pixels are still sensitive, allowing for the collection of many photons in different pixels near-simultaneously. The ASIC clocks allows up to 40 Mhits/s/cm^2, and a minimum time step for the arrival time of 1.56 ns(e.g., Kruth et al., 2010; Zappon et al., 2012; Poikela et al., 2014; Frojdh et al., 2015). A single Timepix3 unit (with a single sensor) consumes

2W of power, which can be reasonably accommodated within the FOXSI-4 power budget. Energy resolution measurements down to 2 keV have been made (e.g., Frojdh et al., 2015), demonstrating the low-noise performance of the ASIC. Fabrication and characterization of a Timepix3 with CdTe sensors (instead of Si) are currently in progress under the lead of UCB/SSL. That development will produce the first detector that will fly in FOXSI-4. Details of the Timepix3 can be found in publications by Kruth et al. (2010), Gaspari et al. (2014), and Frojdh et al. (2015), for example.

3.4   Calibration of the double-side strip detectors

A thorough description of the double-side strip detectors characterization is presented in Glesener (2012) and Vievering (2019) for Si and CdTe detectors, respectively. Although both Glesener (2012) and Vievering (2019) do an extensive job presenting the detector responses, there are a couple of aspects of the Si detector characterization I led in collaboration with Natalie Foster that I want to focus on in this section. I begin by presenting the temperature dependence of the detector's performance ranging from $-30°$ C to $+5°$ C. Then, I describe the results of testing the time response of the detectors when the bias voltage is ramped up and down from 0 to 200V and vice versa. I end the section by showing spectra of photons hitting one, two, or three strips in the Si detectors.

3.4.1   Temperature dependence

The double side strip detectors need to be cooled to operate effectively. The leakage current and trigger noise are substantially reduced when the detectors operate at low enough temperatures. We performed measurements to define an acceptable temperature range to operate the double side strip Si detectors. The upper-temperature limit is characterized by excessive thermal noise. At the other end, the lower limit is set by potential damage to the detector components via a differential thermal expansion to the "bump bonds" (those connecting the semiconductor sensor to the readout system). To lower the temperature of the detectors for the rocket flight configuration, we implemented a variety of methods described in detail by Glesener (2012) and Vievering (2019).

To assess the detector performance as a function of the temperature, we focused on two aspects, the full width at half maximum (FWHM) and the gain for specific emission lines from two sealed radioactive sources (Am241 and Fe55). For the Am241 source, we measured the line at 13.9 keV, while for the Fe55 source, we used the line at 5.9 keV. The detectors were first cooled down to -30° C and very slowly let warm in steps of 5° C. For each temperature step, we measured the FWHM and center of the 5.9 keV Fe55 and 13.9 keV Am241 lines by fitting a simple Gaussian to each line.

The main results of this experiment are shown in figure 3.14. The two panels on the left are the FWHM in keV measured for the 13.9 keV Am241 line (top) and the 5.9 keV
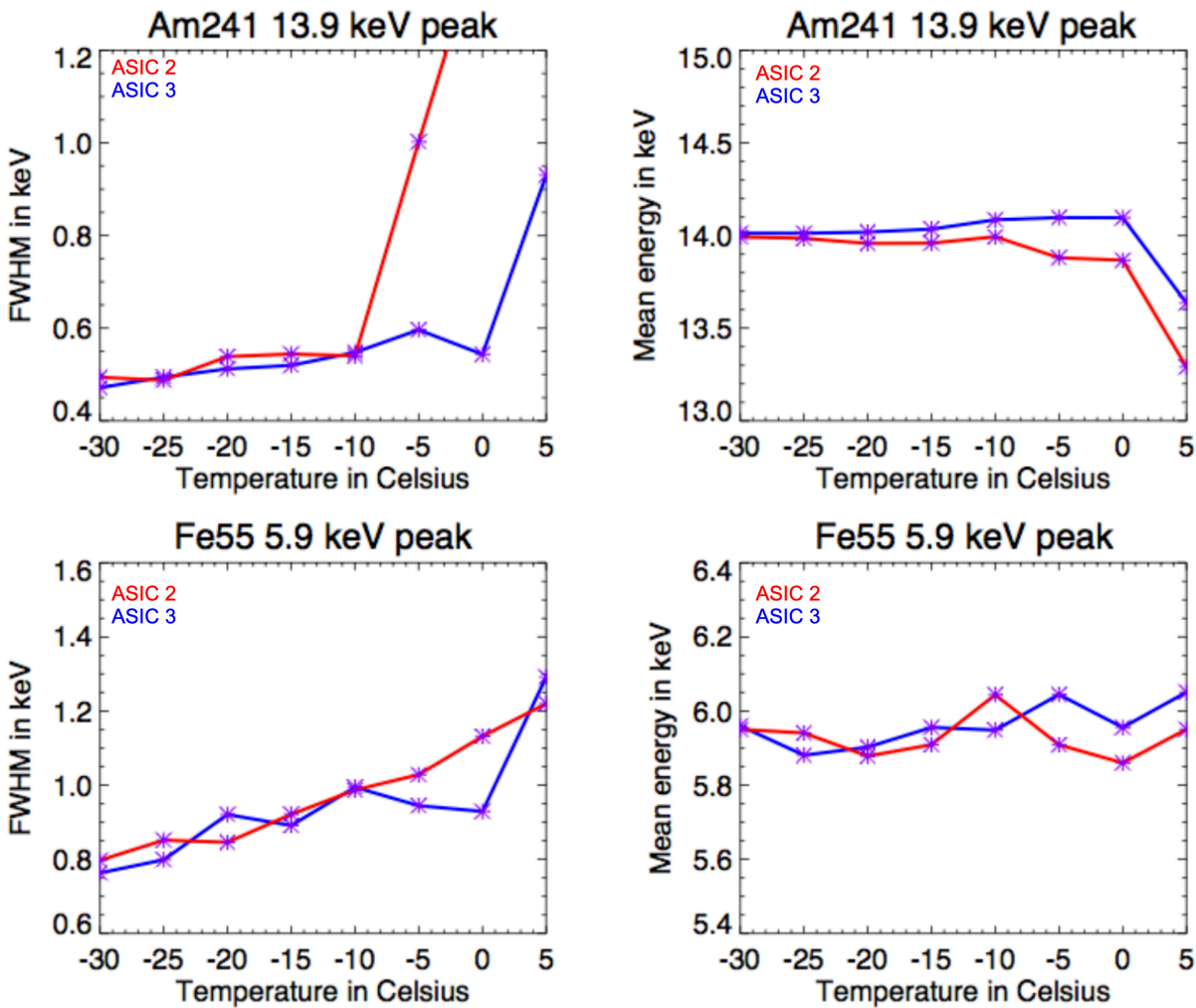
Figure 3.14:   Detector performance vs. temperature for Si sensors. The plots at the top show the FWHM (*left*) and central energy (*right*) measured by fitting a Gaussian over the line at 13.9 keV of Am241. The plots at the bottom show the same two features but measured over the 5.9 keV Fe55 line. Each frame contains two curves, blue and red, corresponding to the two ASIC that control the p-side of the Si detectors. Based on these plots, the Si detectors performance is considered acceptable for temperatures up to ∼ -10 degrees Celsius. The two panels on the right use a nominal calibration for the gain. *Figure created by Natalie Foster*, shared with her permission.

Fe55 (bottom). The two panels on the right show the measured peak center using a nominal calibration for the same two lines. Each plot has two curves, one red and one blue,

corresponding to two different application-specific integrated circuits (ASICs) connected to the p-type part of the detector. The Si double-side strip detectors used in FOXSI have a better energy resolution on the p-side than on the n-side of the sensor. This characteristic is well-known, calibrated, and characterized by Glesener (2012).

From Figure 3.14 it follows that the detector performance departures from the mean value as the temperature increases. However, this variation is still more minor than the energy resolution. From this experiment, we conclude that **the Si detector performance can be considered acceptable for temperatures below $\sim -10°$ C**. The FOXSI detectors have never intentionally cooled down below the lower limit of $-30°$ C. We do not recommend cooling the detectors below this limit to avoid possible component damage (see Glesener, 2012).

3.4.2 Event rate vs. bias voltage

As mentioned in subsection 3.3.1, semiconductor detectors need a bias voltage. For the Si double-sided strip detectors, such voltage is 200 V. The rocket should not be launched with the 200 V already applied to the detectors. Due to environmental conditions changes during the rocket's rise (e.g., decrease of ambient pressure), a spark could more easily flow through the detector. These sparks could severely damage the detector's components and/or performance. To avoid these potential sparks, during a rocket launch, we do not activate the detectors' bias voltages until the rocket reaches an altitude of at least $\sim$25 km (this is 30 seconds after the launch t_0). The bias voltage slowly ramps up for 40 seconds until reaching the nominal 200 V at a time when the rocket is above ~ 100 km (see Figure 3.15). The observations begin a few tens of seconds after 200 V is achieved and run for about six minutes and a half. Then the detectors' bias voltage is slowly ramped down while the payload re-enters to finally land (as seen in Figure 3.15).

We ran an experiment during the detector calibration whose primary goal was to determine how long we needed to wait after applying the detector bias (high voltage, HV) before the detector collected data can be considered of good quality. The detector capacitance and resistivity are 4μF and 10MΩ, respectively. These two values yield an expected RC time constant of 40 seconds.

We evaluate the good events over the total number of frames to assess the detectors' good performance. The double-sided strip detectors produce 500 data frames per second. Not all data frames have events. An event can be triggered by a genuine photon interaction or by noise. When the bias voltage has not been applied, most of the events triggered are noise. The readout system we use contains an *error flag* that gets activated (set to 1) every time a common-mode value is out of nominal ranges. We call *good events* those triggered frames that have an *error flag* of zero. If there are no X-ray sources near the detectors, only cosmic background particles should be registered when the bias voltage is applied. Such detector behavior would constitute good performance. Figure 3.16 shows the results of an
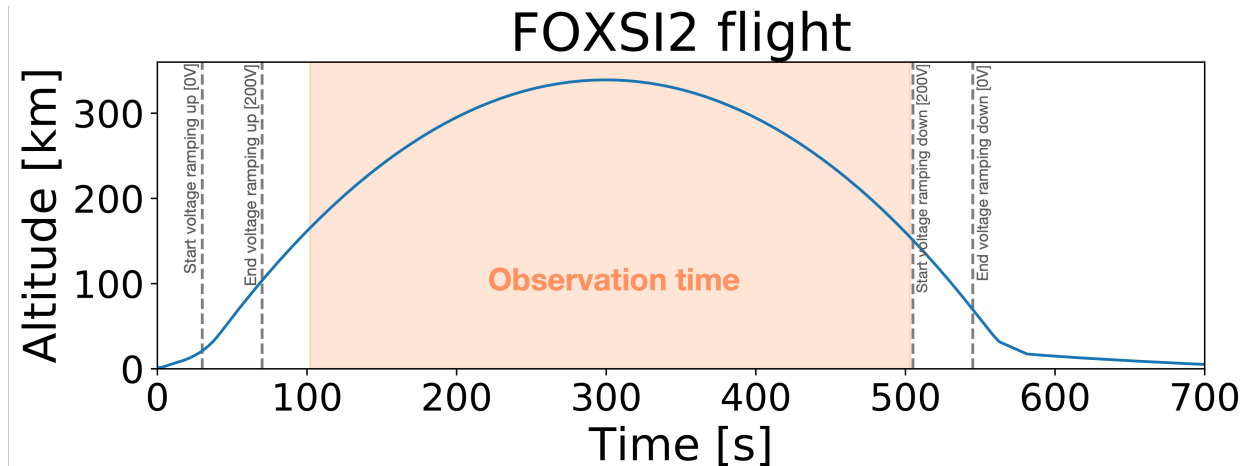
Figure 3.15:   Altitude of the FOXSI2 rocket vs time. The orange region is the observation time. The dashed vertical lines highlight the times at which the detector bias voltages were ramped up and ramped down.

experiment in which we mimic the voltage ramping up (left two plots) and ramping down (right two plots) times during a nominal FOXSI rocket launch. The two plots at the top of Figure 3.16 display the ratio of Good events to total frames of a Si detector when there is no X-ray source nearby. The HV begins to ramp up at $t = 30$ seconds. After approximately 15 seconds ($t \approx 45$ s), the ratio of the good event has already dropped to values on the order of 10^{-3}. When the bias voltage reaches 200 V ($t = 70$ s), the detector performance is already optimal for photon counting. This characteristic was confirmed by repeating the experiment with a Ba133 sealed source near the detector. The results of this experiment are shown in the bottom two panels of Figure 3.16. The green curves correspond to the total number of triggered events with no error flag without filtering on energy. The red curves are the result of filtering the good events by energies around the 30.6 keV, 31.0 keV, 34.9 keV, and 35.0 keV Ba133 lines. At the beginning of the measurements, the red line shows Good events/frames dominated by noise. Once the HV is applied, the noise is significantly reduced. By $t \sim 40$ s, the detector becomes sensitive to the incoming Ba133 radiation. From this point on, and until the HV voltage returns to zero, the Good events/Frames are dominated by Ba133 lines. By the end of the measurements, $t \gtrsim 610$, the Good events/frames got low again and dominated by noise. The curves in Figure 3.16 curves validate the fact that by the time the detector reaches 200 V, it is already suitable for hard X-ray observations. The plot on the right of Figure 3.16 shows that there is a hysteresis effect on the detectors. The detectors keep doing photon-counting for several tens of seconds after the applied bias voltage has reached 0V. The times chosen to do the voltage ramping up and ramping down are optimal to protect the detectors' performance.
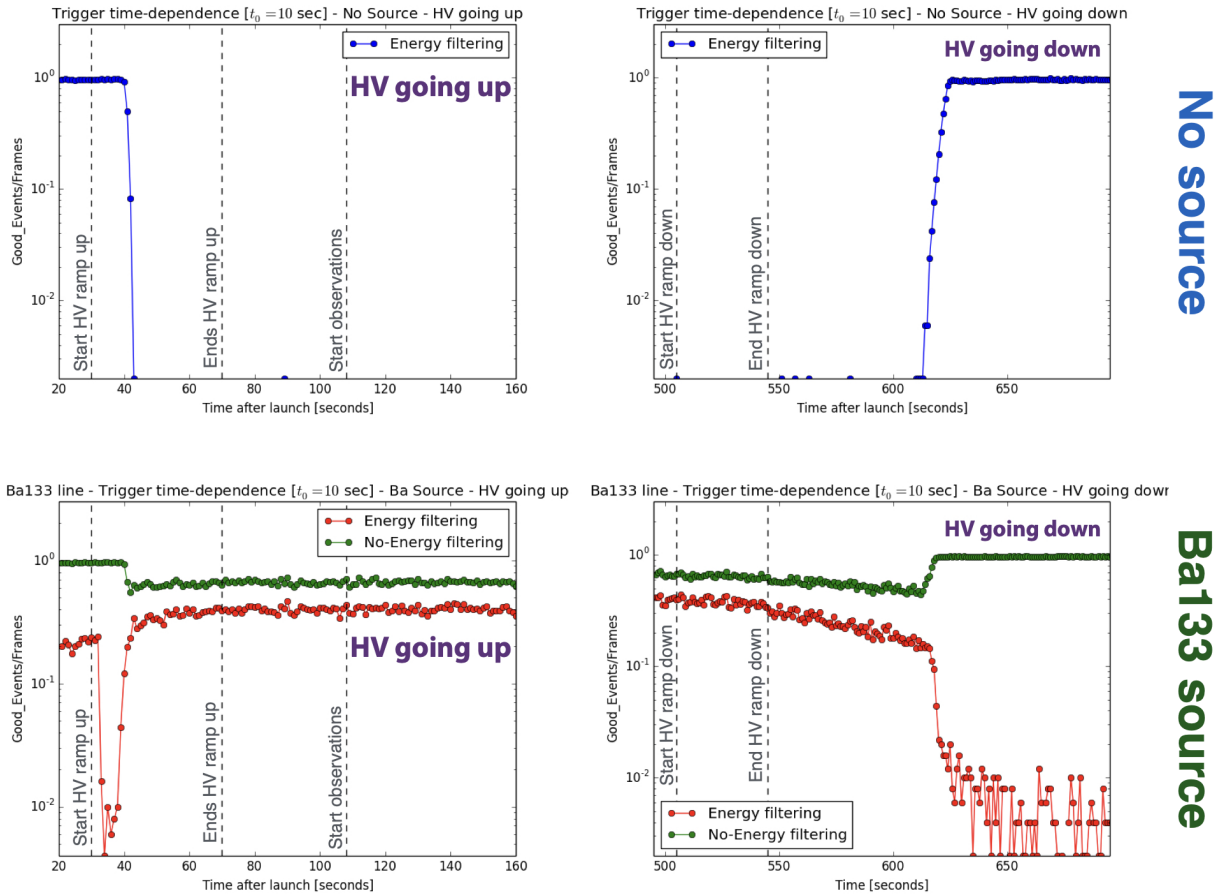
Figure 3.16:   Laboratory measurements of the detector performance vs. time as the bias voltage is ramped up (two panels on the *left*) and ramped down (two panels on the *right*). The time evolution mimics the times of a nominal FOXSI rocket launch. $t = 0$ s is the time the rocket takes off. $t = 30$ s is when the command to raise the voltage is sent. $t = 70$ s is when the high voltage has reached 200 V. $t = 508$ s is when the HV starts to ramp down, and $t = 542$ s is when the detector voltage has returned to zero. The top two panels correspond to an experiment where the detector was isolated from any X-ray source. The two panels on the bottom are the results of placing a Ba133 radioactive source near the detector. The green curves in these plots correspond to the detector performance integrated over the full operative energy range ($\gtrsim 4.5$ keV). The red curves are the outcome of filtering the events around energies close to the 31 keV and the 35 keV Ba133 lines.

3.4.3 Single, double, and triple strip events

X-ray semiconductor detectors using relatively small strips or pixels suffer from charge-sharing. This effect occurs when one incident X-ray causes signals in two or more adjacent strips/pixels. Charge sharing more likely occurs when an incident X-ray hits the proximity of a strip (or pixel) boundary, enabling it to improve the spatial detector resolution down to sub-strip (sub-pixel) scales. Another effect of charge sharing is the worsening of the energy resolution for multiple strip (pixel) events. In this part of the calibration work, we tested for the first time the spectral response of single, double, and triple strip events over a Si FOXSI detector for a group of sealed radioactive sources (Fe55, Ba133, and Am241). We also determined the fraction of double on single strip events. The charge sharing analysis of the FOXSI double-side strip detectors has thoroughly continued focusing on getting sub-strip resolutions via a deconvolution process of the combined FOXSI optical and detector responses. This more extensive study has been led by Jessie Duncan at the University of Minnesota (Duncan, 2022).
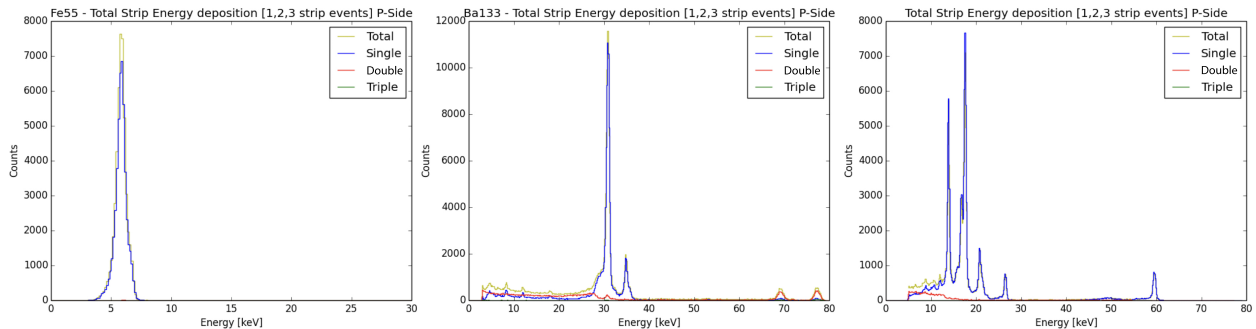
Figure 3.17: Fe55 (*left*), B133 (*center*), and Am241 (*right*) spectra obtained with a Si double-side strip detector. Blue curves show spectra made using single-strip events. Red curves correspond double strip event spectra. Green lines are spectra of triple strip events (almost negligible). And, yellow are spectra generated using single and multi strip events.

Figure 3.17 shows three spectra we took for an Fe55, a B133, and an Am241 sealed radioactive source. From these measurements, we confirmed the best energy resolution is obtained when using single strip events for all radioactive sources. We also found that only about $\sim 0.1\%$ of the total good events are double (or > 1) strip hits for the case of Si detectors (pitch of $75\,\mu m$). The percentage of double strip events gets larger for detectors with smaller strips or pixels. That is the case for the CdTe FOXSI detectors (pitch of $60\,\mu m$) or the Timepix that has pixels of $55\,\mu m \times 55\,\mu m$. There is also a much bigger effect due to the use of CdTe instead of Si for the sensor.

3.5 The Solar Aspect and Alignment System (SAAS)

The NASA LCAS program provides a solar aspect system for sounding rockets that point to the Sun during their flights (the Solar Pointing Attitude Rocket Control System4, SPARCS VII). SPARCS has a high degree of pointing accuracy and stability over three angles (roll, pitch, and yaw) comprised of a coarse (CSS), intermediate (MASS), and fine Sun sensor (LISS). During its first flight, FOXSI measured a pointing stability of 0.12 arcsec and absolute pointing accuracy of ±0.5 arcmins (Christe et al., 2016a). This stability and accuracy are better than the nominal FOXSI requirements (±1 arcminute of absolute pointing accuracy).

Aligning the science instrument with SPARCS is crucial for an LCAS solar rocket campaign. Krucker et al. (2013b) explain how such an alignment was carried out for the first FOXSI campaign and the challenges that made it difficult to quantify the alignment accurately. FOXSI added an alignment element, the Solar Aspect and Alignment System (SAAS), used in the second and third rocket campaigns. The purpose of the SAAS was to improve alignment precision between FOXSI's optical axis and SPARCS. The SAAS is a two-parts (optics and detector) telescope in visible light coupled to both ends of the metering tube to intentionally share FOXSI's optical axis. The SAAS front part (the optics) consisted of three filters placed in front of three lenses, all over the same optical path. The first filter is a neutral density filter (ND 0.3), used only during solar observations. We included an IR cut-off filter for heat rejection (Edmund Optics 53-710) and a hard-coated bandpass filter (Edmund Optics 65-166, centered at 632 nm). Christe et al. (2016a) describes in detail the optics design.

The SAAS optics focus solar photons in visible light down over FOXSI's detector plane, 2 meters apart. The detector used to capture those photons was the Imperx Bobcat IGV-B1310, built around the SONY ICX 445 3.75 micron Interline Transfer CCD image sensor. It generates a solar image in visible light over a matrix of $1296{\times}966$ pixel^2 ($4.86{\times}3.62$ cm^2) at a cadence of 39 frames/s. The CCD's readout was controlled using an ADLINK PC/104 computer (Cool RoadRunner-945GSE) connected to an Advanced Micro Peripherals nanoVTV. The nanoVTV board was needed to convert the real-time images of the Sun captured with the SAAS into an NTSC TV signal. This signal was also concatenated in the telemetry stream for us (the science team) to get in-flight experiment pointing feedback. The most recent iteration of the SAAS (the one used on FOXSI-3) additionally included onboard storage to save full resolution data of scientific value.

Both the ADLINK PC/104 computer and the nanoVTV board needed to be placed at the detector plane of the FOXSI payload together with their independent power supply. Figure 3.18 shows such arrangement. I played a key role in the wiring, mechanical configuration, and environmental testing of the SAAS, in close collaboration with Professor Lindsay Glesener, Dr. Steve Christe, and Van Shourt. Additionally, during the most recent FOXSI campaign, Dr. Daniel Ryan and I led critical experiments to assure an alignment of < 5 arcmin between the SAAS and FOXSI's X-ray telescopes. One of such experiments consisted in
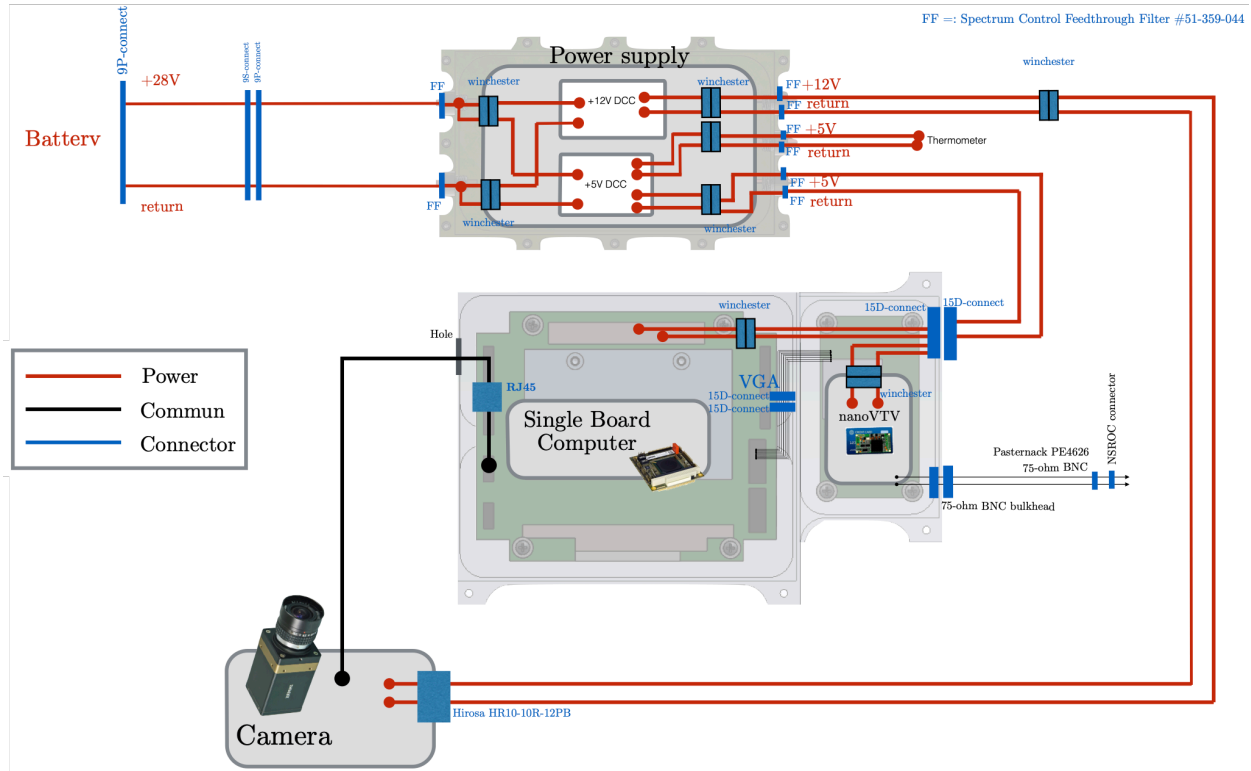
Figure 3.18:   Wire diagram of the SAAS.

observationally determining the optical resolution of the SAAS. We pointed the telescope to the Golden Gate bridge from the Space Sciences Lab patio with only the SAAS mounted on the metering tube (See Figure 3.19). The distance from SSL to the southern column of the Golden Gate is $l \sim 21.8$ km (according to a rough estimate using Google Maps). The smallest distinct features observable with the SAAS are the Golden Gate cables. The nominal diameter of one of such cables is 0.92 m (d). We determined the measured angular resolution of SAAS as $\arctan(d/l) = 8.7 \pm 1.6$ arcsec. This value is in good agreement with the theoretical value estimated in Christe et al. (2016a) (~ 6 arcsec).

3.6   FOXSI-1 and -2 flights

The FOXSI-1 and -2 sounding rocket experiments were launched at 17:55 UTC on November 2, 2012, and at 19:11 UTC on December 11, 2014, respectively. Both rockets took off from the White Sands Missile Range (WSMR) in New Mexico. FOXSI-1 targeted four areas on the solar disk that included multiple active regions and even a fortuitous microflare on the western limb of the Sun. These observations constituted the first time an instrument per-
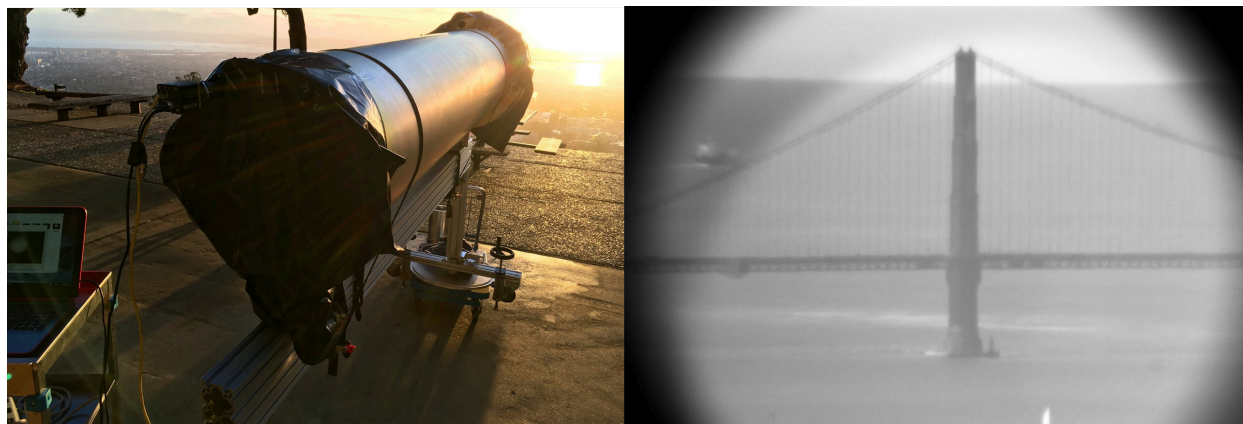
Figure 3.19: Experiment to observationally determine the angular resolution of the SAAS. *Upper left*: SAAS telescope mounted on the metering tube and pointing to the golden gate. *Upper right*: Image of the Golden Gate bridge captured with the SAAS telescope. Note the the smallest distinct features observable in the picture are the bridge cables.

formed solar imaging spectroscopy at energies above five keV using direct focusing (Krucker et al., 2013b). Glesener (2012) presents in extended detail the flight parameters, targets, and scientific outcomes of FOXSI-1. Likewise, Vievering (2019) carried out a thorough description of the FOXSI-2 flight, upgrades, and the work she led analyzing the solar microflares observed during that flight. Among the science targets, FOXSI-2 also included the observation of a region of the quiet Sun. I present a comprehensive analysis of those quiet Sun observations in Chapter 6.

For detailed information about the FOXSI-1 and FOXSI-2 flights, readers should go to Glesener (2012) and Vievering (2019), respectively. The following section intends to give a complete description of the FOXSI-3 observation campaign and solar activity at the time of that flight.

3.7 The FOXSI-3 flight

The third FOXSI rocket campaign took place at the WSMR in the Fall of 2018. The rocket took off at 17:21 UTC on September 7, 2018. Solar observations started at 17:22:44.6 UT and ended at 17:29:14.1 UT, for a total of 389.5 seconds. The flight happened during a period of extremely low magnetic activity of the solar cycle (see Figure 3.20). The Sun was exceptionally quiet on the launch day; only an extremely aged and weak active region was identifiable on the disk, near the western solar limb (see Figure 3.22). This active region remained present for several solar rotations before the FOXSI-3 launch. The first time
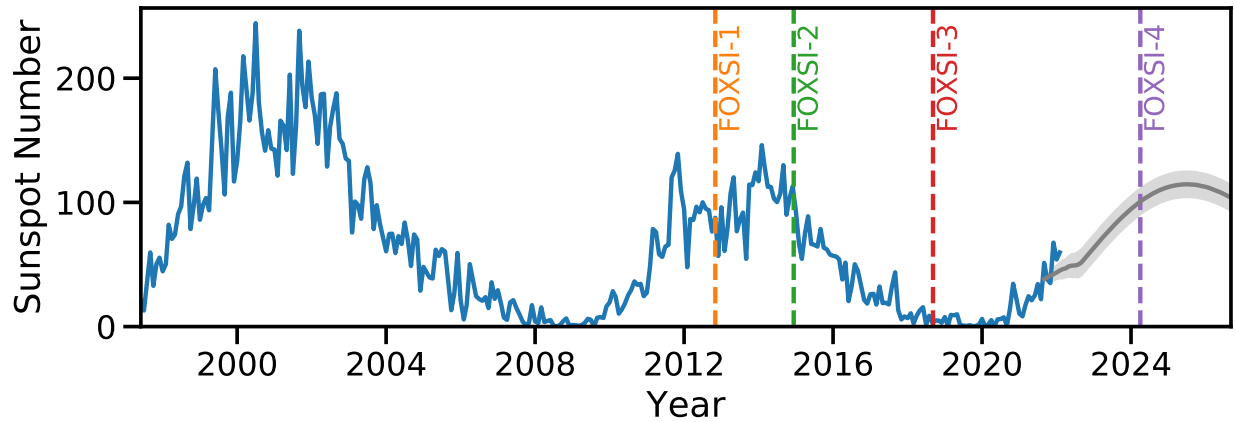
Figure 3.20:   In blue, sunspot number for the last two solar cycles (cycles 23 and 24). The grey line shows the predictions for how the sunspot number will evolve during solar cycle 25. This prediction is based on the consensus of the Solar Cycle Prediction Panel at the U.S. Dept. of Commerce, NOAA, Space Weather Prediction Center (SWPC). The orange, green and red vertial dashed lines show the dates when the FOXSI-1, -2, and -3 flew, respectively. The dashed purple vertical line indicates the nominal date we expect to launch FOXSI-4. This plot was made by modifying one of the examples of the Sunpy gallery (Mumford et al., 2020).

the active region was prominent enough to enter the National Oceanic and Atmospheric Administration (NOAA) catalog was on June 13, 2018. That day the active region acquired the label NOAA AR12713. The active region persisted on disk for the subsequent three solar rotations. However, its activity dropped enough not to enter the NOAA catalog anymore. On the day of the FOXSI-3 launch, the Sun also exhibited a coronal hole over its north pole and a few sparsed EUV brightenings across the disk (see Figure 3.20). Together with Dr. Juliana Vievering (a PhD candidate at the time), I led the FOXSI-3 observation planning to target different regions of the Sun with scientific interest. Table 3.3 summarizes the plan that we executed with just a few slight modifications during flight, the most notable being a tiny shift toward the solar West that our flight commander (P.I. Lindsay Glesener) performed during the observations. The original plan consisted of pointing to the visible aged active region for two minutes. Then, move to the solar north pole and stay there for 30 seconds. The plan included moving to the quiet Sun region over the eastern hemisphere for 2.5 minutes and finalizing the observations returning to the first target. Figure 3.22 shows the the observation sequence during the more than six minutes of FOXSI-3 observations. The same figure shows on the right the field of views of every detector in the payload. The PhoEnIX CMOS sensor offers the largest field of view and the possibility of making a full disk mosaic when integrating data from the totality of the observations (See Figure 3.23).

	Target	Time (s)	Center (arcsec)
T1	Aged Active Region	134	(429.9, 39.5)
T2	North Pole	27	(-0.1, 650.7)
T3	Quiet Sun	147	(-650.8, 39.6)
T4 pos0	Aged Active Region	26	(429.8, 39.6)
T4 pos1	Aged Active Region	37	(550.8, 39.6)

Table 3.3: FOXSI-3 observations summary.

PhoEnIX is one of the multiple instrument updates done for FOXSI-3. Other updates include

- using two CdTe strip detectors thicker than the ones used for FOXSI-2,

- two honeycomb collimators to reduce ghost-ray background, and

- upgrading two additional optics to be 10-mirror modules.

Figure 3.21 summarizes the optics and detector arrange for the FOXSI-3 rocket payload. Vievering (2019) does a detailed description of the updates done for FOXSI-3. An interested reader is welcome to check chapter 3 of her dissertation.

Solar activity is a critical parameter to perform an accurate pointing planning. I developed a tool for getting daily solar activity status starting a couple of weeks before the nominal scheduled rocket launch. That tool included the most recent SDO/HMI magnetograms at the time, SDO/AIA solar images in the 94 and 171 Åchannels, an FeXVIII AIA map, and the latest STEREO-A/EUVI 195 beacon image. The tool rotates and projects all these solar images to the nominal time of the rocket launch so the science team can fine-tune the pointing plan. This tool uses standard Sunpy attributes and is available online to be used by any science team planning a solar pointing with instruments with a limited field of view. An interested reader can find this tool at https://github.com/pymilo/FOXSI3_Forecasting.

Given the extremely quiet condition of the solar activity at the time of the FOXSI-3 flight, both the Si and CdTe strip detectors show only very sparse counts in the 5-20 keV energy range. Chapter 6 contains a thorough analysis of these few counts as a way to assess the hard X-ray emission from the quiet Sun. On the other side, The PhoEnIX instrument did get a tremendous amount of counts in soft X-rays, as expected at these low energies. The high number of photons registered by PhoEnIX allowed us to have solar imaging spectroscopy capabilities in soft X-rays using single-photon counting. Figure 3.23 shows a quite similarity between the most intense emission captured by PhoEnIX and with Hinode/XRT sees in soft X-rays. The most striking difference between PhoEnIX and Hinode/XRT is that PhoEnIX

Pos.	Optics	Charact.	Blocker radii [front & rear in cm]	Miss-align [+/-0.3 arcmin]	Detector
0	X8	New 10S	3.10 - 2.62	0.61	Si (105)
1	X5	7S + 3DPC-J	3DPC-Filter - 3.14	0.68	Phoenix
2	X4	7S + 3DPC	3DPC-3.575 - 3.14	0.42	Si (106)
3	X1	7S	3.75 - 3.14	0.26	CdTe (FEC07)
4	X0	10S	3.10 - 2.62	0.66	Si (102)
5	X2	10S	3.10 - 2.62	0.41	CdTe (FEC09)
6	X7	New 10S	3.10 - 2.62	0.37	Si (101)
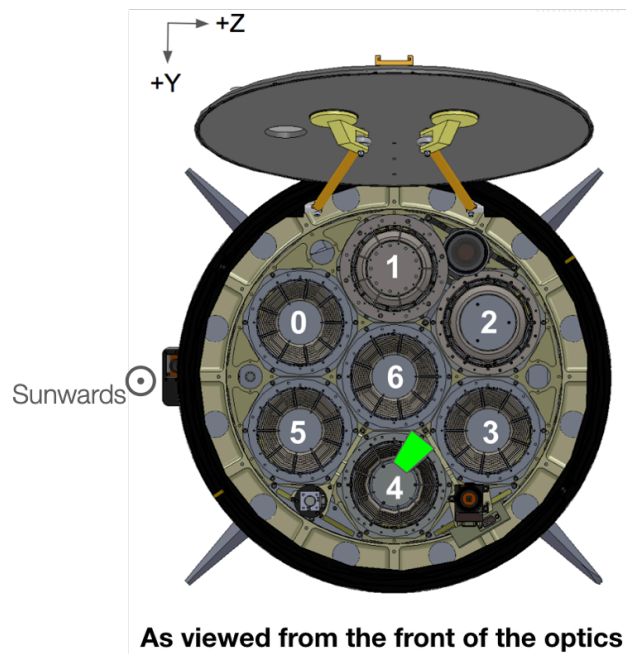
Figure 3.21: Optics and detector arrange for the FOXSI3 rocket payload.
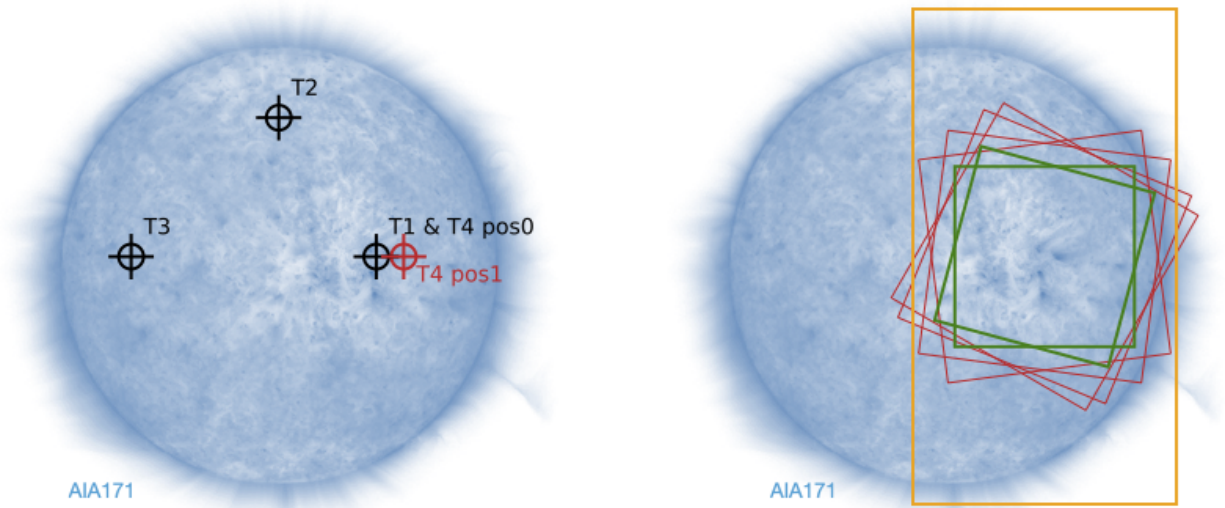
Figure 3.22: Targets and field of views during the FOXSI-3 rocket flight. The SDO/AIA-171 solar disk is displayed in the background to depict the status of the solar activity at the moment FOXSI-3 observed the Sun. *Left*: Target centers where FOXSI-3 pointed. FOXSI-3 stayed at T1 for 134 s, T2 for 27 s, and T3 for 147 s. The last target (T4) was split in two, pos0 (same as T1) where FOXSI-3 stayed for 26 s, and pos1 (shown in red), where the instrument pointed for the remaining 37 s of the observation time. *Right*: Field of views of the seven different FOXSI-3 detectors while pointing to T1. In green are the two CdTe double-side strip detectors. The red squares represent the Si detectors clocked on with respect to each other. The yellow rectangle shows the PhoEnIX CMOS field of view.

performs imaging spectroscopy while Hinode/XRT observes the Sun at a fixed energy range. This ability means that PhoEnIX can provide time evolutions and spectral responses of any desired region of interest within the solar disk (see the bottom part of the right frame in Figure 3.23).

The panel on the right on Figure 3.23 shows in bright green a solar mosaic constructed using the complete list of PhoEnIX counts in the 0.5-5.0 keV energy range captured during the entire FOXSI-3 observation time. Apart from the evident emission from the aged active region, PhoEnIX depicts other very interesting solar features, including sparse bright points and a continuous diffuse soft X-ray emission over the northwest portion of the Sun. There is certainty on the non-ghost-ray background nature of these features. The honeycomb collimator attached to the PhoEnIX optics guarantees images free of ghost-rays during the observations. For more details on ghost-rays and techniques to reduce their effect, see

Chapter 5. The PhoEnIX science team is working closely with the FOXSI team to explore this unique data set. The science outcomes expected from these analyses are assessing the temperature profiles and emission thresholds for different soft X-ray structures (bright points and diffuse regions) in the Sun.
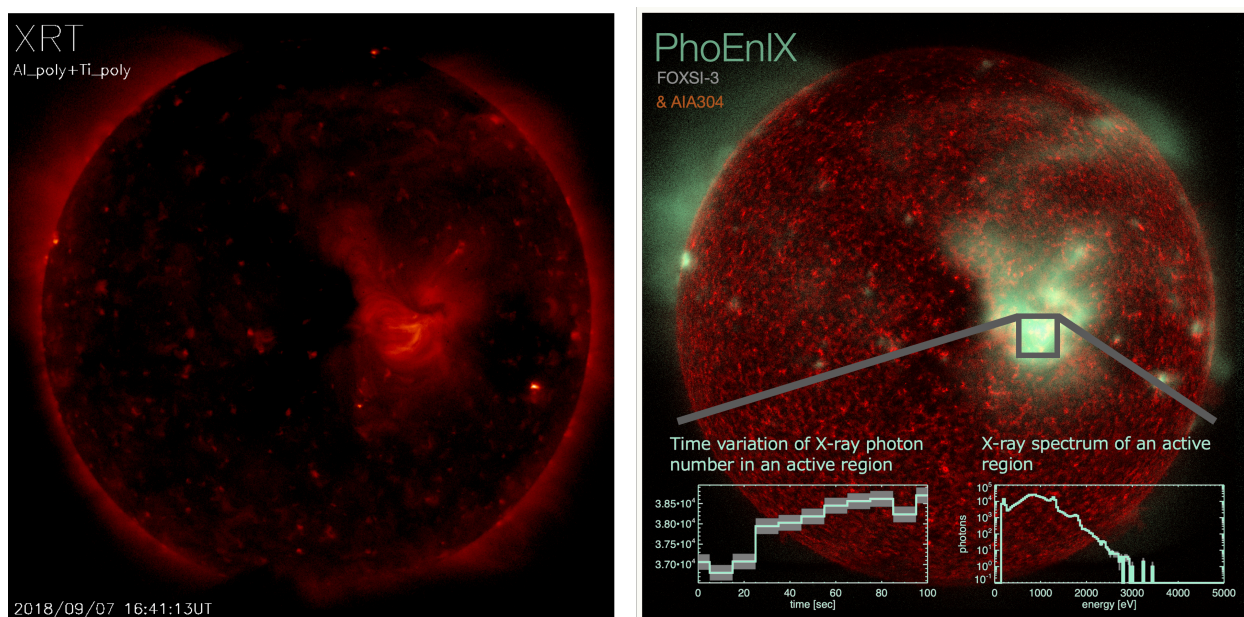
Figure 3.23:   The Sun in soft X-rays at the time of the FOXSI-3 flight. *Left*: Hinode/XRT full disk using the Al_pol + Ti_pol filters. This image was captured ~ 40 minutes before the rocket launch. *Right*: Solar Mosaic containing a SDO/AIA 304 image in the background (for reference) and in bright green the totality of PhoEnIX data collected during the FOXSI-3 flight. The plots on the bottom correspond to the time evolution and spectral response of the emission coming from the grey square. PhoEnIX performed for the first time solar imaging spectroscopy in soft X-rays using photon counting.

3.8   FOXSI-4: The high resolution focusing X-ray rocket payload to observe a solar flare.

This full section contains information published in Buitrago-Casas et al. (2021) in collaboration with the whole FOXSI team members. Although I led the effort of putting together this manuscript for publication, a substantial part of the content was developed when the proposal for FOXSI-4 was written. Many team members contributed to that original writing.

The FOXSI-4 sounding rocket will fly a significantly upgraded instrument in NASA's first solar flare campaign. FOXSI-4 will develop and implement higher angular resolution optics/detector pairs to investigate fine spatial structures (both bright and faint) in a solar flare. FOXSI-4 will use highly polished electroformed Wolter-I mirrors fabricated at the NASA/Marshall Space Flight Center (MSFC) with an improved finish than the one used for previous flights, together with finely pixelated Si CMOS sensors and fine-pitch CdTe strip detectors provided by a collaboration with institutes in Japan. FOXSI-4 will also implement a set of novel perforated attenuators that will enable both the low and high energy spectral components to be observed simultaneously in each pixel, even at the high rates expected from a medium (or large) size solar flare. The campaign will take place during one of the Parker Solar Probe (PSP) perihelia, allowing coordination between this spacecraft and other instruments which observe the Sun at different wavelengths. The FOXSI-4 flight will constitute the first time that a direct focusing hard X-ray instrument observes, in a rather wide energy range, a medium/large solar flare, and will indicate the sort of accomplishments that a solar-dedicated spacecraft based on this technology could achieve in the future.

3.8.1 FOXSI-4 new capabilities

FOXSI-4's new developments encompass two classes: high-resolution imaging for easy separation of sources within flares and high photon count rate capabilities for measuring bright flares. For the first class, FOXSI-4 will use high-precision mirrors coupled with finely pixelated Si CMOS sensors and will implement sub-strip/subpixel resolution in fine-pitch CdTe sensors. For the second class, FOXSI-4 will introduce novel microfabricated attenuators for energy coverage optimization and demonstrate that the sensors' rate capabilities are sufficient for flare measurement. Table 3.4 summarizes the instrument design parameters for FOXSI-4.

3.8.1.1 Overall optics improvements

As described in section 3.2, FOXSI has traditionally used monolithic Wolter-I mirrors manufactured at the NASA/Marshall Space Flight Center (MSFC) via an electroformed nickel alloy replication technique (Ramsey et al., 2002; Ramsey, 2005; Atkins et al., 2013). The standard MSFC mirror fabrication begins with rough cutting a mandrel from an aluminum block, tapering it, and plating it with electroless nickel. Next, the Wolter figures get shaped by diamond turning the hard overcoat, iterating several times until achieving the desired surface roughness. Subsequently, the mandrel is submerged in a nickel-cobalt bath to produce a final thin shell mirror that separates from the mandrel in a chilled water bath. Such mirrors of various radii are coaxially grouped into 7- or 10-shell modules to increase the instrument's effective area. Laboratory measurements show a 4.3 ± 0.6 arcsec full width at

---

[4]The best angular resolution reported here is calculated using the optics FWHM and information of charge sharing effects over the CdTe detectors.

Energy range	2-20 keV (unattenuated)
	3-20 keV (attenuated)
Effective area	$\sim$50 cm^2 at 10 keV (unattenuated)
	$\sim$2 cm^2 at 10 keV (attenuated)
Optics FWHM	$\sim$1" (Nagoya optics)
	$\sim$2" (MSFC optics)
Optics HPD	$\sim$10" (Nagoya & MSFC optics)
Angular resolution (best) [4] (combined optics+detector)	$\sim$1.8" (CMOS)
	$\sim$3.6" (CdTe)
Energy resolution	0.17 keV at 6 keV (CMOS)
	0.8 keV at 14 keV (CdTe)
CdTe detector photon rate	$\sim$5,000 photons/det/s

Table 3.4: FOXSI-4 sounding rocket payload projected performance. A future space mission implementing FOXSI's concept with a longer focal length would automatically have a finer resolution even with no changes in the detector parameters.

half maximum (FWHM) and 27 ± 1.7 arcsec (half-power diameter; HPD) on-axis averaged resolution for a standard optics module (Krucker et al., 2013b; Christe et al., 2016a).

FOXSI-4 will develop new optics on two fronts: one building on the heritage FOXSI optics produced at the MSFC and another via a novel effort focused on extremely high-resolution optics for X-rays at Nagoya University, Japan in collaboration with the University of Tokyo and Natsume optical corporation. The MSFC will implement a deterministic polishing technique (Champey et al., 2019) (using Zeeko) and improved shell separation techniques for the optics to achieve a resolution of 2 arcsec (FWHM) and 10 arcsec (HPD), a 2.5 improvement factor over previous FOXSI payloads (see subsection 3.2.1). For the high-resolution electroformed optics from Nagoya, Nagoya University and their collaborators have already fabricated full-shell X-ray optics. They use a high precision electroforming technique specialized for small ground-based X-ray focusing optics (Mimura et al., 2018). The expected resolution of the Nagoya optics is 10 arcsec (HPD) and 1 arcsec (FWHM).

3.8.1.2 High-resolution MSFC electroformed optics

Each step in the MSFC optics fabrication process will be improved to attain the desired spatial resolution. A deterministic polishing technique will assure an improved mandrel finish and figure (Khan et al., 2010; Kilaru et al., 2019). MSFC has already mastered such a technique and demonstrated it with the mandrels for the MaGIXS rocket experiment (Kobayashi et al., 2018), utilizing a Zeeko IRP 600X computer-numerical-control (CNC) polishing machine. The MaGIXS mandrels significantly reduced axial slope errors (to 0.72

and 1.26 arcsec HPD on the paraboloid and hyperboloid sections, respectively) for spatial wavelengths > 7 mm after applying the polishing technique several times (Champey et al., 2019). For the FOXSI-4 payload, the high optics performance will be enhanced to enable 2 arcsec FWHM by improving the shell formation and separation procedures in four steps: First, two new mandrels will be CNC polished to 1-2 arcsec HPD using the continuously improving MSFC process. Second, the pulse plating procedure will be optimized to reduce the stress in mirror shells during electroforming. Third, the micro-yield strength of the shells will be increased by testing on an improved alloy. Fourth, the mandrel/shell release process will be improved in several ways, including employing interior cooling of the mandrel/shell combination instead of exterior cooling in a water bath, varying the timing of the release process, and investigating the release mechanism using strain gauges to determine the pattern of separation. Additionally, the MSFC will utilize a new physics modeling code using COMSOL to understand better the electric field in the plating bath and find configurations to make the field more uniform, leading to a more consistent thickness and lower stress in the shells. Most of the fabrication protocols follow directly on to the most recent development for MaGIXS (see Kobayashi et al., 2018). The MSFC will deliver three upgraded modules (already produced and calibrated as needed), each containing two high-resolution mirrors, using as much fabrication heritage from FOXSI-3. Two upgraded modules will pair with CdTe (HXR) detectors, and one will pair with a CMOS (SXR) detector.

3.8.1.3 High-resolution optics from Nagoya

Nagoya University (playing a lead role) has partnered with The University of Tokyo and Natsume optical corporation to produce high-resolution X-ray optics for FOXSI-4. They will apply a high-precision electroforming technique, initially developed to fabricate small ground-based X-ray Wolter-I optics. Such previous optics showed to achieve point spread functions with sizes under $1\mu m$ (FWHM) (Mimura et al., 2018). The Nagoya University and collaborators are currently adapting their technology to provide a Wolter-I optics for FOXSI-4. The optics for FOXSI-4 will consist of a monolithic Ni electroformed mirror with a diameter and a length of 60 mm and 100 mm, respectively. The team lead by Nagoya University has already tested FOXSI-4's mirror prototypes, finding minimal figure errors (1-3 μm in PV) for the circumferential profiles. This same team will conduct X-ray irradiation tests in the near future. After alignment and calibrations, the goal is to have two single-shell optics modules, each achieving a 10 arcsec HPD and 1 arcsec FWHM.

3.8.1.4 Advanced attenuators

With the advent of powerful X-ray focusing optics for solar observations comes the need to control the photon rate such that the detectors do not get saturated. With its first large flare observation, FOXSI-4 demands a strategy to maintain fluxes at a controllable level. Such a level of control will be attainable for FOXSI-4 by implementing uniformly thick aluminum

attenuators (inherited from previous FOXSI flights), and novel Microfabricated Pixellated Attenuators (MPAs) designed and built by NASA/Goddard Space Flight Center (GSFC).
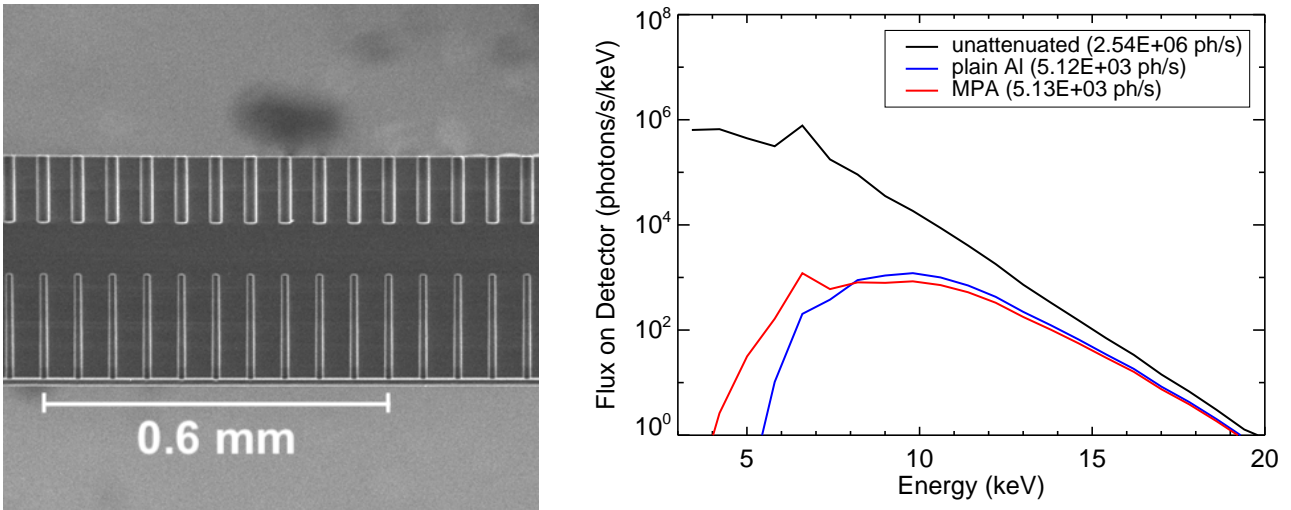
Figure 3.24: Left: Side photo of a prototype attenuator highlighting structural details of the microfabricated piece. Right: Simulated effect of the advanced attenuators after accounting for the optics energy response and blanketing in the payload. The black curve shows the unattenuated X-ray spectrum incident on a detector from a model coronal source in an M3.5 flare after it is focused by a FOXSI optics module. The incident spectrum is attenuated to a rate measurable by the FOXSI detectors with low deadtime (red curve) but maintains measurement of all the spectral features of interest across the entire energy range (including the 6.7 keV line complex), as opposed to traditional single-thickness attenuators (blue) which would cut off the low-energy spectrum..

Previous FOXSI payloads included an attenuator wheel that could insert simple, uniformly thick aluminum attenuators. Five of the FOXSI-4 detectors will use such an attenuator scheme, a fixed (immovable) aluminum window and an insertable attenuator (on a wheel) optimized to limit rates to ∼5,000 photons/detector/sec for a C5 and M3 flare, respectively. The existing ability to monitor rates and command the attenuator from the ground will straightforwardly accommodate a range of flare brightnesses.

Traditional attenuators tend to overly dampen the instrument's low-energy response. FOXSI-4 will debut a novel solution to this issue via the advanced MPAs on two of its telescope modules. The MPAs are being developed by GSFC specifically for pixelated spectroscopic X-ray detectors and can preserve sensitivity between 3-20 keV in a moderate to large flare. MPAs are fabricated by etching small holes in silicon wafers at the same pitch as the detector using a microlithography process (see Figure 3.24). These MPAs allow a small

fraction of low-energy X-rays to reach each pixel without introducing a positional dependency to the detector response. Additionally, the MPAs can be stacked to achieve greater thicknesses with a small hole diameter, and the silicon wafers can be coated with other materials, e.g., gold, for achieving specific attenuating properties.

As an example, an unattenuated spectrum for an M3.5 class flare can easily reach > 3 million photons s^{-1} (black curve in Figure 3.24); to attenuate this flux, one can use a simple 230 μm wafer of Si (blue curve in Figure 3.24). However, this substantially reduces the counts below ~6.5 keV, including part of the emission line complex. We can achieve the same reduction in count rate using a 480 μm thickness MPA with a hole diameter of 6 μm (red curve), but preserving the low energy signal for more reliable spectral fitting. Most notably, the entire emission line complex at 6.7 keV is retained.

The MPAs absorb X-rays at low energies but transmit those at high energies. The small open areas they include over each detector segment help retain effective areas at even low energies. The result is a relatively flat effective area curve, allowing FOXSI to be sensitive across its energy range without being swamped by steep solar flare spectra.

The GSFC will design several attenuators for different flare sizes. The flight versions will be chosen before launch based on estimates of target flares by the flare campaign scientific group. In addition to the MPAs, insertable slab attenuators will additionally reduce low-energy flux in the case of a large flare.

3.8.2 Detector improvements

The detector plan includes upgrades to two heritage detectors - double-sided CdTe strip detectors for HXRs and Si CMOS sensors for SXRs - but also includes the debut of a pixellated CdTe sensor using the Timepix ASIC that has never before been used for solar physics applications. The following sections describe each of these developments. For details about these detectors see sections 3.3.2, 3.3.3, and 3.3.4.

3.9 Science of FOXSI-4

Previous flights of FOXSI developed direct HXR focusing for solar purposes using an angular resolution of the optics limited to 5 arcsec (FWHM) and 25 arcsec (HPD). The development of higher resolution direct solar imagers would revolutionize the study of accelerated electrons in flares. Future, space-based HXR instruments could perform detailed spectroscopic study of coronal acceleration sites, both in and above looptops. Current performance could already separate coronal and footpoint sources (typically tens of arcsec separation) and could separate coronal and high coronal sources. However, the majority of flares have thermal and non-thermal sources in the corona that are separated by <5 arcsec (e.g., Krucker et al., 2008), requiring optics resolutions better than that to resolve them. In addition to studying

particle acceleration, high-resolution capability would also enable a clear characterization of the source of superhot plasma ($>$30 MK, Caspi et al., 2010). As accelerated electrons propagate down flare loops, they collisionally deposit energy and undergo evolution due to several effects, including scattering, turbulence, and return currents (e.g., Alaoui et al., 2017; G. D. Holman et al., 1982; Miller et al., 1997).Meanwhile, upflows of hot plasma from the chromosphere transform the thermodynamics of the flare loops. Current performance could study the looptop and footpoints separately, but high-resolution capability would enable study of the accelerated electrons at several locations along their propagation paths, better determining which of the many propagation factors are at work.

Past studies have found close correlations between HXR and white light flare footpoints and ribbons (Krucker et al., 2011; Martinez Oliveros et al., 2021). RHESSI's best resolution (2.3 arcsec) was sufficient to recognize that HXR and white light ribbons had similar shapes and positions, but RHESSI lacked the dynamic range and sensitivity to observe HXR sources all along the ribbons (e.g., Krucker et al., 2011). The correspondence between HXRs and flare ribbons has large consequences for studies of the evolution of energy release along the arcade and for how energy is transferred into heating of the lower atmosphere. While resolving a single footpoint would require resolution ($<$1 arcsec) that is still out of reach, imaging at RHESSI-scale resolution (2-3 arcsec) but with good sensitivity and dynamic range would reveal whether HXRs are present along the entire ribbons and at all white light footpoints. This would particularly enhance the science that could be performed with HXRs and the Daniel K. Inouye Solar Telescope (DKIST; about to begin operation, Tritschler et al., 2015), studying the response of the lower solar atmosphere to electron beams.

HXR studies of flare-accelerated electrons are ideally complemented by observations at soft X-ray (SXR) and extreme ultraviolet (EUV) wavelengths. High-resolution (1–2 arcsec) SXR spectral information would pinpoint the locations of reconnection-related heating and of energy deposition by accelerated electrons, as well as characterize their thermal properties.

An example of attainable X-ray resolution is shown in Figure 3.25. EUV and SXR thermal measurements would reveal the fine details of the flaring loops, elucidating the plasma structures within which the accelerated electrons propagate. Connecting (and pushing the resolution) in all of these wavelengths will lead to unprecedented energy distribution diagnostics that differentiate heated plasma from regions with non-thermal accelerated electrons. We note that two of the three regimes (HXRs, SXRs) can be provided by FOXSI -4 alone, while the third (EUV) can be provided by the Hi-C FLARE sounding rocket experiment, which will flight almost-simultaneously with FOXSI-4.

Concretely, FOXSI-4 will work toward the following scientific goals:

- Determine the amounts and locations of energy release throughout solar flares.

- Determine how superhot plasma arises.
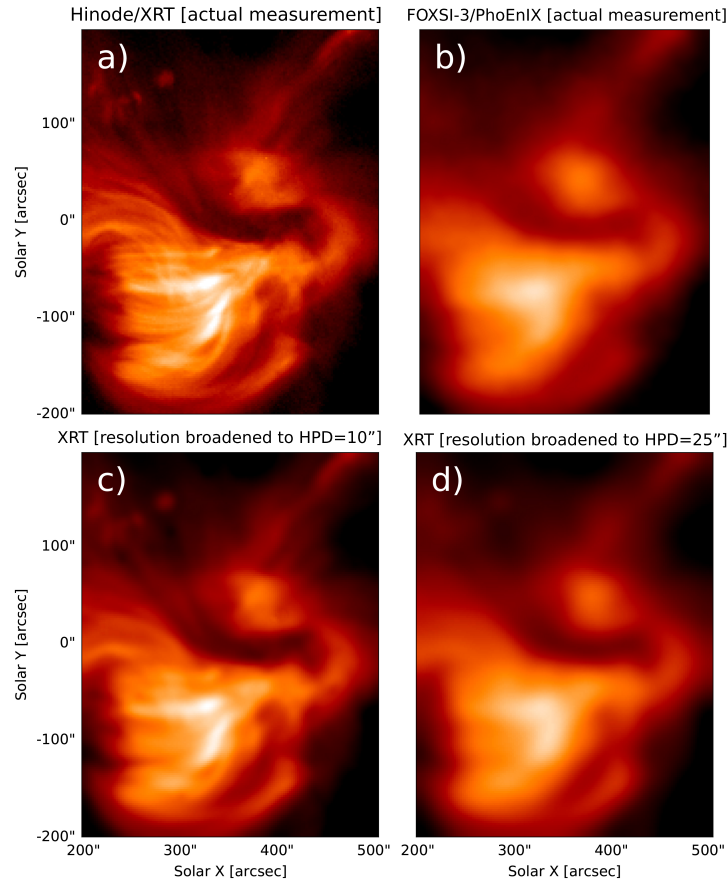
Figure 3.25: XRT thin-Be (panel a) and FOXSI-3/PhoEnIX (panel b) images of the same region on Sept 7, 2018. To make the XRT thin-Be image, we averaged a total of 93 (non-continuous) observation files taken by Hinode along the 17:00:00 UT - 18:00:00 UT hour, each with 16.4 seconds observation time. The PhoEnIX image was generated using continuous observations of that solar region for 197.2 seconds during the FOXSI-3 flight in the 0.5 - 2.5 keV energy range. The XRT image has 2 arcsec (HPD) resolution Golub et al., 2007 but offers no detailed spectral information, while the image from PhoEnIX (as flown on FOXSI -3) gives energies for every photon with an HPD of 25 arcsec. We have convolved the original XRT image with single Gaussians to produce images with equivalent HPDs of 10 arcsec and 25 arcsec, that we show in panels **c** and **d** respectively. The XRT image in panel **c** represents the target angular resolution for FOXSI-4, while the XRT image in panel **d**, and FOXSI-3/PhoEnIX in **b**, show the resolution available with past (FOXSI-3) spectroscopic X-ray imagers. The anticipated improvement in resolution from FOXSI-3 to FOXSI-4 is represented by the progression from panel **b** to panel **c**.

- Understand the interaction between accelerated particles and solar ejections.

- Determine how flares accelerate particles and how flare-accelerated electrons transfer energy to the lower solar atmosphere.

- Measure the energetic input of impulsive heating to the corona.

- Establish the practice of flare observation using sounding rocket experiments.

Possibly not all scientific objectives will be fulfilled for a given single flare, but the range of science ensures completion of some objectives regardless the flare type. If the impulsive phase is missed, FOXSI will make high-sensitivity measurements of particle acceleration and plasma heating in the decay phase, which could contain large amounts of energy.
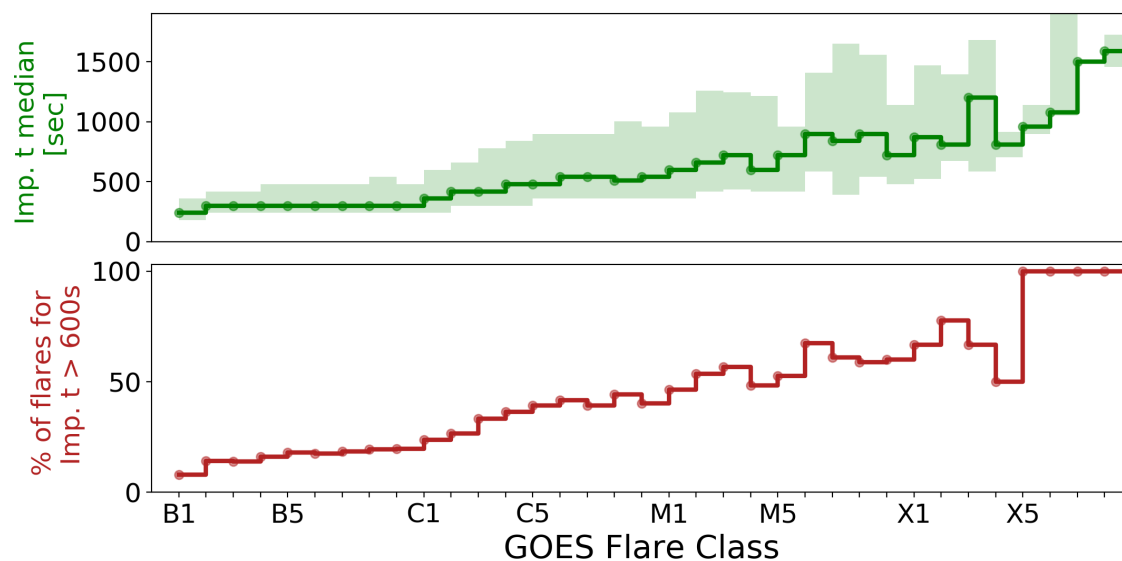
Figure 3.26:   (Top) Impulsive phase durations vs flare class, with (green line) the median duration and (shaded) 25%–75% percentile range shown. (Bottom) Percent of flares with impulsive phases >10 min. ~40% of C5 flares and ~55% of M5 flares meet this criteria and would thus have impulsive phases observable to FOXSI-4.

3.9.0.1   Solar cycle

Figure 3.26 shows impulsive phase durations vs flare size for Solar Cycles 23 and 24; the plots show (top) the duration of the impulsive phase and (bottom) the fraction of flares for which the impulsive phase lasts longer than 10 minutes for flares of various GOES classes. Larger flares have longer impulsive phases, with ~40% of C5 and ~55% of M5 flares having

impulsive phases >10 min (the current expectation for the lag between the flare start and observation start). It is therefore possible, but not certain, that FOXSI-4 will observe during the impulsive phase.

The flare probabilities in the white paper (Winebarger et al., 2019) assume a solar cycle similar to the previous one. If the next cycle were to be weaker, then the probabilities would be lower, but the chance of at least a C flare remains high. In the unlikely case that activity is so reduced that a flare is not likely to be observed, this would be evident in advance, giving NASA ample time to consider alternative launches. FOXSI-4 will be capable of observing at quiescent times and investigating flare-temperature plasma in active regions (to assess impulsive heating of the corona) and searching for hard X-rays in the quiet Sun as signatures of nanoflares, the same scientific goals as previous FOXSI payloads. The major technological goal of achieving the high angular resolution capability necessary for future HXR measurements will still be achieved.

Chapter 4

FOXSI Optics calibration

As described in the previous chapter (chapter 3), FOXSI achieves high sensitivity and a superior dynamic range of solar hard X-rays by imaging the Sun via direct focusing. FOXSI obtains this high imaging performance by using Wolter-I mirrors nested together into optics modules, some containing 7- and others containing 10-mirror shells. The FOXSI rocket payload fits a total of seven optics modules. For FOXSI-1, each of the seven optics modules contained a total of 7 Wolter-I mirrors. For FOXSI-2, two 7-shell modules were upgraded to 10-shell optics due to their higher effective area, especially at higher X-ray energies ($\gtrsim$ 10 keV). For FOXSI-3, there were two additional modules upgraded from 7- to 10-mirror optics, having a total of three 7-shell and four 10-shell optics modules.

This chapter focuses on the optics performance characterization carried out in preparation for the FOXSI-3 rocket flight. I played a leading role in this work, mainly with the help of Dr. Steven Christe from the NASA GSFC. The FOXSI science team and the groups of scientists at MSFC led by Dr. Brian Ramsey and Dr. Amy Winebarger were essential collaborators in accomplishing the results presented in this chapter.

This chapter describes the calibration process and highlights the main results of the methods utilized during the FOXSI mirror module characterization in the Stray Light Facility (SLF) at the MSFC.

4.1 Experimental setup at the Stray Light Facility NASA/MSFC

Facility - The Stray Light Facility at the NASA/MSFC in Huntsville, Alabama, has been used to calibrate and fully characterize the optics performance utilized for FOXSI (See figure 4.1). It consists of a 104 m evacuated guide pipe[1], with an X-ray source at one end and

---

[1]The 104 m is the effective distance between the X-ray source and the center of the optics module being tested. This distance includes the lengths of the bell jar that contains the X-ray source and the main bell

the main bell-chamber over the other end. The X-ray generator is a Trufocus X-ray source (model TFS-6051L with a Mo target). The main bell-chamber has a 3.66 m diameter, 91 cm length, and has a 61 cm diameter bell jar attached to the end. That bell jar terminates with a Be window that allows evacuating the chamber and jar together while having an X-ray detector outside the jar (at atmospheric pressure) to perform the measurements. The main chamber has an optical window gate valve (at the other end from the bell jar) that isolates the chamber from the 104 m evacuated pipe. The valve is activated while any optics are moved in (or out) of the main chamber. Once an optics module is installed in the cradle inside the main chamber, we turn on an alignment laser at the source end (room BC143) to properly align the optics module axis with the evacuated beam pipe. The laser uniformly illuminates the optics front, producing a focused spot 2 m beyond the optics (at the focal plane).
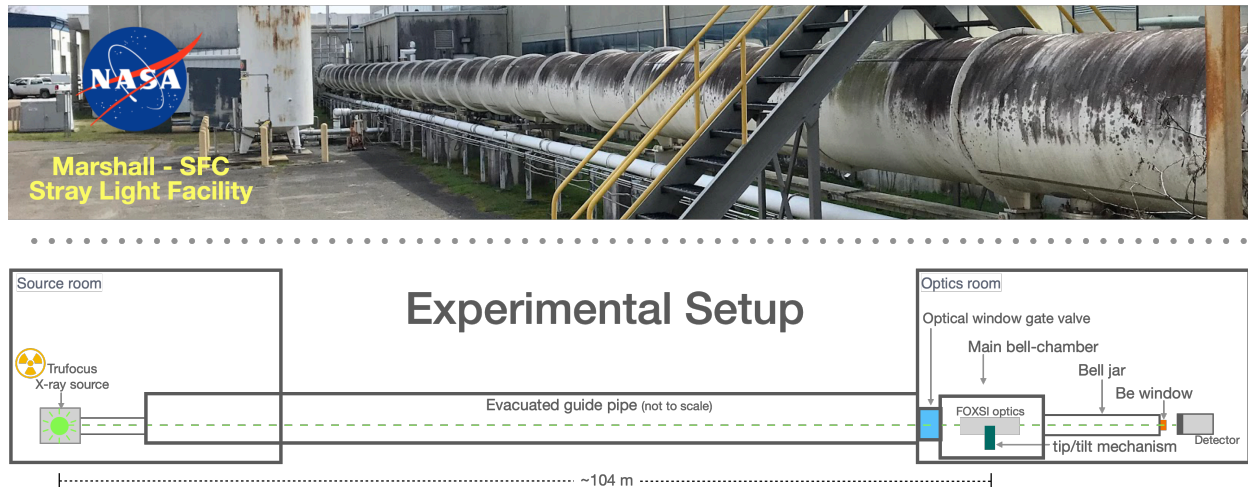
Figure 4.1:   Facility and general experimental setup used to calibrate the FOXSI optics. *Top*: Photograph of the 104 m evacuated guide pipe exterior at the Stray Light Facility (SLF) in MSFC. *Bottom*: Diagram showing the main components of the experimental setup. The 104 m pipe ends at two different rooms. The left contains the X-ray source and the right the main chamber where the optics module sits when performing the calibration measurements.

The optics module sits on a cradle with stepping motors that allow changing the optics off-axis angles in pitch and yaw. A third motor moves the optics parallel to the evacuated pipe axis (z-axis). Once a coarse laser alignment is achieved, the laser is turned off and the Trufocus X-ray source is turned on. The X-ray source voltage is nominally set to 30 kV, and its electrical current varies from ~ 0.04 mA up to ~ 0.4 mA depending on the intensity desired. These settings produce a continuous X-ray spectrum up to 30 keV with Mo Kα lines at 17.374 and 17.479 keV. At this point in the procedure, a detector is placed along the

chamber (see bottom of Figure 4.1)

optical axis 2 m behind the center of a FOXSI optics module (at the focal plane), and the bell jar/chamber pumping down begins.

Two different detectors are usually used at the SLF to carry out the calibrations. The first is a single-pixel Amptek XR-100T CZT detector and a PX2T-CZT power supply[2]. The second is an Andor iKon-L High Dynamic Range CCD camera with a 2048×2048 array and a 13.5 μm pixel pitch[3]. With the corresponding detector in place, and the chamber/jar pumped down, a fine alignment procedure is applied moving the motors in pitch, yaw, and z looking to maximize the counts measured by the detector. Once a fine alignment is achieved, the test procedure begins.

The Amptek CdTe detector is mainly used to characterize the energy optics response (effective area), while the Andor CCD camera is primarily employed to measure the optics spatial resolution (i.e., its points spread function). The CCD camera provides an energy integrated flux image between 200Å and 1100Å. This lack of energy resolution of the CCD is the reason why the CCD is not used for effective area calibrations. In the following sections, I explain these two types of measurements in detail and their results in preparation for the FOXSI-3 rocket campaign. Each optics module produced to be part of the FOXSI rocket experiment has been tested individually. Section 4.2 summarizes the history of the flights and calibration campaigns performed on each of the optics modules in FOXSI.

4.2 Rocket flight and calibration record for each of the optics modules

Since the beginning of the FOXSI rocket project, there have been a total of eight optics modules fabricated and flown as part of the rocket payload of the FOXSI-1, -2, and -3 rocket launches. Some optics have been upgraded from 7- to 10-mirror modules. Also, the blocker sizes have changed, and some were flown with a honeycomb-type collimator in front to reduce ghost-ray backgrounds (see Chapter 5). Figure 4.2 shows a flow diagram that keeps track of what sort of these changes.

4.2.1 Flight and upgrade record

As described in the previous chapter (Chapter 3), the FOXSI rocket payload can fit seven optics modules. The FOXSI-1 team labeled each optics module with the X0, X1, X2, X3, X4, X5, and X6 names. All optics initially were 7-mirror modules and designed to be identical. After the first flight, the X0 and X2 optics were upgraded from 7- to 10-mirror modules. The upgraded X0 and X2 modules, together with X1, X3, X4, X5, and X6, were flown in FOXSI-

---

[2]https://www.amptek.com/internal-products/xr-100t-cdte-cadmium-telluride-detector-efficiency-application-note

[3]https://andor.oxinst.com/products/ikon-xl-and-ikon-large-ccd-series/ikon-l-936
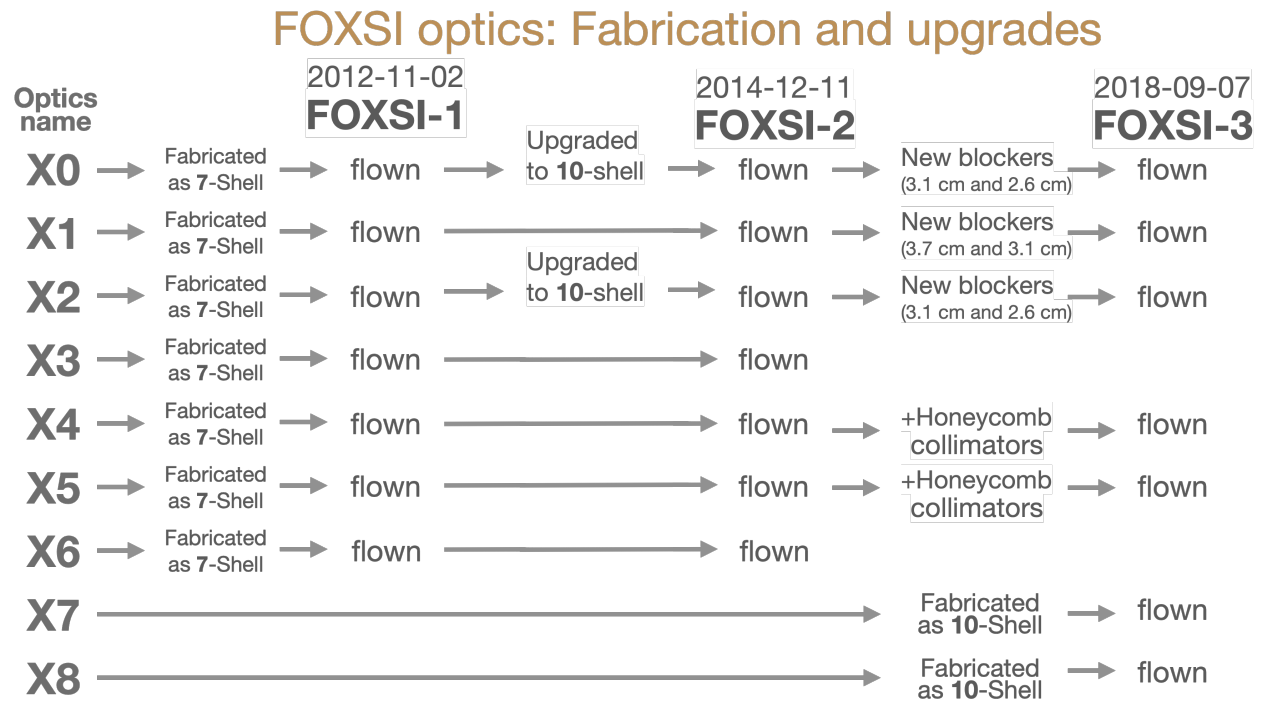
Figure 4.2: Flow diagram tracking when the FOXSI optics were fabricated, what sort of changes were implemented, and whether or not the modules flew in each of the FOXSI rocket flight. X7 and X8 were fabricated including front and rear blockers optimized for 10-shell optics modules (i.e., 3.10 cm and 2.62 cm, respectively). Also, when the honeycomb-type collimators were attached to X4 and X5, blockers of 3.75 cm and 3.14 cm were attach to the front and rear end of the module.

2. After the second rocket flight, additional upgrades were implemented to the optics. New blockers, with sizes optimized to minimize ghost-rays, were added to every optics module intended to fly in FOXSI-3, and honeycomb-type collimators were attached to the front of modules X4 and X5. In preparation for the FOXSI-3 rocket flight, two brand new 10-mirror optics modules were fabricated (X7 and X8). These two new optics were flown as part of the FOXSI-3 rocket payload, together with X0, X1, X2, X4, and X5. The current plan includes re-using two of these optics for the FOXSI-4 payload.

Optics name	FOXSI-1 2011-Feb	FOXSI-1 2011-Apr	FOXSI-1 2011-May	FOXSI-1 2013-Jan	FOXSI-2 2013-May	FOXSI-2 2015-Jan	FOXSI-3 2017-Jul	FOXSI-3 2017-Sep	FOXSI-3 2018-Mar	FOXSI-3 2018-May
X0	EA - Amptek HPD - Amptek PSF - Amptek			EA - Amptek HPD - Amptek PSF - Amptek	PSF - CCD	EA - Amptek	EA - Amptek HPD - Amptek PSF - Amptek	EA - Amptek HPD - Amptek		
X1		EA - Amptek HPD - Amptek PSF - Amptek		EA - Amptek HPD - Amptek PSF - Amptek		EA - Amptek	EA - Amptek HPD - Amptek PSF - Amptek PSF - CCD		PSF - CCD	
X2	EA - Amptek HPD - Amptek PSF - Amptek			EA - Amptek HPD - Amptek PSF - Amptek		EA - Amptek PSF - CCD		EA - Amptek HPD - Amptek PSF - Amptek PSF - CCD	PSF - CCD	
X3		PSF - Amptek	EA - Amptek HPD - Amptek PSF - Amptek	EA - Amptek HPD - Amptek PSF - Amptek		EA - Amptek	PSF - CCD			
X4			EA - Amptek HPD - Amptek PSF - Amptek	EA - Amptek HPD - Amptek PSF - Amptek	PSF - CCD	EA - Amptek		EA - Amptek HPD - Amptek PSF - Amptek PSF - CCD	PSF - CCD	
X5	EA - Amptek HPD - Amptek PSF - Amptek			EA - Amptek HPD - Amptek PSF - Amptek	PSF - CCD	EA - Amptek PSF - CCD				
X6	EA - Amptek HPD - Amptek PSF - Amptek			EA - Amptek HPD - Amptek PSF - Amptek		EA - Amptek	HPD - Amptek PSF - Amptek PSF - CCD			
X7									PSF - CCD	EA - Amptek HPD - Amptek PSF - CCD
X8										EA - Amptek HPD - Amptek PSF - CCD

Table 4.1: List of all optics calibration campaigns carried out to date. X0, X1, X2, X3, X4, X5, X6, X7, and X8 are the optics modules fabricated to fly in FOXSI (see Figure 4.2). Each column in this table corresponds to an optics calibration campaign at MSFC. There were three types of measurements: Effective Area (EA), Half Power Diameter (HPD), and Point Spread Function (PSF). In this table, *Amptek* means that the single-pixel Amptek detector was used to take the measurements. Likewise, *CCD* means that the Andor's High Dynamic Range CCD camera was used instead. Both the raw data and their corresponding analysis can be found in the FTP repository ftp://apollo.ssl.berkeley.edu/pub/foxsi/FOXSI-Optics-Calibration/All_Organized_Data/

4.2.2   Optics calibrations record

The FOXSI optics modules have had several calibration campaigns at the SLF. Table 4.1 encompasses information about what sorts of tests were done and when, for each of the FOXSI optics modules. Both the raw data for each optics calibration campaign and their corresponding analyses are hosted in the FOXSI FTP repository: ftp://apollo.ssl.berkeley.edu/pub/foxsi/FOXSI-Optics-Calibration/All_Organized_Data/. There were three quantities used to assess the optics performance: the effective area (EA), the half-power diameter (HPD), and the point spread function (PSF). The following sections present the details of these analyses and some key results and examples for some optics modules.

4.3   Effective area study

In general, for X-ray telescopes, the concentration power of a particular optic is a key factor in its sensitivity. The effective area as a function of energy is a standard way of expressing this quality.

The FOXSI optics effective area performance was one of the optical parameters measured at the SLF. To perform these measurements, we used the setup shown in Figure 4.1 and placed the Amptek detector behind the Be window at the end of the bell jar (allowing 2 m between the optics in the main bell chamber and the detectors). The optics module is then finely moved in pitch, yaw, and z until getting an optimal focus. Then, the monolithic sensor at the tip of the detector is covered with a 3.0 mm pinhole. We estimate the on-axis effective area as the ratio between the measured fluxes with and without the optics inside the main chamber.

$$EA = A_{\text{pinhole}} \left(\frac{F}{t} \right)_{\text{Optics}} \cdot \left(\frac{t}{F} \right)_{\text{No-optics}}, \tag{4.1}$$

where A_{pinhole} is the area of the pinhole, F is the measured flux, and t is the time over the measurement was done.

The finite 104 m distance of the X-ray generator to the optics at the SLF causes the measured effective area to be a little smaller than for a source at an infinite distance. For finite source distances, fewer X-rays intersect both Wolter-I segments, the paraboloid primary and the hyperboloid secondary. Thus, the measured effective area at the SLF is slightly smaller than the actual effective area for an at-infinity source.

Figure 4.3 displays the most recent effective areas (for a range of off-axis angles) of each of the optics modules flown in FOXSI. Note how the effective area decreases with energy due to decreasing reflectivity limited by the mirrors finish (roughness) and their short 2 m focal length, which determines grazing angles and therefore limits reflectivity. We limited
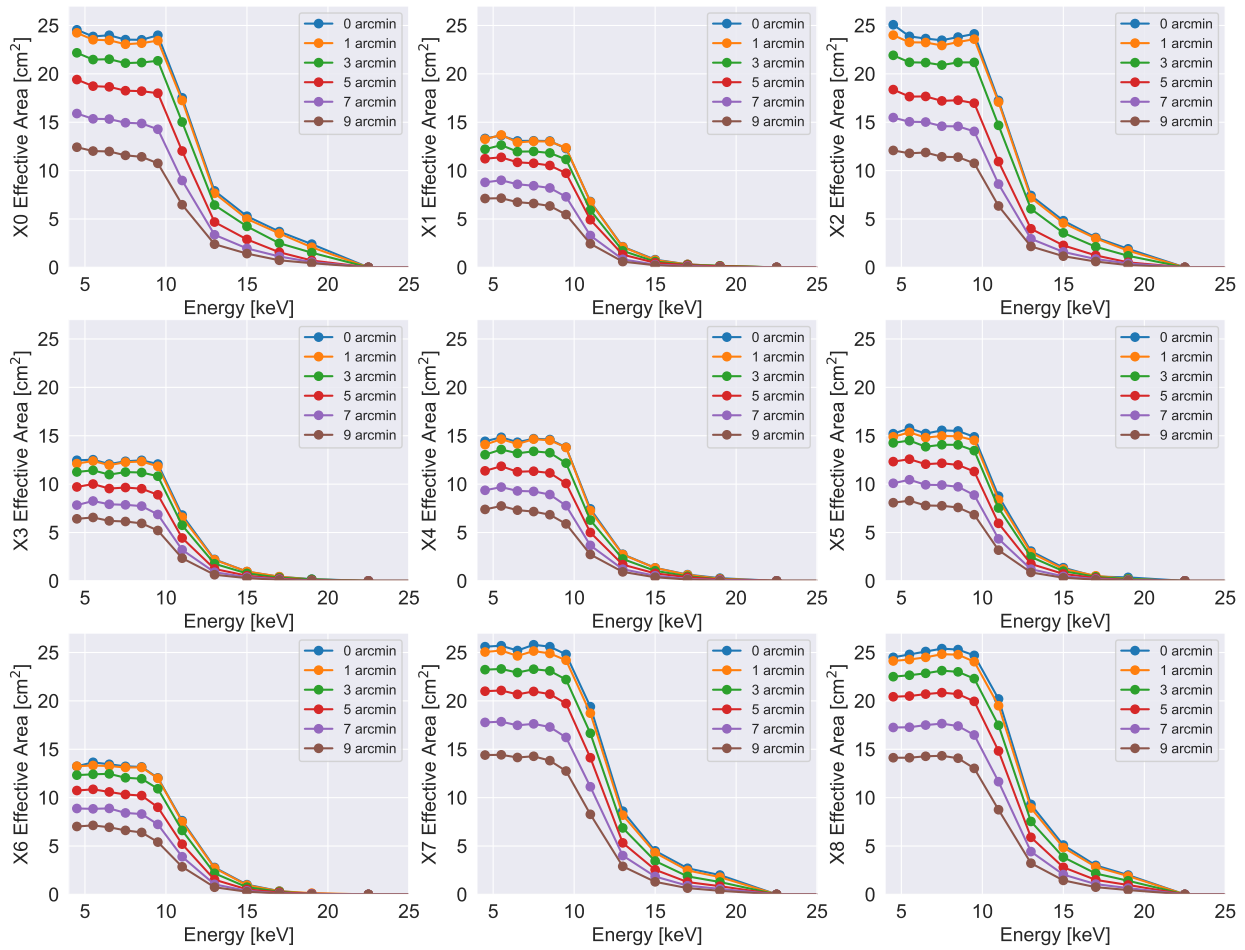
Figure 4.3: Effective areas as a function of energy (for a range of off-axis angles) of each of the optics modules flown in FOXSI. These effective areas are averaged in azimuth angle. X0, X2, X7, and X8 are 10-mirror modules. X1, X3, X4, X5, and X6 are 7-mirror optics. The data plotted here correspond to the most recent measurements for each of the optics module according to Table 4.1.
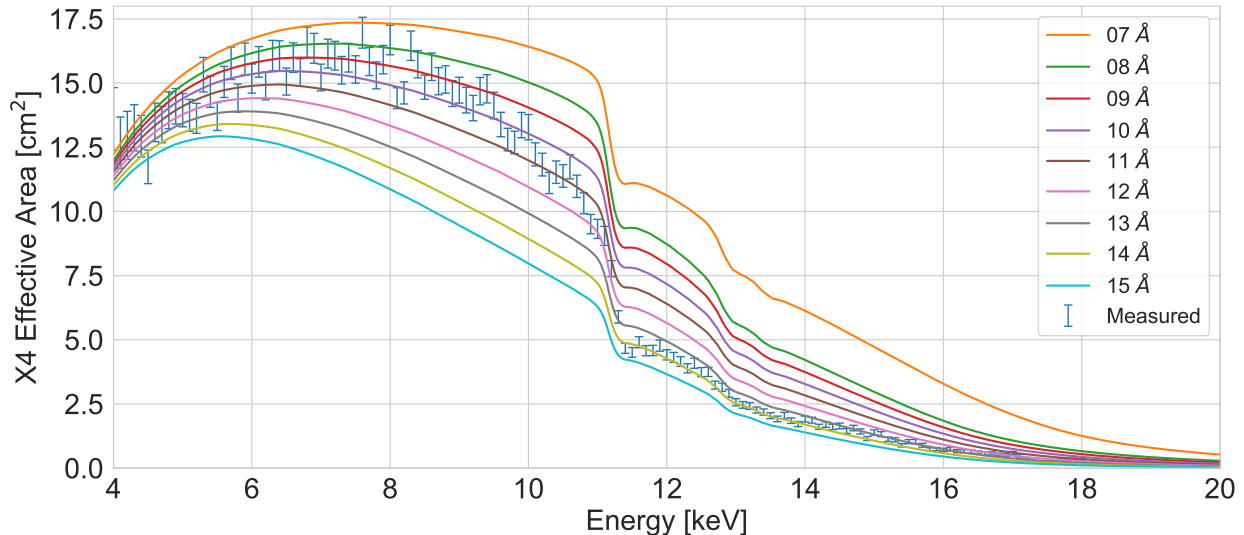
Figure 4.4:   Measured vs theoretically modeled effective area for X4 (7-mirror optics module) on-axis. The error bars correspond to the measured values with a Silicon drift detector (SDD) used during the September 2017 calibration campaign. The solid lines are obtained using the EPDL97 model in the XOP software (see 3.2.2 of chapter 3 for details about how to use this software). The difference among the solid lines is the theoretical mirror RMS roughness in Angstroms. These theoretical curves include also the absorption effect of the 0.5 mm Be window at the end of the bell jar and the 8 cm air gap between the Be window and the detector.

our effective area measurements to sources' off-axis angles of up to 9 arcmin. This upper limit is constrained by the field of view of a standard Si detector (16×16 arcmin^2). Christe et al. (2016b) shows the effective area for FOXSI-2 adding up the individual effective areas for each optics module flown in the payload of the second FOXSI flight. They also show the azimuthal symmetry of the effective area by plotting the effective area for different off-axis angles on tilt and yaw.

As shown in subsection 3.2.2, the X-ray Oriented Programs (XOP) software can be used to estimate the theoretical effective area for a FOXSI assembly of Wolter-I mirrors. Figure 4.4 shows a comparison between the measured effective area for X4 (a 7-shell module) and estimated theoretical effective areas obtained using the EPDL97 model in the XOP software. This same figure shows that non of the theoretical curves match that measured effective area for all energies at once. We see that for energies under ~ 11 keV, the data fits surface roughness of $\sim 9 - 10$ Å. At higher energies, $\gtrsim 11$ keV, root mean square (RMS) roughness of $\sim 13 - 14$Å fit the measured data better. This is physically unrealistic. Dust over the mirror surfaces may be related with the cause of this incongruence. Further exploration of
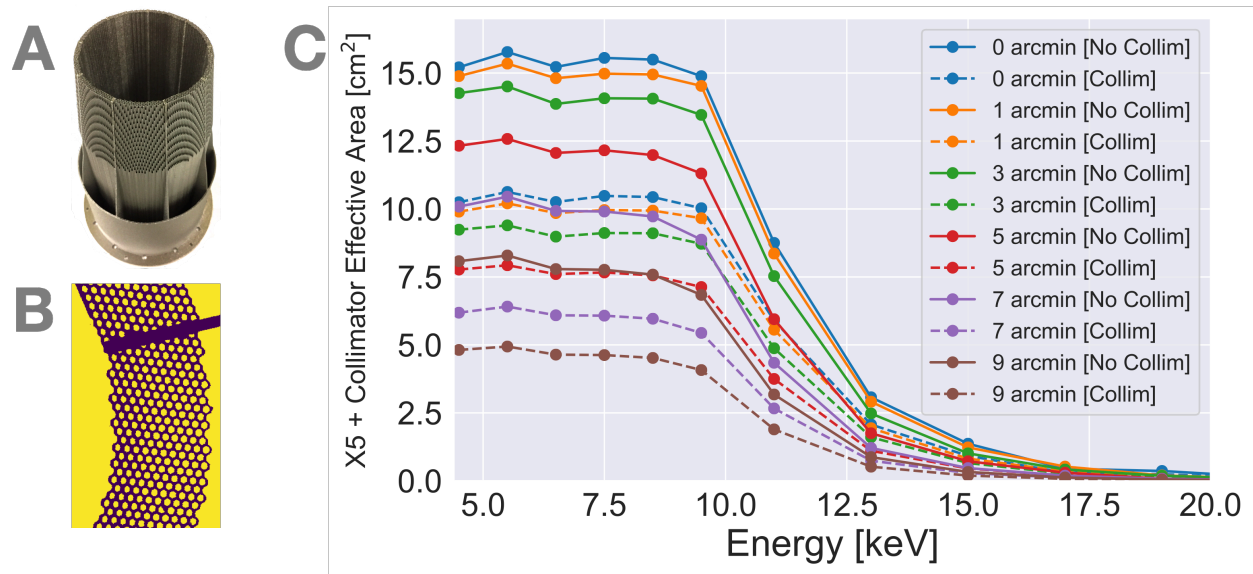
Figure 4.5: Honeycomb collimator impact to the effective area. **A**) Photo of one of the two honeycomb-type collimators attached to the front of the X4 and X5 optics modules (with 7-mirrors) and flown in FOXSI-3. Note the hexagonal holes at the top of the collimator. For more information about the performance of this collimator, see subsection 5.5.2 of Chapter 5. **B**) Collimator on-axis cross-section. This image was captured with the Andor's iKon-L High Dynamic Range CCD camera at the SLF at MSFC, while the X-ray generator illuminated the collimator alone (no optics module attached) inside the main chamber. We measured the on-axis open area across the honeycomb structure and obtained a $35\% \pm 4\%$ throughput. This open area decreases for off-axis X-ray sources given the vignetting effect product of the 200 aspect ratio of the hexagonal holes in the collimator. The plot on the right (**C**) compares the effective area for module X5 with (dashed lines) and without (solid lines) the collimator attached for a range of off-axis angles.

this discrepancy will be required in the future.

4.3.1 Honeycomb-type collimator effective area effect

Section 3.7 in Chapter 3 briefly presented that the FOXSI-3 payload included two honeycomb-type collimators attached to two of the optics modules as a way of mitigating their ghost ray backgrounds (see one of these collimators in panel A of Figure 4.5). The honeycomb structure covers only three innermost mirrors of a 7-mirror module because they are more susceptible to ghost rays. The pay-off of having a collimator along a module's optical path is a net decrease of the telescope's throughput. That reduction heavily depends on the on-axis open area of the collimator honeycomb structure. Panel B in Figure 4.5 shows a

measurement of such an on-axis open area captured with the Andor's iKon-L High Dynamic Range CCD camera at the SLF. From this measurement, we determined a $35\% \pm 4\%$ on-axis throughput of the collimator alone (no optics module attached). Such throughput decreases further for off-axis X-ray sources due to the honeycomb vignetting effect. Panel C in Figure 4.5 contains a plot comparing the effective area for X5 with (dashed lines) and without (solid lines) the collimator attached for a range of off-axis angles. Adding a collimator reduces the effective area of the telescope by about $\sim 33\%$ (this value already take into account that the collimator only covers the four inner most shells of a 7-mirror optics). This effect needs to be accounted for when setting a satisfactory compromise between the ghost ray mitigation performance and the sensitivity of a FOXSI optics module. For FOXSI-3, only two (X4 and X5) out of the seven optics modules had a honeycomb collimator attached. X4 focused X-rays on a double sided strip Si detector, and X5 on a PhoEnIX CMOS sensor. Both telescope assemblies had satisfactory performances. In particular, since the Sun is substantially brighter at soft X-rays than at hard X-rays, the throughput reduction over X5 was not a problem for the success of the PhoEnIX observations. X4 showed similar count rates (5 counts for the whole flight) as its telescope counterparts using hard X-ray strip detectors.

4.4 Point Spread Function assessment

In general, the point spread function (PSF) quantifies the response of a focusing optical system to a point-like source (e.g., Wolf, 1951; Wolf, 2005). A PSF consists of a measured intensity pattern resulting from imaging a point source with an optical system. The PSF blob size is a direct diagnostic for the imaging system quality. Two point sources separated an angular distance smaller than the average width of the PSF cannot be individually resolved. Likewise, extended sources with features smaller than the PSF size cannot be identifiable. Thoroughly characterizing and quantifying the FOXSI optics PSF is critical to determining the solar objects (and features) that the rocket payload can target. Saint-Hilaire et al. (2008), e.g., showed that the average flare footpoint separation lies between ~ 10 arcsec and ~ 100 arcsec for a sample of 53 flares of medium and large GOES class. Warmuth et al. (2013) estimated average nonthermal footpoint sizes from ~ 1.9 arcsec to ~ 4.4 arcsec. They also found that thermal source sizes are in the range of 3.7 - 31.6 arcsec.

In the past, the FOXSI PSF was measured at the SLF by stepping the single-pixel Amptek XR-100T CZT detector across the core region of the PSF on the focal plane (see Chapter 7 in Glesener (2012) for details). An angular resolution of 4.3 ± 0.6 arcsec (on-axis) was determined from those measurements for a 7-mirror FOXSI optics module (Krucker et al., 2014). The Andor iKon-L High Dynamic Range CCD camera offers an alternative way to study the FOXSI PSF using a 2048×2048 pixel image with a 1.39 arcsec per pixel resolution. Starting in the calibration campaign of May 2013 (see Table 4.1), we used this CCD camera to take measurements of the FOXSI PSF.

As for any optical system, the FOXSI PSF is not a point-like distribution (two-dimensional
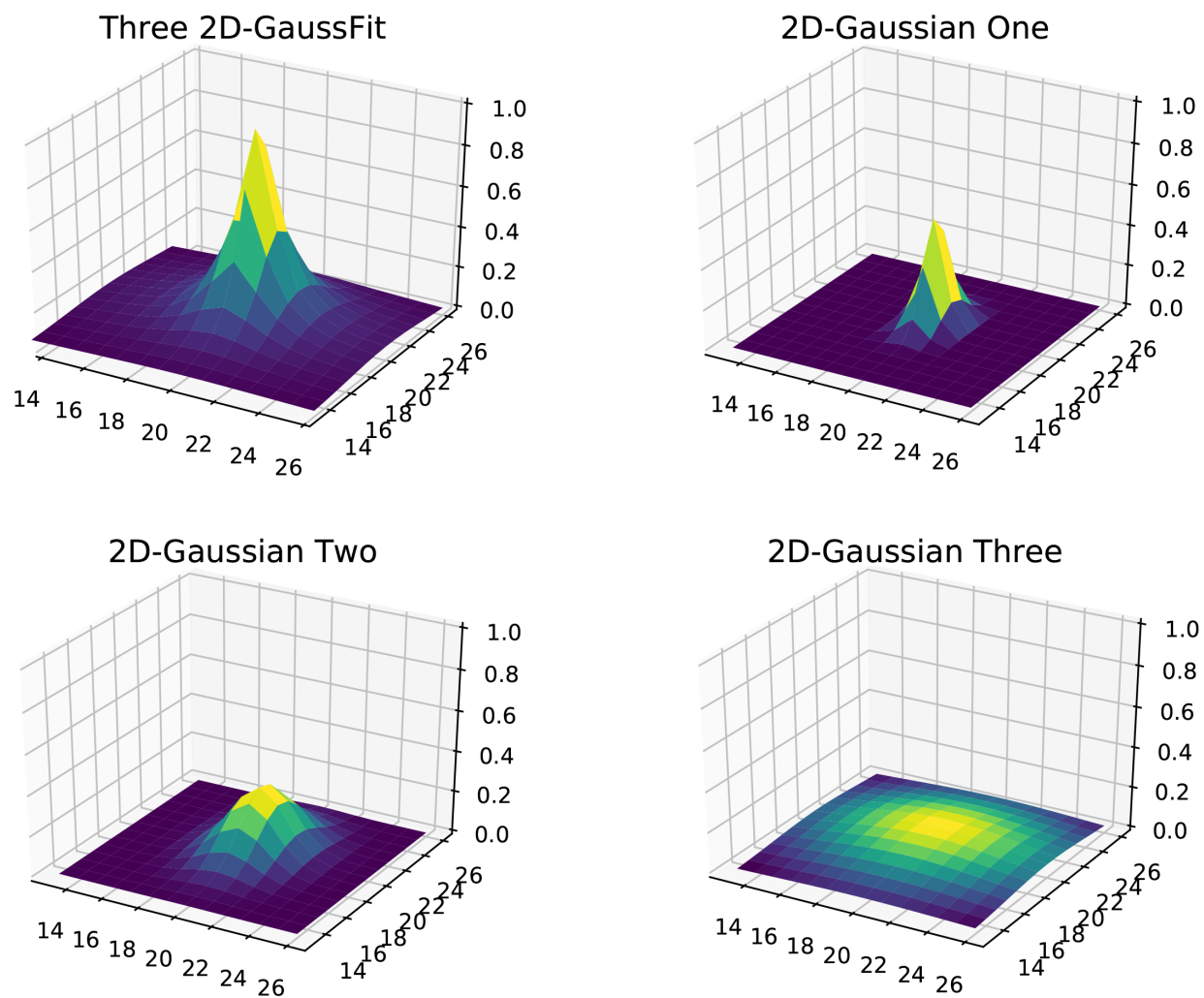
Figure 4.6: Example of three 2D Gaussians added together to fit the PSF of a FOXSI optics module. *Top left*: All three two-dimensional Gaussians added together. All the other three figures show each of the individual three two-dimensional Gaussians. The amplitudes of the Gaussians are normalized to the peak of the sum. The x and y axes are set in arcseconds, with the PSF peak arbitrarily centered at (20", 20").

Dirac delta function). Instead, it depicts some broadening caused by a combination of a range of physical origins. These origins include a small misaligning among the mirrors in a module, a slight discrepancy between the actual shape of the mirrors and a theoretical Wolter-I geometry, and X-ray scattering due to the mirrors' inner surface roughness. For sources relatively far from the optical axis ($\gtrsim$ 12 arcmin) or on-axis sources at a finite distance from a FOXSI telescope aperture, the PSF also contains ghost-rays. Ghost rays are produced when incoming rays do not property reflect twice over a Wolter-I but still can get onto the focal plane. Chapter 5 discusses in detail ghost-ray origin and treatments to minimize their effect on Wolter-I telescope performances.

To evaluate the FOXSI optics PSF, we fitted three two-dimensional Gaussians added together to the intensity pattern captured by the Andor CCD camera. A single Wolter-I mirror PSF falls in two regimes: core and wings. Slight variations of the mirror figure from an actual Wolter-I geometry cause the broadening of the core. This component is strongly peaked. The roughness of the mirror surfaces is the source of the PSF wings. In addition to these two single mirror PSF components, for optics assemblies made of concentrically nested Wolter-I mirrors, a third PSF broadening component is naturally expected caused by slight misaligning among the mirrors. The original motivation of the three two-dimensional Gaussian model was to assign each Gaussian to each of the three physical components expected to be present in the FOXSI PSF.

$$PSF(x, y) = \sum_{i=1}^{3} A_i \exp\left[-a_i(x - \mu_x)^2 - b_i(x - \mu_x)(y - \mu_y) - c_i(y - \mu_y)^2\right], \qquad (4.2)$$

with

$$a_i = \left(\frac{\cos^2\theta}{2\sigma_{x_i}^2} + \frac{\sin^2\theta}{2\sigma_{y_i}^2}\right), \qquad (4.3)$$

$$b_i = \left(\frac{\sin(2\theta)}{2\sigma_{x_i}^2} + \frac{\sin(2\theta)}{2\sigma_{y_i}^2}\right), \qquad (4.4)$$

and

$$c_i = \left(\frac{\sin^2\theta}{2\sigma_{x_i}^2} + \frac{\cos^2\theta}{2\sigma_{y_i}^2}\right). \qquad (4.5)$$

A_i are the amplitudes for each Gaussian. $\sum_{i=1}^{3} A_i$ must be equal to the maximum intensity of the measured PSF. x and y are the 2-dimensional domain of the PSF. μ_x and μ_y are

the centroids on the x-y plane for each Gaussian (we assume they share the same center). σ_{x_i} and σ_{y_i} are the second moments for each i-Gaussian over the two axes x and y. θ is the azimuth angle between the Gaussians x-axis and the horizontal axis of the CCD image (we assume the three Gaussians share the same θ).
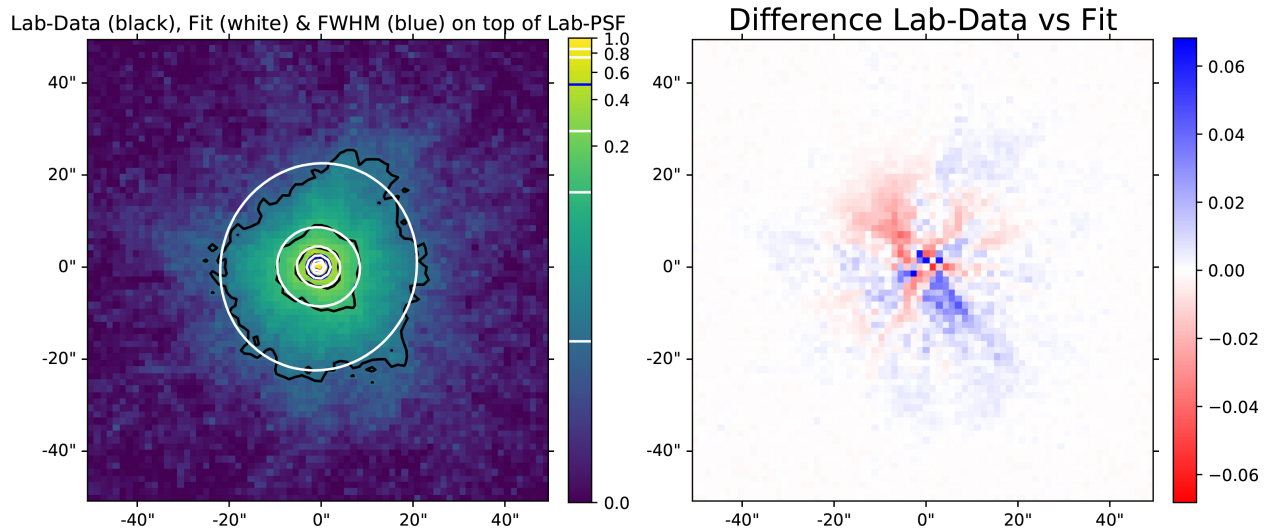
Figure 4.7: Fit of three 2-dimensional Gaussians over the **on-axis** PSF of the X2 FOXSI optics (a 10-mirror module). *Left*: The background image (log scale) is the normalized PSF measured with the Andor CCD camera at the SLF. The black contours correspond to 1%, 10%, 25%, 50%, 75%, and 85% of the image maximum intensity. The white contours show the best fit using three 2-dimensional Gaussians at 1%, 10%, 25%, 50%, 75%, and 85% of the fitting maximum amplitude (see them also in the color bar). The contour in blue highlights the 50% amplitude of the fitting, which sets the PSF full width at half maximum by definition. *Right*: Map of the differences between the actual measured PSF image on the left and the best fit found using three Gaussians. Note that the largest differences lie at the core of the PSF where the non-symmetrical missalignings of the mirrors in the module show their greatest effect. Despite the differences of up to 6%, chi square of this fit is 6.61. The corresponding p-value is 1.0 (given the sample size of 5184). The average FWHM integrated on the azimuth angle is 4.81 arcsec.

Figure 4.6 depicts an example of three Gaussians added together to fit the PSF of a FOXSI optics module. There is a core Gaussian, a broad Gaussian, and the Gaussian wings extending furthest from the core. I compiled python scripts that can easily fit a PSF with Gaussians in the following GitHub repository: https://github.com/pymilo/foxsi3_optics_cal.

The three 2-dimensional Gaussian model is an empirical treatment that offers a low enough chi-square ($\sim$30) when fitting the FOXSI optics PSF (given an image of a couple thousand of pixels). The large sample sizes, together with the low chi-square values lead to

p-values very close to 1.0. The low chi-square values are achieved because of the relatively numerous adjusting parameters in the model (12 free parameters total for the three two-dimensional Gaussian model) and the fact that most of the intensity concentrates at the PSF core. Other fitting approaches resulting in a low chi-square would be equally valid. For instance, since the wings fall off roughly linearly far from the core (see Chapter 7 in Glesener (2012)), two two-dimensional Gaussian plus a Lorentzian would probably be a good fit as well. Other instruments using Wolter-I mirrors use a Gaussian to fit the PSF core and a power law for the wings (e.g., Gaetz et al., 2004).

When fitting a PSF, there should be a compromise on the number of free parameters of the model to avoid over-fittings. The goal of fitting the PSF is to characterize its broadening by determining the full width at half max (FWHM). This goal is also achieved using only one or two two-dimensional Gaussians, but the chi-squares obtained with those approaches are relatively higher ($\gtrsim 30.0$).
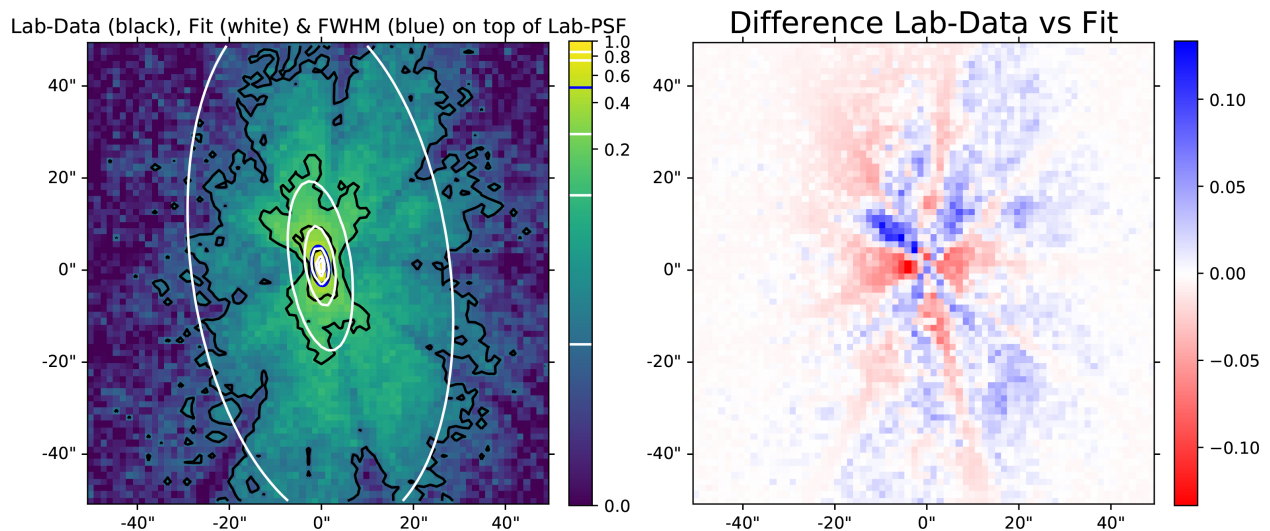
Figure 4.8: Same as Figure 4.7, but for a 9 arcmin off-axis source. Chi square of this fit is 30.42 and the average FWHM over the azimuth angle is 5.71 arcsec.

Figure 4.7 shows an example of the **on-axis** PSF (background image and black contours) and corresponding three two-dimensional Gaussian fit (white contours) for the X2 optics module (a 10-mirror module). Using three two-dimensional Gaussians returns a fit with a 6.61 chi-square for this example, which is a good fit. Figure 4.7 also depicts a map of differences between the fitted model and the actual PSF. That map shows discrepancies of up to 6% at the core, mainly produced by the slight mirror misalignments of X2. These discrepancies are subtle and do not substantially change the FWHM estimates. Following equation 4.2, the parameters that best fit the PSF in Figure 4.7 (with a $\chi^2 = 6.61$ and a $R^2 = 0.987$) correspond to $A_1 = 0.636$, $\sigma_{x_1} = 1.100$, $\sigma_{y_1} = 1.086$, $A_2 = 0.254$, $\sigma_{x_2} = 2.670$,

$\sigma_{y_2} = 3.029$, $A_3 = 0.110$, $\sigma_{x_3} = 7.204$, $\sigma_{y_3} = 6.756$, and $\theta = 19.0°$. The mean FWHM is 4.82 arcsec (averaging over the azimuth angle).

The on-axis PSF in Figure 4.7 is not perfectly symmetrical along the azimuth angle. This non-symmetry has direct effects on the estimate of the FWHM. To account for this dependence, the fitting model produces an FWHM as a function of the azimuth angle. Figure 4.9 shows such dependence for an on-axis source (top two plots) and a nine arcmin off-axis source in yaw[4] (bottom two panels). The polar plots on the right of Figure 4.9 show in blue the FWHM, and the left two panels show the variation of the FWHM magnitude over one azimuth quadrant. Note that the on-axis PSF FWHM only varies by under $\sim 0.7\%$ of its averaged value. For the 9 arcmin off-axis PSF, the FWHM varies from ~ 3.5 arcsec up to ~ 8.34 arcsec (around an 80% variation over its average value, 5.93 arcsec). Figure 4.8 shows the measured point spread function and the best fit with the map of differences at the right for this same configuration of the X2 optics.

For off-axis sources, the optics PSF gets squeezed in one direction (along the line between the source and the optics axis) and stretched in the other—the greater the off-axis angle, the stronger these squeezing and stretching effects. The deviation of the flat detector plane from the curved optics focal plane produces these PSF distortions (much more extensive and no longer round). These optics errors make Wolter-I type mirror performances limited for off-axis sources. When we fit the PSF using the three Gaussians model, all three Gaussians get similarly squeezed and stretched. Figure 4.10 helps visualize these effects by showing in red contours the fitted PSF for a range of different off-axis source locations. For each of the locations displayed in Figure 4.10 I made plots like the ones shown in Figures 4.7, 4.9, and 4.8, for all the optics modules calibrated at the SLF using the Andor CCD camera. All these results are publicly available at the FTP repository ftp://apollo.ssl.berkeley.edu/pub/foxsi/FOXSI-Optics-Calibration/All_Organized_Data/.

4.4.1 Full width at half maximum

The PSFs in Figure 4.10 can be grouped in four sets along axes with azimuth angles of 0°, 45°, 90°, and 135° (0° and 90° correspond to the major axes). For each of the four axes, Figure 4.11 shows the average FWHM (solid lines), and maximum and minimum measured FWHMs (dashed lines) for sources at 0.0, 0.5, 1.0, 1.5, 2.0, 3.0, 5.0, 7.0, and 9.0 arcmin from the optical axis. Despite Figure 4.11 not having error bars, one can observe that the FWHMs for off-axis angles over any of the four axes show a similar tendency with one another. The similitudes among the four axes suggest that the optics modules tend to keep an azimuthally symmetric performance, as is expected. The minimum values of the FWHM in Figure 4.11 represent the most stretched width of the PSF along the azimuth angle. Likewise, the maxima are the broadest parts of the PSF for each off-axis angle measured.

---

[4]A movement in yaw is defined as a rotation around the vertical axis (perpendicular axis to the floor) of the optics module.
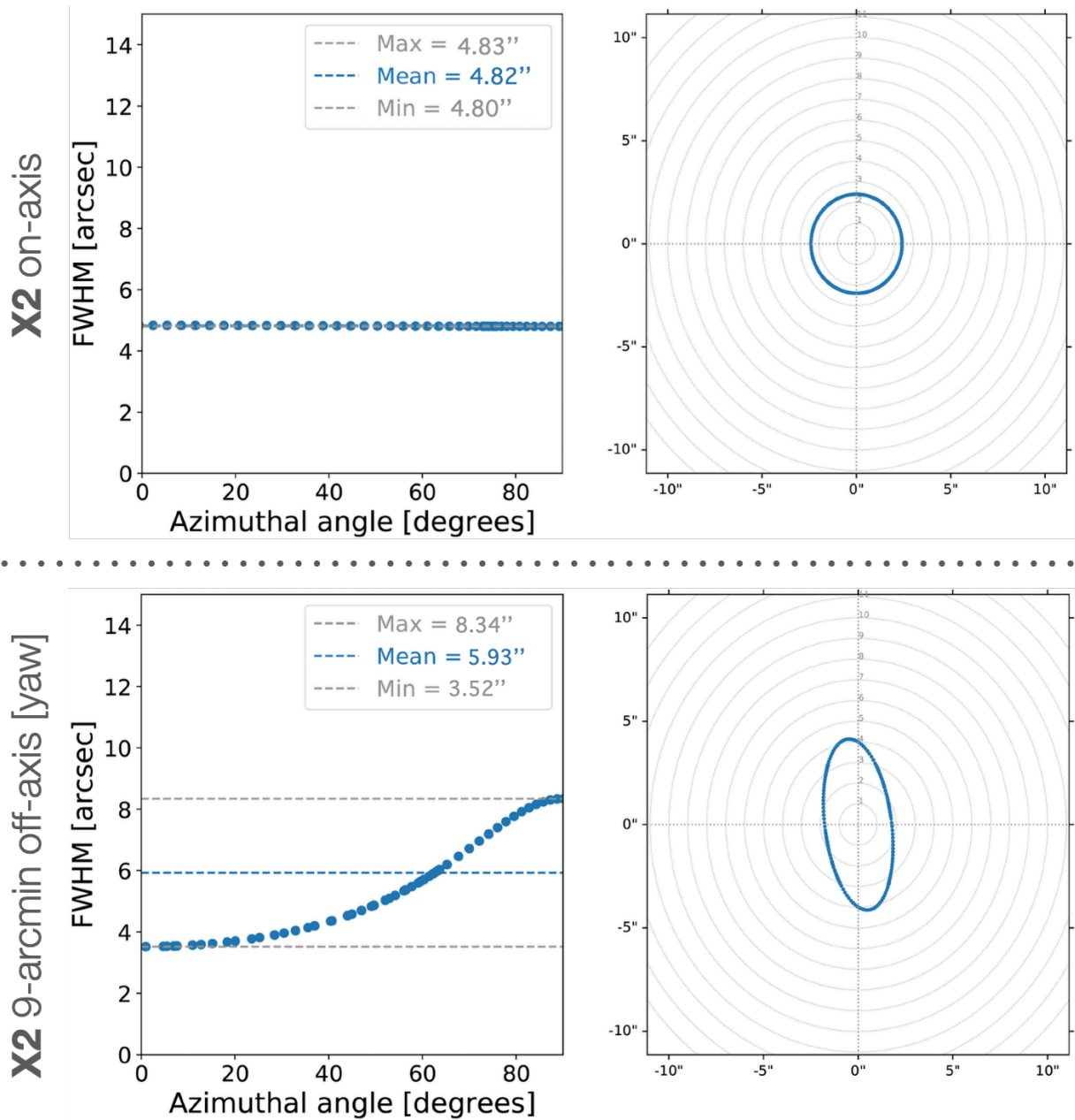
Figure 4.9: PSF full width at half maximum (FWHM) as a function of the azimuth angle. The top (bottom) two panels correspond to the on-axis (9 arcmin off-axis) PSF of the X2 optics module. The azimuth angle in the plots on the left is limited to a single quadrant that ranges from where the FWHM is minimum to where it gets its maximum value (the other three quadrants are redundant).
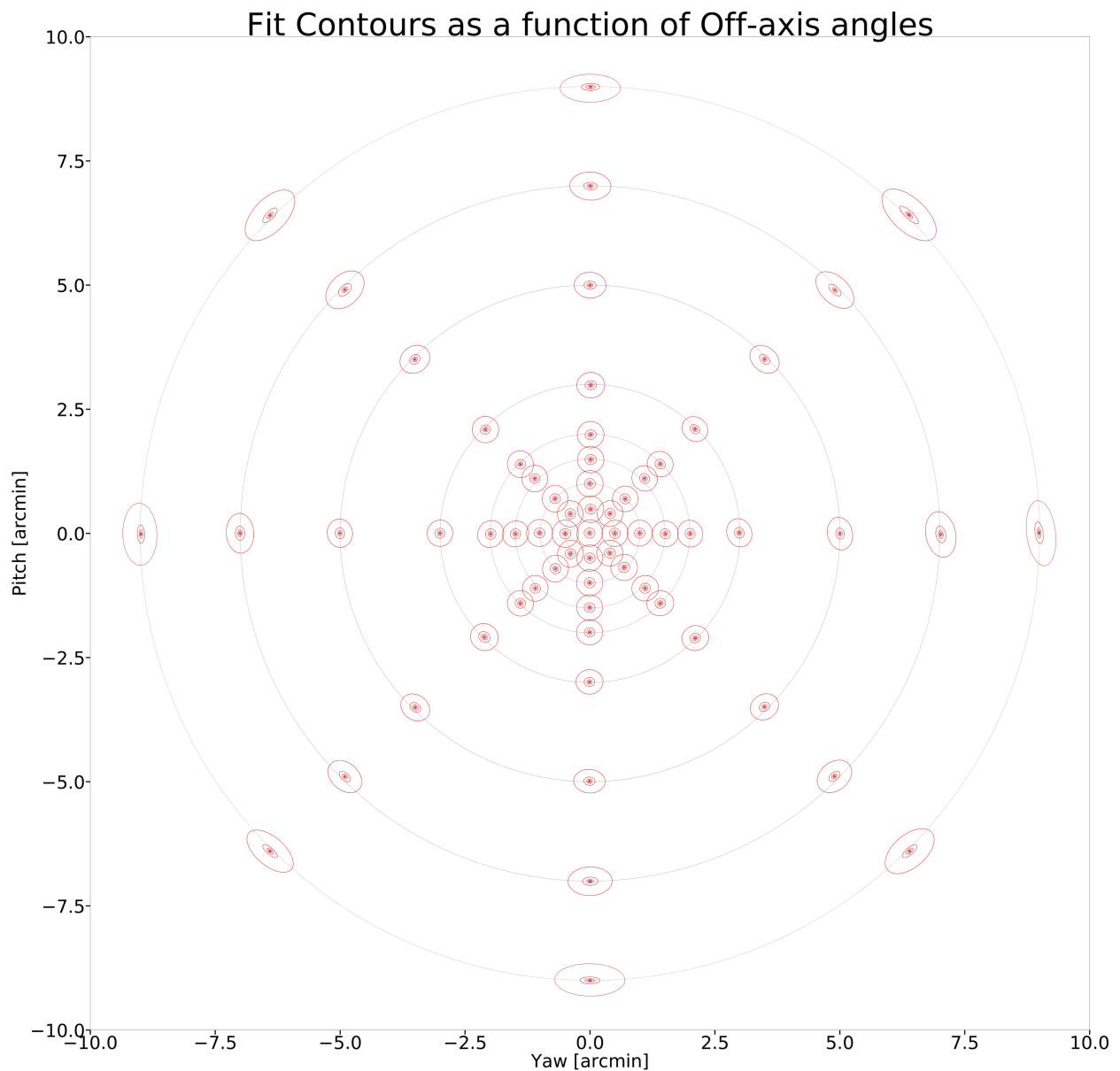
Figure 4.10: Fitted PSF (three two-dimensional Gaussians) for a range of off-axis sources moved in pitch and yaw (for the X2 optics module). Each PSF is displayed as red contours of 1%, 10%, 25%, and 50% of the maximum amplitude. Note that the PSF gets squeezed (stretched) in the direction of (perpendicular to) the off-axis angle. Despite the slight tilting of the red contours along the major axis at 0∘ (probably due to a systematic shift during calibrations), the PSF shows a clear tendency to be symmetric on the azimuth angle.

These two values (min and max), together with the means, show the general tendency of the PSF broadening as a function of the off-axis angle.
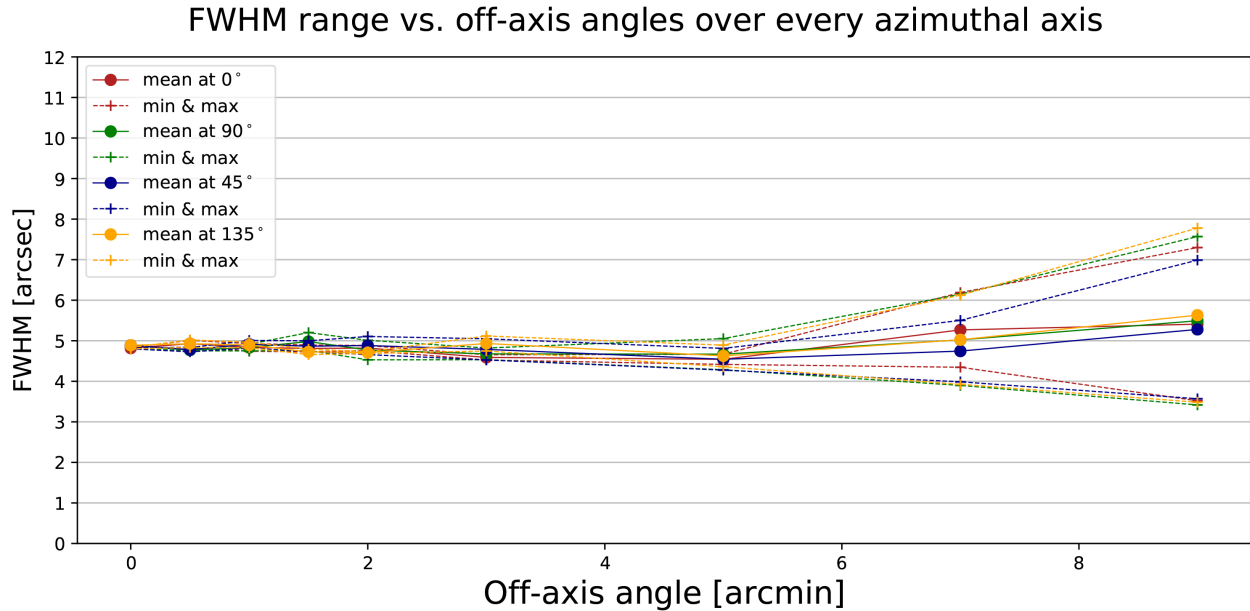
Figure 4.11:   Average (solid lines) and maximum/minimum (dashed lines) FWHMs as a function of the off-axis angle along four azimuthal axes (0°, 45°, 90°, and 135°, differentiate by the colors red, green, blue, yellow, respectively). Note that the four colored groups of curves present a similar tendency: round PSFs on-axis and stretched, not longer symmetric PSFs for off-axis sources. This tendency supports the expected azimuthal symmetry performance of any FOXSI optics modules. In particular, the results displayed in this figure correspond to calibration data taken using the X2 optics module.

4.4.2   Half power diameter

The half-power diameter (HPD), also known as the half energy width (HEW), is the angular diameter of the optics PSF containing half of the flux for a given energy. The primary method to measure the HPD of the FOXSI optics consisted of using pinholes of various diameters (0.05, 0.10, 0.23, 0.38, 0.47, 1.00, and 3.00 mm) in front of the Amptek XR-100T CZT single-pixel sensor. Glesener (2012), in chapter 7, shows the results of these HPD measurements for optics X0, X1, X2, X3, X4, X5, and X6. The on-axis values for these optics modules are 27.31, 26.26, 26.59, 28.28, 25.61, 25.40, and 30.09 arcsec, respectively.

There is an alternative way of estimating the HPD. Using the PSF image captured with the Andor CCD camera, one can numerically determine the circle's diameter (with center at the max of the PSF), which encompasses half of the total flux of PSF. The results of
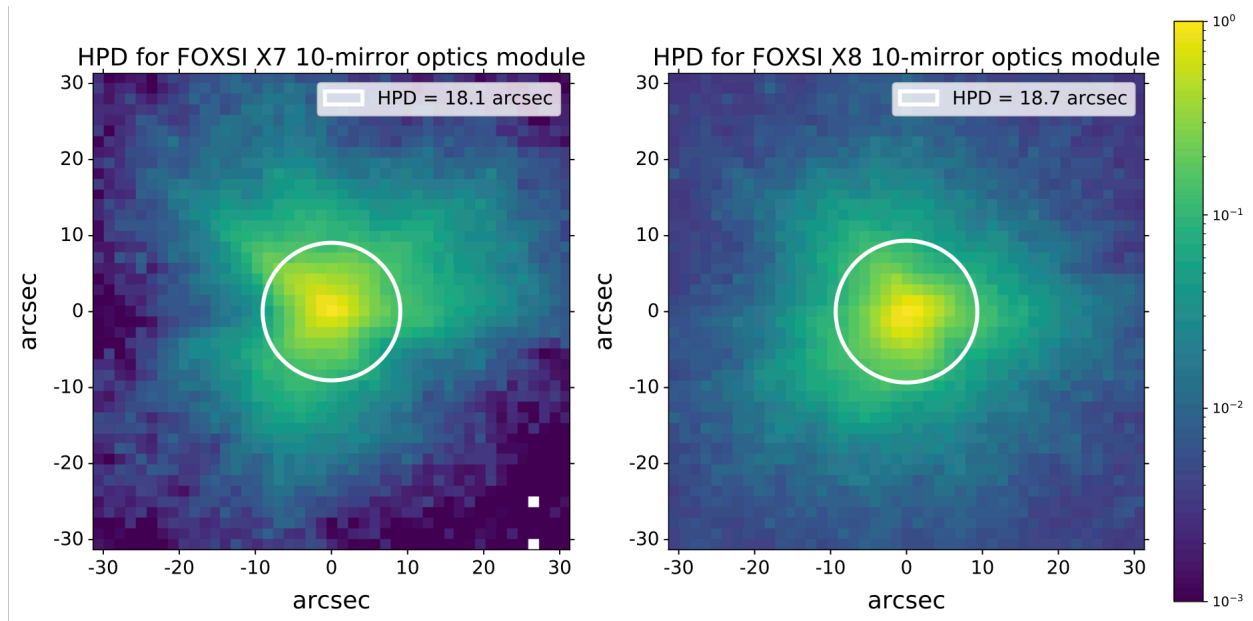
Figure 4.12:   Half power diameter (HPD) for the **new** optics modules X7 and X8 (both are 10-mirror modules). The white circles have diameters equal to the HPDs, encompassing half of the total PSF flux. The HPDs of these two optics modules are 18.1 and 18.7 arcsec, respectively. The HPD improvement of these two optics modules ($\sim$ 30%) is most likely due to a new co-alignment procedure implemented at the MSFC when nesting together the mirrors in a module. An improved version of this co-aligning protocol will be one that the MSFC will implement when assembling the new optics module that will fly as part of the FOXSI-4 sounding rocket payload.

applying this procedure over the on-axis PSF of X7 and X8 are shown in Figure 4.12. The white circle diameters in Figure 4.12 correspond to the HPD for each case. To derivate such a diameter, we implement the following procedure. First, we identify the pixel coordinates with the maximum flux, (x_{max}, y_{max}), on the CCD data, previously corrected by darks and normalized to the maximum value. Next, we run a script that centers a circle of radius r to (x_{max}, y_{max}) and computes the enclosed flux (power). The HPD corresponds to two times r when the enclosed flux in the circle is half the maximum power. For the optics modules X7 and X8 (see Figure 4.12), the computed HPDs are 18.1 arcsec and 18.7 arcsec, respectively. The average 32% improvement of these new optics modules HPDs compared with the older modules (X0, X1, X2, X3, X4, X5, and X6) is most probably due to a new method being implemented for co-aligning the Wolter-I mirrors when assembling a module. The mandrels, electroforming, and coating processes were identical between X7/X8 and the previous modules. So we discard any surface roughness effect on the HPD improvement of the new optics modules. The new protocol that the team at MSFC use for mirror alignment

is based on minimizing a parameter ΔR that characterizes the bending of the shell over the length. This minimization is achieved by measuring errors in the paraboloid/hyperboloid intersection angle at a particular azimuth. At some azimuth values, the angle is above nominal and some below nominal, contributing to the PSF broadening. The Wolter-I shells all have some inherent non-roundness. The team at MSFC adjusts the alignment until that non-roundness is the same at the top, middle, and bottom of every shell in an optics module. This procedure minimizes ΔR, centering the shells with respect to one another.

4.4.3 Remarks

The FWHM and HPD are complementary quantities to assess the performance of focusing X-ray telescopes (e.g., O'Dell et al., 2010). The finer the HPD, the better the optics performance at detecting and measuring the flux from isolated faint unresolved sources. This feature is crucial for non-solar astrophysical objects, which are point-like sources. If the HPD is low, the probability of having a background event (not associated with an on-axis source) is tiny. The HPD compactness of focusing X-ray telescopes is what makes them more sensitive than their non-focusing counterparts. Most of the flux is concentrated in a compact region of the focal plane. For solar applications, having an X-ray focusing telescope with a small HPD enables the search for the faintest sources of coronal X-rays, e.g., small explosive events that emit at these high energies. Wolter-I mirrors have a PSF with two components: a very intense compact core and broad, less intense wings. This peak shape causes the PSF to have a very steep cusp resulting in a small ("very good") FWHM. For grazing incident mirrors, the FWHM is smaller but encompasses little power. However, the FWHM usually contains enough intensity to be the limit over which two point sources are discernible from one another. In solar applications, flare hard X-ray footpoints or looptop sources can be separated if their distances exceed the FWHM. The FWHM also sets the angular resolution limit to resolve source shapes and forms. For the FOXSI sounding rocket experiment, the FWHM angular limit is essential when studying compact sources, e.g., flares and microflares. The HPD sets its high sensitivity to detect the faintest coronal hard X-rays.

Chapter 5

Use of a ray-tracing simulation to characterize ghost rays in the FOXSI rocket experiment

Imaging X-rays by direct focusing offers greater sensitivity and a higher dynamic range compared to techniques based on indirect imaging. The Focusing Optics X-ray Solar Imager (FOXSI) is a sounding rocket payload that uses seven sets of nested Wolter-I figured mirrors to observe the Sun in hard X-rays through direct focusing. Characterizing the performance of these optics is critical to optimize their performance and to understand their resulting data. In this paper, we present a ray-tracing simulation we created and developed to study Wolter-I X-ray mirrors. We validated the accuracy of the ray-tracing simulation by modeling the FOXSI rocket optics. We found satisfactory agreements between the simulation predictions and laboratory data measured on the optics. We used the ray-tracing simulation to characterize a background pattern of singly reflected rays (i.e., ghost rays) generated by photons at certain incident angles reflecting on only one of a two-segment Wolter-I figure and still reaching the focal plane. We used the results of the ray-tracing simulation to understand, and to formulate a set of strategies that can be used to mitigate, the impact of ghost rays on the FOXSI optical modules. These strategies include the optimization of aperture plates placed at the entrance and exit of the smallest Wolter-I mirror used in FOXSI, a honeycomb type collimator, and a wedge absorber placed at the telescope aperture. The ray-tracing simulation proved to be a reliable set of tools to study Wolter-I X-ray optics. It can be used in many applications, including astrophysics, material sciences, and medical imaging. My contributions to this work are described in Buitrago-Casas et al. (2017b), Musset et al. (2019), and Buitrago-Casas et al. (2020).

5.1 Introduction

Since first introduced in 1950 Wolter, 1950, Wolter-I-figured grazing incidence X-ray telescopes have been extensively used in a variety of areas such as synchrotron accelerators, nuclear physics, astrophysics, and space physics (e.g. Cash, 2002; Ogasaka et al., 2008; Mildner et al., 2011; Ferreira et al., 2013). The Wolter-I geometry consists of a combination of two grazing-incidence mirror segments, a paraboloid primary mirror followed by a hyperboloid secondary reflector, referred to as a mirror shell. Frequently, to build up effective area, many individual mirror shells with different diameters are nested together to form a telescope module. On-axis rays which reflect off both mirrors are brought to a focus to form an image on the focal plane. There exists the possibility though, that rays from off-axis sources may reflect only on a single surface and reach the focal plane. These single-reflecting rays are frequently referred to as stray light, or ghost rays (see Figure 5.1) Werner, 1977.

Ghost rays are generally not an issue when observing isolated on-axis point sources since there are then no off-axis sources. This is frequently the case for astrophysical sources; most X-ray sources are far enough away from us that they are point sources and are far enough apart (many arcmin) from each other that they can be considered isolated. However, when observing the Sun, whose angular diameter is ~0.5 deg, it is possible to have multiple bright X-ray sources simultaneously emitting within a relatively small angular extent on the sky. Some of these sources can be off-axis when pointing at a target of interest and can generate ghost rays which may obscure the emission from the primary target, deteriorating the performance of a solar telescope. Previous missions have minimized ghost rays by, for instance, tightly packing and nesting the mirror shells to block the paths of ghost rays as in the case of the Nuclear Spectroscopic Telescope Array (*NuSTAR*) Madsen et al., 2017, through a set of concentric circular sieves at the telescope aperture, in the case of Simbol-X Cusumano et al., 2007, or by using a pre-collimator as described by Spiga (2016).

5.2 The `foxsisim` ray-tracing Simulation

In order to verify and validate the properties of grazing-incidence optics and ghost-ray mitigation strategies, we created and optimized a ray-tracing simulation capability. This tool is referred to as `foxsisim`, though it is generic and can be used for many different grazing-incidence configurations. Written in Python, the source code is open source and available on Github[1](Christe et al., 2019). The software is provided as a Python package with documentation and also provides a simple graphical user interface. The `foxsisim` package provides a class-based approach to ray-tracing. Figure 5.2 shows a flow diagram representing the functional structure of `foxsisim`.

The `Module` class uses a `Surface` subclass, which represents any optical surface with

---

[1]`https://github.com/foxsi/foxsi-optics-sim`
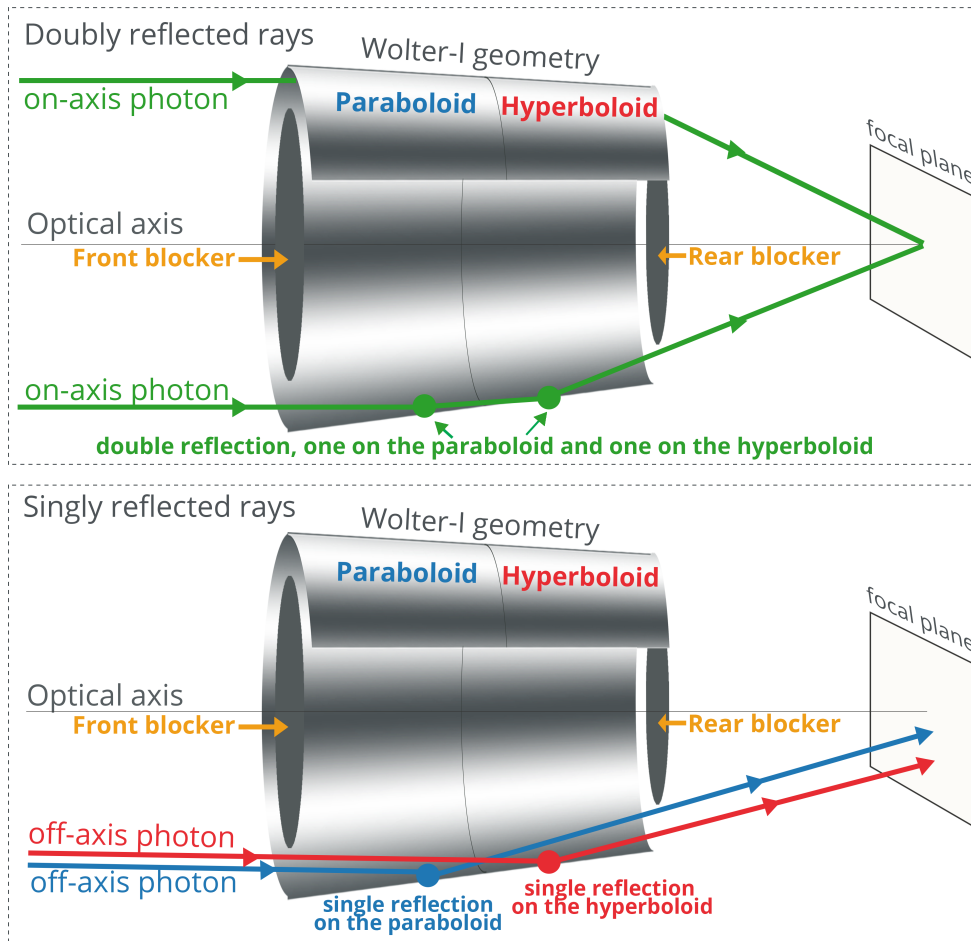
Figure 5.1:   A Schematic of a Wolter-I monolithic mirror shell with the parabolic and
hyperbolic reflecting surfaces showing the difference between on-axis rays (green) that reflect
on both mirror surfaces and those off-axis rays (red and blue) that only reflect off of a single
mirror surface. The optical axis is depicted as a perpendicular line to the focal plane that
goes through the center of the optics. In the **top** panel, on-axis photons reflect first on the
paraboloid segment then on the hyperboloid section and come to a focus on the focal plane.
These are referred to as doubly reflected focused rays. Blockers are primarily used (front
and rear indicated by the yellow arrows) to block rays which would go straight through the
module without reflecting off either surface and reach the focal plane. In the **bottom** panel,
Singly reflected rays coming from off-axis angles interact only with a single mirror surface
(either the paraboloid, blue rays, or hyperboloid, red rays, segment) and can make it to
the focal plane. These singly-reflected rays are frequently referred to as ghost rays because
they can lead to unfocused patterns on the focal plane. The blockers can also reduce the
amount of ghost rays by limiting the angles accessible by off-axis rays to reflect off of mirror
segments.
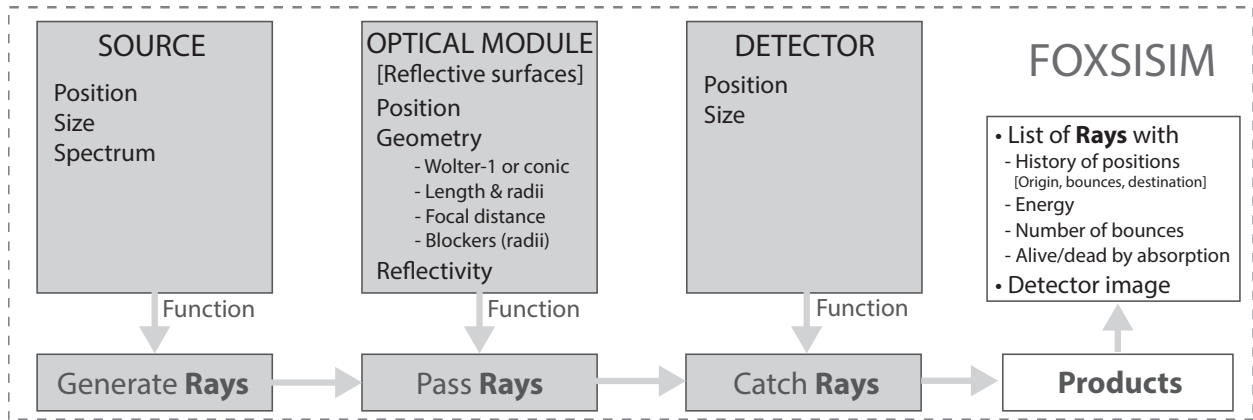
Figure 5.2: The flow diagram for the functional structure of the `foxsisim` ray-tracing simulation tool. The code has three basic classes: `Source`, the source of x-rays, optical `Module` (a telescope module), and a `Detector`. For each component in the simulation, a set of initialization parameters need to be defined. Some examples are shown here which include position, size, spectrum of a source or reflectivity of an optical surface. `Source` implements a function to generate a list of random **rays**. The `pass rays` function defined by `Module` computes the interactions of rays with the module. Finally, the `Detector` class implements a `catch` function which computes which rays land on the detector. The final output is a list of all rays with keywords defining their position histories, their energy, their number of reflections, and a tag indicating whether or not a ray was absorbed on a non-reflecting surface.

which rays may interact. Such a surface is generally represented by a parametric equation in 3 dimensional space. The `SegmentH` and `SegmentP` are subclasses of `Surface` and represent hyperboloid and parabolic mirror segments respectively. A `Shell` class holds both reflecting segments and therefore represents a telescope shell. Finally a full telescope module is potentially composed of many shells and is represented by a `Module` class. An X-ray source is implemented in the `Source` class which implements both isotropic sources as well as sources of perfectly parallel beams. The geometric rays which represent the X-rays themselves are implemented by the `Ray` class. A casting function finds the solution of rays reflecting off of or being stopped by surfaces (reflecting or non-reflective). The spectral properties of the telescope are computed through its reflectivity, which depends on the incoming ray angle. `foxsisim` uses Iridium surfaces with 10Å roughness to compute reflectivities. Finally, a `Detector` class is used to capture the rays at a particular point in space and create an image. The current implementation does not consider any random scattering off of surfaces, detector efficiency, nor prioritize speed, though a future release is planned to address these issues.

5.3 The FOXSI sounding rocket payload and ghost rays

FOXSI's science objectives require high sensitivity and dynamic range observations of the Sun; therefore understanding and mitigating ghost rays is essential. In order to characterize the patterns generated by off-axis sources, a number of measurements were performed on individual telescope modules at the NASA Marshall Stray Light Facility (SLF). The SLF consists of a 100 m evacuated beam line. An optics module is placed inside an evacuated chamber at one end of the facility. Two stages enable the optic to be rotated with a precision down to $\sim$ 3.5 arcsecs. The optics module is then illuminated by a Trufocus 50 keV X-ray generator with a molybdenum target located at the other end of the facility. A cooled Andor CCD iKon-L camera is located at the focal plane. The Andor CCD camera consists of a 204y8$\times$2048 array of pixels, with a pixel pitch of 13.5 microns. This pitch translates to a resolution of 1.3 arcseconds and a measurement field of view (FOV) of 44.4$\times$44.4 arcminutes, much larger than the FOXSI detector field of view. Since the X-ray source cannot be moved, the optic is rotated to simulate rays coming from off-axis positions.

Figure 5.3 shows an example of a ghost ray pattern from an off-axis X-ray source 30 arcmin away from the optical axis. Panel A shows an actual measurement taken at the SLF with the Andor CCD camera. The gray box shows the limited FOXSI field of view with the optical axis (orange cross) at its center. The position of the off-axis source is shown by an orange X mark. A complex ghost ray pattern was measured which is a result of singly-reflected rays from both the hyperboloid and paraboloid mirror shell segments. In this case this is a 10-shell telescope. Each shell creates an individual ring pattern which extends onto the FOXSI field of view. Notches in the rings are caused by the spider spokes which hold the shells seen in Figure 3.9.

Panel B in Figure 5.3 shows the results of a `foxsisim` ray-tracing simulation which compare well with the measured ghost ray pattern. The simulated image is color-coded to show rays that are doubly-reflected (green), reflected only by the hyperbolic segments (red), and reflected only by the parabolic segments (blue). The major features in the ghost ray patterns are rings, one for each of the ten mirror shells. The vertical gap in the rings are caused by one of the spider spokes (seen in Figure 3.9) which partially block the shells. These are not included in the simulation. The blockers are included in the simulation and block some of the ghost rays. A first order quantifiable comparison of the lab data with the simulation was done by measuring the distance from the source location to each of the rings in the patterns. Such comparison shows differences always under $\sim$ 3% for all the rings of the lab data compared to the ones for the simulation.
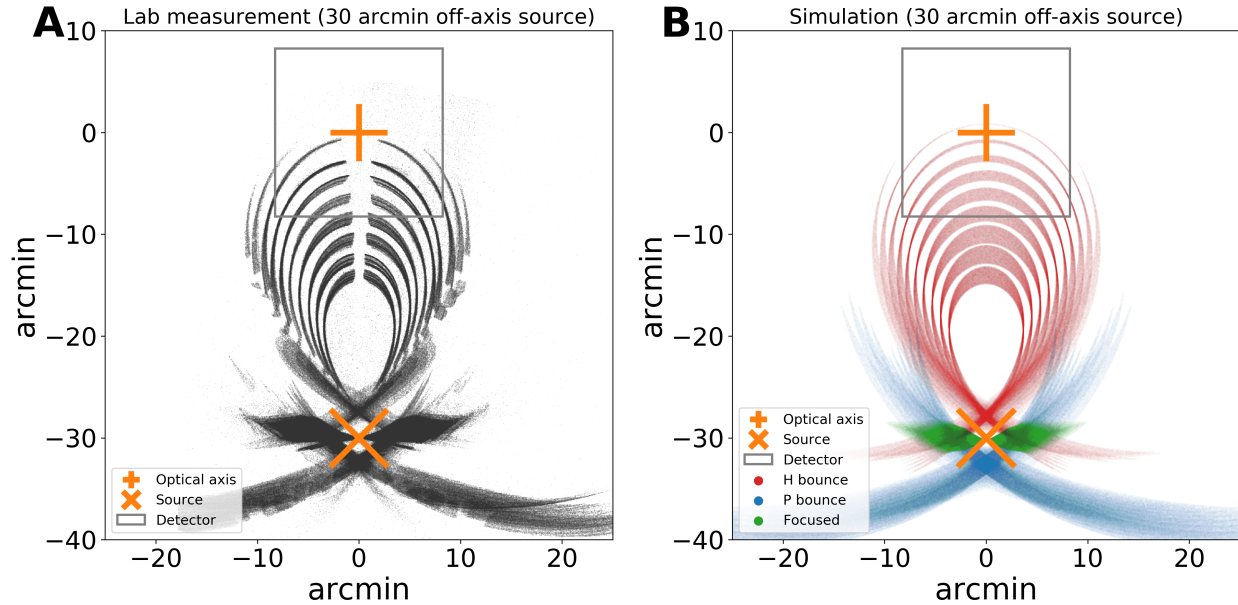
Figure 5.3: The ghost ray image from an X-ray source 30 arcmin off-axis for a 10-shell optics module. In both panels, the grey square represents the on-axis FOXSI field of view. At the center, the optical axis is shown as the orange cross. The location of the off-axis source is denoted by the orange X. Panel **A**: A measured ghost ray image produced by a 10-shell optics module for a source located 30 arcmin off-axis. Data were acquired at the NASA MSFC 104 m Stray Light Facility using a 2048 by 2048 pixel CCD detector placed at the focal plane. Panel **B**: Simulated ghost rays produced by the `foxsisim` ray-tracing code. The green portion of the pattern corresponds to doubly-reflected rays while the blue and red areas are the patterns generated by the paraboloid and the hyperboloid segments, respectively.

5.4 Use of `foxsisim` to study FOXSI ghost-rays

5.4.1 Ghost rays as function of off-axis angle

With the simulation validated and in order to gain a better intuition for how ghost rays evolve as a function of off-axis angle, the simulation was run for a variety of off-axis angles. The results are shown in Figure 5.5 for off-axis angles 0, 4, 8, 12, 16, 20, 24, 28, and 32 arcmin away from the optical axis. It can be seen that as soon as the source is moved off-axis, a ghost-ray pattern emerges but at large angular distances away from the focal plane. These rays do not (yet) infringe on the detectors plane. As the source moves further off-axis, these ghost rays change shape and eventually begin to be seen on the focal plane between 12 and 16 arcmin. A more precise analysis shows that the threshold for ghost rays to impact
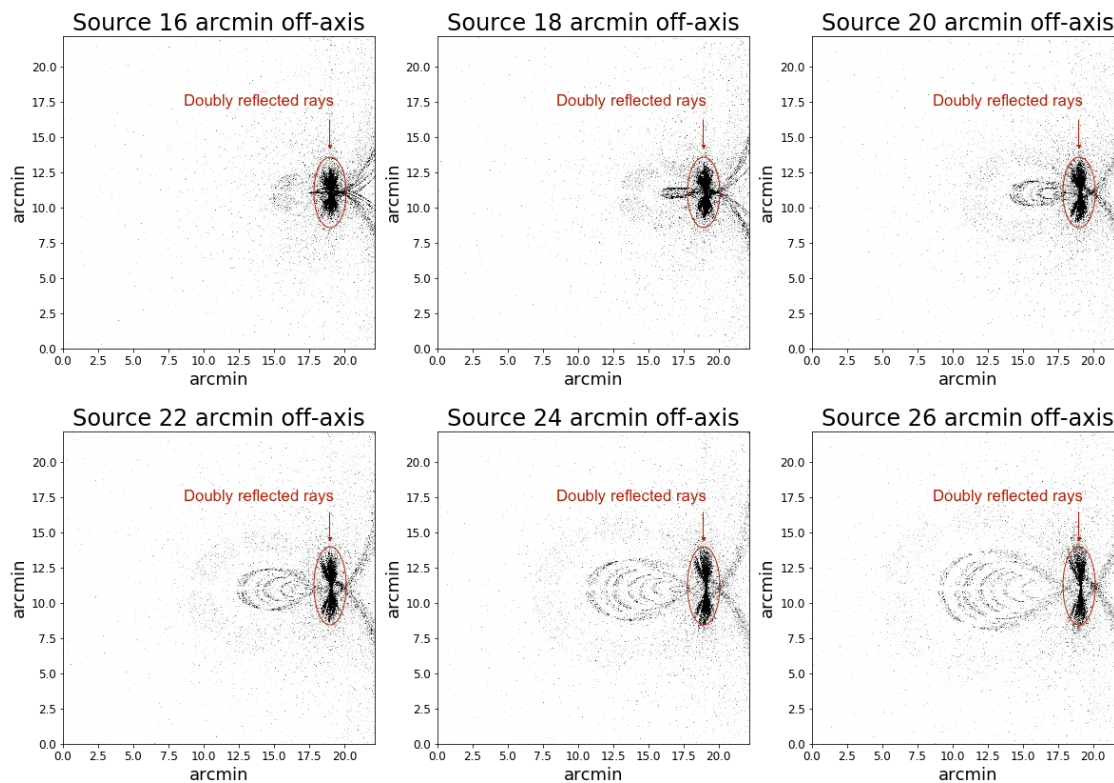
Figure 5.4:   Measured point spread function for a real 7-shell FOXSI optical module for an
X-ray source located at off-axis angles ranging from 16 to 26 arcminutes. The experiment
was performed at the 100-meter-long SLF at the NASA-MSFC using a Trufocus 50 kV X-ray
head, with a Titanium target that generates X-rays with nominal energies up to 50 keV.
The intense patterns enclosed in red circles are doubly reflected rays. All other rays outside
the red circles belong to the singly reflected background. The scale is given in arcminutes
for both X and Y to understand the spatial size of the patterns, but the location of the [0,0]
origin is arbitrary.

the detect plane is at 13 arcmin off-axis for a 10-mirror optics module, and 18 arcmin off-
axis for a 7-mirror optics module. This difference is due to the fact that most ghost rays
originate from the inner most mirrors of the optics. A 10-mirror optics module includes
three additional smaller mirrors to the standard configuration of a standard 7-mirror optics
module, as described in Christe et al. (2016b).

Figure 5.5 matches very well what we have seen in laboratory measurements (see Figure
5.4).
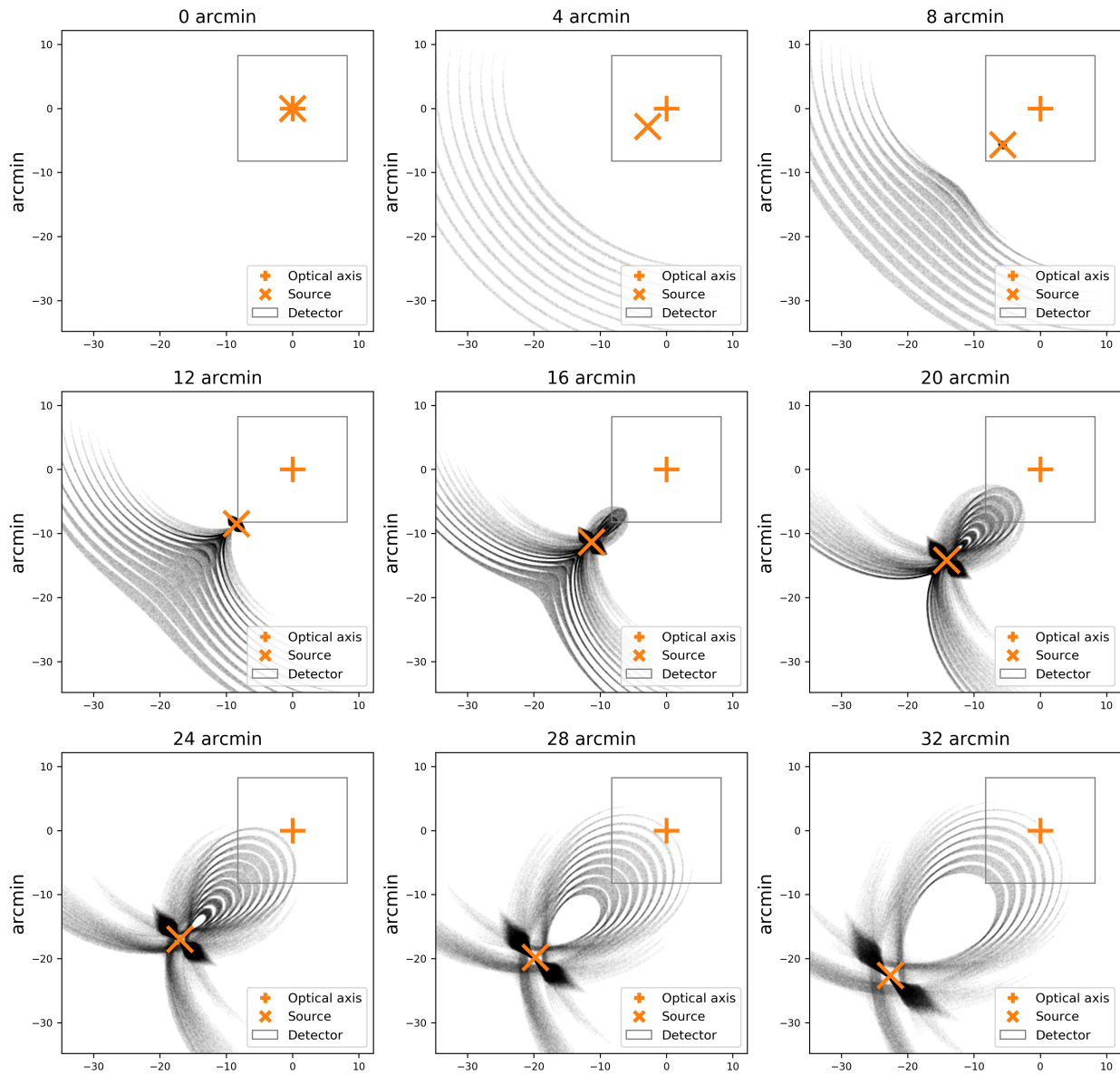
Figure 5.5: Simulated ghost ray images for a 10-shell module as a function of off-axis angle for a source at infinity from 0 to 32 arcmin. The gray square shows the field of view of the FOXSI detectors. The orange symbols show the optical axis and source position. As the source moves away from the optical axis ghost ray patterns appear, at first outside of the detector-bounded field of view. Between 12 and 16 arcmin, these rays begin to infringe on the detector area. The detector-integrated ghost ray flux contamination continues to increase as the pattern increases in size and complexity.

5.4.2 Ghost rays energy dependence

The reflectivity of a Wolter-I mirror depends on the angle of incidence, the surface material, and roughness of the mirror Attwood et al., 2017. The FOXSI optics uses electroformed nickel mirrors coated with a thin layer of iridium. For the simulation, we use the theoretical reflectivity of Iridium with a surface roughness of 10Å^2. Compared to focused rays, ghost rays are generated from rays at large angles yet they are only reflected once so that it is not straightforward to understand their energy dependence. To investigate this, we simulated the energy response of ghost rays.

Figure 5.6 shows the simulated energy dependence of the effective area with energy for doubly- and singly- reflected rays generated by an on-axis source, an off-axis source at 20 arcmin (solid lines), and an off-axis source at 28 arcmin (dashed lines) on a 10-mirror optics integrated over the detector field of view. The input spectrum is assumed to be constant from 0 to 30 keV. On the left panel of figure 5.6, the y-axis is normalized to focused flux at 1 keV (green curve), and it is plotted in log scale. For both panels, the solid blue (red) lines correspond to the paraboloid (hyperboloid) ghost rays reaching the detector area coming from a 20 arcmin off-axis source. The dashed red line corresponds to hyperboloid ghost rays coming from a 28 arcmin off-axis source. The left panel shows that ghost ray fluxes are generally two orders of magnitude smaller than the flux from an on-axis source. On the right, the fluxes are all normalized to each other to better compare the energy dependence. From this panel, it is clear that , above $\sim$6 keV, the ghost ray flux falls off significantly faster than for focused rays. This behavior is even more dramatic for those rays that singly reflect off of the paraboloid. This simulation allow us to conclude that ghost rays provide only a small contribution to the background and are negligible for source-dominated observations. Furthermore their contribution to the background is reduced at high energies.

An analog analysis of ghost rays dependence on off-axis angles and energy, but scaled up to a satellite mission, is presented in appendix 5.7 of this paper.

5.5 Ghost Ray Mitigation Strategies

In this discussion we explore a number of different strategies to reduce the intensity of ghost rays.

5.5.1 Circular Blockers

The concept of circular blockers has already been introduced in section 5.3. These blockers located at the entrance aperture and exit primarily stop X-rays from traveling through the center of the optics. The back aperture blocker also serves to remove some ghost rays. In this section, we investigate the optimization of the size of these blockers, both front and rear. For

---

[2]http://henke.lbl.gov/optical_constants/
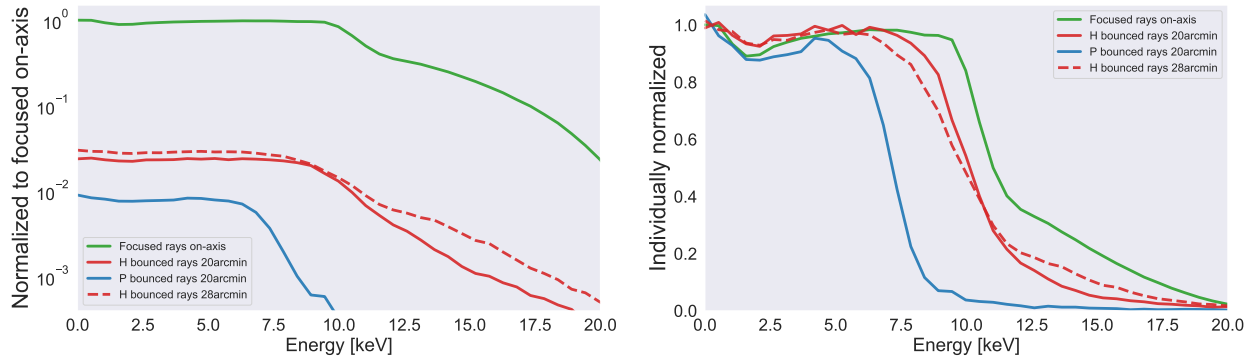
Figure 5.6: The simulated energy response for a point source with a flat spectrum from 0 to 30 keV integrated over the detector field of view from an on-axis (green solid line), 20 arcmin (solid red and blue lines), and 28 arcmin (dashed red line) off-axis. Blue and red lines represent singly-reflected rays from the paraboloid and hyperboloid segment, respectively. *Left.* Detector-integrated fluxes normalized to the focused on-axis (solid green line) at 1 keV. The singly-reflected flux intensity is found to be two orders of magnitude smaller than the focused intensity. *Right.* The same curves from the left but normalized to each other to better compare the energy dependence. It can be seen that the ghost ray intensity falls off significantly faster than the focused rays. This is most pronounced for those singly-reflected rays from the paraboloid segment.

optimized blockers, fewer ghost rays reflected from the hyperboloid segments make it onto the detector. If not correctly sized, small blockers can allow some paraboloid reflected ghost rays to reach the detector area. On the other hand, if the blockers are too large, the focused rays from the smallest mirror are blocked. Optimizing their design is crucial to improve the overall performance of the telescope.

Figure 5.7 shows the impact of different front and rear blocker sizes on a 10-mirror optics module, as a function of the off-axis source location. The y-axis in all plots shows the intensity of rays within the detector, normalized to the maximum flux of doubly reflected rays, i.e. when the sources is on-axis. The top panels show the effect on the focused rays (green); the panels on the left present the impact of front blocker sizes on focused rays, singly reflected rays from paraboloid segments (blue curves on the top and middle panels), and singly reflected rays from hyperboloid segments (red curves on the top and bottom panels). For all three panels on the left, front blocker radii range among 2.875 cm, 3.0967 cm, 3.1334 cm and 3.1700 cm, while there is no rear blocker. The panel at the top-left displays focused (green) and singly reflected (blue and red) rays together to show the relative flux of ghost rays when compared to focused rays. It is observed that ghost ray fluxes never surpass 35% of the on-axis focused flux.

According to the left panels of figure 5.7, it is clear that the larger the front blocker, the less ghost rays impinge into the detector. However, the larger the front blocker, the larger is the reduction effect on the focused rays. An optimized size must balance reducing singly-reflected rays while having the smallest effect on focused rays. In this case, the best size was found to be **3.0967** cm, and **3.7494** cm radius for a 10-mirror and a 7-mirror optics module, respectively.

The three panels on the right of figure 5.7 assess the effect of the rear blocker on the ghost ray background for the innermost mirror of a 10-mirror optics module. In this case, the front blocker was set to a constant radius of 3.0967 cm (optimized size found for the front blocker). These three panels on the right have an analogous structure to the left panels. For the rear blocker, the best trade-off between reducing ghost rays and minimizing vignetting effects is obtained for a radius of 2.62 cm for a 10-mirror optics. An analogous simulation was run for the innermost mirror of a standard 7-mirror optics (not shown here) leading to a radius of 3.14 cm radius as an optimal parameter for the rear circular blocker.

Blockers with optimal sizes were manufactured and implemented on the FOXSI-3 rocket payload. The effectiveness of this strategy was demonstrated with direct lab measurements shown in Figure 5.9 A, which shows the pattern on the focal plane generated by a 30 arcmin off-axis source shining on a 7-mirror module placed at the NASA Marshall SLF. From Figure 5.9 A it is concluded that ghost rays are highly mitigated within a detector (gray box on the figure) by simply implementing the right blocker sizes. For the third flight of the rocket, all optical modules were upgraded to have optimized blockers, which is now a baseline for FOXSI and should be for future Wolter-I optics.

The `foxsisim` toolkit was extensively utilized before the FOXSI-3 rocket campaign to ascertain efficient methods of mitigating ghost rays. In this section, it was shown that optimizing the front and rear blocker sizes is a simple way to minimize ghost rays on the detectors. Although the blockers substantially reduce ghost rays, this strategy does not eliminate all of the ghost ray background. Two additional strategies to further decrease ghost ray background are discussed next.

5.5.2   Honeycomb collimator

Another method to reduce singly-reflected rays is to collimate rays before they arrive at the entrance aperture. Figures 5.5 and 5.7 show that, for a 10-mirror optics, ghost rays are produced by off-axis sources beyond ∼ 13 arcmin. For a 7-mirror optic only rays beyond ∼ 18 arcmin make it onto the detector due to the larger graze angles. In order to remove these rays a collimator was designed and tested. A photograph of this collimator is shown in Figure 5.9 panel C. This honeycomb collimator was 3D printed and consists of a series of parallel, cylindrical, and uniform holes or channels through which X-rays can pass. The longer and thinner the channels, the smaller the angle of acceptance for X-rays and therefore the greater the collimation. The thickness of the walls of the channels must be large enough
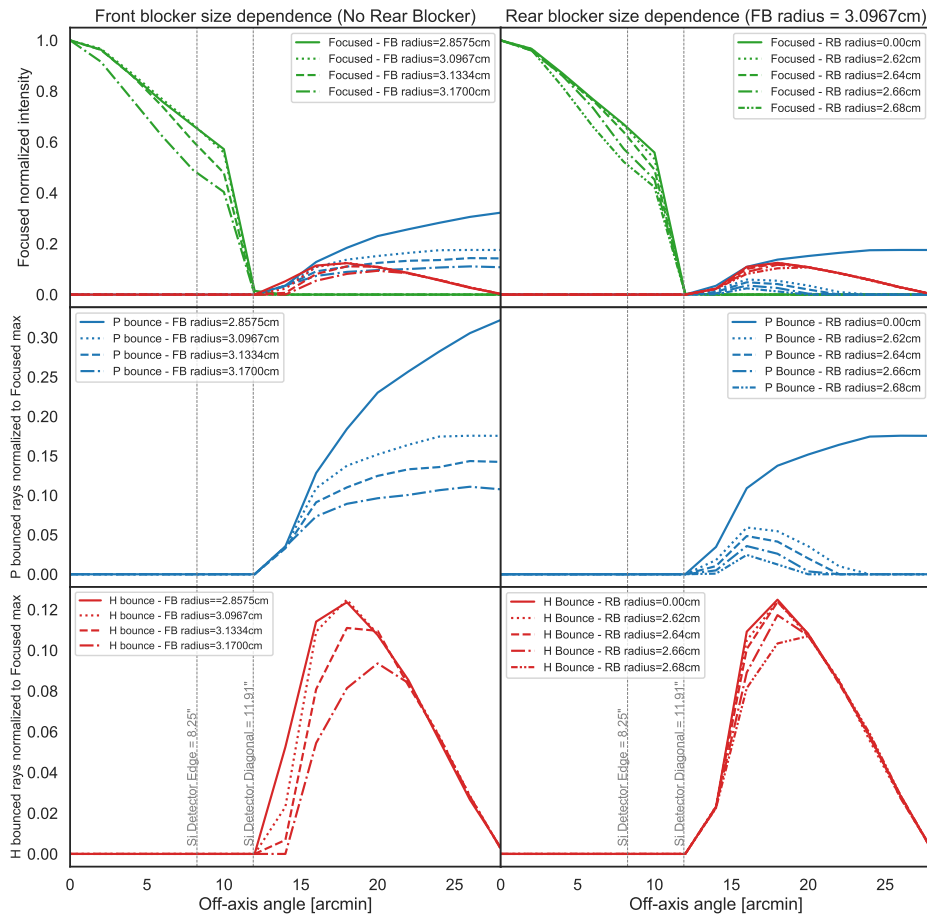
Figure 5.7: Use of `foxsisim` to study the effect that the front (three panels on the left) and the rear (three panels on the right) circular blockers have on focused and ghost rays. The simulation was run for a source at infinity varying its position from on-axis to 28 arcmin off-axis (the horizontal axis of every plot). The simulated optics consisted of a single shell with physical parameters (radii and focal length) of the innermost mirror from a standard 10-shell optic. A standard detector size was used for these simulations (1cm side). We utilized source off-axis positions ranging along a direction defined by the diagonal of such detector. Plots at the top row show focused (green), and ghost rays in blue (red) coming from the paraboloid (hyperboloid) segment. All plots are normalized to the focused flux of an on-axis source. Plots on the second (third) row show singly reflected rays fluxes coming from the paraboloid (hyperboloid) segment. The line style for every curve corresponds to a particular set of blocker radii, as indicated at the legends. The gray dashed vertical lines indicate the minimum (left) and maximum (right) distance from the optical axis to the edge of the squared detector.

stop (absorb) the pertinent X-ray energies (up to ∼20 keV in this case). The thicker the channel walls the larger the reduction of aperture. Since most of the detector-infringing singly- reflected rays come from the inner mirrors, the structure only collimates the four innermost mirrors of a 7-shell optical module, which helped minimize weight. For the large radii mirror shells, less collimation is necessary leading to a reduction in the required channel height at the circumference. The final version of the collimator has a maximum length of 19.5 cm, and 1 mm diameter channels with 120-micron-thick walls between the channels in a hexagonal structure. Further details on the manufacture and dimensions of this collimator can be found in section 3.2 of Buitrago-Casas et al. (2017a).

The effectiveness of the collimator was tested at the MSFC SLF facility. The results can be seen in Figure 5.9 for a collimator optimized for a 7-mirror optic. Panels A and B compare the ghost-rays with and without the collimator for a source 30 arcmin off-axis showing a clear reduction in ghost rays. It can be seen that the collimator removes many ghost rays from the detector. The pay-off is a reduction of focused rays which depends on the open area of the collimator cross-section. The thin outermost ring observed in Figure 5.9 B is due to a narrow gap between the innermost part of the honeycomb structure of the collimator and the front blocker. This gap can easily be removed by adjusting the size of the blockers in future design iteration leading to an image with no ghost rays.

The key parameters that determine the effectiveness of a honeycomb collimator at blocking singly reflected rays are the height, the channel size, and the thickness of the walls between the channels. The thickness of the walls needs to be large enough to stop off-axis rays, and thin enough to reduce the impact on the loss of the on-axis effective area of the telescope. The channel size and height need to be able to geometrically block rays coming from angles greater than a threshold defined by the focal length and radii of the Wolter-I mirrors in a FOXSI optical module. As an example, Figure 5.8 shows the relation among the hole diameter, height, and thickness of the walls required to block any off-axis angle over 13 arcminutes for a FOXSI 10-shell module.

An important limitation of the honeycomb collimator is that this strategy does not block ghost rays near the source for long focal lengths missions (e.g. focal lengths of 10 m or longer).

5.5.3 Bundled fibers in a honeycomb configuration

This solution consists of several cylindrical polycapillary optics bundled together. The fibers are usually tapered to collect X-rays from an X-ray source and focus them to a small spot, but here we use straight cylindrical fibers that ideally do not reflect X-rays. The common application of polycapillary focusing optics is X-ray fluorescence analysis of samples such as circuit boards, alloys, and metals. There are several companies that provide optical fibers for X-rays, but for developing the concept we chose X-ray Optical Systems (XOS). XOS fabricates and distributes polycapillaries for X-rays with energies ranging from 50 eV up to
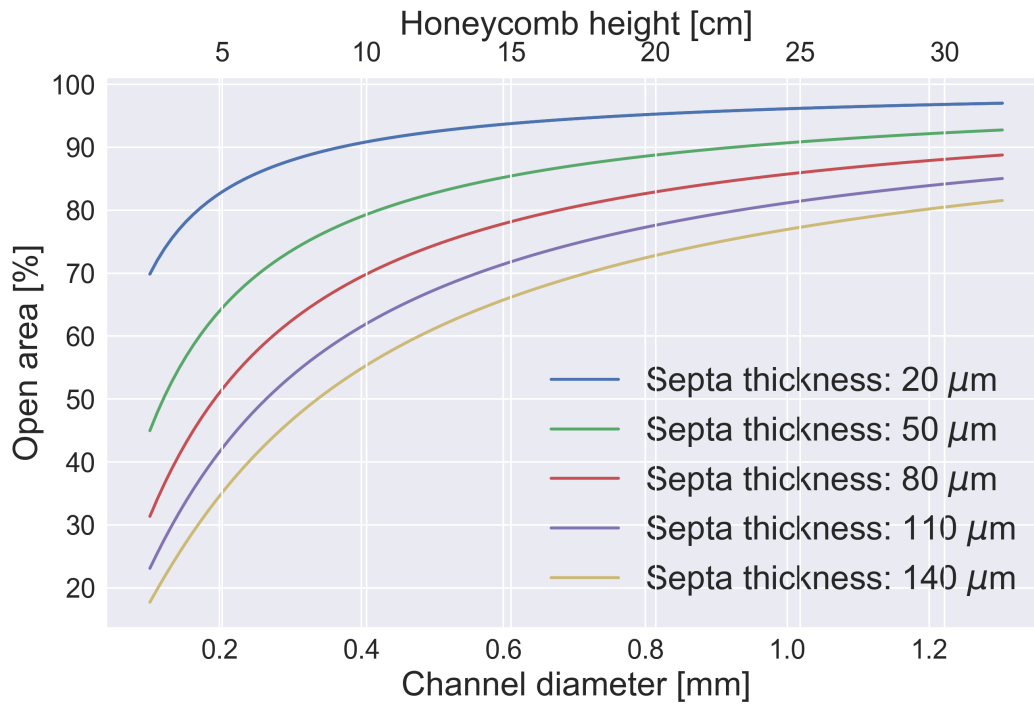
Figure 5.8: Relation between channel size, height and thickness of the walls for a honeycomb collimator designed to block off-axis rays coming from angles over 13 arcminutes for a FOXSI 10-shell optical module.

50 keV.

The wall thickness we chose for the XOS solution, 15μm, allows the collimator to maintain an 80% open area on-axis with a 0.15 mm hole diameter. Since, according to the ray-trace simulation, singly reflected rays come from angles greater than 13 arcminutes for a 10-shell optic (see Figure **??**), a polycapillary with the dimensions described above requires a length of 3.97 cm. Due to the manageable dimensions, geometric consistency along the length of the polycapillaries, lightness, and on-axis open-area, the XOS optical device is an attractive solution for reducing singly reflected X-rays on the FOXSI rocket project and offers a potential technology to be explored and adapted to future satellite missions that use Wolter-I mirrors.

As opposed to typical applications, in which each capillary functions as an optical fiber for X-rays, the FOXSI collimator ideally does not reflect X-rays within each capillary and instead retains the imaging capability of the system. FOXSI also requires a larger structure diameter than typical applications. The FOXSI team and XOS are currently in a design
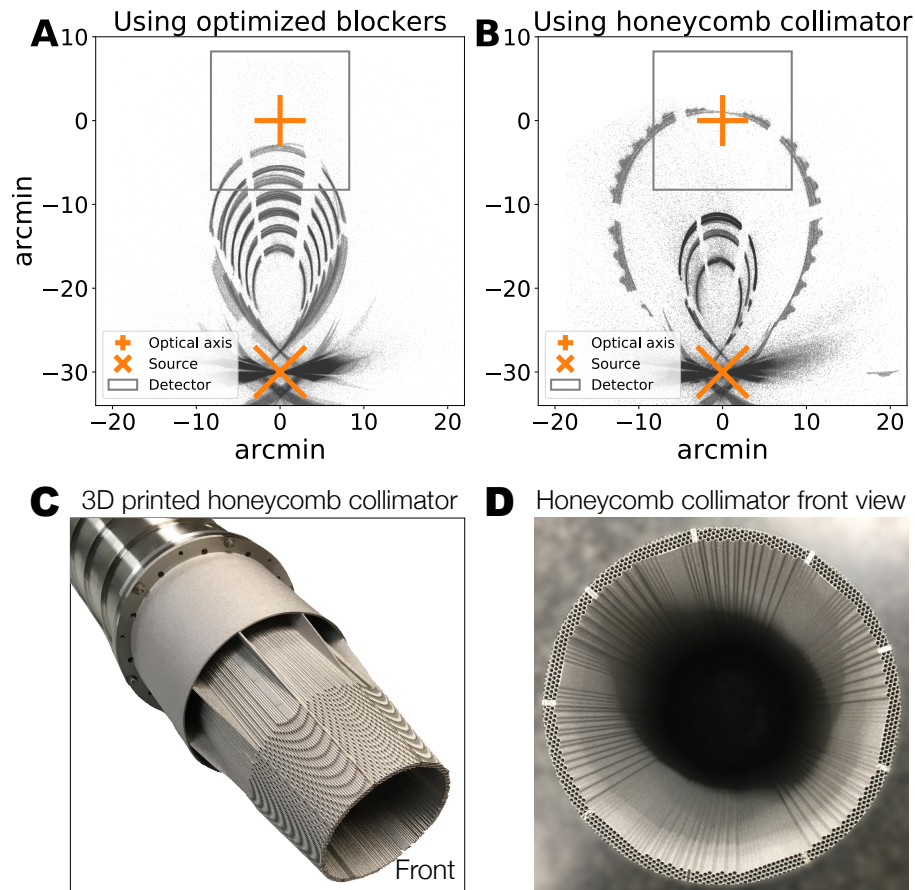
Figure 5.9:   Measured mitigation of ghost rays for a 30 arcmin off-axis X-ray source shining on a 7-mirror module at the NASA Marshall SLF. **A** shows the ghost-rays measurement displayed over the focal plane when optimized blocker sizes are used for the optics module. **B** shows how **by using blockers together with a honeycomb collimator, all ghost rays can be removed**. The thin outer-most ring on the ghost ray pattern is due to X-rays that leak through a narrow gap between the front blocker and the collimator structure. Due to mechanical constraints, we had to use a slightly smaller blocker than the one used on panel A, so that it could be physically attached to the collimator. This gap can easily be reduced to zero to remove all ghost rays from the field of view for future missions. Panels A and B display an orange cross and X mark representing the optical axis and source location, respectively. The gray box shows a detector. **C** presents a picture of the actual honeycomb collimator attached to the entrance of one 7-mirror optics module. **D** shows a head-on view of the collimator and shows the honeycomb structure designed to collimate rays in front of the four innermost mirrors. Every small hexagonal hole has a 1 mm diameter and a wall thickness of 0.12 mm. The honeycomb collimator's length is 20.05 cm, which translates to an aspect ratio of up to 200.
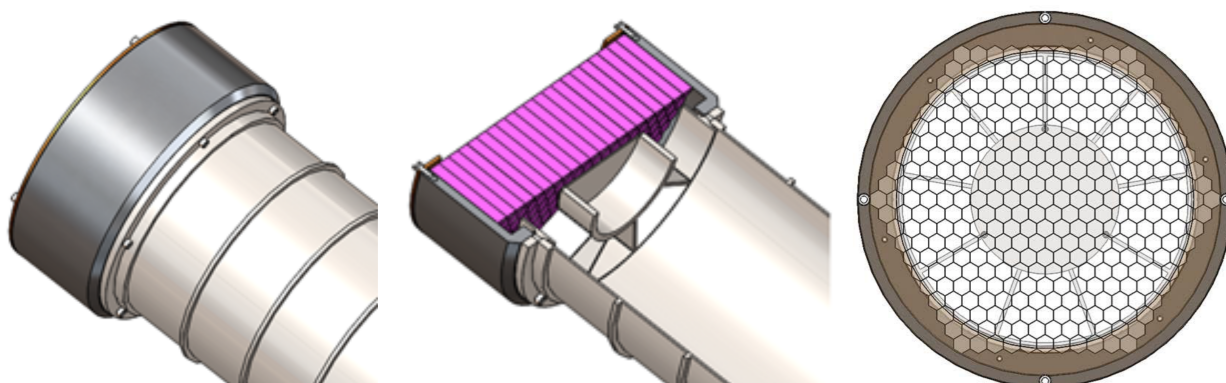
Figure 5.10: XOS polycapillaries. *Left*: Mechanical design of attachment to one of the
FOXSI optical modules. *Center*: Cross-section that shows how many XOS polycapillary
bundles will be bonded together to achieve the required diameter. *Right*: Pupil of one of the
FOXSI telescopes with this kind of collimator at the front.

phase to explore three developments: i) perform etching on sample bundles to confirm our
ability to eliminate reflections within the capillaries; ii) design a process to bond many small
bundles and create the size needed to completely cover a FOXSI telescope aperture; and iii)
design a mount to hold the polycapillaries.

The etching development is still in progress, but the mechanical considerations have been
addressed. XOS has fabricated bundles of capillaries forming cylindrically shaped structures
with a maximum radius of less than one centimeter. To cover the front of one of the FOXSI
telescopes, i.e. a circular cross-section of 5.5 cm radius, several tens of polycapillary bundles
will be bonded together and installed in a mount. The bundling of the polycapillaries is
planned to have a hexagonal shape, with the "corners" oversized compared to the module
interface as shown at the right of Figure 5.10. The FOXSI team at UC Berkeley and XOS
have worked together on the mechanical interface, considering the alignment of the poly-
capillaries with the FOXSI telescope and matching of the thermal expansion coefficient of
the materials. A co-alignment within approximately one arcminute of the optical axis is
required. The collimator mount will be fabricated with 303 Stainless Steel to match the
material used in the optics spider fixture. Details of the mechanical design are shown in
Figure 5.10.

5.5.4 Wedge Absorber

The distribution of singly-reflected rays on the aperture plane suggests another method to
reduce ghost rays. From Figure 5.11 Panel A, it is observed that singly reflected rays from the
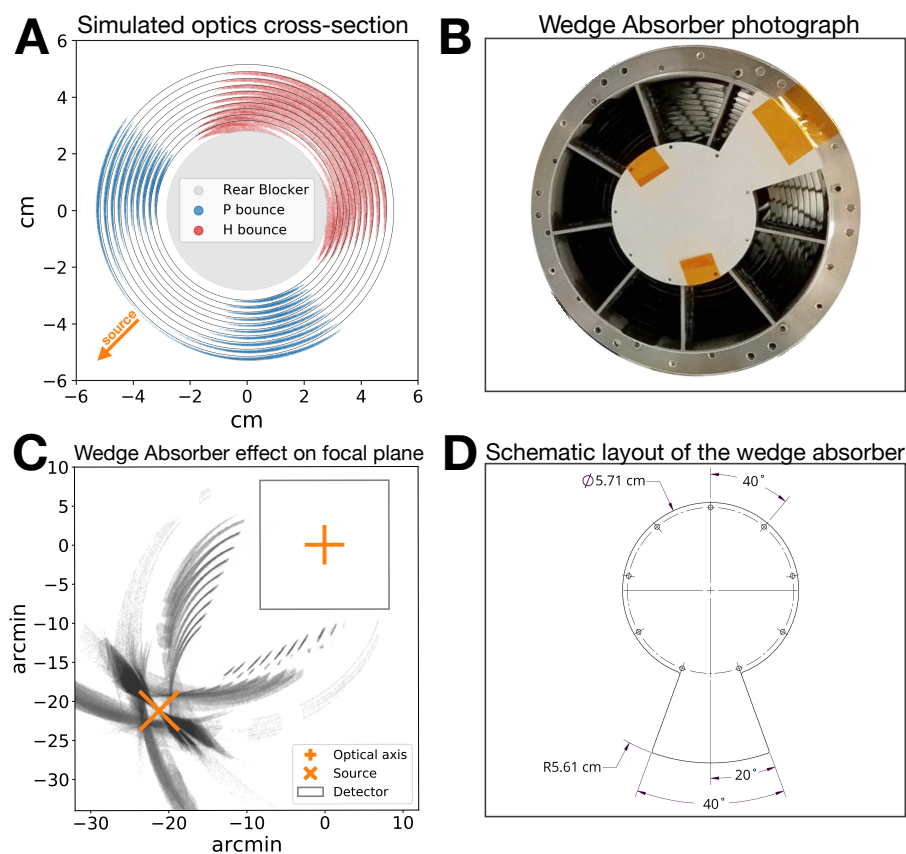
Figure 5.11: A wedge absorber is a successful strategy to clear detectors of ghost ray background when a compact and intense off-axis X-ray source is present. (A) Cross-section of an optics module showing the spatial distribution of simulated singly reflected rays differentiated by color. The paraboloid (blue) and hyperboloid (red) singly reflected rays come from different regions of the optic. (B) Photograph of an aluminium 1.5 mm thick wedge absorber tightly placed at the entrance of a 10-mirror module. That optics + wedge absorber was tested at the NASA Marshall SLF. (C) Measurement of effect that the wedge absorber has on the focal plane pattern when a 30 arcmin off-axis X-ray source illuminates the module at the NASA Marshall SLF. The orange cross and X mark represent the optical axis and the location of the source respectively. The gray box represents a standard detector. As observed in panel C, ghost rays impinging a detector are negligible when implementing the wedge absorber strategy. In panel D, we display a schematic layout for the wedge absorber, made out of a 1.5 mm thick aluminum plate. The wedge disk's center needs to be placed at the optics entrance, in line with the optical axis. The wedge must be clocked according to the X-ray source's location. This wedge blocks all of the rays singly-reflected from the hyperbolic section.

paraboloid segments (blue) and from the hyperboloid segments (red) come from different and confined angular areas of the mirrors. Since it is known that the primary source of ghost-rays are reflections from the hyperboloid segments these can be blocked at the aperture with a wedge-shaped absorber, a photograph of which can be seen in Panel B in front of a 10-mirror module. This method was tested at the MSFC SLF with a 30 arcmin off-axis source. The pattern on the focal plane is observed to be completely clear of ghost rays. The downsides of this method are that the focused rays are reduced by the wedge and that the angle of the absorber must be opposite to the polar angle of the source. This means, that it is required to know of the ghost ray source location in advance and to have control of the wedge angle.

5.5.5   Cylindrical baffles

This concept consists of 12-inch-long, concentric, cylindrical baffles carefully co-aligned to each Wolter-I mirror for every FOXSI optical module. The effectiveness of this solution at reducing singly reflected rays lies in the physical obstruction of the travel path for rays coming from off-axis angles greater than a certain threshold set by the radius and focal length of every Wolter-I mirror in the telescope. Thus, the smaller the radius, or the longer the focal length, the longer the baffle needs to be. This could be a significant disadvantage for bigger space X-ray telescopes using Wolter-I mirrors with focal lengths of tens of meters.

For FOXSI, the focal length is fixed at 2 meters, but radii vary from 3.290 cm up to 5.085 cm, as shown in table 3.1. Figure 5.12 shows results of the ray-trace simulation for the effective area of a 10-shell FOXSI optical module with no baffles, and with baffles 3 inches, 6 inches, 9 inches, and 12 inches long. From that same figure, we conclude that baffles of 12 inches long are needed to significantly reduce singly reflected rays. We considered the possibility of fabricating these baffles by using the same electrodeposition technique that is used to produce the FOXSI Wolter-I mirrors at the NASA-MSFC O'Dell et al., 2015. The major requirement would be to guarantee a low X-ray reflection efficiency, which is easy to obtain by not polishing the mandrels used to fabricate the cylindrical baffles. One big advantage of using the same electroform technique, compared to other ways of fabricating the baffles, is that the cylinders would be thin, relatively light, and would have precise cylindrical shapes. Although baffles are a good solution to reduce singly reflected rays, their long structure has significant implications for other parts of the rocket payload. Other options to reduce the singly reflected background with fewer impacts on the experiment are considered next.

5.5.6   Comparing ghost ray mitigation strategies

A number of strategies are discussed and compared in this section. The first strategy, blockers, was found to effectively reduce ghost rays though they must be optimized. Using the simulation, it is possible to find an optimal size for the blockers that reduces a large amount
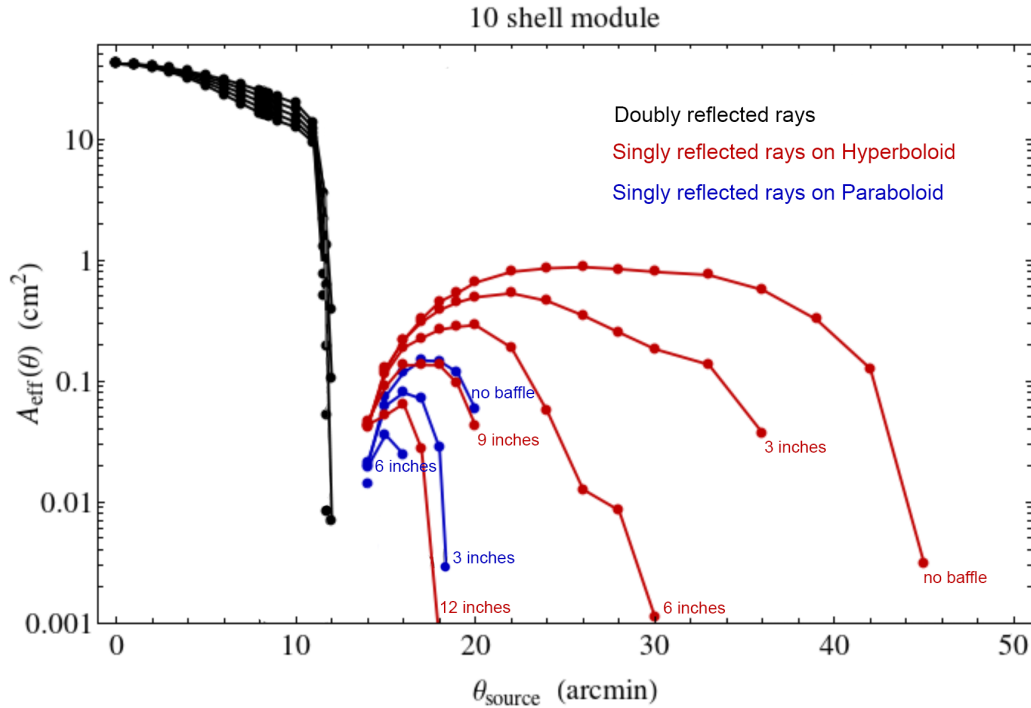
Figure 5.12:   Effective area obtained by convolving the geometric acceptance area of a
FOXSI optical module with the reflectivity of the mirrors (as a function of energy and
angle) multiplied by a 2D rectangular spatial function representing a detector area centered
on an on-axis position. In black is shown the effective area for the doubly reflected rays.
Blue and red lines represent the effective area for singly reflected rays from the paraboloid
and hyperboloid segment, respectively. Cylindrical baffles of 3 inches, 6 inches, 9 inches and
12 inches are used in this simulation in contrast with the case of no-baffle. Note that the
flux of singly reflected rays decreases by increasing the baffle lengths. This figure was made
by Ronald Elsner and was published in Buitrago-Casas et al. (2017a).

of ghost rays with minimal impact on focused rays. **The use of optimized blockers
should be implemented as a baseline for any Wolter-I telescope design**.

The effectiveness of the other two strategies considered in this paper to mitigate ghost
rays, the wedge absorber and honeycomb collimator, are compared in Table 5.1. This trade-
off study contains parameters assessing effects on the optical performance of the instrument
like the efficacy at reducing ghost-rays, and degradation of the telescope effective area. We
also compare the implication of each strategy on their fabrication and coupling with other
parts of a potential mission. The last part of the table evaluates the possible heritage use of
these two strategies for future missions.

One important limitation of the wedge absorber is that the angle of the wedge must be set in accordance with the polar angle of an off-axis source. In the right configuration, it may be possible to block ghost-rays from many sources but generally a wedge absorber can only deal with a single source. The orientation of the wedge could be tuned by either rotating the entire observatory or by adding a mechanism to rotate the wedge. A mechanism could also potentially control multiple wedges that could block multiple sources and stow under each other to return to a single wedge configuration.

There have been several X-ray telescopes with Wolter-I mirrors that have had to deal with ghost rays. All were designed to observe astronomical objects, like Chandra, XMM Newton, and NuSTAR. The latter have been used to observe the Sun where the ghost ray situation is much more intense. Chandra and XMM Newton implemented methods to minimize, but not completely block, ghost rays. NuSTAR had some launch mass constraints that led to abandoning a collimator designed to mitigate stray light and ghost rays optimally.

Chandra suppressed ghost rays within 14 arcmins of the optical axis by placing monolithic baffles at the very front of the telescopes and the optics' central aperture plate's aft surface. A description of the baffles is given in Cusumano et al. (2007), and Gaetz et al. (2000). XMM Newton also implemented X-ray baffles, but different from Chandra's. They were constructed as a series of sieve plates made out of rigid circular strips. These sieves were aligned and mounted to the front face of each telescope module. The axial space available allowed two of such sieves to be incorporated instead of monolithic baffles, blocking $\sim 80\%$ of ghost rays. The sieves designed for XMM Newton block singly reflected rays from just outside the nominal optics FOV (cone angle of 15 arcmins). A detailed description of this method is discussed in Chambure et al. (1999). NuSTAR is affected by stray light and ghost rays. Madsen et al. (2017) discuss how NuSTAR ghost rays and stray light could have been prevented and should be in future observatories. For NuSTAR, some ghost ray mitigation was achieved using a compact shell spacing. Madsen et al. (2017) indicate that to reduce further ghost rays, baffling of some sort is required.

In general, for Wolter-I telescopes with enough space between mirrors, ghost rays can be controlled by baffling within the optics, as fully described by Gaetz et al. (2000). But, highly nested telescopes are challenging to baffle via this method due to the limited space between consecutive mirrors, which is the case for FOXSI. Using monolithic cylindrical baffles at the entrance of every mirror is another method to constrain ghost rays useful only for highly packed Wolter-I mirrors designed for a rather large grazing incidence angle. FOXSI's angles range from 0.23 to 0.37 degrees, with mirror spacing of 0.1-0.2 cm, this translates monolithic cylinders over 50 cm long to block ghost rays entirely. Such long cylinders would have been very challenging to manufacture and attach to each shell and would have doubled the length of the optics. For FOXSI, we also discarded sieves' use since they mitigate but not entirely block ghost rays. We had to develop new ghost ray blocking strategies, leading to the 3D honeycomb collimator and the wedge absorber presented in this paper and summarized in

Table 5.1.

5.6 Input flare spectra

`foxsisim` also has the capability of assessing the optics spectral response. The incident rays distribution has an attribution called spectrum that can be loaded with any theoretical or data-driven input spectrum. `foxsisim` uses the mirrors' material and roughness to estimate reflection probabilities given the rays' incident angles. The rays that mathematically get alive to the detector plane can be plotted in a histogram which constitutes the spectrum after the rays pass through the optics. The optics energy response can be determined by comparing the input and output spectra. Figure 5.13 shows the input and output spectra for a set of two million parallel rays coming into a 10-mirror FOXSI rocket optics. That plot shows how the optics response slightly underperforms at higher energies ($\gtrsim$ 13 keV), as is expected.

5.7 The effect of ghost rays on potential instrument concepts with long focal lengths

The analysis presented in this paper is specific to the FOXSI sounding rocket optics configuration whose focal length (2 m) is limited by the capabilities of modern sounding rockets. In this section, we expand upon this analysis to a configuration that might be appropriate for a future space-based x-ray observatory whose science objectives include investigating the plasma heating and acceleration processes in solar flares. Such an observatory would need to observe both the thermal and non-thermal emission in large flares. The transition between thermal and non-thermal emission in a large flare occurs around 30 keV for some of the biggest flares. Above this energy, the spectrum becomes a power law. To determine the slope of the non-thermal power law, in order to understand the acceleration and transport processes of high energy electrons, requires observations up to $\approx$50 keV. This high energy requirement drives the need for a relatively long focal length of at least 14 meters. To provide sufficient effective area to detect the signature of the acceleration mechanism requires a significant number of mirror shells. The following analysis assumes a Wolter-I optics configuration with 18 mirror shells with (intersection) radii ranging from 9.3 to 6.3 cm and graze angles from 0.1 to 0.06 deg. The spacing between the shells has been optimized to minimize ghost rays. A detector area of 4 cm×4 cm is assumed. The simulated ghost ray pattern is shown in Figure 5.14. In this configuration, the ghost ray patterns are significantly different than those presented in Figure 5.5 primarily due to the long focal length or, equivalently, small graze angles. For a source on-axis, no ghost-rays infringe the focal plane. An inner circle pattern surrounds the focal plane which come from the parabolic segment. The outer circle pattern is caused by rays which go straight between the mirror shells. These rays are much less intense since they are not "focused" by the mirror shells. As the source moves

Parameter	Wedge absorber	3D printed honeycomb collimator
Efficacy at reducing singly reflected rays	Depending on the spatial configuration of the source(s) the efficacy ranges from $\sim 0\%$ up to $\sim 100\%$	Nominally close to 100% for the graze angles of the original design.
Volume and weight	Minimal	Length and mass scale inversely with threshold off-axis angle blocked. FOXSI design (18 arcmin threshold) is 19.5 cm long, has an internal radius of 4.43 cm, an external radius of 5.3 cm, and a mass of 0.8 kg.
Fabrication constraints	Mechanically easy to implement, with a material dense enough to stop X-rays in the working energy range of *FOXSI*	3D printing allows for easy customization of the design to minimize mass, but technology is currently limited to channels no smaller than 0.5 - 1 mm.
Calibration difficulties	Need to characterize the effect that the wedge absorber has on the point spread function.	It needs to be guaranteed that the optics module and collimator optical axes are co-aligned. System mis-alignments lead to a vast degradation of the telescope effective area and ghost rays.
Implications on other parts of the payload	Precise non-trivial roll control during the rocket flight. These maneuvers require careful telemetry command control on the payload roll angle.	Some implications on the location of solar pointing sensors to avoid interference. Extra difficulties at aligning the payload due to the lack of ghost rays used in such process.
Mechanical implications	It should be well attached to the FOXSI spider fixture to keep in place during the flight.	Minor implications mostly due to the co-alignment of the collimator mounting with a FOXSI telescope.
Heritage to satellite missions	Applicable with substantial modifications to allow angular mobility of the blocker. Includes extra complexity on electronics, power, and controller logic. A protocol to decide placement of the wedge need to be set.	If the honeycomb structure is reduced in size it may become an option for a spacecraft, but it can not block small off-axis anlges.

Table 5.1: Comparison of the two strategies considered to reduce singly reflected rays for
the FOXSI rocket experiment.
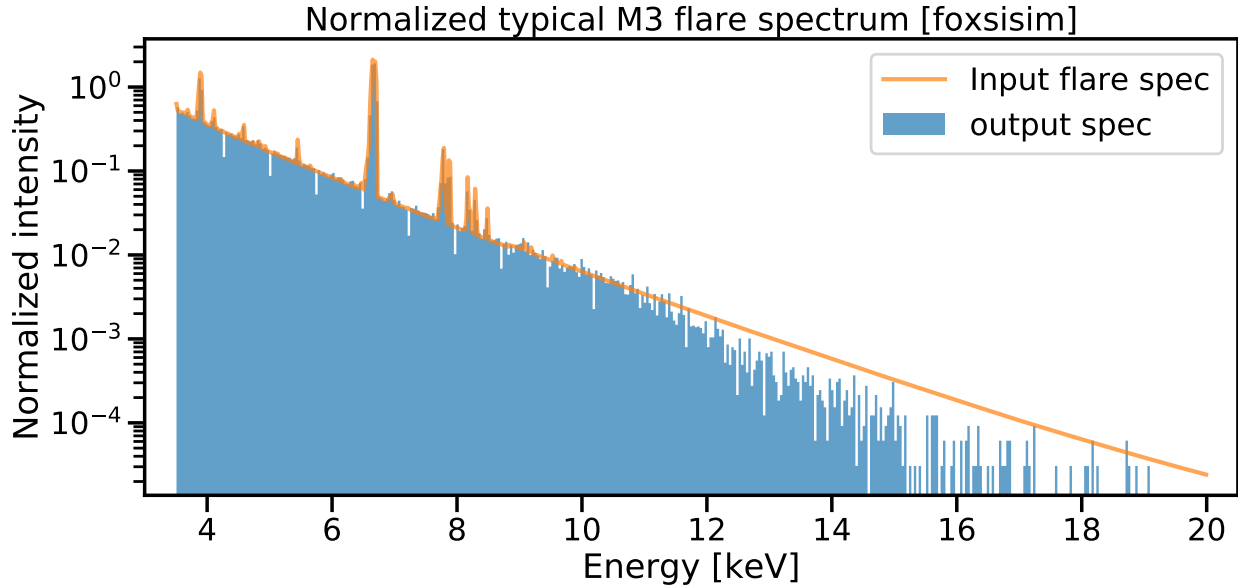
Figure 5.13: Example of a spectral response that `foxsisim` can produce (blue histogram) given an input spectrum (orange line). This example uses as input a typical solar flare spectrum from an M3 GOES class flare created using scaling laws (Battaglia et al., 2005). For this example, `foxsisim` was set to use 1.5 million rays from an infinity source and a FOXSI rocket 10-mirror optics module prescription with optimized blockers. The outcome spectrum shows an expected slightly less performance at higher energies ($\gtrsim$ 13 keV). The `foxsisim` spectral response is being actively used to accomplish a thorough instrument response assessment for FOXSI-4.

off-axis, there is a point at which the properly-reflected source and its ghost rays are observed together and at the same location. Further increasing the off-axis angles leads to ghost rays patterns moving across the focal plane. Sources with off-axis angles greater than $\approx$20 arcmin do not contribute any ghost rays to the imaged focal plane due to the blocking effect of the closely-packed mirrors. For comparison, the Sun is approximately 30 arcmin across. The central 6 arcmin diameter of the field of view is completely free of any ghost rays. This is sufficiently large to contain the emission of an entire eruptive event including typical observatory pointing control requirements.

Figure 5.15 shows a comparison of the flux of properly focused rays from an on-axis source with a flat spectrum compared to ghost rays by a source of the same brightness at an off-axis angle of 16 arcmin. The green line shows that rays up to $\approx$50 keV are focused by this prescription. The grey line shows the spectrum of the straight through rays which simply show the input spectrum since these rays do not interact with the mirrored surfaces.

The blue line shows that the flux of the ghost rays are significantly attenuated by a factor of
> 20 up to 10 keV. Above this energy, the ghost rays are increasingly attenuated compared
to an on-axis focused source; at 20 keV the ghost rays are 1000 times weaker than the same
source on axis. This means that ghost-rays will not significantly affect observations of bright
sources like solar flares or even weaker sources such as active regions as long as the sources
outside of the field of view are of equal intensity. For times when the sources outside of the
field of view are bright and generate ghost rays comparable in flux to the source in the field
view then more advanced deconvolution techniques can be utilized to recover faint sources.

5.8   Summary and Conclusions

All strategies to mitigate ghost rays presented here were established by a comprehensive
use of `foxsisim`. The mission of analysing ghost rays, and reducing them, was an excellent
example to show the versatility and power of our ray tracing simulation toolbox. We present
`foxsisim` as an open-access set of tools to study any X-ray Wolter-I optics. We encourage
the broad scientific community to use the numerical tools presented here. They can be useful
in applications for astronomy, medicine, material sciences, etc. Future scientific results of
the quiet-Sun observations obtained during past flights of the FOXSI rocket will include the
use of `foxsisim` to assess the overall instrument background.

We found that adding blockers optimized to maximize their ghost-ray mitigation should
be a baseline for any Wolter-I telescope design. In addition, we assessed two other strategies
to reduce ghost-rays. One based on a honeycomb collimator and one on a wedge absorber.
The use of either of these two strategies on future spacecrafts imply some payoff that need
to be assessed according to the particular design and constrains of the instrument. For
example, a honeycomb collimator adds a substantial amount of mass but requires minimum,
if any, maneuvering. Opposite to that, the wedge absorber is light, but requires telemetry
and control of the spacecraft to locate the wedge at the right position that optimizes ghost
ray mitigation. The two strategies have a direct impact on the effective area of the optics.
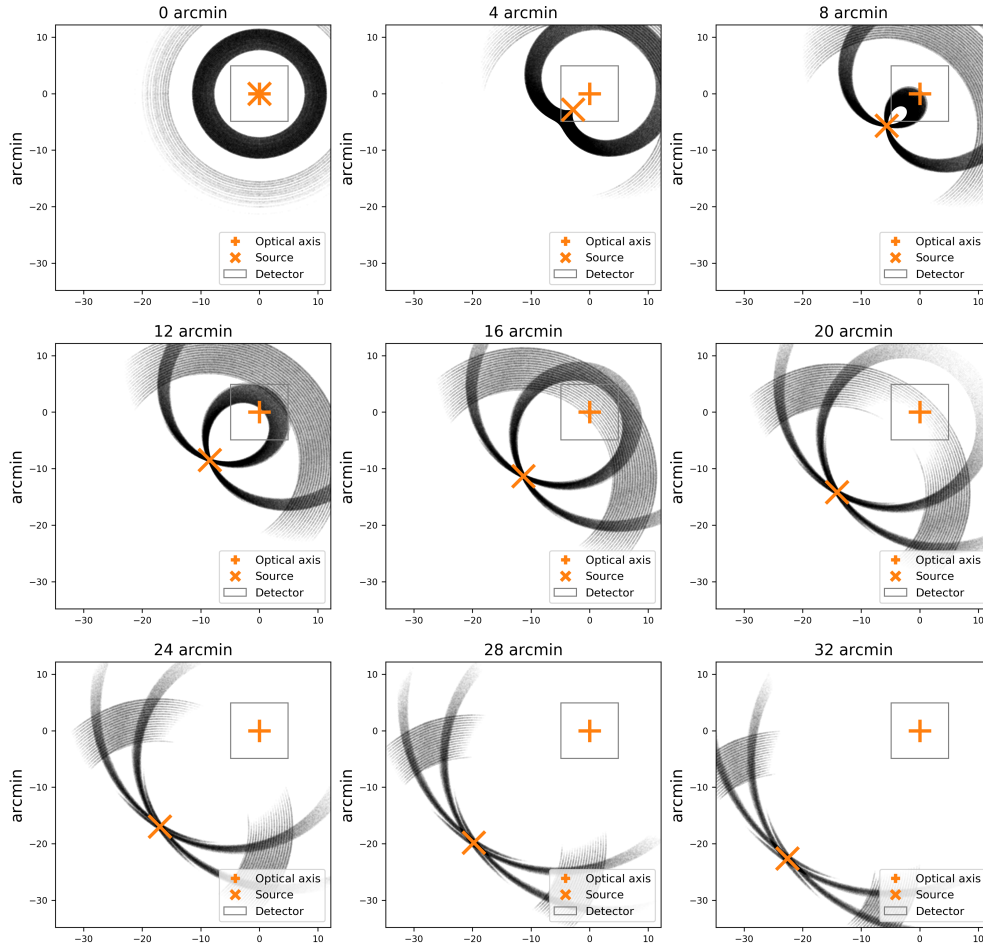
Figure 5.14: Simulated ghost ray images for a 14-m focal length 18-shell telescope module that might be appropriate for a future space-based x-ray observatory whose science objectives include investigating the plasma heating and acceleration processes in solar flares. Ghost ray patterns are simulated for a point source at infinity with off-axis angles from 0 to 32 arcmin. The gray square shows a 4 cm×4 cm field of view. The orange symbols show the optical axis and source position. For a source on-axis, no ghost-rays infringe the focal plane. Single bounce rays from the parabolic mirror segment form the inner circular pattern. Straight-through rays form the outer circular pattern. Sources with off-axis angles greater than ≈20 arcmin do not contribute any ghost rays to the imaged focal plane due to the blocking effect of the closely-packed mirrors. For comparison, the Sun is approximately 30 arcmin across.
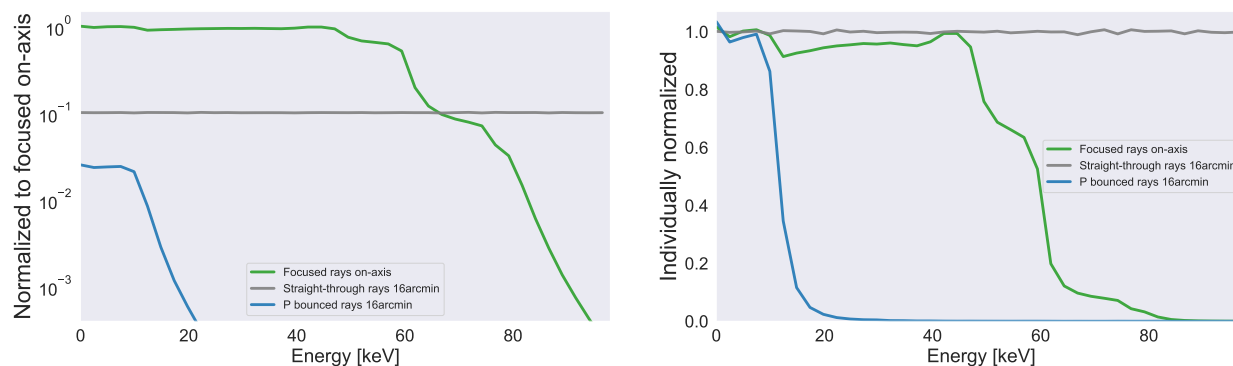
Figure 5.15: A comparison of the flux of properly focused rays from an on-axis source with a flat spectrum compared to ghost rays by a source of the same brightness at an off-axis angle of 16 arcmin. The green line the spectrum of properly focused rays. The grey line shows the spectrum of the straight through rays which simply show the input spectrum since these rays do not interact with the mirrored surfaces. The blue line shows that the flux of the ghost rays which are significantly attenuated by a factor of > 20 up to 10 keV. Above this energy, the ghost rays are increasingly attenuated compared to the on-axis focused source; at 20 keV the ghost rays are 1000 times weaker than the same source on axis.

Chapter 6

Quiet Sun hard X-rays with FOXSI

6.1 Introduction

Solar nanoflares are small impulsive events releasing magnetic energy in the corona. If nanoflares follow the same physics as their larger counterparts, they should emit hard X-rays (HXRs) but with a rather faint intensity. A copious and continuous presence of nanoflares would result in a sustained HXR emission. These nanoflares could deliver enormous amounts of energy into the solar corona, possibly accounting for its high temperatures. To date, there has not been any direct observation of such persistent HXRs from the quiescent Sun. However, Iain G Hannah et al. in 2010 constrained the quiet Sun HXR emission using almost 12 days of quiescent solar-off-pointing observations by RHESSI. These observations set 2σ upper limits at 3.4×10^{-2} photons s^{-1} cm^{-2} keV^{-1} and 9.5×10^{-4} photons s^{-1} cm^{-2} keV^{-1} for the 3-6 keV and 6-12 keV energy ranges, respectively. Observing faint HXR emission is challenging because it demands high sensitivity and dynamic range instruments. The Focusing Optics X-ray Solar Imager (FOXSI) sounding rocket experiment excels in these two attributes when compared with RHESSI. FOXSI completed its second and third successful flights (FOXSI-2 and -3) on December 11, 2014, and September 7, 2018, respectively. This work aims to constrain the quiet Sun emission in the 5-10 keV energy range using FOXSI-2 and -3 observations.

To fully characterize the sensitivity of FOXSI, we assessed ghost ray backgrounds generated by sources outside of the field of view via a ray-tracing algorithm. We use a bayesian approach to provide upper thresholds of quiet Sun HXR emission and probability distributions for the expected flux when a quiet-Sun HXR source is assumed to exist.

We found a FOXSI-2 upper limit of 4.5×10^{-2} photons s^{-1} cm^{-2} keV^{-1} with a 2σ confidence level in the 5-10 keV energy range. This limit is the first-ever quiet Sun upper threshold in HXR reported using $\sim$ 1-minute observations during a period of high solar activity. RHESSI was not able to make sure a measurement of the quiet Sun emission during

active times due to its limited dynamic range. During FOXSI-3's flight, the Sun exhibited a fairly quiet configuration, displaying only one aged non-flaring active region. Using the entire ∼6.5 minutes of FOXSI-3 data, we report a 2σ upper limits of $\sim 10^{-4}$ photons s^{-1} cm^{-2} keV^{-1} for the 5-10 keV energy range. FOXSI-3's upper limits on quiet Sun emission are similar to that reported by Iain G Hannah et al., 2010, but FOXSI-3 achieved these results with only 5 minutes of observations or about 1/2600 less time than RHESSI. A possible future spacecraft using hard X-ray focusing optics like FOXSI's concept would allow enough observation time to constrain the current HXR quiet Sun limits further or perhaps even make direct detections. **All this chapter contains material submitted for publication to the Astronomy and Astrophysics journal**. This is the first report of quiet Sun HXR limits from FOXSI and the first science work using FOXSI-3 observations. My contributions to this work are described in Buitrago-Casas et al. (2022)

6.2 Science context

In solar and heliophysics, the coronal heating problem relates to the puzzle of identifying and understanding the mechanism(s) causing corona's temperatures to be multiple thousands times hotter than the solar surface (e.g., Klimchuk, 2006; Klimchuk, 2015). Among the various plausible hypotheses proposed, the two strongest candidates are i) MHD wave dissipation and ii) copious low energy magnetic reconnections (or "nanoflares" as coined by Parker in 1988) (e.g., Hudson, 1991; Bogachev et al., 2020). Klimchuk (2006) pointed out that, when examined thoroughly, most plausible coronal heating explanations imply non-thermal heating that happens impulsively on individual flux tubes (strands). If such small, impulsive events follow the physics of larger flares, non-thermal electrons energized during the small, ubiquitous reconnections in the corona should be the base for heating the coronal plasma. The emission of hard X-rays (HXRs) is a direct consequence of these non-thermal electrons slowing down in the chromosphere. HXRs have been observed in non-flaring active regions, revealing the presence of hot plasma over 7 million Kelvin (e.g., Ishikawa et al., 2017). Other authors have shown evidence of non-thermal particles in microflares (typical energies of $E \sim 10^{27}$ erg) by directly analyzing their emission in HXRs (e.g., Christe et al., 2008; I. Hannah et al., 2011; Glesener et al., 2020; Duncan et al., 2021a). For nanoflares, with energies of $E \sim 10^{24}$ erg or less, HXRs are far fainter than those from larger flares and challenging to detect due to the limited sensitivity of current instruments. Consequently, the role that nanoflare non-thermal particle processes have in heating the quiescent corona remains rather poorly understood.

In recent years, the Focusing Optics X-ray Solar Imager (FOXSI) sounding rocket experiment has provided high sensitivity (and high dynamic range) solar X-ray observations in the band of ∼4-20 keV, with capabilities to perform imaging spectroscopy at 8.8 arcsec spatial and 0.5 keV energy resolutions (Krucker et al., 2014; Christe et al., 2016a; Musset et al., 2019). FOXSI observed areas in the solar disk free of active regions during its
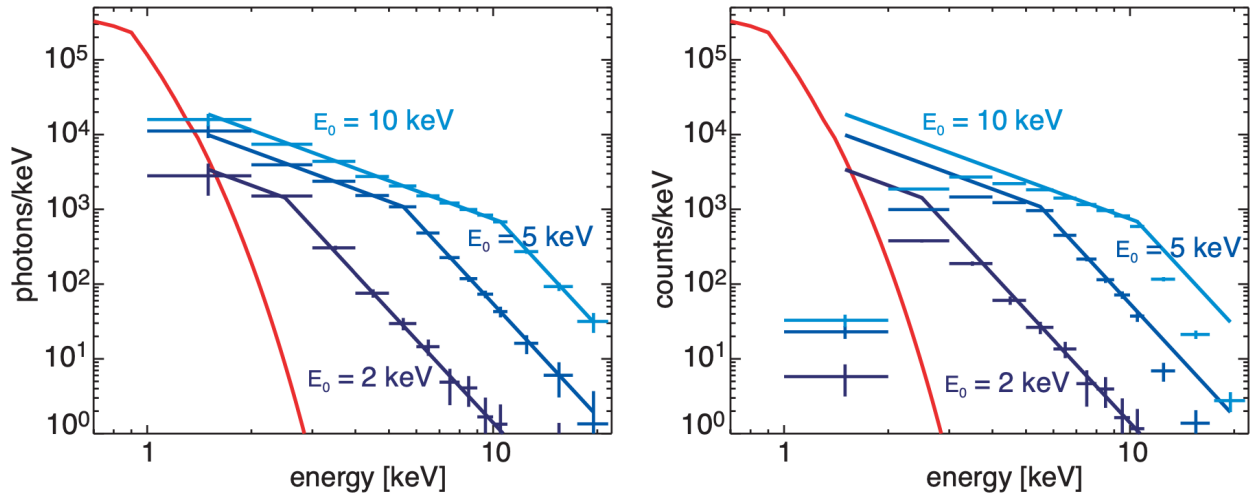
Figure 6.1: 60 s integrated spectra in photons/keV (left) and counts/keV (right) from thermal (red curve) and non-thermal (blue curves) quiet Sun nanoflare emission (assuming T=2 MK and EM=10^{44} cm^{-3}). The three spectra en blue correspond to turnover energies of 2, 5, and 10 keV (as indicated in the plots). The power indexes are -1.7 before and -5.0 after the turnover energies. The data points with error bars show the expected FOXSI measurements. The expected count rates for the three spectra shown are 14, 91, and 245 counts per minute. Figure from Krucker et al. (2011).

second and third flights. Analyzing the very few counts observed with FOXSI when pointing to the quiet Sun is currently the best way we have to evaluate the faintest sources of HXRs from the solar corona, which is the core of this work. The GitHub repository https://github.com/foxsi/foxsi-science contains complete instructions to access and process FOXSI data collected during the first three rocket flights.

The quiet Corona has temperatures below 2 MK (see, e.g., Brooks et al., 2009; Sylwester et al., 2012). Thermal emissions in hard X-rays from this plasma are below FOXSI's sensitivity range, i.e., any observation FOXSI performs in the 5-10 keV energy range coming from the quiet Sun would necessarily be of non-thermal nature. Studies in radio frequencies of the quiet Sun have found non-thermal features similar to those more commonly observed in active regions (see, e.g., Benz et al., 1997; Krucker et al., 1997a; Mondal et al., 2021). Assuming nanoflare non-thermal electrons produce these quiet Sun non-thermal features, these electrons could deposit their energy into the surrounding plasma via a thick target and produce hard X-ray emission. Krucker et al. (2011) simulated such non-thermal hard X-ray spectra for various values of the cutoff energy, E_c (for two power-law indexes, $\delta = 1.5$ and $\delta = 5$), that would be measurable with the FOXSI rocket experiment (see Figure 6.1). For the three cases explored by Krucker et al. (2011), they found that FOXSI quiet Sun

observations should measure 14, 91, or 245 counts per second in the 4-15 keV energy range, respectively. Observing fewer count rates, or not counts at all, would imply that quiet Sun nanoflares follow processes with a different physics than their larger counterparts. Iain G Hannah et al. (2010), e.g., showed how RHESSI quiet Sun observations constrained thick target power-law indexes to be steeper ($\delta = 5$ for $E_c = 0.32$ keV, $\delta = 6$ for $E_c = 0.81$ keV, and $\delta = 7$ for $E_c = 1.24$ keV) than previously expected. These very steep spectra were thought to be implausible for very small flaring events (both nanoflares and microflares). However, more recently, Glesener et al. (2020) reported a spectral index of $\delta = 6.3 \pm 0.7$ for a small solar microflare (GOES class A5.7) observed simultaneously with NuSTAR and RHESSI. Their results imply that X-ray emissions down to < 5 keV are almost entirely non-thermal, contrary to what is usually assumed using RHESSI data alone. Their findings suggest that very vertical power-law spectra may be a common feature of many small flare events. Glesener et al. (2020) results correspond to a single microflare. However, it is reasonable to think their findings could be extended to smaller impulsive energy releases (i.e., nanoflares). Exploring hard X-ray emissions from the quiet Sun with better sensitivity instruments will help us understand how particle acceleration changes across energy scales in flares. The rest of this chapter aims to assess quiet Sun hard X-rays using novel data from the FOXSI-sounding rocket experiment.

6.3   Quiet Sun pointing with FOXSI-2

The FOXSI rocket experiment has successfully flown three times from the White Sands Missile Range. The second launch (FOXSI-2) launched on December 11, 2014, at 19:11:00 UTC and targeted the Sun for 6 minutes and 40.8 seconds starting at 19:12:42 UTC. FOXSI-2's FOV was limited to about a quarter of the solar disk (see Figure 6.2). We targeted five portions of the solar disk during the observation time to maximize science outcomes. The detailed list of FOXSI-2 targets is given in Athiray et al., 2020, and Vievering et al., 2021. One of the targets covered a portion of the quiet Sun at the solar North pole for a total of 92.7 seconds (see Figure 6.2). We will refer to this quiet Sun target as target I, following the terminology coined by Vievering et al., 2021. The dark grey box in Figure 6.2 is the FOV for one of the silicon detectors in FOXSI-2. All other silicon detectors in the payload had the same FOV size but were clocked in a set of different angles with respect to the one shown in Figure 6.2.

For the last 24.2 seconds, pointing at target I, we remotely activated an attenuator wheel that placed thick aluminum disks on top of the detectors for background measurements. Later, in section 6.7, we will use such background measurements to assess the existence, or not, of a source of HXRs of solar origin in target I.

AIA171 - Dec 11, 2014 at 19:17 UT
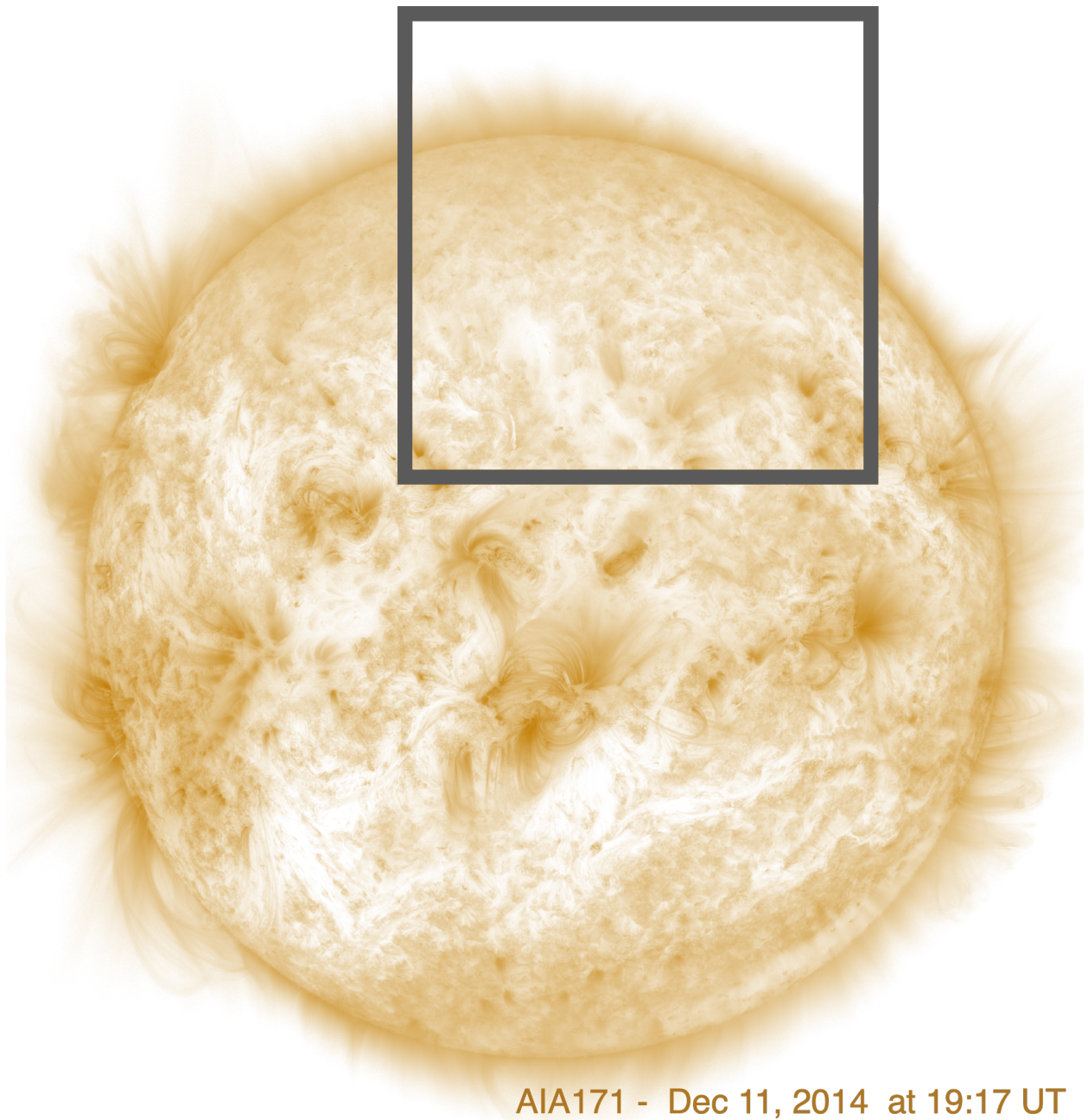
Figure 6.2: FOXSI-2 quiet Sun target, at the north solar pole, observed during the FOXSI-2 rocket flight. The background image is the AIA solar full disk in the 171 Angstrom filter. The black square represents a sample of FOXSI's detectors FOV. The payload pointed to this target for a total of 92.7 seconds on December 11, 2014 (from 19:17:13.5 UTC to 19:18:46.2 UTC). The last 24.2s of this time were used to measure background via shutters placed in front of the detectors.
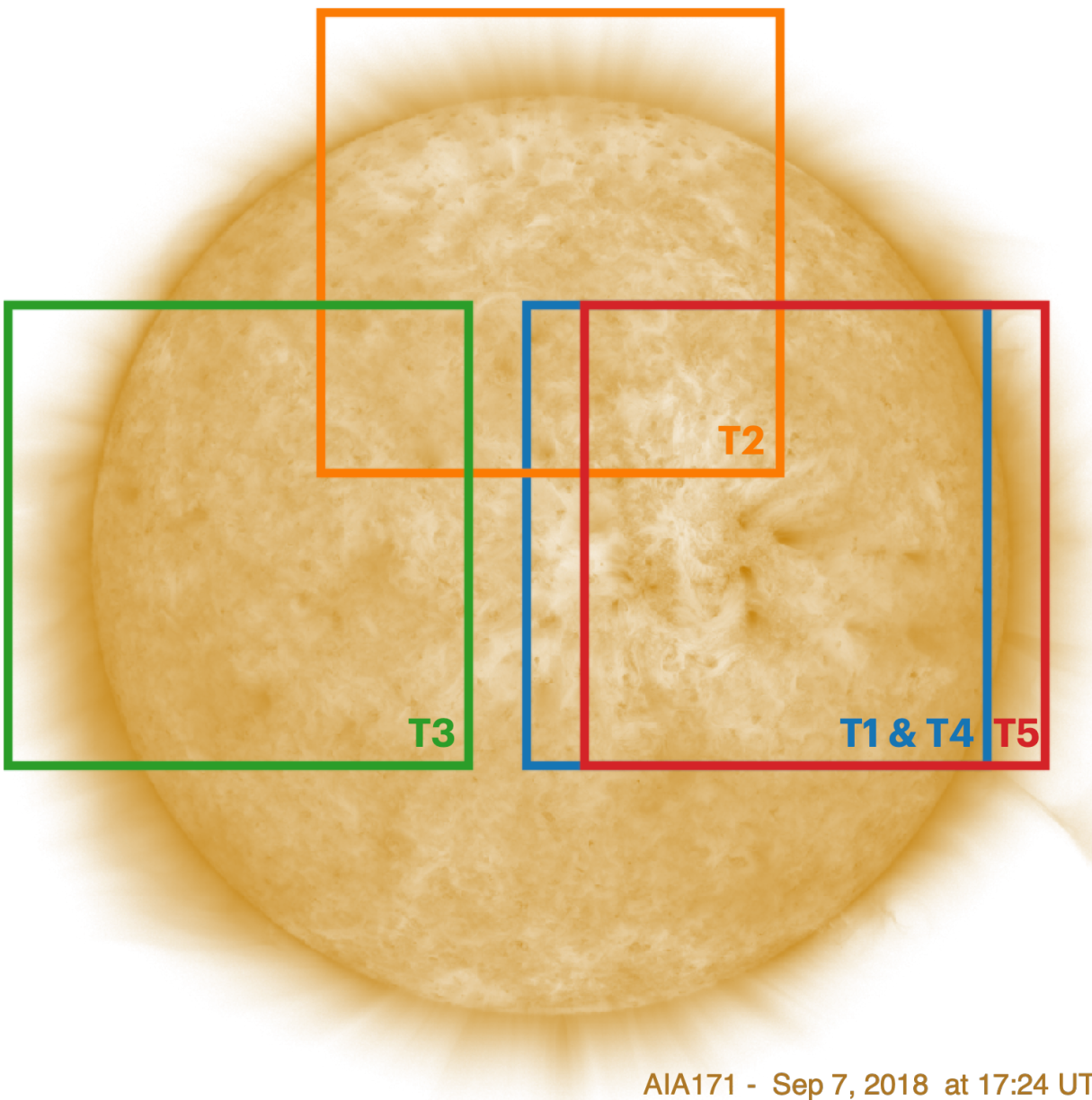
Figure 6.3: The background image is the SDO/AIA 171Å solar entire disk at the time of the FOXSI-3 observations (Sep 7, 2018, at 17:24 UT). Solar activity was very low at the time of the FOXSI-3 rocket launch. A very aged non-flaring active region was located in the western hemisphere. The colored squares represent the approximate FOV of a silicon detector and the targets during the FOXSI-3 observations. We highlight that these boxes are approximate FOVs because every detector is clocked differently.

6.4 Quiet Sun observation with FOXSI-3

The FOXSI-3 rocket campaign took place at the White Sands Missile Range. The rocket launched on September 7, 2018, at 17:21 UT and observed the Sun from 17:22:44.6 UT until 17:29:14.1 UT, for a total of 6 minutes and 29.5 seconds. The payload contained seven Wolter-I optics modules paired with semiconductor detectors. See Musset et al., 2019 for details of the payload. Four detectors had silicon strip sensors; two other detectors worked with finer pitch CdTe strip sensors (60 μm instead of the 75 μm used in the silicon sensors). These six detectors were optimized for observations in the 4-20 keV energy range. The seventh detector (PhoEnIX) was a 2048×2048 pixel CMOS sensor designed for soft X-ray observations (0.5 - 5.0 keV), see Ishikawa et al., 2018 for details.

One of the primary goals for the FOXSI-3 rocket campaign was to place a more stringent HXR upper limit of the quiet Sun than previously reported. The launch of FOXSI-3 happened during a time of extremely low activity in the Sun. Figure 6.3 depicts an SDO/AIA solar image in 171 Å at the time of the FOXSI-3 launch. A non-flaring aged active region can be identified in the western solar hemisphere. This active region was no longer intense enough to be labeled and included in the NOAA catalog. However, that active region existed for several solar rotations and was previously cataloged as NOAA AR12713 last time it was sufficiently active (June 2018). Figure 6.3 also shows a coronal hole at the solar north pole and sparse small EUV brightenings outside the aged active region.

FOXSI-3 pointed to the Sun and recorded data during 367.3 seconds total. FOXSI-3 targeted the aged active region for 128.2 seconds (blue T1 in Figure 6.3), the north pole for 24.0 seconds (orange T2 in Figure 6.3), the eastern quiet Sun limb for 144.6 seconds (green T3 in Figure 6.3), and returned to the aged active region for 26.3 seconds (blue T4 in Figure 6.3). The observations concluded with a 2 arcminutes shift towards the western limb where FOXSI-3 stayed for the remaining 44.2 seconds (red T5 in Figure 6.3). Further details of the rocket campaign, and the upgrades in the payload, can be found in Musset et al., 2019.

For the study using FOXSI-3 data presented here, we limited our analysis only to observations of three silicon detectors flown in the rocket. The fourth silicon detector included in the payload (as well as the two CdTe detectors) presented relatively high electronic noise during the flight, making them unsuitable for low counts analysis. Due to the low solar activity, HXRs recorded by FOXSI-3 were very sparse. The top part of Table 6.2 summarizes the total number of events observed with each of the three silicon detectors (D102, D105, and D106) in the 5-10 keV energy range, for every FOXSI-3 target (T1, T2, T3, T4, and T5).

Because of technical difficulties, we did not activated attenuators for the FOXSI-3 flight.
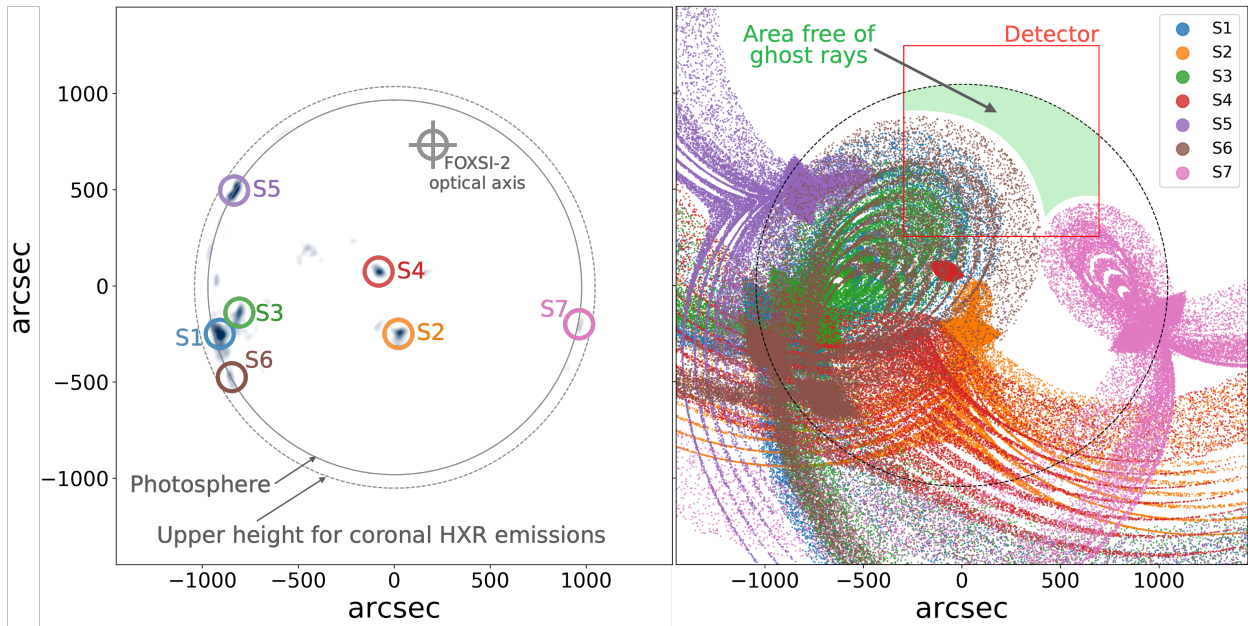
Figure 6.4: *Left*: Full disk FeXVIII map constructed from the 94, 171, and 211 AIA/SDO maps following Del Zanna, 2013. We identify seven intense, hot localized sources. We mark in grey the center of target I at [200", 750"] (FOXSI-2 optical axis). The solid black circle represents the photosphere. The dashed black circle sets the upper radius limit above which quiet Sun HXRs are not expected from (50 Mm above the photosphere). At this height, the ambient electron density gets lowered by more than four orders of magnitude compared to the photosphere, i.e., the HXR bremsstrahlung emission also gets substantially reduced (see, e.g., Aschwanden, 2006). A few structures that are not circled, but seem as bright as others like S7, are ignored. The reason is that because of their short off-axis distances, their ghost rays are negligible, as is the case for sources S2, S4, and S5. *Right*: Simulated ghost rays generated by the five intense sources when pointing to target I. Each of the five source rays is color-coded according to the labels in the figure. The big black dashed circle represents the upper limit radius for coronal HXRs. The area in solid green sets the limit we chose as a region mostly free of ghost rays inside the solar disk. The red box is one of the silicon detector FOV. The other silicon detectors in FOXSI-2 had the same FOV size, but were clocked with respect to the one shown in this figure.

The consequences of not having attenuators for some fraction of the observation time are that we do not have in-flight background measurements.

6.5 Ghost ray treatment

FOXSI uses Wolter-I-figured grazing incidence X-ray telescopes to focus on solar X-rays. The Wolter-I geometry consists of two grazing-incidence mirror segments, a paraboloid primary mirror followed by a hyperboloid secondary reflector, referred to as mirror shells. On-axis rays that reflect on both mirrors are focused into an image on the focal plane. However, there is a possibility that rays from off-axis sources may reflect only on a single mirror shell and reach the focal plane. These single-reflecting rays are broadly referred to as stray light or ghost rays (see the right panel in Figure 6.4). A full description of ghost rays for FOXSI, and strategies to minimize them (honeycomb structures used in FOXSI-3 for example), can be found in Buitrago-Casas et al., 2017b; Musset et al., 2019; Buitrago-Casas et al., 2020.

To assess ghost rays polluting FOXSI's FOV, we need to know every identifiable, off-axis, intense, HXR source at the time of observing target I. We constructed an AIA Fe XVIII map for December 11, 2014, at 18:20 UTC, using the method given by Del Zanna, 2013. This map, displayed as the background image of the right panel on Figure 6.4, shows the hottest components of the coronal plasma at the time of our observations, i.e., potential sources of HXRs. From this Fe XVIII map, seven compact off-axis kernels are easily identifiable as potential sources of ghost rays. We used a FOXSI customized ray-tracing simulation (see Buitrago-Casas et al., 2020) to assess the ghost ray effect that each of the seven compact sources has over the FOXSI-2 FOV. We show the results of such assessment in the right panel of Figure 6.4. Although ghost rays impinge on a significant region within the detectors, they are constrained to an identifiable zone of the FOV. Our goal is not to characterize the intensity of ghost rays. Instead, we are trying to determine locations where ghost rays could reasonably be nonzero to exclude them from our analysis. Taking advantage of the ghost ray confinement, we can mask out ghost rays and define an area within the detector reasonably free of ghost ray light. Since our goal is to evaluate the solar origin of events FOXSI-2 observed, we selected a region, colored in green in the right panel of Figure 6.4, from which coronal HXRs could originate. We study the events observed with FOXSI-2 in that region during the 64.5 seconds the rocket pointed to target I, before activating the attenuators. Additionally, we use the last 24.2 seconds of target I pointing as a background measurement.

6.6 Statistical issue: assessing a weak source mixed with background data

Typically, in high-energy astrophysics and physics, experiments measuring discrete sets of events (counts) may contain multiple signals (source(s) of interest mixed with background(s)). It is common practice to take additional auxiliary measurements to assess the background(s) by setting the experiment in a configuration believed to be free of the source(s) of interest. In these sets of measurements, the goal is usually to establish an actual count rate for the source(s) of interest. For reasonably large numbers of counts, many straightforward

statistical background subtraction techniques are suitable to determine the existence of genuine sources (see, e.g., McIvor, 2000; Piccardi, 2004; Benezeth et al., 2010). For faint sources and backgrounds, the measured counts are so few that usual Gaussian techniques based on normal distributions do not hold. Instead, Poisson and Binomial distributions appropriately describe low count statistics. T.-P. Li et al. in 1983 published a first thorough review of this source and background low count statistics problem. Such a problem is today known as the ON/OFF problem or the Li-Ma problem. Although T.-P. Li et al. (1983) proposed their statistical method originally in the context of gamma-ray astronomy, its generality is so wide that it can be directly applied to other fields in physics and astronomy. Particularly, the Li-Ma problem suits the FOXSI observations considered in this work.

6.7   ON/OFF Li-Ma analysis

It is known that N_{on} integer events measured by a counting experiment during a specific period of time follow the Poisson distribution (see, e.g., T.-P. Li et al., 1983; Gehrels, 1986; Knoetig, 2014; Casadei, 2014):

$$P(N_{on}|\lambda) = \frac{\lambda^{N_{on}}}{N_{on}!}e^{-\lambda}, \tag{6.1}$$

where λ is the non-negative real number of expected events, a.k.a Poisson parameter. In the most simple ON/OFF problem, the Li-Ma problem, the N_{on} measured counts are supposed to result from s expected counts coming from a signal of interest overlaid with b expected counts from a background. The ON/OFF Li-Ma framework assumes that s and b are independent Poisson variables, i.e., the sum $\lambda = s+b$ should follow a Poisson distribution with

$$P(N_{on}|s,b) = \frac{(s+b)^{N_{on}}}{N_{on}!}e^{-(s+b)}. \tag{6.2}$$

If N_{off} represents the number of background counts measured when the experiment was set in an signal-off configuration, the distribution of such background counts is also a Poisson distribution with

$$P(N_{off}|b') = \frac{b'^{N_{off}}}{N_{off}!}e^{-b'}. \tag{6.3}$$

In general, the observation times for the on and off experiment configurations, T_{on} and T_{off}, are not the same. To account for this difference, and others related to the details of

the experiment setup (sensitive area A, detector livetimes lt, observed solid angle Ω, etc.), a parameter α is introduced in the ON/OFF problem framework defined as

$$\alpha = \frac{T_{on} \cdot A_{on} \cdot lt_{on} \cdot \Omega_{on} \cdot ...}{T_{off} \cdot A_{off} \cdot lt_{off} \cdot \Omega_{off} \cdot ...}, \tag{6.4}$$

assumed to have negligible uncertainty (see, e.g., Berge et al., 2007). The expected counts from the background alone in the on- and off-signal of interest experiment setup (b and b' respectively) relate via $b = \alpha \, b'$.

Originally T.-P. Li et al. (1983) proposed to assess the significance of a weak signal mixed with a background by use of a hypothesis test (e.g., Wilks, 1962; Eadie et al., 1971; Gregory, 2005). Later, Knoetig (2014) and Casadei (2014) developed such hypotheses test methods further, proposing objective Bayesian solutions for the ON/OFF Li-Ma problem using the three measurable quantities N_{on}, N_{off}, and α.

For the hypothesis test method, s and b are the unknown parameters, and the *null hypothesis* (H_0) is that $s \equiv 0$, i.e., the only signal is the background. The alternative hypothesis (H_1) considers $s > 0$. The conditional probability of H_0, $P(H_0|N_{on}, N_{off}, \alpha)$, is expressible in terms of Bayes' theorem (e.g., Knoetig, 2014),

$$P(H_0|N_{on}, N_{off}, \alpha) = \frac{P(N_{on}, N_{off}|H_0, \alpha) \, P_0(H_0)}{P(N_{on}, N_{off}|\alpha)}. \tag{6.5}$$

Here, $P(N_{on}, N_{off}|H_0, \alpha)$ represents the probability of measuring N_{on} and N_{off}, given a scenario where H_0 is true. $P(N_{on}, N_{off}|\alpha)$ is a normalization probability, and $P_0(H_0)$ is the *prior* probability for H_0.

There is a discussion among different authors regarding the effectiveness of different priors for the ON/OFF Li-Ma problem (e.g., Berger et al., 2001; Casadei, 2014; Nosek et al., 2016). Nosek et al. (2016) thoroughly analyzed the effect that three well-known priors (scale-invariant, uniform, and Jeffreys) have on the ON/OFF Li-Ma method when applied to weak signals. Nosek et al. (2016) concluded that Bayesian inferences using Jeffreys' prior distributions are generally a safe compromise compared to the other priors they examined (scale invariant and uniform prior, for instance). Although Jeffreys' prior distributions require more complicated calculations based on integral expressions, it leads to reasonably limits of the source existence for close to zero observed counts. Knoetig (2014) implemented Jeffreys' prior and found an analytical solution to the ON/OFF Li-Ma problem in terms of special integral functions (Gamma and hypergeometric). The inputs of Knoetig's analytical solution are N_{on}, N_{off}, and α. The outcomes are $P(H_0|N_{on}, N_{off}, \alpha)$, the Bayesian significance,

$S_b = \sqrt{2}\,\mathrm{erf}^{-1}[1 - P(H_0|N_{on}, N_{off}, \alpha)]$, and a signal upper limit λ_σ, with an uncertainty of σ (See the details of the general analytical solution in section 3.4 of Knoetig (2014)). Knoetig's solution is the one we implement here to analyse FOXSI-2 and -3 observations.

6.8 ON/OFF Li-Ma analysis for FOXSI-2

In the search for HXRs of quiet Sun origin, we applied Knoetig's solution of the ON/OFF Li-Ma problem to the observations of target I in FOXSI-2. The first step is to set the off- and on-signal configurations. The off-signal observations occurred during the last 24.2 seconds of pointing to target I, after the attenuators were activated, i.e., blocking the solar flux from reaching the experiment detectors. The sensitive area was the whole detector for the off-signal configuration, i.e., 16×16 arcmin^2. The on-signal observations consist of the counts recorded by a detector (during the 68.5 seconds of no-attenuators) within the green area described in the right panel of Figure 6.4.

FOXSI-2 flew seven optics/detector assemblies. However, here we use only the most reliable four detectors to apply the ON/OFF Li-Ma analysis (D101, 104, D105, and D108 hereafter). Of the remaining three detectors, two were a bit noisy for weak sources studies, and one was placed on a location in the payload with no attenuator (i.e., with no background measurement). All four detectors we use in this study had a silicon sensor and were positioned behind a 7-mirror optics module. Figure 6.5 shows the counts observed by one of these detectors (D105) during the on-signal configured observation. The ten green dots in Figure 6.5 constitute N_{on}. N_{off} for that same detector is four counts. We calculated α as the ratio of observation time (corrected by the detector livetimes) and the observed areas between the on- and off-configuration. For D105, $\alpha = 0.86$. These values, and the ones for the other three analyzed detectors, are summarized in Table 6.1. Table 6.1 also displays the outcomes of Knoetig's method for the four detectors: The probability of H_0 ($P(H_0|N_{on}, N_{off}, \alpha)$), the significance S_b, and the upper limit with a 2σ (97.72%) confidence.

Knoetig's method produces the distribution function for s, i.e., the probability

$$P(s|N_{on}, N_{off}, \alpha, H_1) \tag{6.6}$$

as a function of the expected signal of interest counts. We can express such a distribution function in terms of the HXR flux from the whole Sun by using the conversion

$$Flux = \frac{s}{\Delta t\,\Delta E\,\Delta A}\frac{\Delta\Omega_\odot}{\Delta\Omega_{on}}, \tag{6.7}$$
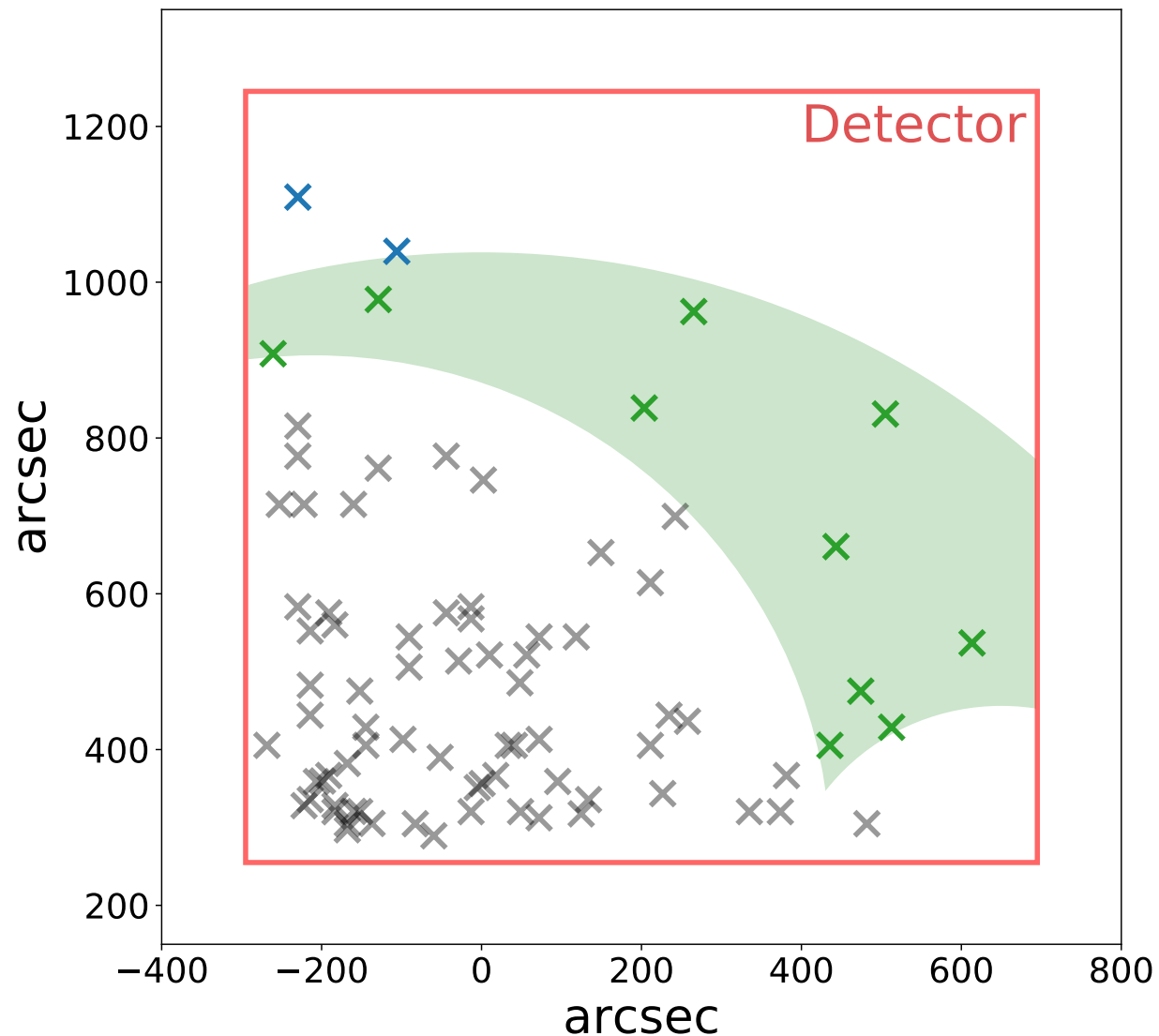
Figure 6.5: Counts registered by one of the FOXSI-2 silicon detectors when pointing to target I. The area in solid green sets the limit we chose as a region mostly free of ghost rays inside the solar disk (see Figure 6.4 for reference). The red square shows one detector FOV. All Xs in the plot are events recorded for one of the detectors. The dots are black if they are classified as ghost rays, green if the events fall within the solar region free of ghost rays, and blue if they are outside the solar disk.

	D101	D104	D105	D108	All four Det
N_{ON} ($\Delta t_{ON} = 68.5$ s)	13	9	10	10	36
N_{OFF} ($\Delta t_{OFF} = 24.2$ s)	3	1	1	4	9
α	0.920	0.872	0.869	0.859	0.887
$P(H_0|N_{ON}, N_{OFF}, \alpha)$	8.3×10^{-3}	5.5×10^{-3}	2.8×10^{-3}	6.2×10^{-2}	1.2×10^{-5}
S_b	2.64	2.78	2.99	1.86	4.4
$\lambda_{2\sigma}$	19.09	15.52	16.83	14.73	10.5

Table 6.1: Input (three first rows) and output (three last rows) parameters of the ON/OFF Li-Ma analysis applied to four of the FOXSI-2 silicon detectors (first four columns). The right most column has the ON/OFF Li-Ma parameters for the case in which we combine data of all four detectors. N_{ON} are the counts recorded during the ON configuration of target I/FOXSI-2 observations (green area of Figure 6.4). N_{OFF} are the counts for the background observations. α is estimated following equation 6.4 (for individual detectors) and equation 6.8 (for the case of all four detectors combined). $P(H_0|N_{ON}, N_{OFF})$ are the probabilities that the null hypothesis (H_0) is true given the particular values of N_{ON}, N_{OFF} and α. S_b is the Bayesian significance for the existence of a hypothetical signal s on top of the background during the ON-configured observations. $\lambda_{2\sigma}$ is the upper limit (in counts) with a 2σ precision for the flux of such a hypothetical source s.

where Δt is the observation time (corrected by the detector livetime), ΔE is the observed energy bandwidth, and ΔA is the optics effective area averaged over the energy bands considered (5-10 keV). We additionally correct by the scale ratio of solid angles $\left(\frac{\Delta \Omega_\odot}{\Delta \Omega_{on}}\right)$ to get an estimate of the flux over the whole observable solar corona. Using the conversion in expression 6.7 we plot the probability distribution function for each of the four detectors in Figure 6.6. Additionally, Figure 6.6 displays vertical dashed lines indicating the upper limits with a 2σ certainty for distribution functions of each of the four detectors. Regardless of the very low count statistics, all four colored distribution functions in Figure 6.6 exhibit similar behaviours, with maximum probabilities around $\sim$0.03 s^{-1} cm^{-2} keV^{-1} and comparable upper limits.

The gray filled curve in Figure 6.6 corresponds to the normalized source distribution function, versus the HXR solar flux, using data from all four detectors put together (accounting for the respective livetimes and effective areas of each detector/optics ensemble). To compute the ON/OFF Li-Ma analysis for the combination of the four detectors, α is transformed into $\alpha_{combined}$ defined as

$$\alpha_{combined} = \frac{\sum_d T_{on} \cdot A_{on} \cdot lt_{on} \cdot \Omega_{on}}{\sum_d T_{off} \cdot A_{off} \cdot lt_{off} \cdot \Omega_{off}}, \tag{6.8}$$
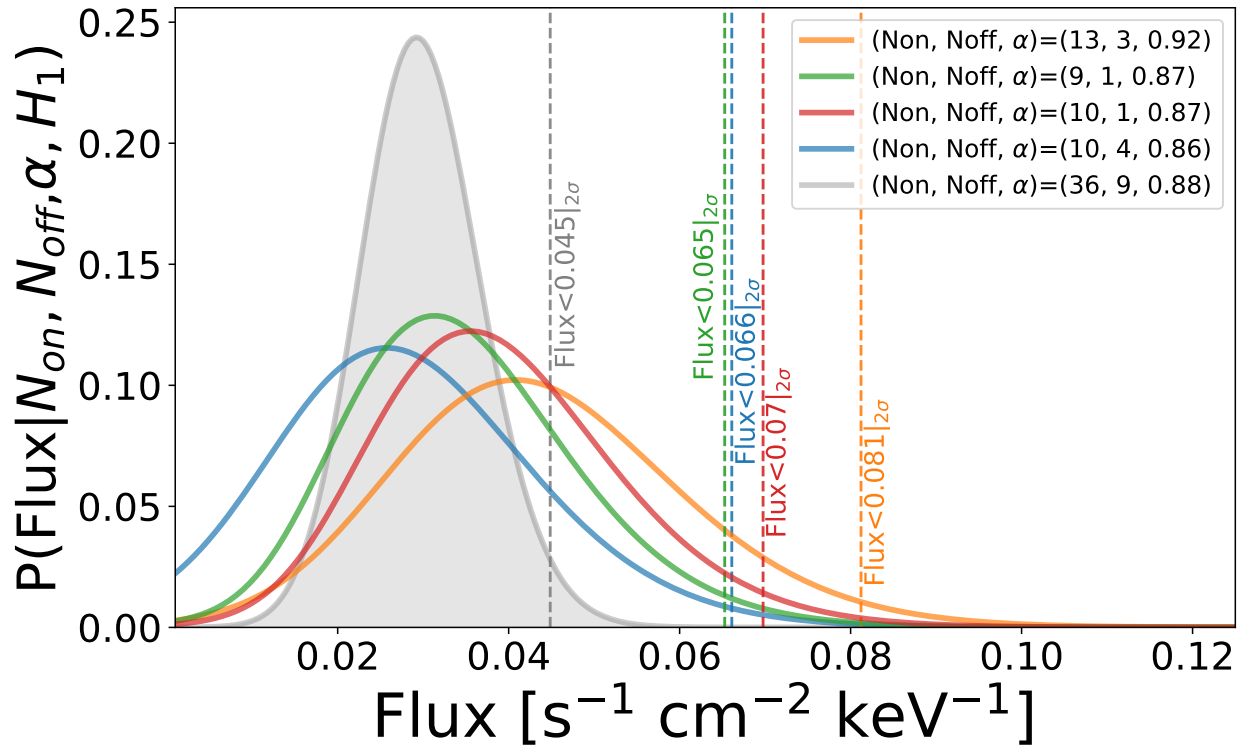
Figure 6.6: Source flux distribution functions for four of the silicon detectors in FOXSI-2. The lines are colored to match Table 6.1. All four colored distribution functions show a similar profile. The slight differences among the lines can be attributed to low count statistical effects. The dashed vertical lines are the upper limits with a 2σ certainty for each of the four distribution functions. The gray-filled curve is the normalized distribution function putting together the observations of all four detectors (accounting for each detector livetime and average optics effective area). The corresponding upper limit (gray dashed line) corresponds to a HXR solar flux of >0.045 s^{-1} cm^{-2} keV^{-1}. The maximum value of the gray distribution function lies at ~ 0.029 s^{-1} cm^{-2} keV^{-1}.

where $\sum_d$ is the sum over each of the four detector/optics sets. When performing the single ON/OFF Li-Ma analysis for the four detectors combined, the statistical significance of the measurements improves, $S_b = 4.4$ (see Table 6.1). In general, such a high significance suggests the detection of a signal. However, we abstain from claiming that that signal comes from the quiet Sun for this particular case. The reason is that although we characterized the most severe sources of ghost rays, there may still be stray light of other origins that we are not accounting for. Such possible additional stray light could come from a relatively slight misalignment among the optics module axes (that we believe to be under ~1.5 arcminutes based on measurements performed before and after the rocket flight). The optics point spread function's wings could also be another source of extra faint stray light. Within the calibration resources available in a sounding rocket program, it is not possible to completely rule out the presence of ghost rays in our measurement area. Instead, we report an upper limit for a signal of solar origin. Our careful ghost ray treatment enables this to be a highly sensitive limit. From the analysis that uses data from all four detectors, we found an upper limit for the HXR quiet Sun flux of 0.045 s^{-1} cm^{-2} keV^{-1} with a 97.72% (2σ) certainty (dashed vertical grey line in Figure 6.6). If we want to be conservative with the claims in this work, we can instead choose the largest of the four limits shown in Figure 6.6. That conservative limit is 0.081 s^{-1} cm^{-2} keV^{-1} (dashed vertical orange line in Figure 6.6).

6.9 Statistical analysis of the FOXSI-3 quiet Sun observations

Because of the lack of in-flight background measurements during the FOXSI-3 observation, we used two alternatives to analyze the quiescent data collected during that flight. The first (Gehrels' method hereafter) sets upper limits assuming a source (or mix of weak sources) described with a Poisson distribution. For our second approach, we use background measurements taken in FOXSI-2 to set upper limits on the FOXSI-3 observations.

6.9.1 Gehrels' method to set upper quiet Sun limits for FOXSI-3

Gehrels, 1986 provided a set of upper limit tables for hypothetical signal rates as the source(s) of a small number of observed events. We used the total number of counts observed by each of the three silicon detectors, summarized in Table 6.2, to set the upper limits in Table 6.3 for a 2σ confidence level. Table 6.3 also contains the upper limit flux ($F_{2\sigma}$) computed using a modified version of equation 6.7 where we replace s in the expression with the values of $\lambda_{2\sigma}$:

$$F_{2\sigma} = \frac{\lambda_{2\sigma}}{\Delta t \, \Delta E \, \Delta A} \frac{\Delta\Omega_\odot}{\Delta\Omega_{on}}. \tag{6.9}$$

	D102	D105	D106	All three Det	Obs. time [s]
T1 counts	3	0	3	6	128.2
T2 counts	0	1	1	2	24.0
T3 counts	1	1	0	2	144.6
T4 counts	1	0	1	2	26.3
T5 counts	0	0	0	0	44.2
All target counts	5	2	5	12	367.3

Table 6.2: FOXSI-3 observation summary. Counts recorded in the 5-10 keV energy range with three silicon detectors (D102, D105, and D106). T1-T5 are the targets pointed during the rocket observations according to figure 6.3. The second to the right most column shows the sum of the counts observed with the three detectors.

	D102	D105	D106	All three Det
$\lambda_{2\sigma}$	11.8	7.3	11.8	21.16
$F_{2\sigma}$ [s^{-1}cm^{-2}keV^{-1}]	2.4×10^{-3}	1.3×10^{-3}	4.1×10^{-3}	6.0×10^{-4}

Table 6.3: FOXSI-3 upper limits with a 2σ confidence level ($\lambda_{2\sigma}$, in counts) evaluating the existence of a hypothetical signal present during the observations. These upper limits are directly extracted from the tables in Gehrels, 1986 for 2, 5, 5, and 12 counts respectively. $F_{2\sigma}$ are the HXR solar fluxes estimated from the $\lambda_{2\sigma}$ values when computed with the instrument response.

Despite the impossibility of doing background removal, applying Gehrels' method over the more than six minutes of observation time during FOXSI-3 gives us upper limits that are over two orders of magnitude lower than what we found for FOXSI-2. This is further evidence that the region identified as free of ghost rays may still contain background X-rays of solar or non-solar origin.

6.9.2   ON/OFF Li-Ma analysis on the FOXSI-3 observations

To implement the ON/OFF Li-Ma method, it is critical to have an OFF configured observation, i.e., a background measurement. We identified D105 as the single silicon detector flown in both FOXSI-2 and FOXSI-3 rocket campaigns. The FOXSI-2 and FOXSI-3 instruments were launched using the same type of rocket, comparable trajectory parameters, and similar ambient conditions for the payload. We can argue that because of the similarities of the two flights, we can use D105 background measurements from FOXSI-2 to apply the ON/OFF Li-Ma method with D105 observations recorded during FOXSI-3. Table 6.4 summarizes the

D105						
N_{ON}	N_{OFF}	α	$P(H_0)$	S_b	$\lambda_{2\sigma}$	$F_{2\sigma}$ [s^{-1}cm^{-2}keV^{-1}]
2	1	16.1	0.89	0.14	5.43	9.6×10^{-4}

Table 6.4: Summary table for the input and output parameters of the ON/OFF Li-Ma method applied exclusively to D105 using solar observations from FOXSI-3 and background measurements from FOXSI-2. N_{ON} are the number of events observed by D105 during the entire 6.49 minutes of observation of FOXSI-3. N_{OFF} are the counts register by D105 during the 24.2 seconds the attenuators were activated during FOXSI-2. α is calculated according to equation 6.4. $P(H_0|N_{ON}, N_{OFF})$ is the probability that the null hypothesis (H_0, for N_{ON}, N_{OFF}, and α given). S_b is the Bayesian significance for the existence of an hypothetical quiet Sun signal s. $\lambda_{2\sigma}$ is the upper limit (in counts) with a 2σ confidence level for such a hypothetical source s. $F_{2\sigma}$ is the same upper limit but in units of s^{-1}cm^{-2}keV^{-1}.

result of applying such an ON/OFF Li-Ma analysis. We highlight that the HXR solar flux with a 2σ confidence level obtained with this method, $F_{2\sigma} = 9.6 \times 10^{-4}$ s^{-1} cm^{-2} keV^{-1}, is of the same order of magnitude as the one found using Gehrels' method (which does not assume a background). The fact that the FOXSI-3 observation time was over six times longer than that of FOXSI-2 causes $\lambda_{2\sigma}$ to be significantly reduced (in this case, around 70 times smaller). Figure 6.7 shows the distribution function for D105 according to the ON/OFF Li-Ma analysis. There are two remarkable traits in Figure 6.7. i) The distribution peak is at zero, consistent with the 89% probability that the null hypothesis is true. The null hypothesis demands no quiet Sun sources observed in the FOXSI-3 data, i.e., all counts being solely background during the ON configured measurements. ii) Consequently, the upper limits dramatically shift to lower values than those obtained for FOXSI-2 (see Figure 6.6). There is a difference of over two orders of magnitude between the limits of FOXSI-2 and FOXSI-3. This difference, again, is the product of longer observation times, larger collecting areas (detectors free of ghost rays), and the fact that the whole Sun was quiet for the FOXSI-3 launch.

In sections 6.5 and 6.7, we presented a thorough analysis to identify regions free of ghost rays during the FOXSI-2 observations. For FOXSI-3, ghost rays are not a concern. The reasons lie in the fact that the Sun exhibited an extremely quiescent atmosphere for FOXSI-3 compared to FOXSI-2. During the FOXSI-3 observations, we scanned most of the solar disk (including the aged active region, which was the hottest part at the time) as depicted in Figure 6.3. During those observations, we did not find a single discernible intense compact source in HXRs. FOXSI-3 only registered sparse data, as shown in Table 6.2. According to Buitrago-Casas et al., 2020, ghost-ray intensities are one order of magnitude fainter than their focused counterparts. Therefore, any ghost-ray background in FOXSI-3 would have been one order of magnitude lower than what we observed within the detector's field of
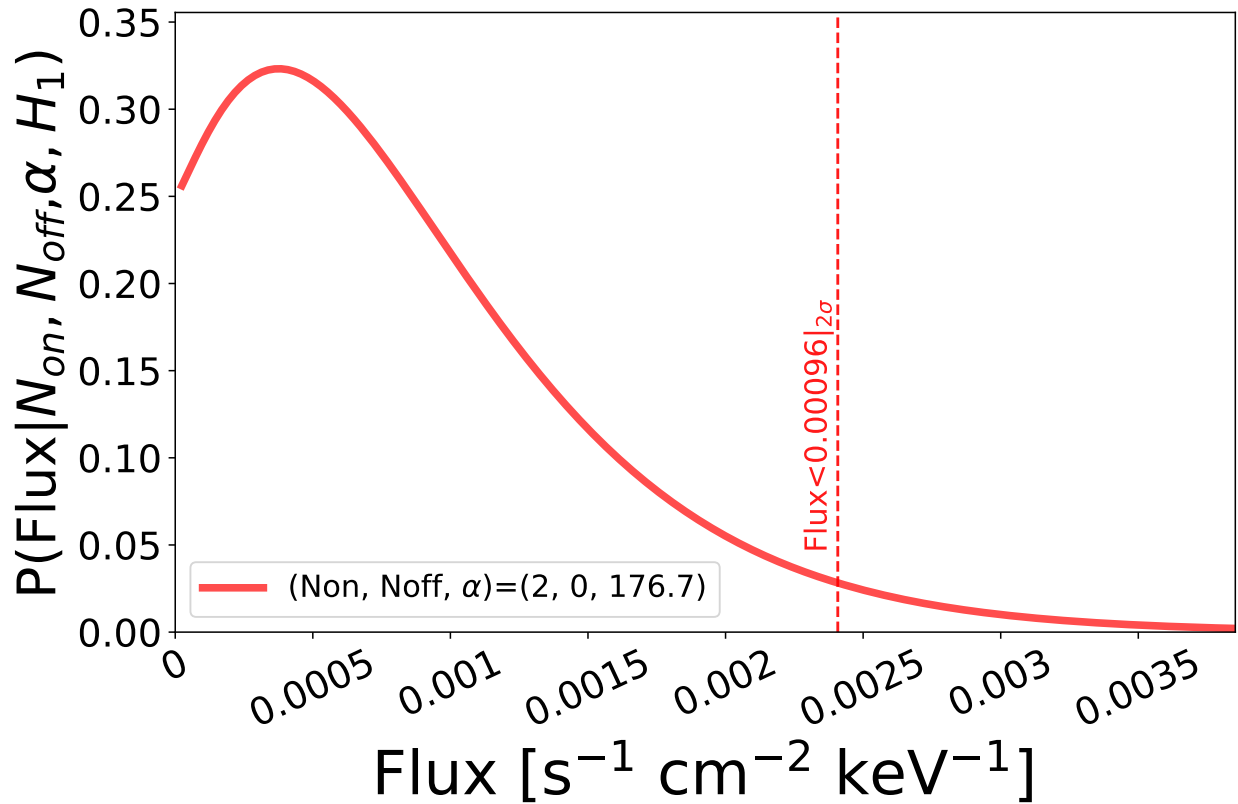
Figure 6.7: Probability distribution function of a hypothetical HXR solar source as a function of its expected flux. This curve is constructed by implementing the ON/OFF Li-Ma method using FOXSI-3 observations and FOXSI-2 background measurements as the ON and OFF configurations, respectively. This figure corresponds to data registered by D105 which was the only silicon detector flown in FOXSI-2 and -3.

views. Since for FOXSI-3, both ghost rays and on-axis photons would have the same origin (quiet Sun HXRs), the upper limits we report still hold.

6.10   Comparing our upper limits with those previously reported

Iain G Hannah et al., 2010 used off-pointing RHESSI data to estimate upper limits for HXR quiet Sun emission. They reported upper thresholds for the photon flux as shown in the Figure 6.8. We overlap in the same Figure 6.8 three upper limits from our analyses. In orange we plot the upper limit we obtained by combining FOXSI-2 data from four silicon

detectors (4.5×10^{-2} s^{-1}cm^{-2}keV^{-1}). In red, we show the upper limit we calculate using the ON/OFF Li-Ma method applied to D105 observations during FOXSI-3, and background measurements from FOXSI-2 (that is 9.6×10^{-4} s^{-1}cm^{-2}keV^{-1}). The blue upper limit in Figure 6.8 (6.0×10^{-4} s^{-1}cm^{-2}keV^{-1}) is computed using Gehrels' method over data from three silicon detectors flown in FOXSI-3. For reference, Iain G Hannah et al. upper limits for the 3-6 keV and 6-12 keV are 3.4×10^{-2} s^{-1}cm^{-2}keV^{-1} and 9.5×10^{-4} s^{-1}cm^{-2}keV^{-1}, respectively. The FOXSI-2 and -3 limits found in this work are similar to with the deepest limits for solar HXR emission yet reported (Iain G Hannah et al., 2010).

Iain G Hannah et al. (2010) used the limits they found with RHESSI to constrain the parameter space of an isothermal model and thin-target emission models (power-law and kappa distributions) for the solar corona. Iain G Hannah et al. (2010) showed with their limits that it is unlikely for nanoflares with non-thermal effects to be involved in heating the corona. They concluded that showing that such nanoflares would require a steep electron spectrum $E^{-\delta}$ with $\delta > 5$ extending to very low energies into the thermal energy range (<1 keV). Remarkably, the upper limits we found using FOXSI-3 data are in statistical agreement with those reported by Iain G Hannah et al. (2010). Thus, all the conclusions asserted by Iain G Hannah et al. (2010) about the nature of nanoflares still hold.

6.11 Discussion and conclusions

In this chapter, we provided for the first time a quantitative limit of the quiet Sun HXR flux using data taken with the FOXSI sounding rocket instrument exclusively. We used data from FOXSI's second and third flights, corresponding to high and low solar cycle activity periods, respectively.

Because of the high solar activity during the FOXSI-2 flight, the Sun had several bright compact HXR sources distributed all over the disk. When located off-axis, such compact sources produced ghost rays extending partially into FOXSI's detector areas. We characterized the ghost rays impact on the instrument by implementing a ray-tracing simulation. Using those algorithms, we identified areas within the detectors mostly free of ghost rays. This approach allowed us for the first time to assess the flux in HXRs of a quiescent solar region during a time of substantially high solar activity. This is something that has never been possible to do before with solar HXR telescopes that use indirect imaging techniques, like RHESSI. We implemented a Bayesian analysis optimized for very low statistics (the Li-Ma ON/OFF method) to estimate an upper threshold of 0.045 s^{-1}cm^{-2}keV^{-1} for the HXR flux (5-10 keV) within the identified quiet Sun area almost entirely free of ghost rays.

This doctoral work is also the first science work that uses FOXSI-3 data. The Sun was at solar minimum when FOXSI-3 flew. Only a very aged active region observable in EUV was present on the solar disk. No compact source in HXRs was discernible during the time the
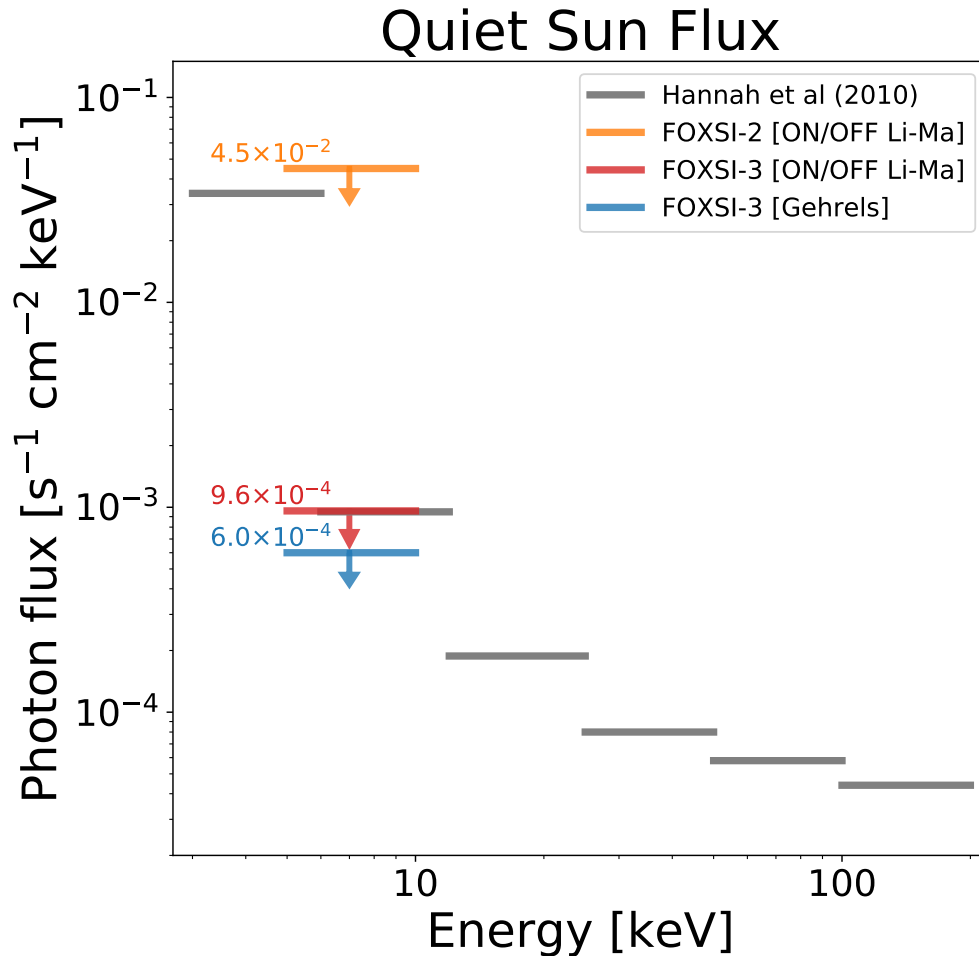
Figure 6.8: Upper limits of the quiet Sun photon flux spectrum. The thresholds in gray are taken from Iain G Hannah et al., 2010. They correspond to 2σ limits calculated based on the analysis of 11.9 days of solar off-pointing observations with RHESSI during solar quiescent conditions. We overlap three upper limits we found using FOXSI-2 and -3 data, all three in the 5-10 keV energy range. The limit in orange (4.5×10^{-2} s^{-1}cm^{-2}keV^{-1}) is calculated by implementing the ON/OFF Li-Ma method over an area free of ghost rays during ~ 1 minute of FOXSI-2 observations. The threshold in red (9.6×10^{-4} s^{-1}cm^{-2}keV^{-1}) corresponds to the upper limit obtained by combining FOXSI-3 measurements of only one detector that also had background measurements from the FOXSI-2 flight. This limit was also computed by implementing the ON/OFF Li-Ma method. The blue bar (6.0×10^{-4} s^{-1}cm^{-2}keV^{-1}) is the upper threshold estimated from the 6.49 minutes of observations with three FOXSI-3 silicon detectors combined. For this last threshold (blue), we used Gehrels, 1986 approach to set the upper expected rate of a hypothetical source of solar origin.

FOXSI-3 payload targeted the Sun. We used the entire 6.49 minutes of rocket observation time to assess the HXR quiet Sun flux for this period of minimum solar activity. We set upper limits for this flux implementing two independent techniques. We calculated an upper limit of $9.6{\times}10^{-4}$ $\mathrm{s}^{-1}\mathrm{cm}^{-2}\mathrm{keV}^{-1}$ applying the Li-Ma ON/OFF method over data of one detector flown in FOXSI-2 (for background measurements) and FOXSI-3 (for direct quiet Sun observations). The lowest quiet Sun HXR flux upper limit we report here is $6.0{\times}10^{-4}$ $\mathrm{s}^{-1}\mathrm{cm}^{-2}\mathrm{keV}^{-1}$. We obtained this limit using data from three silicon detectors combined (all flown in FOXSI-3) and applying Gehrels' method, purely based on Poisson statistics.

The exact nature of why the FOXSI-2 upper limit is almost two orders of magnitude higher than the FOXSI-3 limits is not fully clear. Naïvely, this difference suggests that the quiet Sun HXR flux during a time of intense solar activity (the case for FOXSI-2) might be higher than its counterpart during a minimum in the solar cycle (scenario for FOXSI-3). We can not entirely rule out such a possibility. However, there is a caveat we want to manifest in this case. For FOXSI-2, we isolated a region within the solar disk free of the most intense ghost rays. Yet, some remnant ghost rays from other weaker sources could potentially still be getting into the detectors, affecting our estimated FOXSI-2 constraints. Direct focusing HXRs brings the possibility of assessing quiet Sun emission during periods of high solar activity. But, additional optical elements need to be part of the instrument to diminish ghost rays. Future space-based solar HXR telescopes using Wolter-I optics should implement ways to minimize (if not entirely block) ghost rays to analyze quiet Sun emission during maximums of solar activity. Further observations will give a definite answer on whether or not quiet Sun HXR fluxes correlate with the solar cycle.

The HXR upper limits we calculate here using FOXSI data can be compared with prior reported constraints. Figure 6.8 compares our FOXSI limits (in the 5-10 keV energy range) with those estimated by Iain G Hannah et al. (2010) using almost 12 cumulated days of RHESSI solar off-pointing observations during periods of minimum activity. Iain G Hannah et al. (2010) binned the limits using the following energy bins; 3-6 keV, 6-12 keV, 12-25 keV, 25-50 keV, 50-100 keV, and 100-200 keV. The upper limits Iain G Hannah et al. (2010) report for the 3-6 keV and the 6-12 keV energy range, with a 2σ confidence level, are 3.4×10^{-2} $\mathrm{s}^{-1}\mathrm{cm}^{-2}\mathrm{keV}^{-1}$ and 9.5×10^{-4} $\mathrm{s}^{-1}\mathrm{cm}^{-2}\mathrm{keV}^{-1}$, respectively. All the quiet Sun HXR limits we report in this work are in agreement with those thresholds calculated by Iain G Hannah et al. (2010). In particular, the FOXSI-3 limits that correspond to a period of minimum solar activity lie in the same order of magnitude as the 6-12 keV limit from Iain G Hannah et al. (2010), $\sim 10^{-3}$ $\mathrm{s}^{-1}\mathrm{cm}^{-2}\mathrm{keV}^{-1}$.

Iain G Hannah et al. (2010) not only reported upper limits, they also presented interpretations of what these limits imply over possible solar physical processes with the potential of producing HXR emissions. Such interpretations include the assessment of nanoflare isothermal emission, nanoflare non-thermal thick-target and thin-target emissions, and solar Axions. Since the FOXSI limits are not substantially lower than those from Iain G Hannah et al.,
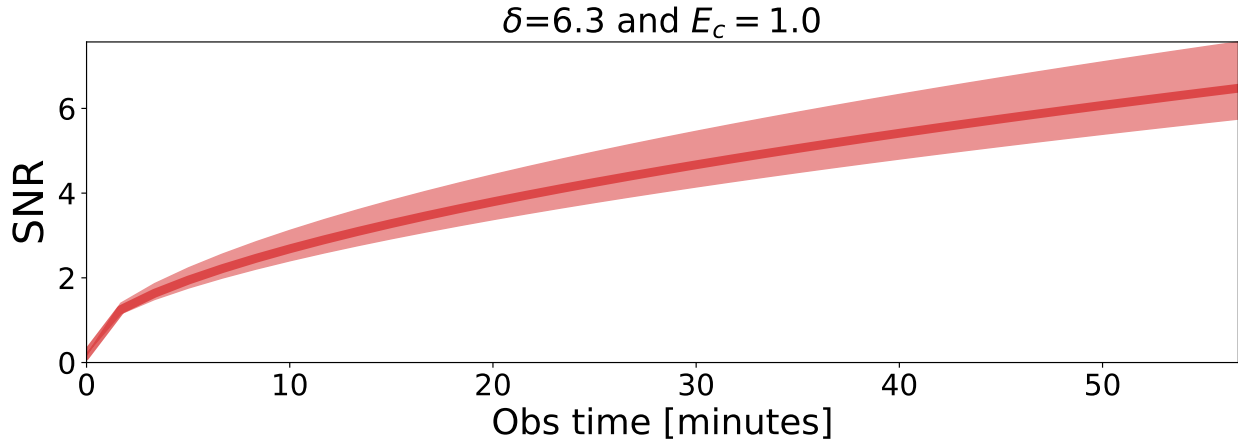
Figure 6.9: Signal to noise ratio (SNR) as a function of time, assuming the existence of a power-law hard X-ray spectrum ($\delta = 6.3$ and $E_c = 1.0$ keV) produced via nanoflare accelerated electrons in a thick target process. This assumed nanoflare source of hard X-rays would produce a flux of $\sim$23 counts per minute measured by FOXSI. The hypothetical existence of a hard X-rays nanoflare source with these characteristics would demand observing the quiet Sun for at least 45 minutes to have a SNR > 5.

2010, all their physical interpretations still hold. In particular, FOXSI limits continue to agree with the isothermal emission constraints that Iain G Hannah et al., 2010 (see Figure 3 in their paper) estimated and compared with results from previous missions that observed the quiet Sun in X-rays, like Sphinx (Sylwester et al., 2010).

More recently, in 2017, Marsh et al. searched for HXR emission in the quiet solar corona with the Nuclear Spectroscopic Telescope Array (NuSTAR) satellite. They used the first observations of the quiet Sun with NuSTAR, which occurred on 2014 November 1. At the time of these observations, an off-axis solar active region contributed a notable amount of ghost rays. Marsh et al., 2017 were interested in searching for transient HXR brightenings present in the quiet Sun. To do so, they looked for increases in HXRs on timescales of 100 s in two energy bands, 2.5-4 keV and 10-20 keV. For the 10-20 keV, they additionally searched brightenings with timescales of 30 and 60 s. Marsh et al., 2017 set upper limits of $\sim$17 s^{-1}cm^{-2}keV^{-1} for the 2.5-4 keV energy range, and 0.17 s^{-1}cm^{-2}keV^{-1} for 4-20 keV. This last limit is almost four times higher than the FOXSI-2 upper quiet Sun threshold and two orders of magnitude higher than the limits from FOXSI-3. Marsh et al., 2017 discussed that during their quiet Sun NuSTAR observations, the nonsolar background would be the dominant source of high energy emission in the NuSTAR FoV. Marsh et al., 2017 cited Wik et al., 2014, who give incident background rates of $\sim$2$\times$10^{-5} s^{-1}cm^{-2}keV^{-1} for 4-20 keV, to support their argument.

We highlight that with observations of only $\sim$ one minute for FOXSI-2 and $\sim$ six minutes for FOXSI-3, we obtained quiet Sun HXR upper limits comparable with previous observations $\sim$ 12 days long (Iain G Hannah et al., 2010). As demonstrated by Sylwester et al., 2010, with observations extending over months of low levels of solar X-ray activity, the sensitivity increases for quiet Sun emission assessments. Particularly for a satellite mission version of FOXSI, we anticipate a two to three orders of magnitude increased sensitivity. This increase will be a direct result of increasing the observation time. Using the background rate observed with FOXSI-2 together with the expected hard X-ray rates from nanoflares (see, e.g., Krucker et al. (2011) and Iain G Hannah et al. (2010)), we can estimate the minimum observation time required to get direct evidence of nanoflare emission in hard X-rays. Figure 6.9 shows an example of signal-to-noise ratio (SNR) as a function of time, assuming nanoflares produce a flux of $\sim$23 counts per minute in the energy band measurable by FOXSI. Figure 6.9 suggests that the FOXSI rocket payload would need to observe the quiet Sun for at least an hour to accumulate enough statistics to make a direct detection of such hypothetical nanoflare non-thermal hard X-rays. A sounding rocket offers only a few minutes of observation time ($\gtrsim$ 6 minutes). A longer-term space platform (a satellite) is demanded to assess thoroughly quiet Sun hard X-rays, i.e., their connection with the physics of small impulsive energy releases in the corona. Figure 6.9 corresponds to a particular hypothetical case, as an example, in which we assume nanoflares accelerate electrons that subsequently emit Bremsstrahlung hard X-rays with a power-law spectrum of $\delta = 6.3$ and $E_c = 1.0$ keV. If accelerated electrons in nanoflares had any of the three power laws Iain G Hannah et al. (2010) highlight in Figure 4 of their paper ($\delta = 5$ for $E_c = 0.32$ keV, $\delta = 6$ for $E_c = 0.81$ keV, and $\delta = 7$ for $E_c = 1.24$ keV), the FOXSI rocket payload would need at least two hours of observation time to record sufficient hard X-rays to claim a detection. Whether nanoflares accelerate electrons via a thick target process is still uncertain. More so to know a priori what the parameters δ and E_c should be. However, longer FOXSI observations times will constrain the parameter space more, enabling us to explain the physics of any detected nanoflare signature accurately.

Chapter 7

Summary and Conclusions

The Sun's corona constitutes the hottest region of the upper solar atmosphere. It also hosts the most powerful explosive events of the solar system, solar flares. Solar flares produce hard X-rays with time, space, and energy distributions whose shapes depend on the physical properties and dynamics of electrons accelerated during the explosive event. Larger flares emit a higher number of hard X-rays, i.e., they have been easily and commonly observed with solar-dedicated telescopes that implement indirect imaging techniques (like RHESSI and STIX). However, given RHESSI's and STIX's limited sensitivity and dynamic ranges, smaller flares have been challenging to measure because of their fainter fluxes in hard X-rays. Yet, the smallest flare-like solar events (nanoflares), seen only in extreme ultraviolet and soft X-rays to date, are being continuously explored as a plausible explanation for the coronal heating problem. This open problem in heliophysics investigates why the corona maintains an average peak temperature up to one thousand times higher than the photosphere even during periods of minimum solar activity.

Assuming nanoflares follow an equivalent dynamic as their larger counterparts, a sustained faint emission in hard X-rays would be expected due to a nanoflares' hypothetical copious and steady presence in the corona. Such a faint emission in hard X-rays has not been directly observed in the quiet corona yet. But, using ∼12 days of quiescent solar-off-pointing observations of RHESSI, Iain G Hannah et al. in 2010 set upper limits for quiet Sun emissions in hard X-rays. Together with observations at other wavelengths, these limits can constrain the physical properties of the still individually unresolved hard X-ray sources (nanoflares). This doctoral work investigated ways to set quiet Sun hard X-ray upper limits using observations from the FOXSI sounding rocket experiment, which excels in dynamic range and sensitivity when compared with RHESSI.

Chapter 3 introduced the FOXSI sounding rocket payload experiment. It discussed the challenges of focusing X-rays and showed novel ways of achieving this goal using a wide range of optical components. It highlighted solar and astrophysical applications of these components when available. The same chapter presented an overview of the different ele-

ments in the FOXSI telescope for each of the three successful past rocket flights and the fourth coming rocket campaign. It described solar activity and flight pointing for the second and third rocket flights. Data from these two flights are used in the subsequent chapters to analyze the emission in hard X-rays from the quiet Sun targeted with FOXSI.

A crucial aspect of analyzing very faint emissions in astrophysics is to understand and characterize instrument response thoroughly. Chapter 4 focused on the calibration of the optics modules that have been part of the FOXSI rocket payload. It described the experimental setup and results for the optics effective area and characterization of the point spread functions via analyzes of their full width at half maximums and half power diameters.

The FOXSI optics performs splendidly for on-axis point (or very compact, a few arcmin in size) sources. However, off-axis hard X-ray sources can reflect incompletely (only once) on the optics and still get to the focal plane. These singly-bounced rays can cause ghost-ray backgrounds that deteriorate the net sensitivity of the instrument. Chapter 5 comprehensively investigated ways to minimize the number of ghost rays via designing additional optical components (e.g., honeycomb-type collimators and blockers) and using a ray-tracing simulation that characterizes their background patterns. That ray-tracing simulation, `foxsisim`, is a tangible product of this doctoral work. `foxsisim` is a publicly available tool able to study the optical performance of Wolter-I mirrors using either a proper paraboloid/hyperboloid geometry or a conic approximation figure (which is the case for the NuSTAR telescope for example). The numerical tools is also able to assess the energy response of the optics given an optics prescription, a mirror material, and a surface finish.

FOXSI-2 targeted a region of quiet Sun near the solar north pole for about a minute. A few solar hard X-ray sources were located off-axis for that pointing, causing the quiet Sun observations to be "contaminated" with ghost rays. Those ghost rays did not cover the entire field of view. Instead, they were primarily enclosed within a detector sub-region. By using `foxsisim` for the FOXSI-2 quiet Sun pointing configuration, it was possible to characterize the ghost ray pattern and isolate detector areas with minimal ghost ray backgrounds. These detector areas, mostly free of ghost rays, had the necessary sensitivity for assessing hard X-ray emissions from the quiet Sun. Chapter 6 presented this ghost ray analysis and a Bayesian study of the quiet Sun observations performed over FOXSI-2 and -3 data. This Bayesian approach resulted in setting upper thresholds of quiet Sun hard X-ray emission and probability distributions for the expected flux when quiet Sun sources are assumed to exist. For FOXSI-2 (a time of high solar activity), the reported upper limit was of $\sim 10^{-2}$ s^{-1}cm^{-2}keV^{-1} order of magnitude, while for FOXSI-3 (when the Sun was passing for a minimum of the solar cycle) the upper limit lied on the $\sim 10^{-4}$ s^{-1}cm^{-2}keV^{-1} order of magnitude. Chapter 6 concluded with some plausible explanations for the discrepancy between the FOXSI-2 and -3 upper limits and a short discussion of the potential of direct focusing optics for the study of the quiet Sun in hard X-rays. This doctoral work suggests that a possible future spacecraft using FOXSI's concept would allow enough observation time

to constrain the current hard X-ray quiet Sun limits further or perhaps even make direct detections.

Although the building blocks are already in place for a FOXSI satellite instrument, further advances are needed to equip the next generation of solar X-ray explorers. The FOXSI rocket instrument is currently funded and under development for its fourth flight (FOXSI-4) to occur in Spring 2024. This rocket will fly a significantly upgraded payload in NASA's first solar flare campaign. FOXSI-4 will use higher angular resolution optics/detector pairs to investigate fine spatial structures (both bright and faint) in a medium/large solar flare. High-resolution hard X-ray observations of large solar eruptions can significantly enable our understanding of the physics of solar flares. These observations will allow us to discern between individual footpoints and coronal sources where particles get accelerated in the corona. In addition to studying particle acceleration, FOXSI-4's high-resolution capability will also enable precise characterizations of the superhot plasma (> 30 MK) sources. The rocket campaign will occur during one of the Parker Solar Probe (PSP) perihelia, allowing coordination between this spacecraft and other instruments that observe the Sun at different wavelengths. These instruments include the recently launched Solar Orbiter, the Daniel K. Inouye Solar Telescope (DKIST), and sounding rocket payloads launching in the same solar flare campaign (Hi-C and SNIFS), and other observatories that recurrently perform solar observations. This co-observation of a solar flare simultaneously with multiple instruments will enhance the multimessenger science conducted with hard X-rays, different wavelengths, and even in-situ particle detection onboard the solar probes.

Bibliography

Acton, L et al. "The Yohkoh mission for high-energy solar physics". In: *Science* 258.5082 (1992), pp. 618–625.

Adelberger, Eric G et al. "Solar fusion cross sections. II. The p p chain and CNO cycles". In: *Reviews of Modern Physics* 83.1 (2011), p. 195.

Alaoui, Meriem and Gordon D. Holman. "Understanding Breaks in Flare X-Ray Spectra: Evaluation of a Cospatial Collisional Return-current Model". In: *ApJ* 851.2, 78 (Dec. 2017), p. 78. DOI: 10.3847/1538-4357/aa98de. arXiv: 1706.03897 [astro-ph.SR].

Alaoui, Meriem et al. "Role of suprathermal runaway electrons returning to the acceleration region in solar flares". In: *The Astrophysical Journal* 917.2 (2021), p. 74.

Alexander, C. E., G. Del Zanna, and R. C. Maclean. "Hinode observations and 3D magnetic structure of an X-ray bright point". In: *Astronomy and Astrophysics* 526, A134 (Feb. 2011), A134. DOI: 10.1051/0004-6361/201014045.

Alvarado-Gómez, JD et al. "Magneto-acoustic energetics study of the seismically active flare of 15 February 2011". In: *Solar Physics* 280.2 (2012), pp. 335–345.

Antolin, Patrick et al. "Reconnection nanojets in the solar corona". In: *Nature Astronomy* 5.1 (2021), pp. 54–62.

Aquila, Andrew Lee. *Development of extreme ultraviolet and soft x-ray multilayer optics for scientific studies with femtosecond/attosecond sources*. University of California, Berkeley, 2009.

Archontis, V et al. "Emergence of magnetic flux from the convection zone into the corona". In: *Astronomy & Astrophysics* 426.3 (2004), pp. 1047–1063.

Arnold, H et al. "Electron Acceleration during Macroscale Magnetic Reconnection". In: *Physical Review Letters* 126.13 (2021), p. 135101.

Artzner, Guy Edouard, Jean Pierre Delaboudiniere, and Xueyan Song. "Photon sieves as EUV telescopes for solar orbiter". In: *Innovative Telescopes and Instrumentation for Solar Astrophysics*. Vol. 4853. International Society for Optics and Photonics. 2003, pp. 158–161.

Aschwanden, Markus J. "Do EUV nanoflares account for coronal heating?" In: *Physics of the Solar Corona and Transition Region*. Springer, 2000, pp. 233–247.

— "Irradiance observations of the 1–8 Å solar soft X-ray flux from GOES". In: *Solar Physics* 152.1 (1994), pp. 53–59.

— *New millennium solar physics*. Vol. 458. Springer, 2019.

Aschwanden, Markus J. "Particle acceleration and kinematics in solar flares". In: *Particle acceleration and kinematics in solar flares* (2002), pp. 1–227.

— *Physics of the solar corona: an introduction with problems and solutions*. Springer Science & Business Media, 2006.

— "Reconciling Power Law Slopes in Solar Flare and Nanoflare Size Distributions View all abstracts by submitter". In: *Solar Physics E-print Archive* (2022).

— "Self-organized criticality in solar and stellar flares: Are extreme events scale-free?" In: *The Astrophysical Journal* 880.2 (2019), p. 105.

Aschwanden, Markus J and Paul Boerner. "Solar corona loop studies with the atmospheric imaging assembly. I. Cross-sectional temperature structure". In: *The Astrophysical Journal* 732.2 (2011), p. 81.

Aschwanden, Markus J and Manuel Güdel. "Self-organized Criticality in Stellar Flares". In: *The Astrophysical Journal* 910.1 (2021), p. 41.

Aschwanden, Markus J and R. Nightingale. "Elementary Loop Structures in the Solar Corona Analyzed from TRACE Triple-Filter Images". In: *The Astrophysical Journal* 633.1 (Nov. 2005), pp. 499–517. DOI: 10.1086/452630.

Aschwanden, Markus J, Yan Xu, and Ju Jing. "Global energetics of solar flares. I. Magnetic energies". In: *The Astrophysical Journal* 797.1 (2014), p. 50.

Aschwanden, Markus J et al. "Automated temperature and emission measure analysis of coronal loops and active regions observed with the Atmospheric Imaging Assembly on the Solar Dynamics Observatory (SDO/AIA)". In: *Solar Physics* 283.1 (2013), pp. 5–30.

Aschwanden, Markus J et al. "The coronal heating paradox". In: *The Astrophysical Journal* 659.2 (2007), p. 1673.

Aschwanden, Markus J et al. "Time variability of the "Quiet" sun observed with TRACE. II. Physical parameters, temperature evolution, and energetics of extreme-ultraviolet nanoflares". In: *The Astrophysical Journal* 535.2 (2000), p. 1047.

Athay, R Grant. *The solar chromosphere and corona: Quiet Sun.* Vol. 53. Springer Science & Business Media, 2012.

Athiray, PS et al. "Calibration of the hard x-ray detectors for the FOXSI solar sounding rocket". In: *UV, X-Ray, and Gamma-Ray Space Instrumentation for Astronomy XX.* Vol. 10397. International Society for Optics and Photonics. 2017, 103970A.

Athiray, PS et al. "FOXSI-2 solar microflares. i. multi-instrument differential emission measure analysis and thermal energies". In: *The Astrophysical Journal* 891.1 (2020), p. 78.

Atkins, C et al. "X-ray optic developments at NASA's MSFC". In: *Damage to VUV, EUV, and X-ray Optics IV; and EUV and X-ray Optics: Synergy between Laboratory and Space III.* Vol. 8777. International Society for Optics and Photonics. 2013, 87770W.

Attwood, David. *X-Rays and Extreme Ultraviolet Radiation: Principles and Applications.* 2016.

Attwood, David and Anne Sakdinawat. *X-rays and extreme ultraviolet radiation: principles and applications.* Cambridge university press, 2017. Chap. 3.

Aulanier, G et al. "The standard flare model in three dimensions-ii. upper limit on solar flare energy". In: *Astronomy & Astrophysics* 549 (2013), A66.

Bahcall, JN and M. Cribier. "The Standard Solar Model". In: *Inside the Sun.* Ed. by Gabrielle Berthomieu and Michel Cribier. Dordrecht: Springer Netherlands, 1990, pp. 21–41. ISBN: 978-94-009-0541-2.

Bahcall, JN, M Fukugita, and PI Krastev. "How does the sun shine?" In: *Physics Letters B* 374.1-3 (1996), pp. 1–6.

Bakke, Helle, Lars Frogner, and Boris Vilhelm Gudiksen. "Non-thermal electrons from solar nanoflares-In a 3D radiative MHD simulation". In: *Astronomy & Astrophysics* 620 (2018), p. L5.

Ballmoos, Peter von et al. "CLAIRE: First light for a gamma-ray lens". In: *Experimental Astronomy* 20.1 (2005), pp. 253–267.

Barrière, Nicolas et al. "MAX, a Laue diffraction lens for nuclear astrophysics". In: *Focusing Telescopes in Nuclear Astrophysics.* Springer, 2006, pp. 269–278.

Basu, Sarbani. "Plot Thickens in Solar Opacity Debate". In: *Physics* 12 (2019), p. 65.

Battaglia, Marina, Paolo C Grigis, and Arnold O Benz. "Size dependence of solar X-ray flare properties". In: *Astronomy & Astrophysics* 439.2 (2005), pp. 737–747.

Battaglia, Marina, Galina Motorina, and Eduard P Kontar. "Multithermal representation of the kappa-distribution of solar flare electrons and application to simultaneous X-ray and EUV observations". In: *The Astrophysical Journal* 815.1 (2015), p. 73.

Baty, H, TG Forbes, and ER Priest. "The formation and stability of Petschek reconnection". In: *Physics of Plasmas* 21.11 (2014), p. 112111.

Benezeth, Yannick et al. "Comparative study of background subtraction algorithms". In: *Journal of Electronic Imaging* 19.3 (2010), p. 033003.

Benz, Arnold O. "Flare observations". In: *Living Reviews in Solar Physics* 14.1 (2017), pp. 1–59.

— *Kinetic processes in solar and stellar coronae.* 2002.

Benz, Arnold O and Säm Krucker. "Energy distribution of microevents in the quiet solar corona". In: *The Astrophysical Journal* 568.1 (2002), p. 413.

Benz, Arnold O et al. "Fine structure of the X-ray and radio emissions of the quiet solar corona." In: *Astronomy and Astrophysics* 320 (1997), pp. 993–1000.

Berge, David, S Funk, and J Hinton. "Background modelling in very-high-energy γ-ray astronomy". In: *Astronomy & Astrophysics* 466.3 (2007), pp. 1219–1229.

Berger, James O et al. "Objective Bayesian methods for model selection: Introduction and comparison". In: *Lecture Notes-Monograph Series* (2001), pp. 135–207.

Bewsher, D, CE Parnell, and RA Harrison. "Transition Region Blinkers–I. Quiet-Sun Properties". In: *Solar Physics* 206.1 (2002), pp. 21–43.

Bilderback, Donald H. "Review of capillary x-ray optics from the 2nd International Capillary Optics Meeting". In: *X-Ray Spectrometry: An International Journal* 32.3 (2003), pp. 195–207.

Bilenko, Irina A and Ksenia S Tavastsherna. "Coronal hole and solar global magnetic field evolution in 1976–2012". In: *Solar Physics* 291.8 (2016), pp. 2329–2352.

Birn, J et al. "Geospace Environmental Modeling (GEM) magnetic reconnection challenge". In: *Journal of Geophysical Research: Space Physics* 106.A3 (2001), pp. 3715–3719.

Biskamp, Dieter. "Magnetic reconnection in plasmas". In: *Astrophysics and Space Science* 242.1 (1996), pp. 165–207.

Blake, Richard L et al. "Interpretation of X-Ray Photograph of the Sun." In: *The Astrophysical Journal* 137 (1963), p. 3.

Bogachev, Sergey Aleksandrovich et al. "Microflares and nanoflares in the solar corona". In: *Physics-Uspekhi* 63.8 (2020), p. 783.

Boggs, Steven E. "The advanced compton telescope mission". In: *New Astronomy Reviews* 50.7-8 (2006), pp. 604–607.

Bradshaw, Stephen J and James A Klimchuk. "What dominates the coronal emission spectrum during the cycle of impulsive heating and cooling?" In: *The Astrophysical Journal Supplement Series* 194.2 (2011), p. 26.

Brejnholt, Nicolai F et al. "Demonstration of multilayer reflective optics at photon energies above 0.6 MeV". In: *Optics express* 22.13 (2014), pp. 15364–15369.

Brooks, David H et al. "Hinode/extreme-ultraviolet imaging spectrometer observations of the temperature structure of the quiet corona". In: *The Astrophysical Journal* 705.2 (2009), p. 1522.

Brosius, Jeffrey W, Adrian N Daw, and DM Rabin. "Pervasive faint Fe XIX emission from a solar active region observed with EUNIS-13: evidence for nanoflare heating". In: *The Astrophysical Journal* 790.2 (2014), p. 112.

Brown, John C. "On the thermal interpretation of hard X-ray bursts from solar flares". In: *Symposium-International Astronomical Union*. Vol. 57. Cambridge University Press. 1974, pp. 395–412.

— "Thick target X-ray bremsstrahlung from partially ionised targets in solar flares". In: *Solar Physics* 28.1 (1973), pp. 151–158.

Buitrago-Casas, J. C. et al. "FOXSI-4: the high resolution focusing X-ray rocket payload to observe a solar flare". In: *UV, X-Ray, and Gamma-Ray Space Instrumentation for Astronomy XXII*. Vol. 11821. International Society for Optics and Photonics. 2021, p. 118210L.

Buitrago-Casas, J. C. et al. "Methods for reducing singly reflected rays on the Wolter-I focusing mirrors of the FOXSI rocket experiment". In: *Society of Photo-Optical Instrumentation Engineers (SPIE) Conference Series*. Vol. 10399. Society of Photo-Optical Instrumentation Engineers (SPIE) Conference Series. Aug. 2017, 103990J. DOI: 10.1117/12.2274675.

Buitrago-Casas, J. C. et al. "Methods for reducing singly reflected rays on the Wolter-I focusing mirrors of the FOXSI rocket experiment". In: *Optics for EUV, X-Ray, and Gamma-Ray Astronomy VIII*. Vol. 10399. International Society for Optics and Photonics. 2017, 103990J.

Buitrago-Casas, J. C. et al. *On the faintest solar coronal hard X-rays observed with FOXSI*. 2022. DOI: 10.48550/ARXIV.2205.04291. URL: https://arxiv.org/abs/2205.04291.

Buitrago-Casas, J. C. et al. "Use of a ray-tracing simulation to characterize ghost rays in the FOXSI rocket experiment". In: *Journal of Instrumentation* 15.11 (2020), P11032.

Camattari, Riccardo et al. "Thick self-standing bent crystals as optical elements for a Laue lens for applications in astrophysics". In: *Experimental Astronomy* 46.2 (2018), pp. 309–321.

Cargill, Peter J. "Some implications of the nanoflare concept". In: *The Astrophysical Journal* 422 (1994), pp. 381–393.

Cargill, PJ, Stephen J Bradshaw, and James A Klimchuk. "Enthalpy-based thermal evolution of loops. II. Improvements to the model". In: *The Astrophysical Journal* 752.2 (2012), p. 161.

— "Enthalpy-based thermal evolution of loops. III. Comparison of zero-dimensional models". In: *The Astrophysical Journal* 758.1 (2012), p. 5.

Carlsson, Mats, Bart De Pontieu, and Viggo H Hansteen. "New view of the solar chromosphere". In: *Annual Review of Astronomy and Astrophysics* 57 (2019), pp. 189–226.

Carmichael, HUGH. "54 A PROCESS FOR FLARES". In: *Proceedings of a Symposium Held at the Goddard Space Flight Center, Greenbelt, Maryland, October 28-30, 1963*. Vol. 50. Scientific and Technical Information Division, National Aeronautics and . . . 1964, p. 451.

Carroll, Bradley W and Dale A Ostlie. *An Introduction to Modern Astrophysics and Cosmology*. 2010.

Casadei, Diego. "Objective Bayesian analysis of "on/off" measurements". In: *The Astrophysical Journal* 798.1 (2014), p. 5.

Cash, Webster C. *Medical uses of focused and imaged x-rays*. US Patent 6,359,963. Mar. 2002.

Caspi, A. and R. P. Lin. "RHESSI line And Continuum Observations Of Super-Hot Flare Plasma". In: *The Astrophysical Journal* 725.2 (Dec. 2010), pp. L161–L166. DOI: 10.1088/2041-8205/725/2/l161. URL: https://doi.org/10.1088/2041-8205/725/2/l161.

Cassak, PA, JF Drake, and MA Shay. "A model for spontaneous onset of fast magnetic reconnection". In: *The Astrophysical Journal Letters* 644.2 (2006), p. L145.

Chambure, Daniel de et al. "X-ray baffle of the XMM telescope: development and results". In: *Design and Engineering of Optical Systems II*. Vol. 3737. International Society for Optics and Photonics. 1999, pp. 396–408.

Champey, Patrick et al. "X-ray evaluation of the Marshall Grazing Incidence X-ray Spectrometer (MaGIXS) nickel-replicated mirrors". In: *Optics for EUV, X-Ray, and Gamma-Ray Astronomy IX*. Vol. 11119. International Society for Optics and Photonics. 2019, p. 1111917.

Chandrasekhar, S. *An Introduction to the Study of Stellar Structure*. Astrophysical monographs. Dover Publications, 1957. ISBN: 9780486604138. URL: https://books.google.com/books?id=VwPLAgAAQBAJ.

Che, H and GP Zank. "Electron Acceleration from Expanding Magnetic Vortices During Reconnection with a Guide Field". In: *The Astrophysical Journal* 889.1 (2020), p. 11.

Chen, Bin et al. "Particle acceleration by a solar flare termination shock". In: *Science* 350.6265 (2015), pp. 1238–1242.

Cheung, Mark CM et al. "Thermal diagnostics with the atmospheric imaging assembly on board the solar dynamics observatory: a validated method for differential emission measure inversions". In: *The Astrophysical Journal* 807.2 (2015), p. 143.

Chitta, LP, HN Smitha, and Sami K Solanki. "Solar photosphere". In: *Oxford Research Encyclopedia of Physics*. 2020.

Christe, Steven et al. "Foxsi-2: Upgrades of the focusing optics x-ray solar imager for its second flight". In: *Journal of Astronomical Instrumentation* 5.01 (2016), p. 1640005.

Christe, Steven D, Juan Camilo Buitrago-Casas, and Robert Taylor. *foxsi/foxsi-optics-sim*. Version v1.0. Sept. 2019. DOI: 10.5281/zenodo.3445460. URL: https://doi.org/10.5281/zenodo.3445460.

Christe, Steven D et al. "FOXSI-2: Upgrades of the Focusing Optics X-ray Solar Imager for its Second Flight". In: *Journal of Astronomical Instrumentation* 5.1 (Mar. 2016), pp. 1640005–1640625.

Christe, Steven D et al. "RHESSI microflare statistics. I. Flare-finding and frequency distributions". In: *The Astrophysical Journal* 677.2 (2008), p. 1385.

Christensen-Dalsgaard, J. "Solar structure and evolution". In: *Living Reviews in Solar Physics* 18.2 (2021), pp. 1–189.

Cieślak, Michał J, Kelum AA Gamage, and Robert Glover. "Coded-aperture imaging systems: Past, present and future development–A review". In: *Radiation Measurements* 92 (2016), pp. 59–71.

Cirtain, Jonathan W et al. "Energy release in the solar corona from spatially resolved magnetic braids". In: *Nature* 493.7433 (2013), pp. 501–503.

Cirtain, Jonathan W. et al. "Evidence for the release of magnetic free energy using Hi-C observations". In: *AAS/Solar Physics Division Abstracts #44*. Vol. 44. AAS/Solar Physics Division Meeting. July 2013, p. 200.01.

Collaboration, Borexino et al. "Experimental evidence of neutrinos produced in the CNO fusion cycle in the Sun". In: *Nature* 587.7835 (2020), pp. 577–582.

Cooper, Kristopher et al. "NuSTAR observation of a minuscule microflare in a solar active region". In: *The Astrophysical Journal Letters* 893.2 (2020), p. L40.

Cooper, Kristopher et al. "NuSTAR observations of a repeatedly microflaring active region". In: *Monthly Notices of the Royal Astronomical Society* 507.3 (2021), pp. 3936–3951.

Cox, A.N., W.C. Livingston, and M.S. Matthews. *Solar Interior and Atmosphere*. Space Science Series. University of Arizona Press, 1991. ISBN: 9780816538614. URL: https://books.google.com/books?id=lT9IDwAAQBAJ.

Craig, IJD, AN McClymont, and JH Underwood. "The temperature and density structure of active region coronal loops". In: *Astronomy and Astrophysics* 70 (1978), p. 1.

Cranmer, Steven R. "Coronal holes". In: *Living Reviews in Solar Physics* 6.1 (2009), pp. 1–66.

Cusumano, Giancarlo et al. "Simbol-X: x-ray baffle for stray-light reduction". In: *Optics for EUV, X-Ray, and Gamma-Ray Astronomy III*. Vol. 6688. International Society for Optics and Photonics. 2007, p. 66880C.

Davila, Joseph M. "High-resolution solar imaging with a photon sieve". In: *Solar Physics and Space Weather Instrumentation IV*. Vol. 8148. International Society for Optics and Photonics. 2011, 81480O.

De Pontieu, Bart et al. "On the prevalence of small-scale twist in the solar chromosphere and transition region". In: *Science* 346.6207 (2014).

DeForest, CE, PL Lamy, and A Llebaria. "Solar polar plume lifetime and coronal hole expansion: Determination from long-term observations". In: *The Astrophysical Journal* 560.1 (2001), p. 490.

Del Zanna, G. "The multi-thermal emission in solar active regions". In: *Astronomy & Astrophysics* 558 (2013), A73.

Del Zanna, G, BJI Bromage, and HE Mason. "Spectroscopic characteristics of polar plumes". In: *Astronomy & Astrophysics* 398.2 (2003), pp. 743–761.

Del Zanna, G and HE Mason. "Elemental abundances and temperatures of quiescent solar active region cores from X-ray observations". In: *Astronomy & Astrophysics* 565 (2014), A14.

Del Zanna, G et al. "CHIANTI–An atomic database for emission lines. Version 8". In: *Astronomy & Astrophysics* 582 (2015), A56.

Dennis, BR et al. "Very high-resolution solar X-ray imaging using diffractive optics". In: *Solar Physics* 279.2 (2012), pp. 573–588.

Dhez, P. "Polarizers and polarimeters in the X-UV range". In: *Nuclear Instruments and Methods in Physics Research Section A: Accelerators, Spectrometers, Detectors and Associated Equipment* 261.1-2 (1987), pp. 66–71.

Dijkstra, JH, W De Graaff, and LJ Lantwaard. "Construction of apodised zone plates for solar X-ray image formation". In: *Symposium-International Astronomical Union*. Vol. 41. Cambridge University Press. 1971, pp. 207–210.

Doschek, GA and U Feldman. "The solar UV–x-ray spectrum from 1.5 to 2000 Å". In: *Journal of Physics B: Atomic, Molecular and Optical Physics* 43.23 (2010), p. 232001.

Drake, JF, MA Shay, and M Swisdak. "The Hall fields and fast magnetic reconnection". In: *Physics of Plasmas* 15.4 (2008), p. 042306.

Dreicer, Hz. "Electron and ion runaway in a fully ionized gas. I". In: *Physical Review* 115.2 (1959), p. 238.

Duncan, Jessie. *Energy Release in Solar Microflares and New Methods for X-ray Imaging Spectroscopy*. University of Minnesota. PhD thesis in preparation., 2022.

Duncan, Jessie et al. "NuSTAR Observation of Energy Release in 11 Solar Microflares". In: *The Astrophysical Journal* 908.1 (2021), p. 29.

Duncan, Jessie McBrayer et al. "Modeling Effects of Charge Sharing on the Response of the FOXSI Sounding Rockets". In: *AGU Fall Meeting 2021*. AGU. 2021.

Eadie, William Templeton, Daniel Drijard, and Frederick E James. "Statistical methods in experimental physics". In: *Amsterdam: North-Holland* (1971).

Ebrahimi, Zanyar, Kayoomars Karami, and Roberto Soler. "The effect of a twisted magnetic field on the phase mixing of the kink magnetohydrodynamic waves in coronal loops". In: *The Astrophysical Journal* 845.1 (2017), p. 86.

Eff-Darwich, Antonio and Sylain G Korzennik. "The dynamics of the solar radiative zone". In: *Solar Dynamics and Magnetism from the Interior to the Atmosphere.* Springer, 2012, pp. 43–56.

Elwert, G. "X-ray picture of the sun taken with Fresnel zone plates". In: *Structure and Development of Solar Active Regions.* Springer, 1968, pp. 439–443.

Engström, P et al. "A submicron synchrotron X-ray beam generated by capillary optics". In: *Nuclear Instruments and Methods in Physics Research Section A: Accelerators, Spectrometers, Detectors and Associated Equipment* 302.3 (1991), pp. 547–552.

Fan, Yuhong. "Magnetic fields in the solar convection zone". In: *Living Reviews in Solar Physics* 6.1 (2009), pp. 1–96.

Feldman, U and KG Widing. "Elemental abundances in the solar upper atmosphere derived by spectroscopic means". In: *Space Science Reviews* 107.3 (2003), pp. 665–720.

Ferreira, Desiree Della Monica et al. "Hard x-ray/soft gamma-ray telescope designs for future astrophysics missions". In: *Optics for EUV, X-Ray, and Gamma-Ray Astronomy VI.* Vol. 8861. International Society for Optics and Photonics. 2013, p. 886116.

Fleishman, Gregory D et al. "Energy budget of plasma motions, heating, and electron acceleration in a three-loop solar flare". In: *arXiv preprint arXiv:2104.00811* (2021).

Fletcher, L and Hugh Hudson. "Impulsive phase flare energy transport by large-scale Alfvén waves and the electron acceleration problem". In: *The Astrophysical Journal* 675.2 (2008), p. 1645.

Fontenla, JM, EH Avrett, and R Loeser. "Energy balance in the solar transition region. I-Hydrostatic thermal models with ambipolar diffusion". In: *The Astrophysical Journal* 355 (1990), pp. 700–718.

— "Energy balance in the solar transition region. III-Helium emission in hydrostatic, constant-abundance models with diffusion". In: *The Astrophysical Journal* 406 (1993), pp. 319–345.

Frojdh, E et al. "Timepix3: first measurements and characterization of a hybrid-pixel detector working in event driven mode". In: *Journal of Instrumentation* 10.01 (Jan. 2015), pp. C01039–C01039. DOI: 10.1088/1748-0221/10/01/c01039. URL: https://doi.org/10.1088/1748-0221/10/01/c01039.

Frontera, F et al. "HAXTEL: A Laue lens telescope development project for a deep exploration of the hard X-ray sky (¿ 60 keV)". In: *Experimental Astronomy* 20.1 (2005), pp. 241–251.

Furukawa, Kento et al. "Development of 60 μm pitch CdTe double-sided strip detectors for the FOXSI-3 sounding rocket experiment". In: *Nuclear Instruments and Methods in Physics Research Section A: Accelerators, Spectrometers, Detectors and Associated Equipment* 924 (2019), pp. 321–326.

Furukawa, Kento et al. "Imaging and spectral performance of a 60μm pitch CdTe Double-Sided Strip Detector". In: *Nuclear Instruments and Methods in Physics Research Section A: Accelerators, Spectrometers, Detectors and Associated Equipment* 978 (2020), p. 164378.

Gabriel, AH. "A Discussion on the physics of the solar atmosphere-A magnetic model of the solar transition region". In: *Philosophical Transactions of the Royal Society of London. Series A, Mathematical and Physical Sciences* 281.1304 (1976), pp. 339–352.

Gaetz, Terrance J et al. "Calibrating the wings of the Chandra PSF". In: *X-Ray and Gamma-Ray Instrumentation for Astronomy XIII*. Vol. 5165. SPIE. 2004, pp. 411–422.

Gaetz, Terrance J et al. "Orbital verification of the CXO high-resolution mirror assembly alignment and vignetting". In: *X-Ray Optics, Instruments, and Missions III*. Vol. 4012. International Society for Optics and Photonics. 2000, pp. 41–52.

Gaspari, M De et al. "Design of the analog front-end for the Timepix3 and Smallpix hybrid pixel detectors in 130 nm CMOS technology". In: *Journal of Instrumentation* 9.01 (Jan. 2014), pp. C01037–C01037. DOI: 10.1088/1748-0221/9/01/c01037. URL: https://doi.org/10.1088/1748-0221/9/01/c01037.

Gehrels, Neil. "Confidence limits for small numbers of events in astrophysical data". In: *The Astrophysical Journal* 303 (1986), pp. 336–346.

Gehrels, Neil et al. "The Swift gamma-ray burst mission". In: *The Astrophysical Journal* 611.2 (2004), p. 1005.

Gibson, David and Walter Gibson. "Polycapillary optics: an enabling technology for new applications". In: *Advances in X-ray Analysis* 45 (2002), pp. 286–297.

Glesener, Lindsay. *Faint coronal hard X-rays from accelerated electrons in solar flares*. University of California, Berkeley, 2012.

Glesener, Lindsay et al. "Accelerated electrons observed down to¡ 7 keV in a NuSTAR solar microflare". In: *The Astrophysical Journal Letters* 891.2 (2020), p. L34.

Glesener, Lindsay et al. "NuSTAR hard X-ray observation of a sub-A class solar flare". In: *The Astrophysical Journal* 845.2 (2017), p. 122.

Glesener, Lindsay et al. "The FOXSI solar sounding rocket campaigns". In: *Proceedings of the SPIE, Volume 9905, id. 99050E 12 pp. (2016)*. Vol. 9905. Society of Photo-Optical Instrumentation Engineers (SPIE) Conference Series. SPIE, 2016, 99050E. DOI: 10.1117/12.2232262.

Golub, L. et al. "Solar X-ray bright points". In: *The Astrophysical Journal* 189 (1974), p. L93.

Golub, L. et al. "The Solar-B Mission and the Forefront of Solar Physics". In: *ASP Conf. Ser.* Vol. 325. 2004.

Golub, L. et al. "The X-Ray Telescope (XRT) for the Hinode Mission". In: *Solar Physics* 243.1 (July 2007), pp. 63–86. ISSN: 0038-0938, 1573-093X. DOI: 10.1007/s11207-007-0182-1. URL: http://link.springer.com/10.1007/s11207-007-0182-1 (visited on 11/30/2013).

Gonzalez, Walter and Eugene Parker. "Magnetic reconnection". In: *Astrophysics and Space Science Library* 427 (2016), p. 542.

Gordovskyy, M, PK Browning, and GE Vekstein. "Particle acceleration in a transient magnetic reconnection event". In: *Astronomy & Astrophysics* 519 (2010), A21.

Goryaev, FF et al. "An iterative method in a probabilistic approach to the spectral inverse problem-Differential emission measure from line spectra and broadband data". In: *Astronomy & Astrophysics* 523 (2010), A44.

Grefenstette, Brian W et al. "The first focused hard X-ray images of the Sun with NuSTAR". In: *The Astrophysical Journal* 826.1 (2016), p. 20.

Gregory, Phil. *Bayesian Logical Data Analysis for the Physical Sciences: A Comparative Approach with Mathematica® Support.* Cambridge University Press, 2005.

Grimes, Richard, Balázs Pintér, and Huw Morgan. "Observation of Differential Rotation Within a Sunspot Umbra During an X-Class Flare". In: *Solar Physics* 295.6 (2020), pp. 1–8.

Gubarev, Mikhail, Cheryl Alexander, and Brian D Ramsey. "Alignment, assembly, and testing of high-energy x-ray optics". In: *Optics for EUV, X-Ray, and Gamma-Ray Astronomy II.* Vol. 5900. International Society for Optics and Photonics. 2005, 59000T.

Gubarev, Mikhail et al. "Technology development for high-energy x-ray optics". In: *Space Telescopes and Instrumentation II: Ultraviolet to Gamma Ray.* Vol. 6266. SPIE. 2006, pp. 442–449.

Guennou, Chloé et al. "On the accuracy of the differential emission measure diagnostics of solar plasmas. Application to SDO/AIA. I. Isothermal plasmas". In: *The Astrophysical Journal Supplement Series* 203.2 (2012), p. 25.

Gullikson, E.M. *Optical constants.* 2021. URL: https://henke.lbl.gov/optical_constants/ (visited on 11/03/2021).

Gurnett, DA and WS Kurth. "Plasma densities near and beyond the heliopause from the Voyager 1 and 2 plasma wave instruments". In: *Nature Astronomy* 3.11 (2019), pp. 1024–1028.

Hannah, Iain G and Eduard P Kontar. "Differential emission measures from the regularized inversion of Hinode and SDO data". In: *Astronomy & Astrophysics* 539 (2012), A146.

Hannah, Iain G et al. "Constraining the hard X-ray properties of the quiet sun with new RHESSI observations". In: *The Astrophysical Journal* 724.1 (2010), p. 487.

Hannah, Iain G et al. "First limits on the 3-200 keV X-ray spectrum of the quiet sun using RHESSI". In: *The Astrophysical Journal* 659.1 (2007), p. L77.

Hannah, Iain G et al. "Joint X-Ray, EUV, and UV Observations of a Small Microflare". In: *The Astrophysical Journal* 881.2 (2019), p. 109.

Hannah, Iain G et al. "RHESSI microflare statistics. II. X-ray imaging, spectroscopy, and energy distributions". In: *The Astrophysical Journal* 677.1 (2008), p. 704.

Hannah, IG et al. "Microflares and the statistics of X-ray flares". In: *Space science reviews* 159.1 (2011), pp. 263–300.

Hansen, Carl J, Steven D Kawaler, and Virginia Trimble. *Stellar interiors: physical principles, structure, and evolution.* Springer Science & Business Media, 2012.

Harrison, Fiona A et al. "The nuclear spectroscopic telescope array (NuSTAR) high-energy X-ray mission". In: *The Astrophysical Journal* 770.2 (2013), p. 103.

Henke, Burton L, Eric M Gullikson, and John C Davis. "X-ray interactions: photoabsorption, scattering, transmission, and reflection at E= 50-30,000 eV, Z= 1-92". In: *Atomic data and nuclear data tables* 54.2 (1993), pp. 181–342.

Hirayama, T. "Theoretical model of flares and prominences". In: *Solar Physics* 34.2 (1974), pp. 323–338.

Holman, G. D., M. R. Kundu, and K. Papadopoulos. "Electron pitch angle scattering and the impulsive phase microwave and hard X-ray emission from solar flares". In: *The Astrophysical Journal* 257 (June 1982), p. 354. DOI: 10.1086/159994. URL: https://doi.org/10.1086/159994.

Holman, Gordon D. "Acceleration of runaway electrons and Joule heating in solar flares". In: *Symposium-International Astronomical Union*. Vol. 107. Cambridge University Press. 1985, pp. 191–196.

— "DC electric field acceleration of ions in solar flares". In: *The Astrophysical Journal* 452 (1995), p. 451.

Holman, Gordon D et al. "Implications of X-ray observations for electron acceleration and propagation in solar flares". In: *Space science reviews* 159.1-4 (2011), p. 107.

Howells, Malcolm R et al. "Theory and practice of elliptically bent x-ray mirrors". In: *Optical Engineering* 39.10 (2000), pp. 2748–2762.

Huba, JD and LI Rudakov. "Hall magnetic reconnection rate". In: *Physical review letters* 93.17 (2004), p. 175003.

Hudec, Rene et al. "Kirkpatrick Baez X-ray optics for astrophysics: Recent status". In: *Contributions of the Astronomical Observatory Skalnate Pleso* (2018).

Hudson, Hugh. "A purely coronal hard X-ray event". In: *The Astrophysical Journal* 224 (1978), pp. 235–240.

— "Solar flares add up". In: *Nature Physics* 6.9 (2010), pp. 637–638.

— "Solar flares, microflares, nanoflares, and coronal heating". In: *Solar Physics* 133.2 (1991), pp. 357–369.

Hughes, D.W., R. Rosner, and N.O. Weiss. *The Solar Tachocline*. Cambridge University Press, 2007. ISBN: 9781139462587. URL: https://books.google.com/books?id=1WD5xUp8fWIC.

Hurford, Gordon J. "X-ray imaging with collimators, masks and grids". In: *Observing photons in space*. Springer, 2013, pp. 243–254.

Ishikawa, Shin-nosuke et al. "Constraining hot plasma in a non-flaring solar active region with FOXSI hard X-ray observations". In: *Publications of the Astronomical Society of Japan* 66.SP1 (2014).

Ishikawa, Shin-nosuke et al. "Detection of nanoflare-heated plasma in the solar corona by the FOXSI-2 sounding rocket". In: *Nature Astronomy* 1.11 (2017), pp. 771–774.

Ishikawa, Shin-nosuke et al. "High-speed X-ray imaging spectroscopy system with Zynq SoC for solar observations". In: *Nuclear Instruments and Methods in Physics Research Section A: Accelerators, Spectrometers, Detectors and Associated Equipment* 912 (2018), pp. 191–194.

Jackson, John David. *Classical electrodynamics*. 1999.

Janvier, Miho. "Three-dimensional magnetic reconnection and its application to solar flares". In: *Journal of Plasma Physics* 83.1 (2017).

Ji, Hantao et al. "Magnetic reconnection with Sweet-Parker characteristics in two-dimensional laboratory plasmas". In: *Physics of Plasmas* 6.5 (1999), pp. 1743–1750.

Kane, SR. "Impulsive (flash) phase of solar flares: Hard X-ray, microwave, EUV and optical observations". In: *Symposium-International Astronomical Union*. Vol. 57. Cambridge University Press. 1974, pp. 105–141.

Kashyap, Vinay and Jeremy J Drake. "Markov-Chain Monte Carlo reconstruction of emission measure distributions: application to solar extreme-ultraviolet spectra". In: *The Astrophysical Journal* 503.1 (1998), p. 450.

Kasper, JC et al. "Parker Solar Probe enters the magnetically dominated solar corona". In: *Physical review letters* 127.25 (2021), p. 255101.

Khan, Gufran S et al. "Deterministic computer-controlled polishing process for high-energy x-ray optics". In: *Optical Fabrication and Testing*. Optical Society of America. 2010, OThB2.

Kilaru, Kiranmayee et al. "Full-shell x-ray optics development at NASA Marshall Space Flight Center". In: *Journal of astronomical telescopes, instruments, and systems* 5.2 (2019), p. 021010.

Kiplinger, AL et al. "Fast variations in high-energy X-rays from solar flares and their constraints on nonthermal models". In: *The Astrophysical Journal* 287 (1984), pp. L105–L108.

Kipp, L et al. "Sharper images by focusing soft X-rays with photon sieves". In: *Nature* 414.6860 (2001), pp. 184–188.

Kirkpatrick, Paul and Albert V. Baez. "Formation of optical images by X-rays." In: *Journal of the Optical Society of America* 38 9 (1948), pp. 766–74.

Klimchuck, J. "How do we Solve the Coronal Heating Problem?" In: *SOHO 15 Coronal Heating*. Vol. 575. 2004, p. 2.

Klimchuk, JA, S Patsourakos, and PJ Cargill. "Highly efficient modeling of dynamic coronal loops". In: *The Astrophysical Journal* 682.2 (2008), p. 1351.

Klimchuk, James A. "Key aspects of coronal heating". In: *Philosophical Transactions of the Royal Society A: Mathematical, Physical and Engineering Sciences* 373.2042 (2015), p. 20140256.

— "On solving the coronal heating problem". In: *Solar Physics* 234.1 (2006), pp. 41–77.

Knödlseder, Jürgen et al. "GRI: focusing on the evolving violent universe". In: *Experimental Astronomy* 23.1 (2009), pp. 121–138.

Knoetig, Max L. "Signal discovery, limits, and uncertainties with sparse on/off measurements: an objective bayesian analysis". In: *The Astrophysical Journal* 790.2 (2014), p. 106.

Knoll, Glenn F. *Radiation detection and measurement*. John Wiley & Sons, 2010.

Kobayashi, Ken et al. "The Marshall Grazing Incidence X-ray Spectrometer (MaGIXS)". In: *Proc. SPIE*. Vol. 10699. Society of Photo-Optical Instrumentation Engineers (SPIE) Conference Series. July 2018, p. 1069927. DOI: 10.1117/12.2313997.

Kohl, John L et al. "Ultraviolet spectroscopy of the extended solar corona". In: *The Astronomy and Astrophysics Review* 13.1-2 (2006), pp. 31–157.

Kontar, EP et al. "Deducing electron properties from hard X-ray observations". In: *Space science reviews* 159.1 (2011), pp. 301–355.

Kopp, Greg, George Lawrence, and Gary Rottman. "The total irradiance monitor (TIM): science results". In: *The Solar Radiation and Climate Experiment (SORCE)*. Springer, 2005, pp. 129–139.

Kopp, RA and GW Pneuman. "Magnetic reconnection in the corona and the loop prominence phenomenon". In: *Solar Physics* 50.1 (1976), pp. 85–98.

Kosugi, Takeo et al. "The Hinode (Solar-B) mission: an overview". In: *The Hinode Mission* (2007), pp. 5–19.

Kramer, G, HJ Einighammer, and H Brauninger. "Imaging of solar active regions with Fresnel zone plates". In: *X-ray imaging*. Vol. 106. SPIE. 1977, pp. 79–85.

Kretzschmar, Matthieu et al. "The effect of flares on total solar irradiance". In: *Nature Physics* 6.9 (2010), pp. 690–692.

Krucker, Säm and M Battaglia. "Particle densities within the acceleration region of a solar flare". In: *The Astrophysical Journal* 780.1 (2013), p. 107.

Krucker, Säm, AO Benz, and J-P Delaboudiniere. "Coronal EUV and radio variability and heating". In: *Fifth SOHO Workshop: The Corona and Solar Wind Near Minimum Activity*. Vol. 404. 1997, p. 465.

Krucker, Säm and Arnold O Benz. "Are heating events in the quiet solar corona small flares? Multiwavelength observations of individual events". In: *Solar Physics* 191.2 (2000), pp. 341–358.

Krucker, Säm et al. "First Images from the Focusing Optics X-Ray Solar Imager". In: *Astrophysical Journal, Letters* 793.2, L32 (Oct. 2014), p. L32. DOI: `10.1088/2041-8205/793/2/L32`.

Krucker, Säm et al. "Hard X-ray emission from the solar corona". In: *The Astronomy and Astrophysics Review* 16.3-4 (2008), pp. 155–208.

Krucker, Säm et al. "Hard X-ray Microflares down to 3 keV". In: *The Reuven Ramaty High-Energy Solar Spectroscopic Imager (RHESSI)*. Springer, 2003, pp. 445–456.

Krucker, Säm et al. "Solar flare electron spectra at the Sun and near the Earth". In: *The Astrophysical Journal Letters* 663.2 (2007), p. L109.

Krucker, Säm et al. "The Focusing Optics X-ray Solar Imager (FOXSI)". In: *Optics for EUV, X-Ray, and Gamma-Ray Astronomy IV. Edited by O'Dell, Stephen L.; Pareschi, Giovanni. Proceedings of the SPIE, Volume 7437 (2009)., article id. 743705, 10 pp. (2009)*. Vol. 7437. Society of Photo-Optical Instrumentation Engineers (SPIE) Conference Series. SPIE, 2009, p. 743705. DOI: `10.1117/12.827950`.

Krucker, Säm et al. "The focusing optics X-ray solar imager (FOXSI)". In: *Optics for EUV, X-Ray, and Gamma-Ray Astronomy V*. Vol. 8147. SPIE. 2011, pp. 45–58.

Krucker, Säm et al. "The focusing optics x-ray solar imager (FOXSI): instrument and first flight". In: *Solar Physics and Space Weather Instrumentation V*. Ed. by Silvano Fineschi and Judy Fennelly. Vol. 8862. Society of Photo-Optical Instrumentation Engineers (SPIE) Conference Series. Sept. 2013, 88620R. DOI: `10.1117/12.2024277`.

Krucker, Säm et al. "The spectrometer/telescope for imaging X-rays (STIX)". In: *Astronomy & Astrophysics* 642 (2020), A15.

Krucker, Säm et al. "X-ray network flares of the quiet sun". In: *The Astrophysical Journal* 488.1 (1997), p. 499.

Kruth, A et al. "GOSSIPO-3: measurements on the prototype of a read-out pixel chip for Micro-Pattern Gaseous Detectors". In: *Journal of Instrumentation* 5.12 (Dec. 2010), pp. C12005–C12005. DOI: 10.1088/1748-0221/5/12/c12005. URL: https://doi.org/10.1088/1748-0221/5/12/c12005.

Kulsrud, Russell M. "Magnetic reconnection: Sweet-parker versus petschek". In: *Earth, Planets and Space* 53.6 (2001), pp. 417–422.

Landi, E, U Feldman, and KP Dere. "CHIANTI—An atomic database for emission lines. V. Comparison with an isothermal spectrum observed with SUMER". In: *The Astrophysical Journal Supplement Series* 139.1 (2002), p. 281.

Landi, E et al. "CHIANTI—an atomic database for emission lines. VII. New data for X-rays and other improvements". In: *The Astrophysical Journal Supplement Series* 162.1 (2006), p. 261.

Lang, KR. "Book-Review-Astrophysical Formulae". In: *Journal of the Royal Astronomical Society of Canada* 74 (1980), pp. 183–184.

Leenaarts, Jorrit, Mats Carlsson, and L Rouppe Van Der Voort. "The formation of the Hα line in the solar chromosphere". In: *The Astrophysical Journal* 749.2 (2012), p. 136.

Leo, William R. *Techniques for nuclear and particle physics experiments: a how-to approach.* Springer Science & Business Media, 2012.

Li, T-P and Y-Q Ma. "Analysis methods for results in gamma-ray astronomy". In: *The Astrophysical Journal* 272 (1983), pp. 317–324.

Li, Ting, Eric Priest, and Ruilong Guo. "Three-dimensional magnetic reconnection in astrophysical plasmas". In: *arXiv e-prints*, arXiv:2104.05174 (Apr. 2021), arXiv:2104.05174. arXiv: 2104.05174 [astro-ph.SR].

Li, Xiaocan et al. "Particle acceleration during magnetic reconnection in a low-beta plasma". In: *The Astrophysical Journal* 843.1 (2017), p. 21.

Lin, R. "Relationship of solar flare accelerated particles to solar energetic particles (SEPs) observed in the interplanetary medium". In: *Advances in Space Research* 35.10 (2005), pp. 1857–1863.

Lin, Robert et al. "Solar hard X-ray microflares". In: *The Astrophysical Journal* 283 (1984), pp. 421–425.

Lin, Robert P et al. "The Reuven Ramaty high-energy solar spectroscopic imager (RHESSI)". In: *The Reuven Ramaty High-Energy Solar Spectroscopic Imager (RHESSI)*. Springer, 2003, pp. 3–32.

Lin, RP. "The Flash Phase of Solar Flares: Satellite Observations of Electrons". In: *Symposium-International Astronomical Union*. Vol. 57. Cambridge University Press. 1974, pp. 201–223.

Lin, RP and HS Hudson. "Non-thermal processes in large solar flares". In: *Solar Physics* 50.1 (1976), pp. 153–178.

Liu, Yi-Hsin et al. "First-Principles Theory of the Rate of Magnetic Reconnection in Magnetospheric and Solar Plasmas". In: *arXiv preprint arXiv:2203.14268* (2022).

Longcope, Dana. "Solar flares". In: *Oxford Research Encyclopedia of Physics*. 2020.

Longcope, Dana, Loren Acton, and Charles Kankelborg. "Practical, corrected Kirkpatrick-Baez telescope for x-ray astronomy". In: *Applied Optics* 58.18 (2019), pp. 4969–4980.

Madjarska, Maria S. "Coronal bright points". In: *Living Reviews in Solar Physics* 16.1 (2019), pp. 1–79.

Madsen, Kristin K et al. "Observational artifacts of Nuclear Spectroscopic Telescope Array: ghost rays and stray light". In: *Journal of Astronomical Telescopes, Instruments, and Systems* 3.4 (2017), p. 044003.

Malyshkin, Leonid M. "Model of hall reconnection". In: *Physical review letters* 101.22 (2008), p. 225001.

Mariska, John T. *The solar transition region*. Vol. 23. Cambridge University Press, 1992.

Marsh, Andrew J et al. "First NuSTAR limits on quiet sun hard X-ray transient events". In: *The Astrophysical Journal* 849.2 (2017), p. 131.

Marsh, Andrew J et al. "Hard X-Ray Constraints on Small-scale Coronal Heating Events". In: *The Astrophysical Journal* 864.1 (2018), p. 5.

Martinez Oliveros, J et al. "The Solar PolArization and Directivity X-Ray Experiment (PADRE)". In: *American Astronomical Society Meeting Abstracts*. Vol. 53. 6. 2021, pp. 313–09.

McIntosh, Scott W and Joseph B Gurman. "Nine years of EUV bright points". In: *Solar Physics* 228.1 (2005), pp. 285–299.

McIvor, Alan M. "Background subtraction techniques". In: *Proc. of Image and Vision Computing* 4 (2000), pp. 3099–3104.

McTiernan, JM. "RHESSI/GOES observations of the nonflaring Sun from 2002 to 2006". In: *The Astrophysical Journal* 697.1 (2009), p. 94.

Melrose, DB. "Particle beams in the solar atmosphere: General overview". In: *Solar physics* 130.1 (1990), pp. 3–18.

Miceli, M et al. "X-ray emitting hot plasma in solar active regions observed by the SphinX spectrometer". In: *Astronomy & Astrophysics* 544 (2012), A139.

Miesch, Mark S. "Large-scale dynamics of the convection zone and tachocline". In: *Living Reviews in Solar Physics* 2.1 (2005), pp. 1–139.

Mildner, DFR and MV Gubarev. "Wolter optics for neutron focusing". In: *Nuclear Instruments and Methods in Physics Research Section A: Accelerators, Spectrometers, Detectors and Associated Equipment* 634.1 (2011), S7–S11.

Miller, James A et al. "Critical issues for understanding particle acceleration in impulsive solar flares". In: *Journal of Geophysical Research: Space Physics* 102.A7 (Jan. 1997), pp. 14631–14659. DOI: 10.1029/97ja00976. URL: https://doi.org/10.1029/97ja00976.

Milligan, Ryan O. "Solar Irradiance Variability Due To Solar Flares Observed in Lyman-alpha Emission". In: *Solar Physics* 296.3 (2021), pp. 1–13.

Mimura, Hidekazu et al. "Advanced fabrication technologies for ultraprecise replicated mirrors for x-ray telescopes". In: *Space Telescopes and Instrumentation 2020: Ultraviolet to Gamma Ray*. Vol. 11444. SPIE. 2020, pp. 163–170.

Mimura, Hidekazu et al. "Fabrication of a precise ellipsoidal mirror for soft X-ray nanofo-cusing". In: *Review of Scientific Instruments* 89.9, 093104 (Sept. 2018), p. 093104. DOI: 10.1063/1.5035323.

Mitalas, R and KR Sills. "On the photon diffusion time scale for the sun". In: *The Astrophysical Journal* 401 (1992), p. 759.

Mondal, Surajit et al. "First radio evidence for ubiquitous magnetic reconnections and impulsive heating in the quiet solar corona". In: *EGU General Assembly Conference Abstracts*. 2021, EGU21–14168.

Müller, Daniel et al. "The solar orbiter mission-science overview". In: *Astronomy & Astrophysics* 642 (2020), A1.

Mumford, Stuart et al. "SunPy: a python package for solar physics". In: *Journal of Open Source Software* 5.46 (2020).

Musset, Sophie et al. "Ghost-ray reduction and early results from the third FOXSI sounding rocket flight". In: *UV, X-Ray, and Gamma-Ray Space Instrumentation for Astronomy XXI*. Vol. 11118. International Society for Optics and Photonics. 2019, p. 1111812.

Nakariakov, VM et al. "TRACE observation of damped coronal loop oscillations: Implications for coronal heating". In: *Science* 285.5429 (1999), pp. 862–864.

Narukage, Noriyuki et al. "High-speed back-illuminated CMOS sensor for photon-counting-type imaging-spectroscopy in the soft X-ray range". In: *Nuclear Instruments and Methods in Physics Research Section A: Accelerators, Spectrometers, Detectors and Associated Equipment* 950 (2020), p. 162974.

Neupert, Werner M. "Comparison of solar X-ray line emission with microwave emission during flares". In: *The Astrophysical Journal* 153 (1968), p. L59.

Ning, Zongjun. "RHESSI microflares with quiet microwave emission". In: *The Astrophysical Journal* 686.1 (2008), p. 674.

Noglik, JB and RW Walsh. "Investigation of a color-color method to determine temperatures along coronal structures using trace data". In: *The Astrophysical Journal* 655.2 (2007), p. 1127.

Nosek, Dalibor and Jana Nosková. "On Bayesian analysis of on–off measurements". In: *Nuclear Instruments and Methods in Physics Research Section A: Accelerators, Spectrometers, Detectors and Associated Equipment* 820 (2016), pp. 23–33.

O'Dell, Stephen L et al. "High-resolution x-ray telescopes". In: *Adaptive X-Ray Optics*. Vol. 7803. International Society for Optics and Photonics. 2010, 78030H.

O'Dell, Stephen L et al. "X-ray optics at NASA Marshall Space Flight Center". In: *SPIE Optics+ Optoelectronics*. International Society for Optics and Photonics. 2015, pp. 951003–951003.

Oda, M. "X-ray imaging techniques—modulation collimator and coded mask". In: *Advances in Space Research* 2.4 (1982), pp. 207–216.

Oda, Minoru. "High-resolution x-ray collimator with broad field of view for astronomical use". In: *Applied Optics* 4.1 (1965), pp. 143–143.

Ogasaka, Yasushi et al. "Characterization of a hard x-ray telescope at synchrotron facility SPring-8". In: *Japanese Journal of Applied Physics* 47.7R (2008), p. 5743.

Ohmori, Hitoshi et al. "A high quality surface finish grinding process to produce total reflection mirror for x-ray fluorescence analysis". In: *International Journal of Extreme Manufacturing* 2.1 (2020), p. 015101.

Okoshi, Takanori. *Optical fibers*. Elsevier, 2012.

Paraschiv, AR, Alessandro Bemporad, and AC Sterling. "Physical properties of solar polar jets-A statistical study with Hinode XRT data". In: *Astronomy & Astrophysics* 579 (2015), A96.

Parker, Eugene. "Acceleration of cosmic rays in solar flares". In: *Physical Review* 107.3 (1957), p. 830.

— "Nanoflares and the solar X-ray corona". In: *The Astrophysical Journal* 330 (1988), pp. 474–479.

Parnell, CE and PE Jupp. "Statistical analysis of the energy distribution of nanoflares in the quiet Sun". In: *The Astrophysical Journal* 529.1 (2000), p. 554.

Peter, H. "On the nature of the transition region from the chromosphere to the corona of the Sun". In: *Astronomy & Astrophysics* 374.3 (2001), pp. 1108–1120.

Petrosian, Vahé. "Particle acceleration in solar flares and associated CME shocks". In: *The Astrophysical Journal* 830.1 (2016), p. 28.

Petschek, Harry E. "Magnetic field annihilation". In: *NASA Special Publication* 50 (1964), p. 425.

Phillips, K.J.H. *Guide to the Sun*. Cambridge University Press, 1995. ISBN: 9780521397889. URL: https://books.google.com/books?id=idwBChjVP0gC.

Phillips, Kenneth JH, Uri Feldman, and Enrico Landi. *Ultraviolet and X-ray Spectroscopy of the Solar Atmosphere*. Vol. 44. Cambridge University Press Cambridge, 2008.

Phillips, KJH et al. "Solar flare X-ray spectra from the solar maximum mission flat crystal spectrometer". In: *The Astrophysical Journal* 256 (1982), pp. 774–787.

Piana, Michele et al. *Hard X-Ray Imaging of Solar Flares*. 2022.

Piccardi, Massimo. "Background subtraction techniques: a review". In: *2004 IEEE International Conference on Systems, Man and Cybernetics (IEEE Cat. No. 04CH37583)*. Vol. 4. IEEE. 2004, pp. 3099–3104.

Poikela, T et al. "Timepix3: a 65K channel hybrid pixel readout chip with simultaneous ToA/ToT and sparse readout". In: *Journal of Instrumentation* 9.05 (May 2014), pp. C05013–C05013. DOI: 10.1088/1748-0221/9/05/c05013. URL: https://doi.org/10.1088/1748-0221/9/05/c05013.

Priest, ER. *Magnetohydrodynamics of the Sun*. 2014. DOI: 10.1017/CBO9781139020732.

— "The structure of coronal loops". In: *Solar Physics* 58.1 (1978), pp. 57–87.

Priest, ER and TG Forbes. "The magnetic nature of solar flares". In: *The Astronomy and Astrophysics Review* 10.4 (2002), pp. 313–377.

Ramsey, Brian D. "Replicated Nickel Optics for the Hard-X-Ray Region". In: *Experimental Astronomy* 20.1-3 (Dec. 2005), pp. 85–92. DOI: 10.1007/s10686-006-9033-6.

Ramsey, Brian D and Martin C Weisskopf. "Hard-X-Ray Optics Development at Marshall Space Flight Center". In: *arXiv preprint astro-ph/0403449* (2004).

Ramsey, Brian D et al. "First Images from HERO, a Hard X-Ray Focusing Telescope". In: *Astrophysical Journal* 568.1 (Mar. 2002), pp. 432–435. DOI: 10.1086/338801.

Reale, Fabio. "Coronal loops: observations and modeling of confined plasma". In: *Living Reviews in Solar Physics* 11.1 (2014), pp. 1–94.

Reale, Fabio, James M McTiernan, and Paola Testa. "Comparison of Hinode/XRT and RHESSI detection of hot plasma in the non-flaring solar corona". In: *The Astrophysical Journal* 704.1 (2009), p. L58.

Ren, Xiaoxia et al. "Chianti: a tool for change impact analysis of java programs". In: *Proceedings of the 19th annual ACM SIGPLAN conference on Object-oriented programming, systems, languages, and applications.* 2004, pp. 432–448.

Reva, Anton et al. "Estimate of the upper limit on hot plasma differential emission measure (DEM) in non-flaring active regions and nanoflare frequency based on the Mg XII spectroheliograph data from CORONAS-F/SPIRIT". In: *Solar Physics* 293.10 (2018), pp. 1–15.

Río, Manuel Sánchez del and Roger J Dejus. "XOP v2. 4: recent developments of the x-ray optics software toolkit". In: *Advances in computational methods for X-ray optics II.* Vol. 8141. International Society for Optics and Photonics. 2011, p. 814115.

Rutherford, Ernest. "The scattering of α and β particles by matter and the structure of the atom". In: *Philosophical Magazine* 92.4 (1911), pp. 379–398.

Ryan, Daniel F et al. "The thermal properties of solar flares over three solar cycles using GOES X-ray observations". In: *The Astrophysical Journal Supplement Series* 202.2 (2012), p. 11.

Saar, S, S Farid, and E Deluca. "Thermal And Statistical Properties of X-ray Bright Points". In: *AIP Conference Proceedings.* Vol. 1094. 1. American Institute of Physics. 2009, pp. 756–759.

Sahu, Suraj et al. "Hard X-ray emission from an activated flux rope and subsequent evolution of an eruptive long-duration solar flare". In: *The Astrophysical Journal* 897.2 (2020), p. 157.

Saint-Hilaire, Pascal and Arnold O Benz. "Thermal and non-thermal energies of solar flares". In: *Astronomy & Astrophysics* 435.2 (2005), pp. 743–752.

Saint-Hilaire, Pascal, Säm Krucker, and R. P. Lin. "A Statistical Survey of Hard X-ray Spectral Characteristics of Solar Flares with Two Footpoints". In: *Solar Physics* 250.1 (July 2008), pp. 53–73. DOI: 10.1007/s11207-008-9193-9. arXiv: 1111.4247 [astro-ph.SR].

Schlickeiser, Reinhard and James A Miller. "Quasi-linear theory of cosmic ray transport and acceleration: the role of oblique magnetohydrodynamic waves and transit-time damping". In: *The Astrophysical Journal* 492.1 (1998), p. 352.

Schmelz, JT et al. "Hinode X-ray telescope detection of hot emission from quiescent active regions: a nanoflare signature?" In: *The Astrophysical Journal* 693.2 (2009), p. L131.

Schmitz, Robert. *Simulation of polycapillary and multichannel plate x-ray optics.* 2011.

Schrijver, CJ et al. "Estimating the frequency of extremely energetic solar events, based on solar, stellar, lunar, and terrestrial records". In: *Journal of Geophysical Research: Space Physics* 117.A8 (2012).

Shibata, K. et al. "Hot-Plasma Ejections Associated with Compact-Loop Solar Flares". In: *The Astrophysical Journal* 451 (Oct. 1995), p. L83. DOI: 10.1086/309688.

Shimizu, Toshifumi. "Energetics and occurrence rate of active-region transient brightenings and implications for the heating of the active-region corona". In: *Publications of the Astronomical Society of Japan* 47 (1995), pp. 251–263.

Simões, P and E Kontar. "Implications for electron acceleration and transport from non-thermal electron rates at looptop and footpoint sources in solar flares". In: *Astronomy & Astrophysics* 551 (2013), A135.

Simon, George W and Robert W Noyes. "Observed heights of EUV lines formed in the transition zone and corona". In: *Solar Physics* 22.2 (1972), pp. 450–458.

Skinner, Gerry K et al. "Science enabled by high precision inertial formation flying". In: *International Journal of Space Science and Engineering 5* 1.4 (2013), pp. 331–348.

Somov, Boris V. *Physical processes in solar flares*. Vol. 172. Springer Science & Business Media, 2012.

— *Plasma Astrophysics, Part I: Fundamentals and Practice*. Vol. 391. Springer Science & Business Media, 2012.

— *Plasma Astrophysics, Part II: Reconnection and Flares*. Vol. 392. Springer Science & Business Media, 2012.

Soufli, Regina and Eric M Gullikson. "Reflectance measurements on clean surfaces for the determination of optical constants of silicon in the extreme ultraviolet–soft-x-ray region". In: *Applied Optics* 36.22 (1997), pp. 5499–5507.

Soufli, Regina et al. "Development and testing of EUV multilayer coatings for the atmospheric imaging assembly instrument aboard the Solar Dynamics Observatory". In: *Solar Physics and Space Weather Instrumentation*. Vol. 5901. SPIE. 2005, pp. 173–183.

Spiga, Daniele. "Analytical computation of stray light in nested mirror modules for x-ray telescopes". In: *Optics for EUV, X-Ray, and Gamma-Ray Astronomy VII*. Vol. 9603. International Society for Optics and Photonics. 2016, 96030H.

Spiller, Eberhard Adolf. "Enhancement of the reflectivity of multilayer x-ray mirrors by ion polishing". In: *Optical Engineering* 29.6 (1990), pp. 609–613.

Strong, Keith T et al. "Observations of the variability of coronal bright points by the Soft X-ray Telescope on YOHKOH". In: *Publications of the Astronomical Society of Japan* 44 (1992), pp. L161–L166.

Sturrock, PA. "Model of the high-energy phase of solar flares". In: *Nature* 211.5050 (1966), pp. 695–697.

Subramanian, Srividya et al. "Energetics of Hi-C EUV brightenings". In: *Astronomy & Astrophysics* 615 (2018), A47.

Svestka, Zdenek. *Solar flares*. Vol. 8. Springer Science & Business Media, 2012.

Sweet, Peter A. "The neutral point theory of solar flares". In: *Electromagnetic phenomena in cosmical physics*. Vol. 6. 1958, p. 123.

Sylwester, J et al. "RESIK: a bent crystal X-ray spectrometer for studies of solar coronal plasma composition". In: *Solar Physics* 226.1 (2005), pp. 45–72.

Sylwester, J et al. "SphinX measurements of the 2009 solar minimum X-ray emission". In: *The Astrophysical Journal* 751.2 (2012), p. 111.

Sylwester, Janusz et al. "The Sun's X-ray Emission During the Recent Solar Minimum". In: *EOS Transactions* 91.8 (Feb. 2010), pp. 73–74. DOI: 10.1029/2010EO080002.

Tandberg-Hanssen, Einar and A Gordon Emslie. *The physics of solar flares*. Vol. 14. Cambridge University Press, 1988.

Tayler, R.J. *The Sun as a Star*. Cambridge University Press, 1997. ISBN: 9780521468374. URL: https://books.google.com/books?id=PqTiEv88j7AC.

Testa, Paola, Vanessa Polito, and Bart De Pontieu. "IRIS observations of short-term variability in moss associated with transient hot coronal loops". In: *The Astrophysical Journal* 889.2 (2020), p. 124.

Testa, Paola et al. "Evidence of nonthermal particles in coronal loops heated impulsively by nanoflares". In: *Science* 346.6207 (2014), p. 1255724.

Thompson, William T et al. "The COR1 inner coronagraph for STEREO-SECCHI". In: *Innovative Telescopes and Instrumentation for Solar Astrophysics*. Vol. 4853. International Society for Optics and Photonics. 2003, pp. 1–11.

Tian, Hui. "Probing the solar transition region: current status and future perspectives". In: *Research in Astronomy and Astrophysics* 17.11 (2017), p. 110.

Tritschler, A. et al. "DKIST: Observing the Sun at High Resolution". In: *18th Cambridge Workshop on Cool Stars, Stellar Systems, and the Sun*. Ed. by G. T. van Belle and H. C. Harris. Vol. 18. Cambridge Workshop on Cool Stars, Stellar Systems, and the Sun. Jan. 2015, pp. 933–944.

Trivedi, Ayushi et al. "Study of energy dependent behaviour of half-lens polycapillary optics using synchrotron x-rays". In: *AIP Conference Proceedings*. Vol. 2265. 1. AIP Publishing LLC. 2020, p. 030187.

Tsuneta, S et al. "The soft X-ray telescope for the SOLAR-A mission". In: *Solar Physics* 136.1 (1991), pp. 37–67.

Tsuneta, Saku. "Particle acceleration and magnetic reconnection in solar flares". In: *Publications of the Astronomical Society of Japan* 47 (1995), pp. 691–697.

— "Structure and dynamics of magnetic reconnection in a solar flare". In: *The Astrophysical Journal* 456 (1996), p. 840.

Turecek, Daniel et al. "Application of Timepix3 based CdTe spectral sensitive photon counting detector for PET imaging". In: *Nuclear Instruments and Methods in Physics Research Section A: Accelerators Spectrometers, Detectors and Associated Equipment* 895 (July 2018), pp. 84–89. DOI: 10.1016/j.nima.2018.04.007. URL: https://doi.org/10.1016/j.nima.2018.04.007.

Ugarte-Urra, I et al. "Signature of oscillations in coronal bright points". In: *Astronomy & Astrophysics* 418.1 (2004), pp. 313–324.

Uzdensky, Dmitri A. "Petschek-like reconnection with current-driven anomalous resistivity and its application to solar flares". In: *The Astrophysical Journal* 587.1 (2003), p. 450.

Van Ballegooijen, AA et al. "Heating of the solar chromosphere and corona by Alfvén wave turbulence". In: *The Astrophysical Journal* 736.1 (2011), p. 3.

Van Beek, H Frank et al. "The hard X-ray imaging spectrometer (HXIS)". In: *Solar Physics* 65.1 (1980), pp. 39–52.

VanSpeybroeck, LP and RC Chase. "Design parameters of paraboloid-hyperboloid telescopes for X-ray astronomy". In: *Applied Optics* 11.2 (1972), pp. 440–445.

Vievering, Juliana T. "First Solar Images Using a Photon Sieve". In: (2012).

— "Nature of Energy Release and Transfer for Solar and Stellar Flares Using High-Sensitivity Hard X-ray Instrumentation". PhD thesis. University of Minnesota, 2019.

Vievering, Juliana T. et al. "FOXSI-2 Solar Microflares. II. Hard X-ray Imaging Spectroscopy and Flare Energetics". In: *The Astrophysical Journal* 913.1, 15 (May 2021), p. 15. DOI: `10.3847/1538-4357/abf145`. arXiv: `2011.04753 [astro-ph.SR]`.

Vigil, Genevieve D et al. "Marshall Grazing Incidence X-ray Spectrometer Slitjaw Imager Implementation and Performance". In: *Solar Physics* 296.6 (2021), pp. 1–16.

Virgilli, Enrico. "Laue Lenses in Hard X-ray Astronomy". In: *The WSPC Handbook of Astronomical Instrumentation: Volume 5: Gamma-Ray and Multimessenger Astronomical Instrumentation*. World Scientific, 2021, pp. 1–25.

Vlahos, Loukas, Heinz Isliker, and Nikos Sioulas. "Are Nanoflares Responsible for Coronal Heating?" In: *arXiv preprint arXiv:2108.01722* (2021).

Warmuth, A and G Mann. "Thermal and nonthermal hard X-ray source sizes in solar flares obtained from RHESSI observations-I. Observations and evaluation of methods". In: *Astronomy & Astrophysics* 552 (2013), A86.

Warren, Harry P and Amy R Winebarger. "Density and temperature measurements in a solar active region". In: *The Astrophysical Journal* 596.1 (2003), p. L113.

Weber, MA et al. "Isothermal Bias of the "Filter Ratio" Method for Observations of Multithermal Plasma". In: *The Astrophysical Journal Letters* 635.1 (2005), p. L101.

Werner, W. "Imaging properties of Wolter I type x-ray telescopes". In: *Applied optics* 16.3 (1977), pp. 764–773.

Wik, Daniel R et al. "NuSTAR observations of the bullet cluster: constraints on inverse compton emission". In: *The Astrophysical Journal* 792.1 (2014), p. 48.

Wilhelm, Klaus. "Solar coronal-hole plasma densities and temperatures". In: *Astronomy & Astrophysics* 455.2 (2006), pp. 697–708.

Wilks, Samuel S. *Mathematical statistics*. 1962.

Williams, Thomas et al. "Evidence for and Analysis of Multiple Hidden Coronal Strands in Cross-sectional Emission Profiles: Further Results from NASA's High-resolution Solar Coronal Imager". In: *The Astrophysical Journal* 902.2 (2020), p. 90.

Williams, Thomas et al. "Is the high-resolution coronal imager resolving coronal strands? Results from AR 12712". In: *The Astrophysical Journal* 892.2 (2020), p. 134.

Wilson, R. Mark. "Borexino experiment detects neutrinos from the Sun's carbon-nitrogen-oxygen cycle". In: *Physics Today* 74.2 (2021), p. 12.

Windt, David L. "IMD—Software for modeling the optical properties of multilayer films". In: *Computers in physics* 12.4 (1998), pp. 360–370.

Winebarger, Amy, Lindsay Glesener, and Kathy Reeves. "A White Paper on the Scientific Motivation and Feasibility of Introducing Routine Solar Flare Campaigns for Sounding

Rockets". In: *NASA Sounding Rocket Working Group Website* 1 (2019). URL: https://rscience.gsfc.nasa.gov/keydocs/SolarFlareCampaign.pdf.

Winebarger, Amy et al. "Using a differential emission measure and density measurements in an active region core to test a steady heating model". In: *The Astrophysical Journal* 740.1 (2011), p. 2.

Withbroe, George L and Robert W Noyes. "Mass and energy flow in the solar chromosphere and corona". In: *Annual review of astronomy and astrophysics* 15.1 (1977), pp. 363–387.

Wolf, Emil. *Progress in optics.* Vol. 47. Elsevier, 2005.

— "The diffraction theory of aberrations". In: *Reports on Progress in Physics* 14.1 (Jan. 1951), pp. 95–120. DOI: 10.1088/0034-4885/14/1/304.

Wolter, Hans. "Spiegelsysteme streifenden Einfalls als abbildende Optiken für Röntgenstrahlen". In: *Annalen der Physik* 445.1 (Jan. 1952), pp. 94–114. DOI: 10.1002/andp.19524450108.

— "Zur frage des lichtweges bei totalreflexion". In: *Zeitschrift für Naturforschung A* 5.5 (1950), pp. 276–283.

Woods, Thomas N et al. "Solar irradiance variability during the October 2003 solar storm period". In: *Geophysical research letters* 31.10 (2004).

Yamada, Masaaki. *Magnetic Reconnection: A Modern Synthesis of Theory, Experiment, and Observations.* Vol. 47. Princeton University Press, 2022.

— "Review of controlled laboratory experiments on physics of magnetic reconnection". In: *Journal of Geophysical Research: Space Physics* 104.A7 (1999), pp. 14529–14541.

Yamada, Masaaki, Russell Kulsrud, and Hantao Ji. "Magnetic reconnection". In: *Reviews of Modern Physics* 82.1 (2010), p. 603.

Yamauchi, Kazuto et al. "Two-dimensional submicron focusing of hard X-rays by two elliptical mirrors fabricated by plasma chemical vaporization machining and elastic emission machining". In: *Japanese journal of applied physics* 42.11R (2003), p. 7129.

Yang, Kai E et al. "Observationally quantified reconnection providing a viable mechanism for active region coronal heating". In: *Nature communications* 9.1 (2018), pp. 1–8.

Yokoyama, T and K Shibata. "What is the condition for fast magnetic reconnection?" In: *The Astrophysical Journal* 436 (1994), pp. L197–L200.

Zappon, F et al. "GOSSIPO-4: an array of high resolution TDCs with a PLL control". In: *Journal of Instrumentation* 7.01 (Jan. 2012), pp. C01081–C01081. DOI: 10.1088/1748-0221/7/01/c01081. URL: https://doi.org/10.1088/1748-0221/7/01/c01081.

Zhang, Jie, Mukul R Kundu, and Stephen M White. "Spatial distribution and temporal evolution of coronal bright points". In: *Solar Physics* 198.2 (2001), pp. 347–365.

Zharkova, Valentina V et al. "Recent advances in understanding particle acceleration processes in solar flares". In: *Space science reviews* 159.1-4 (2011), p. 357.

Zweibel, Ellen G and Masaaki Yamada. "Magnetic reconnection in astrophysical and laboratory plasmas". In: *Annual review of astronomy and astrophysics* 47 (2009), pp. 291–332.

— "Perspectives on magnetic reconnection". In: *Proceedings of the Royal Society A: Mathematical, Physical and Engineering Sciences* 472.2196 (2016), p. 20160479.